Faculty of Sciences
Department of Analytical Chemistry
X-ray Microspectroscopy and Imaging

Optimization and applications of mobile, laboratory and synchrotron X-ray based non-destructive microanalysis techniques for the study of cultural heritage objects

Thesis submitted in fulfillment of the requirements for the degree of
Doctor of Sciences: Chemistry

by

Lien Van de Voorde

Supervisor: Prof Dr Laszlo Vincze
Co-supervisor: Prof Dr Peter Vandenabeele
Co-supervisor: Dr Bart Vekemans

8th of October, 2015

Dankwoord

De titel “Dankwoord” hier zien staan op mijn computerscherm, zorgt voor een enorm gevoel van opluchting. De allerlaatste zweetdruppels worden met veel plezier in dit allerlaatste deel van dit werk gestopt want heel wat mensen zijn dit woord van dank meer dan waard. Deze laatste woorden betekenen ook een einde van een eerste periode in mijn professioneel leven die ervoor gezorgd hebben dat ik het diploma van Doctor in de Chemie naast dat van de lerarenopleiding mag toevoegen aan mijn collectie en dat ik mij met volle overgave en met een hernieuwde boost van energie kan storten op mijn nieuwe job in OCAS. Dat enkel de volgende woorden door de meeste mensen worden gelezen , weet ik maar al te goed maar wie zich toch door het volledige werk heeft gewaagd: “Chapeau!”, ik hoop dat je ervan genoten hebt en dat ik je heb kunnen overtuigen van n van mijn leuzes in mijn leven, namelijk dat “METEN, WETEN IS”.

De eerste persoon die ik in dit woord van dank wil vermelden, is mijn promotor prof. dr. Laszlo Vincze, die mij de kans gegeven heeft om in zijn onderzoeksgroep mijn doctoraat uit te voeren. Het geduld dat ik moest opbrengen voor het wachten op verbeteringen heeft me enkele grijze haren bezorgd, maar je steun en toeverlaat, Laszlo, tijdens alle andere momenten, is meer dan goud waard. Je altijd blijvende vriendelijkheid, lach en appreciatie voor mijn talenten hebben er meer dan ooit voor gezord dat dit werk tot een goed einde is gekomen. Dankjewel daarvoor, Laszlo, en ik hoop van harte dat we op latere tijdstippen nog kunnen samenwerken aan gemeenschappelijke projecten.

De volgende personen in volgorde van erkentelijkheid zijn mijn copromotoren prof. dr. Peter Vandenabeele en dr. Bart Vekemans. Peter, jij hebt met je kritische houding ervoor gezorgd dat ik altijd scherp gebleven ben en de kleine duwtjes in de rug die je op de gepaste tijden gaf waren meer dan welkom. Ook al je naleeswerk van mijn papers vormt een belangrijk aandeel in het succes van mijn onderzoekswerk. Bart, de relatie met jou verliep de voorbije jaren stroever dan ik zelf wou, maar toch heb je me geleerd om hierdoor assertiever in het leven te staan, je hebt me een olifantenvel aangekweekt en dit is een waarde die ik zeker kan gebruiken in mijn verdere carrire en waarbij ik altijd een stuk aan jou zal terugdenken.

Zon doctoraat voer je niet heleml alleen in je eentje uit, het onderzoekswerk wordt draaglijker met de dagelijkse steun van je collegas, uit dezelfde onderzoeksgroep, waarbij elk van hen op n of andere manier geholpen hebben om vol te houden en door te gaan tot het effectieve einde. De laatste twee jaar, Pieter, ben ik samen met jou op een bureau op de derde verdieping beland, ons “schoon verdiep”, en echt waar, dat was n van de beste beslissingen doorheen mijn carrire op S12. Voor jouw engelengeduld en blijvende hulp zijn er nooit voldoende woorden van dank. In de laatste *maanden van stress en al de bijhorende grillen en zuchten, bleef je desondanks een steun waar ik terecht kon met al mijn vragen/problemen van LateX, figuren, statistiek, $\cdots$ en wanneer nodig liet je mij lachen en konden we alles even vergeten waardoor we daarna weer met onze volle goesting konder verdergaan. Dank u!, dank u!, dank u Pieter! Ik hoop contact te kunnen blijven houden. Voor ik richting derde verdieping trok, was het grote bureau, "Ons Eiland" op het eerste verdiep mijn biotoop. Eerst als in een treintje, de opstelling van de bureaus deed mij altijd aan een trein denken met Tom als machinist, en Björn ernaast als conducteur. Jullie waren reeds aanwezig in de trein, en ik sprong erop met een lege rugzak. Tom en Björn, jullie hebben ervoor gezorgd dat de eerste stappen in de wereld van X-stralen, synchrotron metingen en Linux, succesvol waren, waardoor mijn rugzakje steeds meer en meer gevuld raakte met kennis en ervaring. Ook Geert heeft hier aan bijgedragen, al heb je jammergenoeg na n jaar van mijn doctoraat andere onderzoeksoorden opgezocht want ik meen te mogen denken dat jouw steun als postdoc nog een extra stimulans had kunnen zijn.*

Na bovenstaande heren kwam een nieuwe generatie collegas waarbij ik meer en meer voorop werd gesteld als machinist/oudste van de groep en waarbij het eiland als bureauopstelling is gevolgd. Eva, jij liet het aandeel vrouwen verdubbelen in 2011 wat voor mij een aangename aanvulling was van het mannelijke bastion die de XMI-groep tot dan toe was. Onze praatjes over hoe het was in ons leven, wat we hadden gedaan in het weekend en onze gedeelde passie over fietsen, zorgde voor de nodige afwisseling tijdens de uren van computerwerk. Maar ook je mening bij vragen over mijn onderzoek en je gevatte antwoorden die ik altijd kon gebruiken, zal ik niet snel vergeten. Hopelijk gaan we ooit nog eens samen een ritje maken. Brecht, wij hebben slechts goed anderhalf jaar samen in S12 vertoeft en mijn laatste jaar waren jouw eerste stappen in het onderzoeksleven en geloof mij, het moet allemaal nog beginnen. Je stond ook altijd klaar met raad en daad wanneer ik iets kwam vragen en daarvoor is een woord van dank zeker op zijn plaats. Een laatste collega uit de XMI-groep is onze Jan, een bodemloos vat energie, en een hulp op een manier die weinigen kunnen evenaren. Alles wat met computers te maken heeft, had voor mij vele geheimen maar jij was er altijd om deze te ontrafelen. Je altijd openstaande deur hoop ik in al mijn volgende jobs ook terug te vinden bij andere mensen.

In mijn onderzoek heb ik voor twee projecten kunnen samenwerken met zeer aangenamen mensen van de voorheen Artesis Hogeschool, nu Universiteit Antwerpen. In de eerste maanden van mijn doctoraat werd mij het majolica project aangereikt door Melissa Vandevijvere die met vele vragen zat over deze unieke tegelcollectie en die graag enkele analytische toepassingen wou gebruiken om meer te weten te komen. Dit project sprak me direct aan en gedurende een dikke drie jaar hebben wij vele dagen samen aangenaam doorgebracht tijdens de vele meetdagen. Jij leerde me alles over de kunsthistorische wereld waarbij ik jou op mijn beurt alles aanleerde over het technische van de metingen en de verwerking van de resultaten. Ik hoop van harte dat jij ook op jouw beurt de meer kunsthistorische inval van dit project tot een goed einde kan brengen en de titel van doctor in de wacht kan slepen. In mijn laatste jaar is de samenwerking die er was tussen de Raman groep en Eddy Verhaeven uitgebreid naar onze onderzoeksgroep en was je een meer dan welgekomen hulp in mijn onderzoek op de pigmenten met de Surface Monitor. Eddy, ik wens je het allerbeste toe in het verder onderzoek met dit toestel.

Naast inspanning, is ook ontspanning van groot belang. En vele collegas van S12 stonden altijd klaar om een luisterend oor te zijn wanneer dit nodig bleek te zijn. Jolien, jij bent een vriendin die dag en nacht klaarstond en waarop ik altijd kon rekenen. Je hebt me zelfs de eer gegeven om een zeer fiere meter te zijn van jouw tweede zoon Wout. De kans dat ik ergens anders nog zon steun en toeverlaat zal vinden is miniem. Ons dagelijks contact mis ik nu al enorm en ik hoop je tussen nu en 50 jaar nog regelmatig tegen te komen en met onze zonen en hun vriendinnen te kunnen terugkijken op een succesvol leven bij een goed glas wijn (ik trakteer)! Door de organisatie van de zomer-BBQ, team-building, drinks, recepties werd er aan een opperbeste sfeer binnen S12 gewerkt en van die sfeer heb ik altijd genoten. Kris, Sylvia, Tine dank voor al deze organisaties en ook om steeds met veel interesse te luisteren naar alles wat ik weer te vertellen had. Tine, om me de wondere wereld van de practica te laten ontdekken en mijn talent hierin te laten ontplooien. Sylvia, om bij je te mogen langskomen met elk probleem, hoe klein of groot het ook was, je hielp altijd waar je kon. Vele van jullie waren ook aanwezig over de middag om onze lunch te verorberen in de keuken en om mijn vele verhalen te aanhoren en een lach op mijn gezicht te toveren wanneer nodig. Asha, Davy, Karen, Kris, Veerle horen zeker bij deze middag-buddies! Veerle, we kunnen het nog een beetje verder zetten in OCAS maar de anderen gaan we jammer genoeg moeten missen. Jullie verdienen allen een uniek plaatsje in mijn hart en daar blijven jullie zeker en vast. Er is nu wel n troost: het zal heel wat rustiger en stiller worden in S12 tot dat een nieuwe "Lien" langskomt.

Naast collegas zijn familie en vrienden onontbeerlijk in het behalen van dit grote doel. Want ik werkte maar zo optimaal, als ik ook over voldoende afleiding kon beschikken naast de uren. Mijn ouders, broer, zus, schoon-ouders, schoonbroers en schoonzussen, neefjes en nichtjes dank ik voor de vele leuke familieuitstappen en etentjes. Vele van mijn studievrienden (Jolien, Nik, Sander, Seppe, Polet, Sarah, Greet, Lot, Elena, Evi) voor de leuke verzetjes en de nodige fysieke ontspanning met de Cannibale/Cannibalette als ons voorlopig fietshoogtepunt in 2014. Op naar de volgende bergen die we klein krijgen met onze fiets.

Als laatste maar wel de allerbelangrijkste steun, al voor bijna 10 jaar en de laatste twee jaar als man en vrouw is mijn echtgenoot Lieven. Je was er altijd om mij thuis op te vangen: goed of slecht gezind: je hebt me altijd door dik en dun gesteund en toverde een lach op mijn gezicht met een van je goedgeplaatste mopjes waardoor ik even alles kon vergeten. Als ik het minder zag zitten, was jij er om mijn doorzettingsvermogen aan te wakkeren en te zorgen dat ik verder deed op een succesvolle manier! En zeker in de laatste maanden, na de geboorte van ons eerste zoontje Arne, was je er nog extra om ook deze laatste bakens succesvol te verzetten. Opnieuw, er zijn onvoldoende woorden om deze steun op een gepaste manier uit te drukken. Lieve kleine Arne, je bent nu net 3 maanden oud, ooit ga je dit boekje in huis ontdekken. Weet dat jij het beste bent wat ons tot nu toe ooit is overkomen en dat jij deze laatste maanden mij geholpen hebt door elke keer als ik je vastnam een lach op mijn gezicht te toveren en alle stress even hielp vergeten.

In woorden van dank is het altijd gevaarlijk om mensen te vergeten en indien ik jou zou vergeten zijn, sorry daarvoor, ik maak dit goed met een goed glas bier in de hand! Ik heb de afgelopen zes jaar een enorme levenservaring opgedaan en ik kan enkel wensen dat het op een zelfde manier doorgaat *in het vervolg van mijn leven! En ik zal nooit vergeten: samen kunnen we alles!*

Lien Van de Voorde
Moerbeke-Waas, September 2015

Contents

Chapter 1: Introduction and aim

Archaeologists studying the past are unable to observe human behaviour in a direct way. Unlike historians, they also lack access to written records of the past. Instead, they must attempt to infer human behaviour, habits and beliefs from the surviving remains of what people made and used, before they can start with the interpretation of the past. One of the fundamental enquirers in archaeological objects is the relationship between residues, artefacts, buildings and monuments, and human behaviour. Luckily, archaeological chemistry is highly advanced and it is the application of chemical knowledge that greatly helps to solve problems in archaeology. Finding archaeological sites, dating, analyzing archaeological objects: all rely on strong collaborations between archaeologists and experts in the field of natural sciences, including analytical chemists and technicians. More and more researchers in the field of natural sciences show a keen interest in solving mysteries hidden in archaeology. The emerging interest in the analysis of archaeological objects, for example, is clearly indicated by the fact, that starting from 2002, regular international meetings have been organized on a worldwide scale to discuss archaeological subjects in the context of equal partnerships with X-ray based techniques.

It is clear that scientific analysis in archaeology is very interesting and diverse, providing information, among others, about chronologies, provenances, uses, past landscapes and climates, diets, health of people and conservation issues. It is important to note that next to the analytical investigations of archaeological objects, based on the availability of non-destructive techniques and instrumentation, mobile or not, also the development of associated mathematical methods as tools for data treatment is an essential step in helping the archaeologists, historians and conservators. Good skills in analytical chemistry are essential when working with unique cultural heritage/historical objects that cannot be damaged during investigation. When analyzing such objects, an important barrier associated with this type of research is represented by the need to obtain a maximum of information in the shortest possible time frame, because the time that is given to the researchers to analyze the objects is often very short. Besides that, there are often restrictions in terms of available space to investigate the object, coupled with limitations in taking sample materials without damaging the artefact. There are also strong limitations due to the fact that the measurements often cannot be repeated. If possible, only non-destructive analytical methods should be used to preserve e.g. a unique piece of art as well as to be able to apply several analytical techniques on the same (micro) sample.

Experiments on cultural heritage materials require many hours of preparation, optimization of techniques, and often demand work under considerable pressure to perform e.g. on-site analysis of unique cultural heritage materials, and so it is very interesting to carry out a PhD research work in this field.

In this work, different mobile and laboratory based analytical techniques are used to examine a wide range of culturo-historical objects. Most of the used analytical techniques in this thesis are based on X-rays, which is a type of electromagnetic radiation with short wavelength between approximately 0.01 and 10 nm. Next to the analyses using the available mobile and laboratory based X-ray instruments, also some additional non-destructive measurements were performed using synchrotron radiation based techniques. All these techniques give valuable elemental information about the investigated object but often it is also useful to obtain simultaneously molecular, crystallographic or mineralogical information of the same objects. While performing this work, we had access to a mobile Raman spectrometer (Mobile Art Analyser) and a mobile X-ray fluorescence/X-ray diffraction spectrometer (the Surface Monitor) in many investigations of the artefacts. In addition to the investigations using these instruments, laboratory measurements using scanning electron microscopy was performed in one case study.

Among the studied archaeological materials, pigments were among the most attractive targets for my scientific studies, not only because their colorful appearance represents a great source of beauty, but mainly because they provide means for unraveling ancient skills and recipes associated with their preparation and can be used as a tool to identify the origin of the studied artifact. The main aim of this work is to explore the possibilities of identifying these pigments originating from different cultural heritage objects and to study in which way the recovered chemical information can reveal more about provenance, influence and authenticity of the investigated objects by the use of the spectroscopic data, obtained as a result of different data collection and treatment steps. Furthermore, a new mobile X-ray fluorescence/X-ray diffraction instrument is characterized and tested in this work and an outlook is given towards three-dimensional elemental, chemical state analysis for future applications in palaeontology

Chapter 2 gives an overview of the most important cultural heritage objects/materials investigated during this work, referring to the results of these investigations that can be found in the following chapters. This chapter also provides the required background in X-ray fluorescence (XRF) and X-ray diffraction (XRD) techniques, on which most analytical techniques used in this work are based. An introduction to the underlying physical aspects of XRF and XRD is given, along with the characterization of the different components of the XRF spectrometers. In addition, the specific laboratory and mobile X-ray instruments used in our studies are described along with their working principles. The second chapter concludes with a brief description of scanning electron microscopy and Raman spectroscopy, two other techniques which have been used in the investigation of the presented artefacts.

Chapters 3 and 4 cover our work on majolica, which refers to earthenware materials covered with a thin layer of white opaque glaze and bright coloured glazes to create appealing decorations. From the beginning of the 16^{th} century until the end of the 17^{th} century, Antwerp was an important majolica production center, being the origin of a unique set of 30 archaeological majolica tiles investigated using laboratory and synchrotron radiation induced X-ray fluorescence spectroscopy beside a SEM-EDX spectrometer. Chapter 3 describes the history of Antwerp majolica and the importance to investigate this type of cultural heritage objects. This is followed by the presentation of results corresponding to the investigation of the used materials with respect to elemental/structural information, discussing also the similarity in the majolica collection from different production sites. In addition to the collection of isolated tiles and fragments, also a majolica tile floor, located in one of the towers of the Rameyenhof castle (Gestel, Belgium) has been investigated. This unique and only known 16^{th} century Antwerp majolica tile floor was the subject of *in situ* non-destructive XRF/Raman spectroscopic investigations which can not be missed in the examination of Antwerp majolica in its entirety. Chapter 4 presents the results of the *in situ* exploration of the floor using a handheld XRF spectrometer and the MartA Raman instrument revealing the characteristic major/minor and trace element signature of 16^{th} century Antwerp majolica used in this floor and providing valuable information about its originality.

Chapter 5 describes the results obtained from another type of cultural heritage object using the same type of non-destructive portable/mobile instruments (handheld XRF and MArtA) next to the mobile XRF/XRD Surface Monitor. These techniques were used to obtain elemental/molecular information on pigments originating from the painting ”Mad Meg” by Pieter Bruegel the Elder, the Flemish renaissance artist, exhibited in the Museum Mayer van den Bergh (Antwerp, Belgium). This chapter reports on the *in situ* chemical characterization of this masterpiece and the verification of two important historical hypotheses.

Chapter 6 focuses on the testing and characterization of a new, commercially available, mobile system combining X-ray diffraction and X-ray fluorescence, namely the Surface Monitor of the Assing S.p.A. company (Italy), that was acquired by the UGent X-ray Microspectroscopy and Imaging (XMI) group in 2012. From the beginning of 2013, after initial problems with this prototype instrument, it was finally possible to start the characterization and to discover the possibilities of this instrument in the investigations of cultural heritage objects. All details of this process are described in this chapter, as well as how the main goal of all this trial and error is reached: the investigation of real cultural heritage objects.

Chapter 7 provides an outlook concerning the use of more advanced three-dimensional (3D) micro-XRF and X-ray absorption near edge structure (XANES) spectroscopy for the non-destructive analysis of paleontological samples. While in the previous chapters samples of cultural heritage represented the central theme, in chapter 7 we studied insects trapped in amber also by using non-destructive ways of investigation, including synchrotron based confocal micro-X-ray fluorescence and X-ray absorption near edge structure (XANES) spectroscopy. The goal of the investigation was to demonstrate the potential of these techniques for the non-destructive chemical analysis of unique paleontological samples for future studies on such unique ancient samples, representing our heritage from nature.

The results obtained throughout this work are summarized in chapters 8 and 9, along with a number of conclusions.

Chapter 2: Materials and Methods

This chapter introduces the principles of investigations on archaeological and cultural heritage objects. An overview of the materials and objects, examined during this PhD work, is given followed by the description of the theoretical aspects of the employed analytical techniques and the used instruments which were needed to investigate these objects. These techniques include X-ray fluorescence (XRF) spectroscopy, X-ray diffraction (XRD) analysis, scanning electron microscopy (SEM) and Raman spectroscopy.

2.1 Cultural Heritage

Archaeology and chemistry are both subjects which are large, rich, dense and at the same time very different from each other. Archaeology belongs to the humanities or social sciences and is sometimes qualified as historical science, which is usually associated with the outdoors, ruins, excavations, piles of dirt, and artefacts of stone, ceramic, or metal. Chemical analysis, on the other hand, typically happens indoor, in the laboratory, and is part of exact science involving complex measuring techniques and complex chemical terms and formulas. In the popular imagination, this science is associated with e.g. beakers and acids, Bunsen burners, strange smells and lab coats. One wonders how two so fundamentally different fields can fit together? Archaeological chemistry is located at the junction between these two branches of the tree of knowledge and the combination of these fields provides an exciting multidisciplinary science where many extraordinary discoveries are being made [1].

The application of sciences to answer questions of archaeology and history of art dates back to the 18^{th} century, but the establishment of laboratories dedicated to this type of work appeared slightly later. The first of these, the Königliche Laboratory in Berlin, was established in 1888 but unfortunately did not survive the First World War. However, the same conflict led the British Museum to appoint its first historical scientist in 1920, in response to the deteriorated condition of objects that had been stored underground for safe-keeping during the war years. Regardless of the object of investigation, whether it is an ancient axe or an oil painting, the identification of its material is critical to the complete understanding of the reasons for its corrosion or deterioration and to the determination of the appropriate treatment and storage environment [2].

A second region of interest involves the application of chemical science to understand issues such as where an object was made (its provenance) and the details of its manufacture. Radiocarbon dating, for example, is the archaeological technique that is most familiar to the general public, however, starting from the 1960s a lot of other scientific methods have been used to investigate archaeological objects in the so-called “New Archaeology”. Since then, the scientific and more specifically chemical/structural analysis has become an important tool of archaeologists and historians. A fundamental guiding principle in the investigations of cultural heritage materials is that unnecessary damage should be avoided [2].

Objects and monuments of culturohistorical significance comprise a wide range of materials (metals, ceramics, glass, rocks, textile, wood, paper, parchment, paintings, etc.) and usually exhibit a fairly complex three-dimensional structure and a heterogeneous chemical composition. Cultural heritage objects are often composed of various materials, consisting of a base material covered with one or more layers of pigments. For the study, conservation and restoration of such materials and artefacts of culturohistorical value, there is a well-defined need for analytical methods that are able to provide information on (see ***Fig. 2.1***) [3, 4]:

- the chemical nature/composition of selected parts of cultural heritage artefacts and materials in order to elucidate their provenance.
- the state of alteration (on the surface and/or in the interior) of objects as a result of short-, medium- or long-term exposure to particular environmental conditions.
- the effect/effectiveness of the applied conservation/restoration strategies.

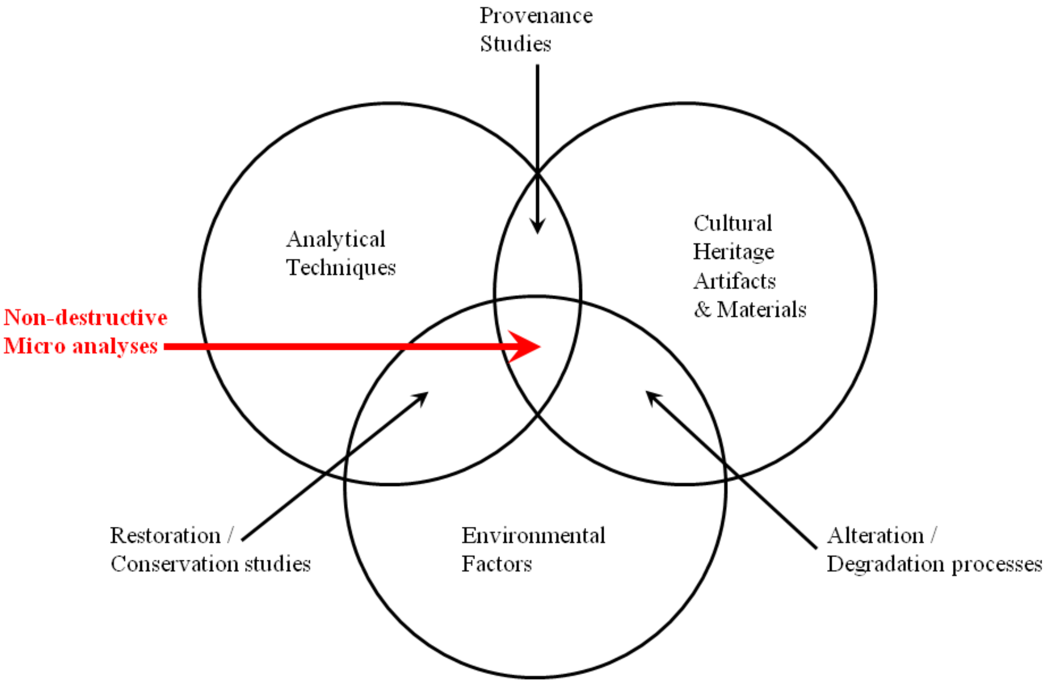

Figure 2.1: *Interaction between cultural heritage materials, use of analytical techniques and environmental factors [4].*

The ideal method for analysing objects of artistic, historic or archaeological nature should be [3, 4]:

- *non-destructive*, i.e. respecting the physical integrity of the material/object. Often valuable objects can only be investigated when the analysis does not result in any (visible) damage. Usually this completely eliminates sampling or limits it to very small amounts.

- *fast*, so that large numbers of similar objects may be analysed or a single object investigated at various positions on its surface; this property is very valuable since this is the only way of being able to discern general trends in the data and to find outlier data points.

- *universal*, so that by means of a single instrument, many materials and objects of various shapes and dimensions can be analysed with minimal sample pre-treatment.

- *versatile*, allowing with the same technique average compositional information to be obtained, but also local information of small areas (e.g. millimeter to micrometer-sized) from heterogeneous materials.

- *sensitive*, so that object grouping and other types of provenance analyses can be done not only by means of major elements but also by means of trace element fingerprints.

- *multi-elemental*, so that in a single measurement, information on many elements is obtained simultaneously and, more importantly, so that also information is obtained on elements which were not initially thought to be relevant to the investigation.

- *mobile*, in general laboratory equipment performs better than mobile instrumentation because during the design of a mobile instrument some concessions must be made in order to create a compact and stable instrument. The biggest advantage of mobile equipment is clearly its ability to record data of artefacts not only in a totally non-destructive way, but also *in situ*, which means, in the place where the artworks or artefacts are located.

There is a huge amount of analytical techniques, based on all spectral regions of the electromagnetic spectrum, which fulfill several, but usually not all, requirements described above. After the overview of the cultural heritage objects and materials investigated during this PhD work, the theoretical background of the used analytical techniques and instruments will be given. More information on the analytical techniques used in the examination of culturohistorical artefacts, but which are out of scope of this work, can be found in Refs. [1, 2, 4].

2.1.1 Overview of the investigated cultural heritage objects

During this PhD work, the most important project in terms of analytical investigation of culturohistorical objects was devoted to Antwerp majolica tiles, related to tin-glazed pottery of Italian origin , dating from the 16th and 17th century. A snapshot of these tiles can be seen in ***Fig. 2.2***. These tiles are decorated in bright colours on a white background, frequently depicting historical and legendary scenes. Conservators are interested in different aspects of the material, including information on its chemical composition, and the production techniques to be able to derive the relation between the current status of the material and the mandatory knowledge on the causes of degradation.

Figure 2.2: *Antwerp majolica from the 16th and 17th century. Left: Snapshot of a selection of tiles, Right: Investigation of the tiles using X-ray fluorescence based analytical technique.*

As mentioned above, many of the archaeological artefacts are built up starting from a base material covered by different layers, which is also the case of majolica tiles. These tiles consist of an earthenware body covered by a layer of lead-tin glaze, decorated by colourful paintings, which are applied on the earthenware in different baking processes. While investigating these majolica tiles in their entirety, using various analytical techniques, the obtained information typically corresponds to the surface layer or to the combined multilayer structure without providing knowledge on the individual layers. For the cross-sectional studies, therefore, small fragments from the edge of the majolica tiles were cut which allowed us to investigate each layer separately using micro-beam XRF techniques. ***Fig. 2.3*** illustrates the method of the applied sampling technique and the subsequent investigation (see ***Fig. 2.4***) of the fragments of the majolica tiles that took place. In chapter 3, all details about this research and the corresponding results can be found.

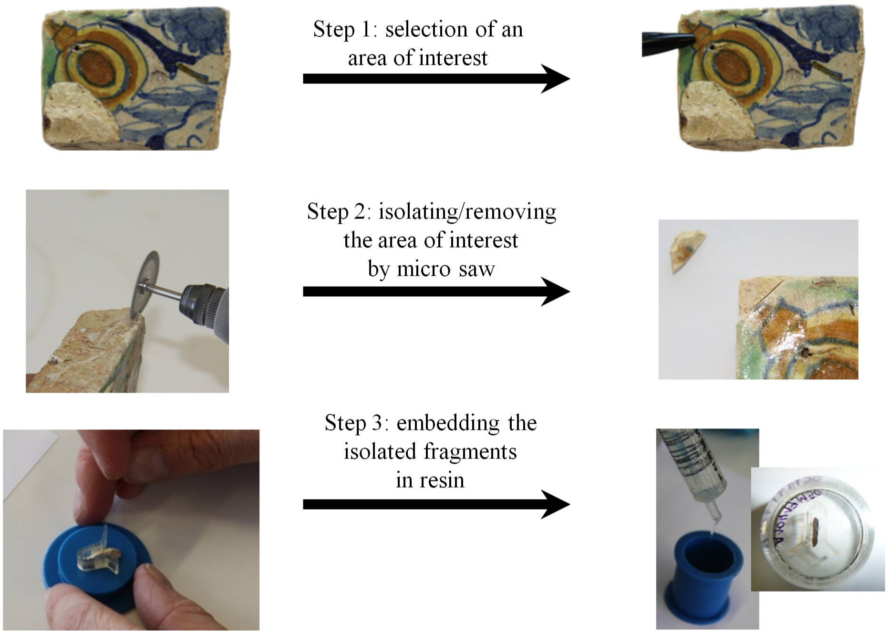

Figure 2.3: *The main sample preparation steps of the majolica tile fragments to be studied.*

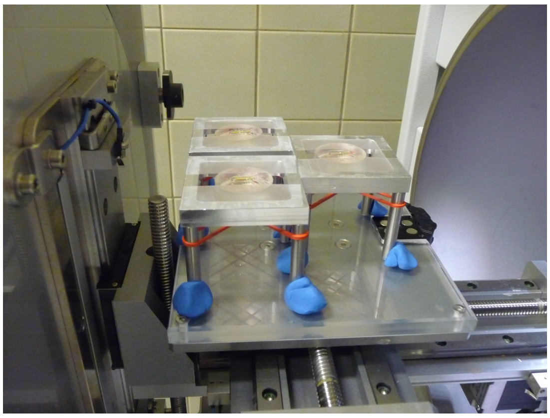

Figure 2.4: *Investigation of the embedded fragments using an X-ray fluorescence based analytical technique.*

Combined with the studies on the above mentioned irreplaceable Antwerp majolica tiles collection, also an *in situ* study was performed on a unique majolica floor located in the chapel of the Rameyenhof castle in Gestel, near the Belgian city of Lier. This majolica chapel floor is the only known majolica floor in this region, originating from the early 16th century, with a decorative pattern spread over the entire floor with 60 to 70 tiles in one compartment, as can be seen in ***Fig. 2.5***. This captivating majolica floor is in an extremely good condition both in terms of preservation and in terms of artistic quality, reflecting the exceptional material technical skills of the craftsman producing the tiles. It is truly exceptional to find such a piece of well-preserved artwork for *in situ* analysis. Conservators were interested in the chemical makeup of the used materials for the majolica tiles and whether this floor has been effectively made by using Antwerp majolica or not. More information, results and answers on the art-historical questions about this unique piece of art can be found in chapter 4.

Figure 2.5: *Antwerp majolica floor present in a chapel of the Rameyenhof castle. Left: Snapshot of the floor during investigations, Right: Details of some tiles present in the floor.*

Another application of non-destructive X-ray and Raman analysis during this PhD work was the investigation of the "Dulle Griet", also known as "Mad Meg", which is a figure of Flemish folklore and which is the subject of a 1562 oil on panel by the Flemish renaissance artist Pieter Bruegel the Elder. The painting depicts a peasant woman, Mad Meg, who leads an army of women to pillage Hell. It is currently held and exhibited in the Museum Mayer van den Bergh in Antwerp, Belgium. Analysis of this artwork was done using a multi-method approach, including mobile XRF and Raman spectroscopy. A photograph taken during the *in situ* analysis is shown in ***Fig. 2.6***. More details about this research can be found in chapter 5.

Figure 2.6: *Photograph taken during the* in situ *analysis of Mad Meg, Museum Mayer Van den Bergh, Antwerp, Belgium.*

A last important subject of this PhD work is related to an outlook towards a more advanced type of three-dimensional spatially resolved confocal-XRF and XANES microanalysis to be used for the non-destructive studies of unique paleontological samples, which can be considered as our heritage from nature. In chapter 7, a demonstrative example is given for the above mentioned analysis of insects trapped in tree resin which, over the course millions of years, fossilizes into amber with the insect inside, as can be seen in ***Fig. 2.7***.

Figure 2.7: *Left: Picture of insect trapped in amber, Right: Method of preservation of these important biological objects.*

In the subsequent sections of this chapter, the analytical techniques used to examine the objects and materials described above will be discussed in detail.

2.2 X-ray fluorescence

Since X-ray based analysis meets most of the requirements for the investigation of objects with artistic and/or archaeological value, it is fairly common to use conventional X-ray fluorescence. It is in fact one of the most often applied methods for obtaining qualitative and semi-quantitative information on the elemental composition of materials of which the investigated objects are made of.

X-rays can be generated in nature by e.g. the deceleration of electrons in the outer field of an atomic nucleus or by changing the bound states of electrons involving transitions between the inner electronic shells of an atom. These X-rays are classified as short wavelength electromagnetic radiation compared to other radiation varieties, as can be seen in ***Fig. 2.8***. Generally the wavelength of this type of electromagnetic radiation is between 0.01 and 10 nm which corresponds to an energy range of approximately 0.1 tot 100 keV [5]. A unique property of X-rays is their highly penetrating character and their ability to interact strongly with the inner shell electrons of atoms. The penetrating property of X-rays is dependent on their energy: high energy X-rays will penetrate materials more deeply than low energy X-rays. Another property is their straight propagation in between interactions, much the same way as individual photons of visible light.

X-rays were discovered by Wilhelm Conrad Röntgen. He noticed in 1895, during his experiments with Crookes tubes (discharge tubes), that a green glow was emitted by a fluorescent screen painted with $BaPt(CN)_4$, positioned closely to an operational tube. Röntgen named the new type of radiation as "X" rays, to mark that it was an unknown type of radiation which propagated along straight lines. In 1901, Röntgen was awarded with the first Nobel Prize in Physics for this discovery [6]. Up to this day, the most common use of X-rays, leading to its application in diagnostic medicine is under the form of radiography due to the penetrating power of X-rays. Different X-ray absorption properties of different materials explain the underlying principle of radiography: for a given energy, materials with a lower electron density tend to absorb less X-rays than those with higher electron density.

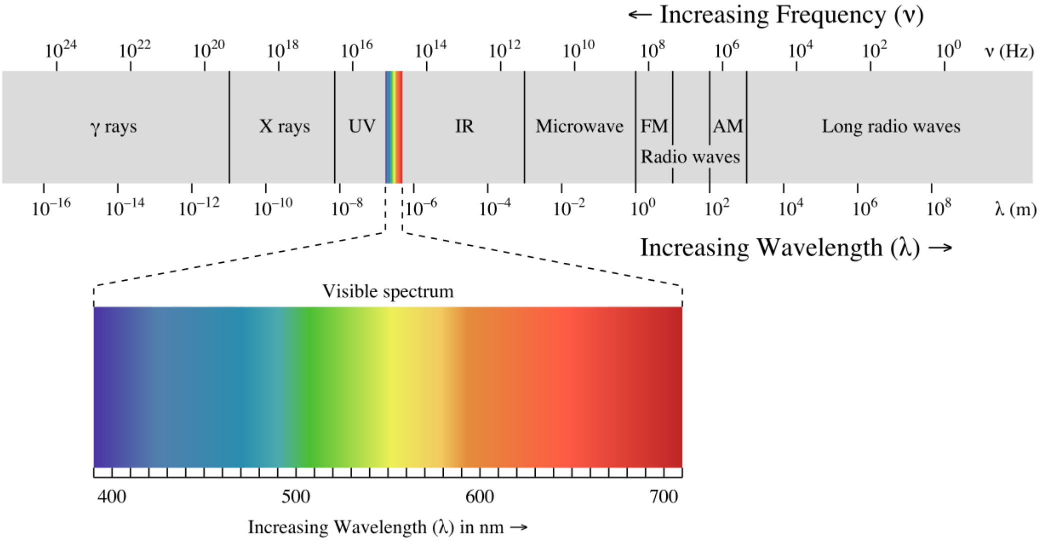

Figure 2.8: *The electromagnetic spectrum. Source: http://www.pion.cz (17/05/2015).*

This can be clearly seen in one of the first X-ray transmission images ever taken (inset ***Fig. 2.9***), made by Röntgen, in which the hand of his wife Anna Berthe Röntgen is imaged. The darker areas correspond to the bony structures, which are made up primarily of calcium phosphates and will absorb considerably more of the (low energy) X-rays compared to the tissues which contain mostly organic material (composed of C, H, O, S, P and N).

2.2.1 Interaction of X-rays with matter

When an X-ray photon interacts with a sample, three separate phenomena can occur in the relevant X-ray energy range of 1-100 keV: Rayleigh scattering, Compton scattering and photoelectric effect. A photon can also pass through the sample without any interaction, especially in case of high X-ray energies and thin samples [5].

Scattering

Two types of X-ray photon scattering can occur: Rayleigh and Compton scattering. Rayleigh scattering refers to the elastic scattering of X-ray photons, by atomic electrons, during which the energy of the scattered photons remains unchanged (***s*ee Fig. 2.10**). Rayleigh scattering occurs mainly with low energy X-rays, heavier metals have also a higher chance to interact with X-ray photons through Rayleigh scattering [5–7].

Compton scattering is a form of inelastic scattering indicating that the photon will have a lower energy after the interaction (see ***s*ee Fig. 2.10**). This effect, discovered by Arthur Compton in 1923, results in the transfer of part of the energy of the scattered photon to an outer shell electron (has lower binding energies than inner shell electrons and thus easier to eject from an atom), which recoils and is subsequently ejected from the atom. The remaining energy is taken by the scattered

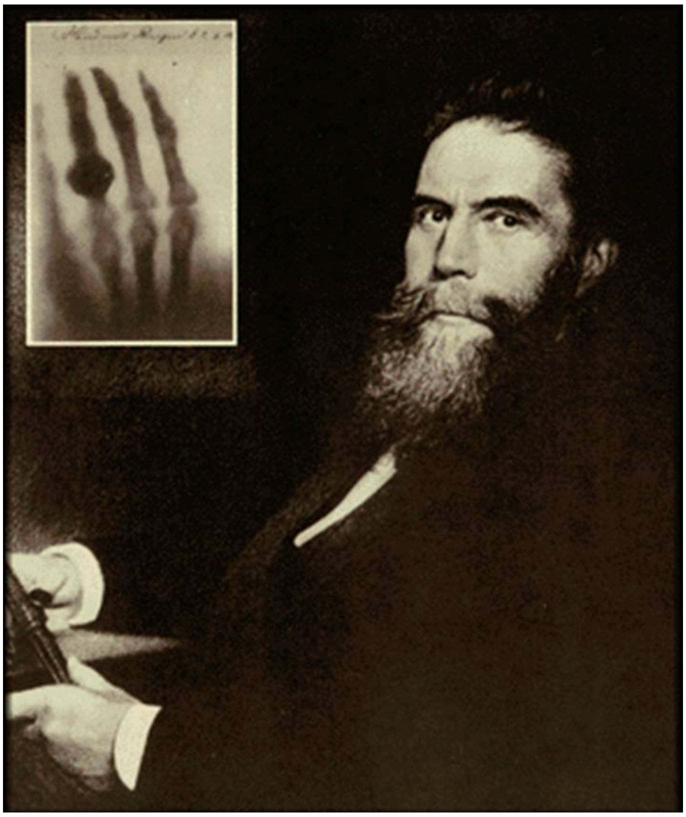

Figure 2.9: *Wilhelm Conrad Röntgen in ca. 1895. Inset photo: Radiograph of the hand of Röntgen's wife. The darker areas correspond to the bones in the fingers and to the ring around the middle finger. Source: http://farmahuis.nl/vooruitgang/grotenamen/wilhelm-rontgen-ontdekt-rontgenstralen (17/05/2015).*

photon [8]. With the Compton formula, the energy E_C of the Compton scattered photon can be calculated:

$$E_C = \frac{E_0}{1 + \frac{E_0}{m_e c^2}(1 - cos\theta)} \tag{2.1}$$

where $m_e c^2$ corresponds to the electron's rest mass energy of 511 keV and E_0 and θ to the initial photon energy and scattering angle, respectively.

Scattering processes may generate high intensity X-ray radiation directed (also) towards the detector, without providing direct elemental information in the form of X-ray fluorescence. However, the Compton scatter probability depends on the electron density of the sample. By looking at the Compton and Rayleigh scatter intensity ratio, one can get information about the so called effective (or average) atomic number of the matrix and on the irradiated sample mass [5, 8, 9].

The angular dependence of the Compton and Rayleigh scatter probabilities, $\frac{d\sigma_C}{d\Omega}$ and $\frac{d\sigma_R}{d\Omega}$ respectively, can be calculated using equations 2.2 and 2.3 corresponding to the Compton and Rayleigh differential cross-sections assuming a degree of linear polarization p for the incident beam. The angle ϑ described here is the scattering angle between the source beam and the X-rays going towards the detector [8].

$$\frac{d\sigma_C}{d\Omega}(\vartheta, \phi, E) = \frac{r_e^2}{2}\left(\frac{E}{E_0}\right)^2 \left[\frac{E}{E_0} + \frac{E_0}{E} - sin^2\vartheta(1 - p + 2pcos^2\phi)\right] S(x, Z) \tag{2.2}$$

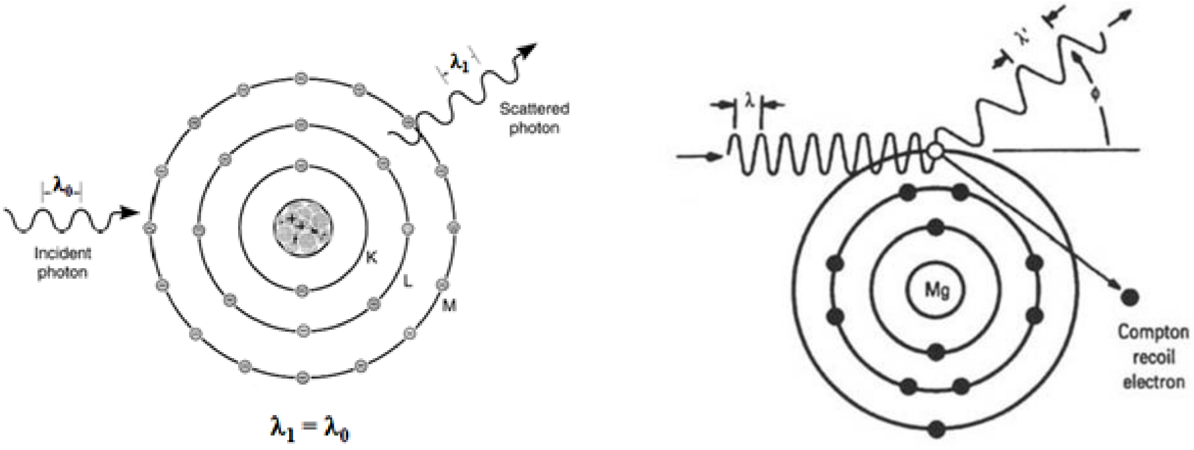

Figure 2.10: *Schematic overview of scattering phenomena. Left: Rayleigh scattering, Right: Compton scattering [4].*

$$\frac{d\sigma_R}{d\Omega}(\vartheta, \phi, E) = \frac{r_e^2}{2}\left[2 - sin^2\vartheta(1 - p + 2pcos^2\phi)\right] F^2(x, Z) \tag{2.3}$$

In these equations, Ω is the detector solid angle, ϕ is the angle in which the detector deviates from the plane of polarization, E is the energy of the scattered photon, E_0 is the energy of the incident photon, r_e is the classical electron radius, p is the degree of polarization, S is the incoherent scattering function and F is the atomic form factor. Both F and S can be obtained through Xraylib [10]. They are functions of the atomic number Z and x, where $x = sin(\vartheta/2)/\lambda\,[^\circ A^{-1}]$ [11].

When a beam is linearly polarized, p equals 1 and ϕ equals 0° when one measures in the plane of polarization. When this is the case, one can calculate that, and if ϑ equals 90 ° the Rayleigh scattering cross-section equals zero and the Compton scattering cross-section is minimal. As the detector does not have an infinitely small dimension however, Rayleigh scattering from angles different from $\vartheta=$ 90° will be detected as for those angles the scatter probability is larger than zero. For unpolarized sources, such as X-ray tubes, p equals 0 [8, 11]. More information about the angular dependence of the Compton and Rayleigh scatter probabilities can be found in [12] and in ***Fig. 2.11***.

It is advantageous to minimize the Compton and Rayleigh scattering intensities during XRF measurements, as this will reduce the risk of overloading the detector with X-ray photons that hold no element specific information. This can be achieved, as shown by the above equations, by performing the measurement using a linearly polarized X-ray beam and by placing the detector in the plane of polarization, under an angle of 90° with respect to the beam.

Photoelectric effect

A third interaction type is the photoelectric effect. This phenomenon was first observed by Heinrich Hertz in 1887 for visible light and corresponding to the emission of electrons from a material that is irradiated with sufficiently energetic photons. In the X-ray regime, the ejected electrons, so called photoelectrons, are produced when an X-ray photon is fully absorbed by the atom, transferring its energy to a bound electron in a given shell of the target atom as can be seen in ***Fig. 2.12***. For

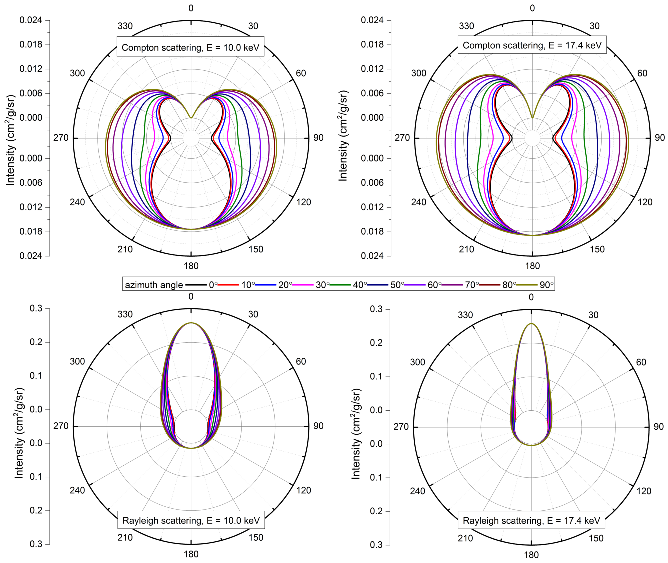

Figure 2.11: *Compton and Rayleigh differential cross sections for polarised radiation as a function of scattering and azimuth angle for two different energies [12].*

this to occur, the photon must have an energy greater than the binding energy of the electron. After emission, the electron possesses a kinetic energy (E_{e-}) equal to the difference of the energy of the incoming photon and electron binding energy (E_b) [13]:

$$E_{e^-} = h\nu - E_b \tag{2.4}$$

where h is Planck's constant ($6.626068.10^{-34} m^2 kg/s$) and ν the frequency of the incoming X-ray photon.

X-ray attenuation in matter

The relation between the incoming beam intensity (I_0), passing through a sample with given thickness (x) and density (ρ), and the outgoing beam intensity (I) can be calculated using the law of Lambert-Beer:

$$I(x) = I_0 e^{-\mu_\rho \rho x} = I_0 e^{-\mu_L x} \tag{2.5}$$

with μ_ρ the mass attenuation coefficient and $\mu_L = \mu_\rho \rho$ the linear attenuation coefficient. If the interactions occur in the relevant energy region of 1 - 100 keV, the mass attenuation coefficient for a single element can be written as follows:

$$\mu_\rho\left(E,Z\right) = \tau_\rho\left(E,Z\right) + \sigma_{\rho,R}\left(E,Z\right) + \sigma_{\rho,C}\left(E,Z\right) \tag{2.6}$$

with $\tau_\rho(E,Z)$ the photoelectric cross-section, $\sigma_{\rho,R}(E,Z)$ the Rayleigh (elastic) scattering cross-section and $\sigma_{\rho,C}(E,Z)$ the Compton (inelastic) cross-section, all function of the incident beam energy (E) and the atomic number (Z). For three elements (Ar, Si and Ge), the contribution to the mass attenuation coefficient of the three interaction effects as function of the photon energy is shown in

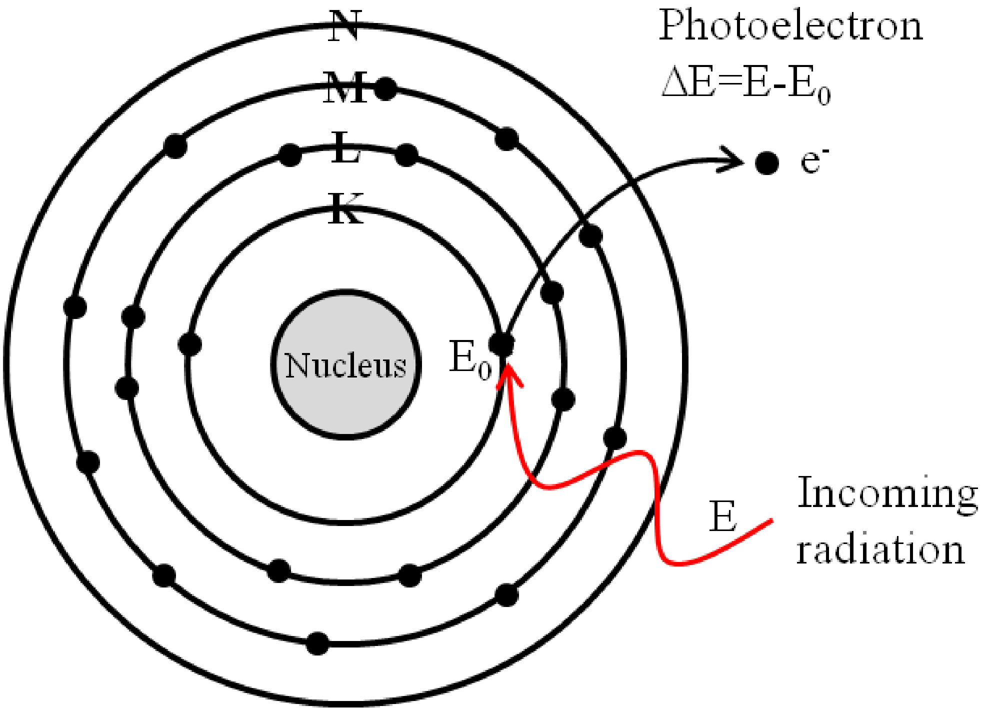

Figure 2.12: *Schematic overview Photoelectric effect.*

Fig. 2.13. Equation 2.6 is only valid if there is one element present in the sample. For multiple elements present in the sample the mass attenuation coefficient can be written as the sum of the weight fractions (ω_i) times the mass attenuation coefficient for each element $\mu_\rho(E, Z_i)$.

$$\mu_\rho\left(E, Z_1, ..., Z_n\right) = \sum_{i=1}^{n} \omega_i \mu_\rho\left(E, Z_i\right) \tag{2.7}$$

It is important to note that if higher X-ray energies are used (E > 1.022 MeV), pair production and photonuclear absorption will also occur. Since these last two interaction types do not occur at lower energies, they will not be discussed further in this work.

The discontinuities of the photoelectric cross section curves correspond to the energy dependent contributions of the different occupied shells an atom possesses, each having different electron binding energies. This implies that such a cross section profile must be considered as a superposition of a number of partial photoionization cross section profiles, one for each occupied shell.

X-ray fluorescence

The photoelectric effect has the potential of providing true quantitative and qualitative information about the composition of the sample, through the subsequent emission of characteristic X-ray photons as the result of the process called X-ray fluorescence. This takes place through an electron transition from a higher shell to the vacancy created by the photoelectric interaction [6]. The difference between the binding energies of the two shells involved in the transition is released as a characteristic X-ray fluorescent photon as can be seen in red in ***Fig. 2.14***. This fluorescence X-ray photon possesses

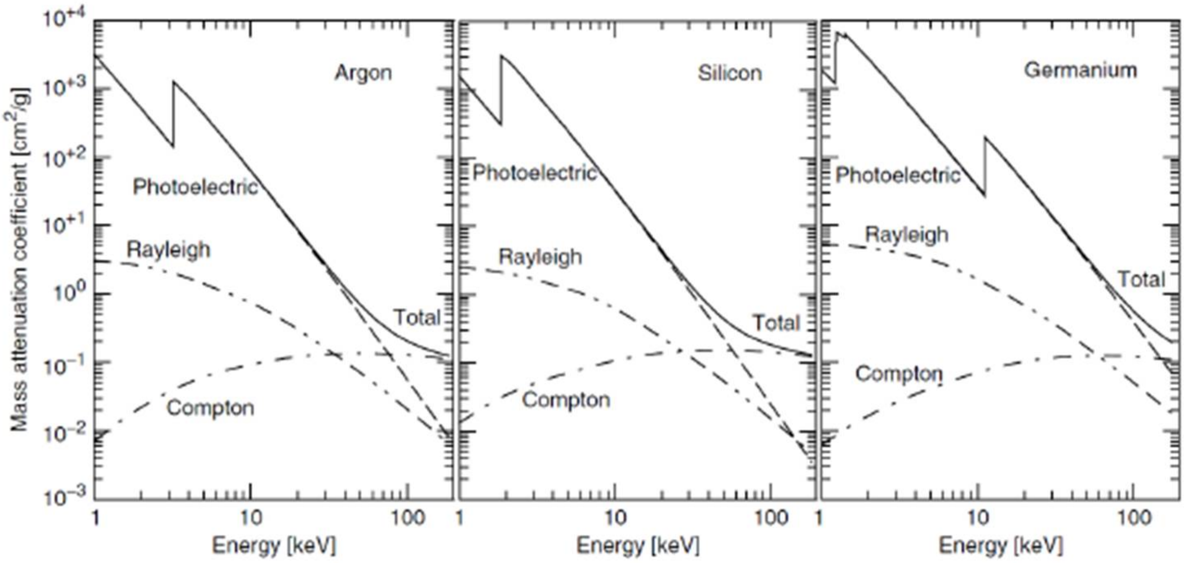

Figure 2.13: *Mass attenuation coefficients, photoelectric, Compton and Rayleigh components for the elements Argon, Silicon and Germanium [5].*

an energy equal to the difference between the higher energy state from which the electron arose and the lower energy state the inner shell vacancy had [13]. Since the binding energy of the shells are characteristic for a given element, the energy difference between two such shells, and therefore also the energy of the fluorescence X-ray photon, will be characteristic for a given element [5].

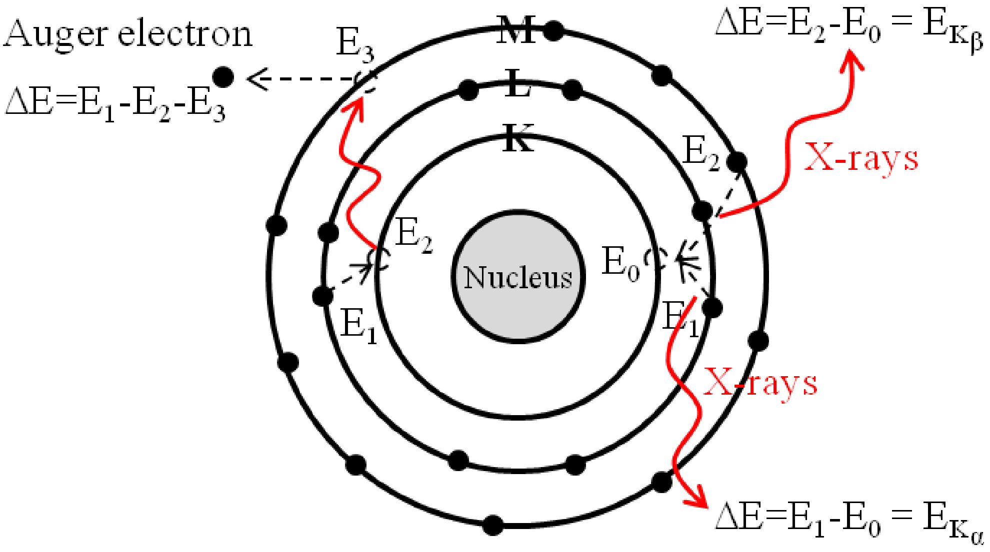

Figure 2.14: *Electron cascade from the outer to the inner shell, causing characteristic X-ray fluorescence radiation (right side of the figure) or the emission of Auger electrons (left side of the figure).*

In a competing process, instead of X-ray fluorescence emission, the relaxation of the excited state can also occur through the ejection of an outer shell electron, referred to as Auger electron. This phenomenon is referred to as the Auger effect which is a radiationless relaxation where no new X-rays are created. During XRF spectroscopy one wants to measure as many fluorescence photons as possible, therefore, it is clear that this Auger electron emission is an undesirable outcome of the photelectric effect. For low Z elements the Auger effect will occur with higher probability, making the detection of low Z elements, next to more pronounced absorption effects, rather inefficient. A special case of electron transitions can be observed in shells that have subshells, such as L and M: it is possible that electron transition takes place within the subshells [5]. For example, an initial excitation of the L_1 shell may lead to a non-radiative transition of an electron coming from the L_2 or L_3 subshells. The vacancy created in the L_2 or L_3 shell may at this point be filled by a radiative transition. This sub-shell electron transition effect is referred to as a Coster-Kronig transition and is usually quite strong. If the photon ejects an electron from an atom by photoelectric effect, the relaxation can occur by either X-ray fluorescence or Auger electron emission, as discussed above. The probability that a fluorescence X-ray will be emitted after the photoelectric effect is described by the fluorescence yield ω, which is dimensionless and specific to each atom and shell involving the vacancy [13].

2.3 X-ray fluorescence spectrometers

Commonly speaking, XRF spectrometers consist of an X-ray source, a sample stage and a detector system. Optionally, the spectrometers may have monochromatizing and focusing optics after the X-ray source and in front of the sample. The optics after the source can reduce the beam dimensions to (sub-)microscopic levels, allowing for micro- and nano-XRF applications. XRF spectrometer systems are classified based on the detection scheme into two categories: energy dispersive (ED) and wavelength dispersive (WD) XRF. The latter is achieved by having the scattered photons and XRF lines originating from the sample separated by Bragg diffraction. This is accomplished by using an adjustable crystal-detector geometry. In general, WD-XRF spectrometers have much better energy resolution than ED-XRF spectrometers which do not contain an analyzing crystal. However, due to the increase in optical components, WD-XRF spectrometers have typically a lower overall efficiency than ED-XRF spectrometers and, hence, require a higher power X-ray tube (which can add to the cost of the instrument). There are two types of WD-XRF spectrometers: simultaneous and sequential as can be seen in ***Fig. 2.15***. In simultaneous WD-XRF spectrometers, multiple detectors, placed at different Bragg angles, are used to analyze multiple elements simultaneously. In sequential WD-XRF Spectrometers, the crystal Bragg angle is scanned while elements are analyzed sequentially. In this work, only ED-XRF will be considered, therefore throughout the rest of the manuscript the acronym XRF should be considered as an implicit reference to ED-XRF spectroscopy. The next sections of this chapter present an overview of the different components that make up an ED-XRF spectrometer.

2.3.1 X-ray sources

There are three ways to produce X-rays: by using radioisotopes, an X-ray tube or synchrotron radiation sources. The last two sources produce X-rays through the acceleration of electrons and/or

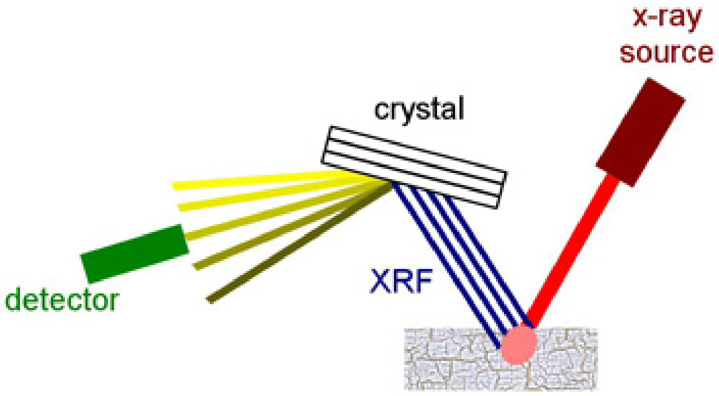

Figure 2.15: *The two types of WD-XRF spectrometers: simultaneous (multiple detectors) and sequential (turned analyzing crystal). Source: http://http://www.horiba.com/scientific/products/x-ray-fluorescence-analysis/tutorial/wavelength-dispersive-xrf (26/08/2015).*

electronic transitions instead of nuclear decay processes in radioisotopes, where X-rays are produced using natural or artificially produced radioactive materials. A radioisotope is a isotope of a chemical element that has an unstable nucleus and emits radiation during its decay to a stable form.

Certain radioisotopes such as ^{55}Fe and ^{109}Cd produce X-rays when decaying through electron capture [14]. In this case, a K-shell electron of the isotope is captured by the nucleus, transforming a proton to a neutron, creating a new isotope with a reduced atomic number in an unstable excited state. This unstable state is due to the electron vacancy that is formed by this process which will decay by the transition of an electron from a higher shell by producing characteristic X-ray photons and Auger electrons. Radioisotopes are frequently used in medical applications, although they are also used as a source of X-rays in (portable) XRF spectrometers [15, 16]. Because of safety issues and time-dependent radioactivity, the radioisotopes are less popular in the research field.

X-ray tube

The method by which X-rays were produced in Röntgen's first experiments is basically the one still used today: an X-ray tube [17, 18]. In these devices, a high voltage electric field causes electrons emitted by a negatively charged metal surface (the cathode) to accelerate and bombard a positively charged metal plate (the anode). In current X-ray tubes (rather Coolidge X-ray tubes, referring to the inventor William Coolidge) however, the electrons are created by a thermionic effect which occurs by heating the cathode filament, usually made from Tungsten (***Fig. 2.16***). The tube current is defined by the temperature of the cathode, thereby becoming the control means for selecting the X-ray tube intensity. The applied high voltage between the cathode and the anode speeds up the electrons towards the anode surface, where the electron beam interactions generate X-rays by two electron-matter interaction types: Bremsstrahlung and Impact ionization. Because X-ray production is very inefficient (99% of incident energy is converted to heat) the waste of heat at the focal spot is one of the main limitations on the power which can be used [18].

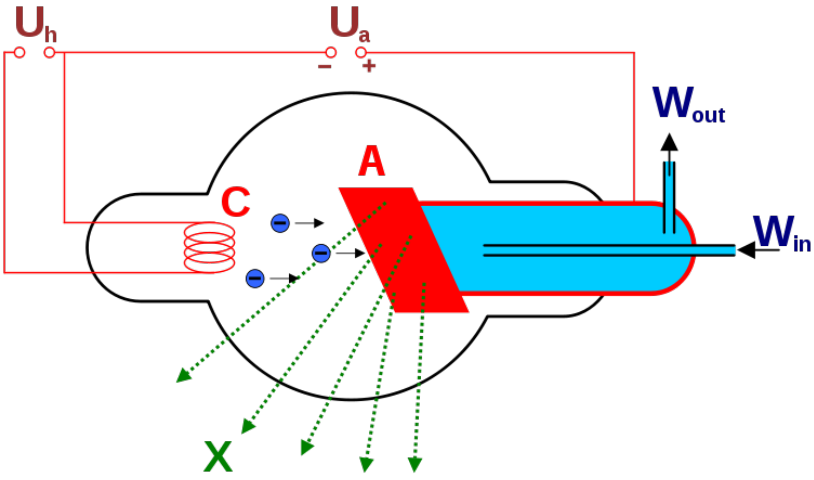

Figure 2.16: *Coolidge side-window tube schematic: filament C, anode A, cooling device with water inlet* W_in *and outlet* W_out*. Reproduced from Wikipedia.*

Bremsstrahlung electrons are decelerated and deviated as they approach an atomic nucleus. The electron loses kinetic energy, which is converted into photons due to the conservation of energy. The energy spectrum that is formed through this phenomenon is continuous, but since the photons may interact with the anode material on their way out through the photoelectric effect, discrete lines will also be generated [13].

Impact ionization high-energy electrons impacting the anode material may eject electrons from the inner shells of anode atoms, thereby producing vacancies which are filled by transitions from higher shells. If the transition is radiative then an X-ray fluorescence photon, characteristic of the anode material, will be emitted, at a considerably higher intensity than those produced through Bremsstrahlung and subsequent photoionization [13].

In case of high-power X-ray tubes, the anode is often mounted on a rotor shaft (see ***Fig. 2.17***). This rotating anode tube is an improvement of the Coolidge tube. By sweeping the anode past the focal spot the heat load can be spread over a larger area, greatly increasing the power rating. The anode consists of a disc with an annular target close to the edge. The anode can be rotated by electromagnetic induction from a series of stator windings outside the evacuated tube. Because the entire anode assembly has to be contained within the evacuated tube, adequate heat removal must be assured since direct cooling by conduction or convection, as in the Coolidge tube, is difficult [13, 19].

Synchrotron radiation

Synchrotron radiation sources in so-called electron/positron storage rings are the ultimate sources of X-rays for a wide range of spectroscopic applications (see ***Fig. 2.18***). For over a century, it has been known that the acceleration of a charged particle will result in the radiation of electromagnetic energy [20]. The first experimental observation of artificially generated (“man made”) synchrotron radiation from electrons orbiting in a 70 MeV synchrotron accelerator in 1947 by Elder et. al. was followed by the development of the betatron and synchrotron electron accelerators [21]. Synchrotron radiation

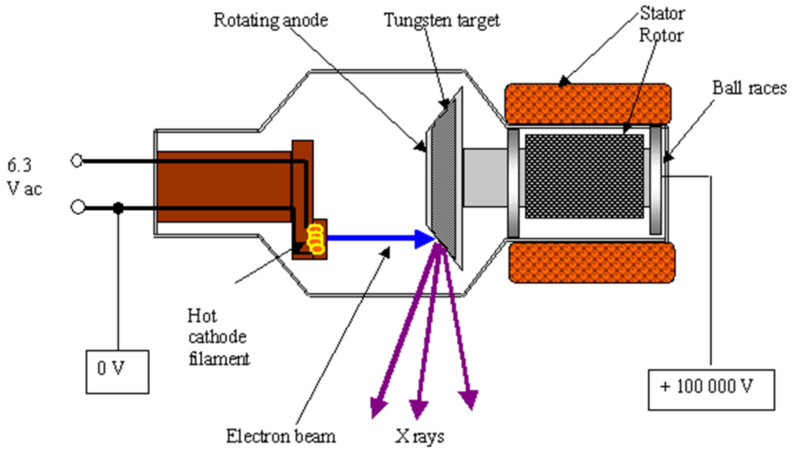

Figure 2.17: *Schematic of a typical rotating anode X-ray tube. Source: www.antonine − education.com/Pages/Physics_5_Options/Medical_Physics/MED_07/med_phys_7.html (17/05/2015).*

(SR) is the electromagnetic radiation which is produced by the radial acceleration of relativistic electrons (or in some cases positrons) when forced to follow curved paths. The recognition of the unique properties of the synchrotron radiation led to an explosive level of development activities aiming at the construction of more and more advanced sources for the production of SR and using the radiation in fundamental and applied science [13].

Figure 2.18: *Photograph of the European Synchrotron Radiation Facility in Grenoble, France. Source: www.esrf.eu (17/05/2015).*

The original, so called first generation synchrotron facilities, were developed for use in high energy physics research, such as particle collision experiments. The unavoidably generated SR was considered a “nuisance” in these facilities, as it resulted in an energy loss for the accelerated particles. However, due to the unique properties of SR, it was already used for some experiments in so-called parasitic mode. Starting from the 1980s, so-called second generation SR facilities were built with conditions specifically optimized for the production of SR mainly in the X-ray energy range [13]. The so-called third generation synchrotron radiation facilities were built during the 1990s as shown schematically in ***Fig. 2.19***). These complex large scale facilities consist of a linear accelerator

(LINAC) which first accelerates electrons or positrons to energies up to a few 100 MeV. The accelerated electron/positron beam is brought into a so-called booster accelerator ring were the electrons or positrons are gradually accelerated to the design energy of the storage ring (several GeV's), and eventually are injected into the storage ring via the injection system (1) [5, 18].

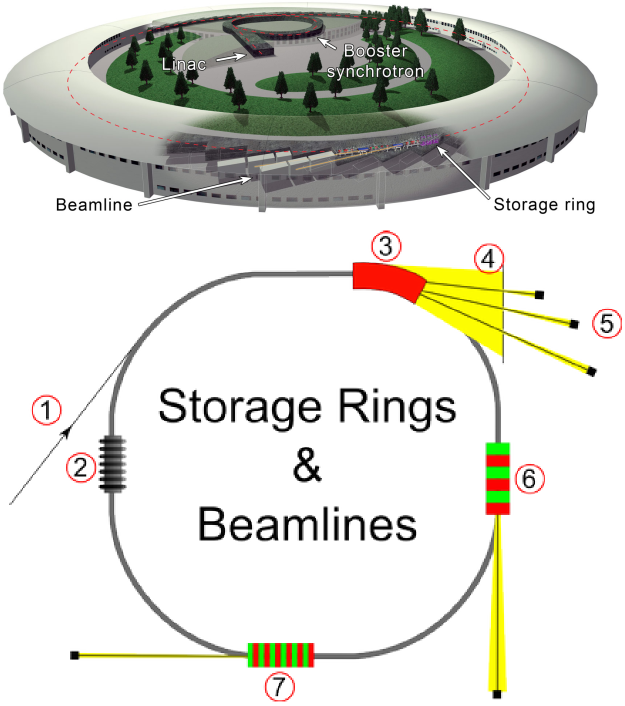

Figure 2.19: *Schematic overview of the different components of a third generation synchrotron device. Top: LINAC and accelerator ring. Bottom: (1) Injection system (coming from LINAC), (2) RF cavities, (3) Bending Magnet, (4) Beamlines, (5) Experimental hutches, (6) Wiggler, (7) Undulator. Source: www.hasylab.be (17/05/2015).*

The high vacuum environment of the storage ring is surrounded by a lattice of magnets to guide/accelerate the electrons/positrons on a closed orbit. This lattice of magnets includes the so-called bending magnets (BM), guiding the electrons or positrons in orbit by means of the Lorentz force. The emission of electromagnetic radiation occurs when forcing the highly relativistic electrons or positrons (their speed is nearly the speed of light) in a curved path which causes the emission of the so-called synchrotron radiation, covering a wide range of the electromagnetic spectrum, including hard X-rays. To carry out a wide range of spectroscopic experiments using synchrotron radiation, the emitted radiation is guided to the experimental station through so-called beamlines by using different X-ray optics as illustrated by ***Fig. 2.20*** [5, 11].

The so-called third generation facilities were built with radically reduced source sizes and divergences compared to second generation devices, in which the main sources of SR are insertion devices: periodic magnetic structures (undulators or wigglers) inserted in the straight sections of the synchrotron storage ring, depicted in ***Fig. 2.21***. These are special magnetic structures consisting of a large number of magnets in a series with alternating magnetic poles. They cause the electrons or positrons to follow an oscillating path while passing through the alternating magnetic fields, resulting in specific emission spectra. The so-called wigglers will simply make the electrons and positrons undergo

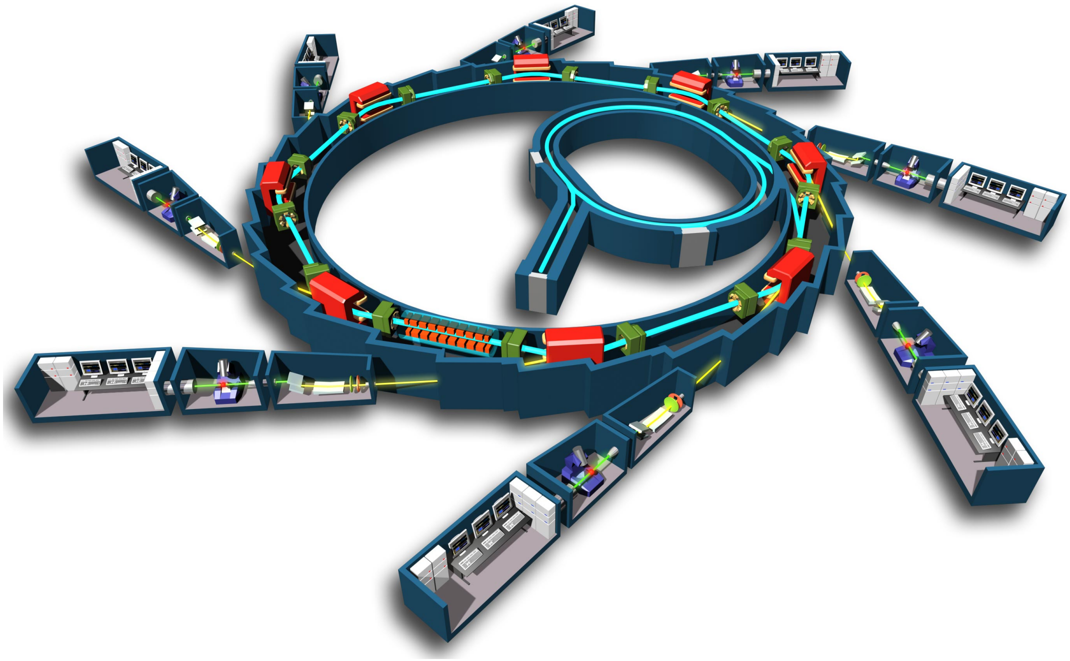

Figure 2.20: *Schematic representation of a typical synchrotron, storage rind and beamlines where a wide range of spectroscopic experiments get place. Source: www.esrf.eu (17/05/2015).*

more bends, resulting in a more intense X-ray spectrum than the normal bending magnets. Another insertion device is the undulator which makes use in a more pronounced way of the wave properties of X-rays, generating the waves in such a way that the emission intensity at certain X-ray energies will be enhanced by constructive interference, and at other energies the intensities will be suppressed by destructive interference. This results in a spectrum with very intense energy bands [11].

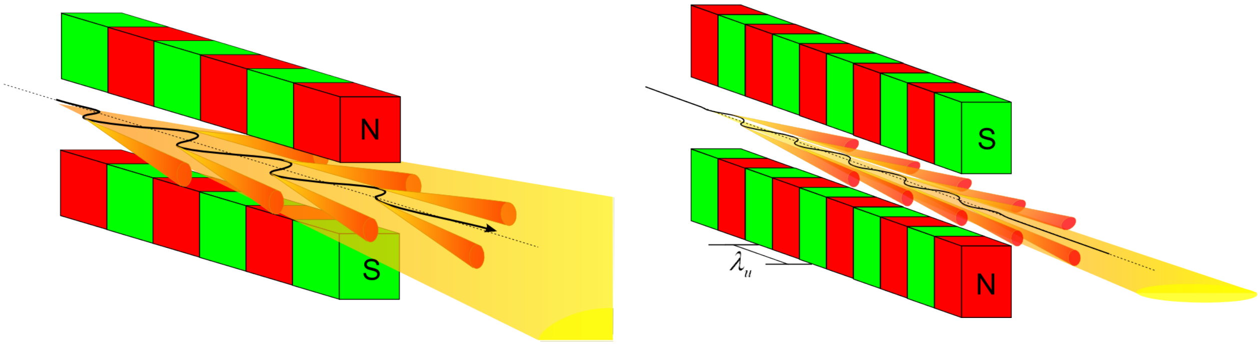

Figure 2.21: *Schematic overview of insertion devices. The distance between the magnets, in which the electrons or positrons flow, is called the gap. By modifying this gap one can select the energy of the generated X-rays. Left: Wiggler. Right: Undulator. Source: www.hasylab.be (17/05/2015).*

2.3.2 X-ray optics

As mentioned earlier, all X-ray spectrometers have a similar design with the same main components (see ***Fig. 2.22***): Excitation source (2.3.1), sample positioning system, detector and optional primary and secondary optics. Primary optics, positioned between the X-ray source and the sample, are used to change the energy distribution of the radiation or perform a beam shaping. Changes of the energy distribution are possible with filters, secondary targets or monochromators, the shape of the excitation beam can be influenced by collimators or X-ray optics. Often with X-ray optics both shape and energy distribution of the beam are influenced. Similar optics can be used as secondary optics, positioned in front of the detector. Depending on the requirements, specialized focusing optics can be used to improve spatial resolution, a filter can be used to improve peak-to-background ratios, or one can use a dispersive optic as a tunable monochromator [22].

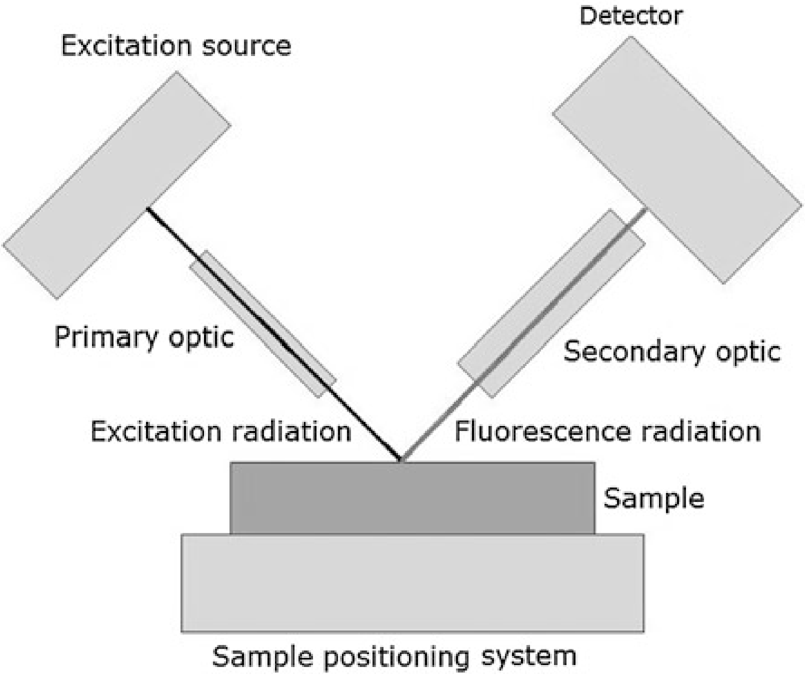

Figure 2.22: *Scheme of the main components of an X-ray spectrometer [22].*

All X-ray optics use the already discussed interaction types and wave phenomena of electromagnetic radiation with matter. In particular the following optic types can be distinguished:

- Scattering at periodical structures by interference of the scattered waves (Bragg scattering) in crystal optics and synthetic multilayer structures.
- Bragg scattering on reflecting zone plates (Fresnel structures).
- Refraction of X-rays in refractive lenses or in transmission zone plates (Fresnel optics).
- Total reflection by using very small incident angles for total reflection (mirrors, capillary optics).

These optics both shape the beam and influence the energy distribution of the spectrum, they can be used as primary as well as secondary optics. There are many different kinds of X-ray optics of which only the most important types will be discussed below. Note, that many more can be found in literature [5, 22].

Slits and pinholes

Pinholes and slits are among the most simple optics which can be represented by basically a metal plate containing a microscopically small hole or vertical gap as can be seen in ***Fig. 2.23***. Such pinholes in front of the X-ray tube restrict the area illuminated by the X-rays during analysis, used in case of the Surface Monitor (see further: 2.3.3). Pinholes in front of the detector (typical sizes are in the range of a few tens to a few hundreds of micrometers) collimate an X-ray beam in such a way that only fluorescence X-rays from a certain area on the sample can reach the detector. In the situation of the Surface Monitor, slits with the shape of a vertical gap where used in front of the detector to obtain more narrow peaks and resulting in a higher energy resolution. On the other hand, by choosing a narrow slit, the positioning of the sample becomes critical and decreases the photon flux to the detector which can cause a problem in cases of samples producing low count rate. It should be noted that the material which the pinhole is made of is relevant as well. In case of using pinholes and slits made of Cu, one can expect Cu fluorescent X-ray lines in the spectrum as well.

Figure 2.23: *Slits and pinholes of sizes between 0.5 mm and 2.0 mm which can be used for the Surface Monitor (see further: 2.3.3).*

Polycapillaries

A more advanced focusing optic is the polycapillary which consists of a large number of narrow hollow glass tubes with micron sized internal diameter. The optics collects X-rays that emerge from an X-ray source within a large solid angle and redirects them, by multiple external total reflections, to form either a focused beam or a parallel beam, as illustrated in ***Fig. 2.24***. Based on the principle of total reflection, polycapillaries guide the photons through the capillary fibres: when an X-ray hits a surface with an angle of incidence smaller than the so-called critical angle of total reflection θ_c, the X-ray will be totally reflected. In this way, an X-ray can be guided through a polycapillary fibre as depicted in ***Fig. 2.25***. The critical angle for glass polycapillaries is dependent on the X-ray energy and is in the order of a few *mrad* in case of the X-ray energy region of 1 to 20 keV which means that the bending curvature of the capillary has to be gentle and the capillary diameter has to be small to maintain the total reflection conditions. The typical radius of curvature of the individual hollow glass tubes within polycapillary optics is about a few hundreds of millimeters and the channel diameter ranges anywhere from a few μm to a few tens of μm [23].

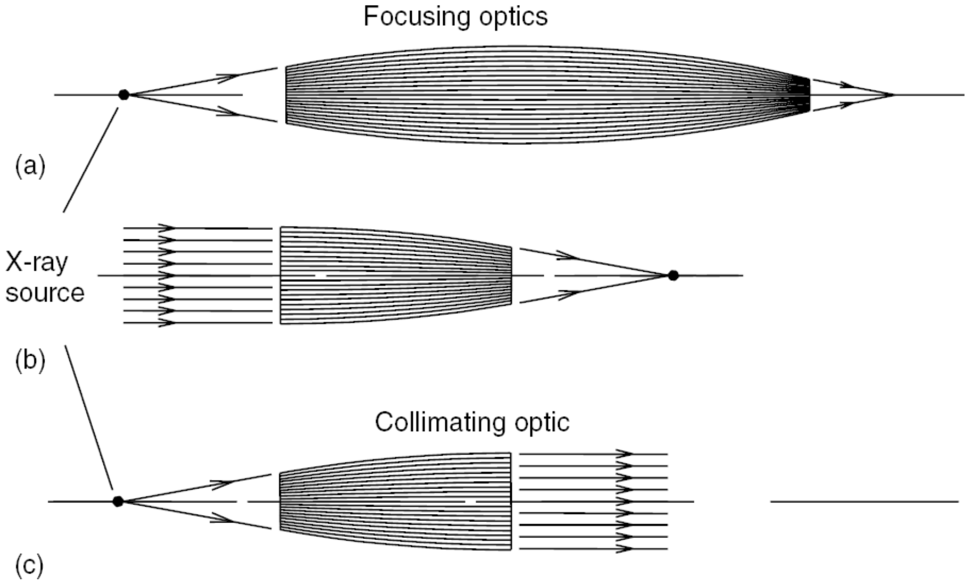

Figure 2.24: *Polycapillary X-ray optics that produce a focused (a,b) or parallel beam (c), starting from an X-ray point source (a,c) or a quasi-parallel X-ray source (b: synchrotron) [23].*

The dependence of the critical angle θ_c on the energy has its effects on the transmission probability of high-energy X-rays through the polycapillary, influencing the sensitivity of higher atomic number elements. Due to the 1/E dependence of the critical angle on the photon energy, high energy X-rays will have a very small critical angle of total reflection, causing even the smallest deviation towards a larger angle of incidence to result in a full attenuation of the photon rather than its transmission. On the other hand, low energy X-rays will have a larger critical angle, and may have larger angles of incidence before the photons will be attenuated by the capillary fibre wall. It should be noted that the capillary fibres are made of very thin glass tubes. As such, it is also possible for highly energetic X-rays to pass through the capillary wall when their angle of incidence is larger then the critical angle. When this happens the X-rays will not follow the curvature of the capillary, but will penetrate straight through the glass. Therefore, for high energy fluorescent X-rays, the polycapillary detector lens will have limited imaging properties and will have a greatly reduced efficiency [11].

Next to their use as focusing optics (see ***Fig. 2.26***), polycapillaries are also frequently used as a detector collimator by mounting them in front of a detector. This so-called confocal XRF arrangement has been applied succesfully in studies of geological, extraterrestrial, biological and artistic samples [24–28]. The use of a polycapillary half-lens in front of the detector allows the XRF detection from a microscopic sub-volume within the sample, allowing three-dimensional analysis. This also leads to the elimination of single and to some extent multiple scattering from outside the microvolume

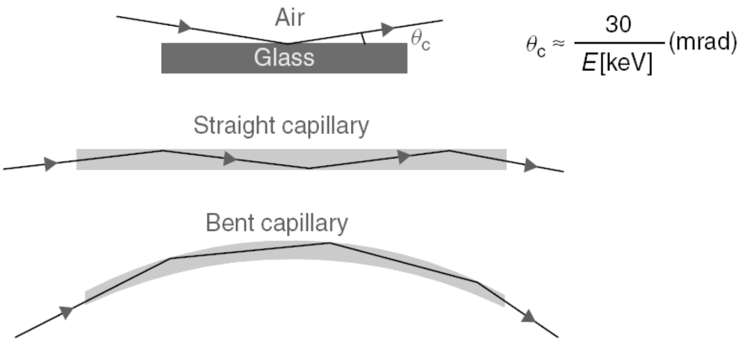

Figure 2.25: *Schematic representation of the principles of capillary optics. θ_c is the critical angle for total reflection [23].*

of detection, and due to its high-energy filtering, it further suppresses high-energy scatter peaks, progressively cutting down background intensity above 25 keV. This imposes a practical limit for the detection of high-energy XRF lines as well as limiting the usage of this method in general for energies above 20-25 keV in terms of fluorescence energy.

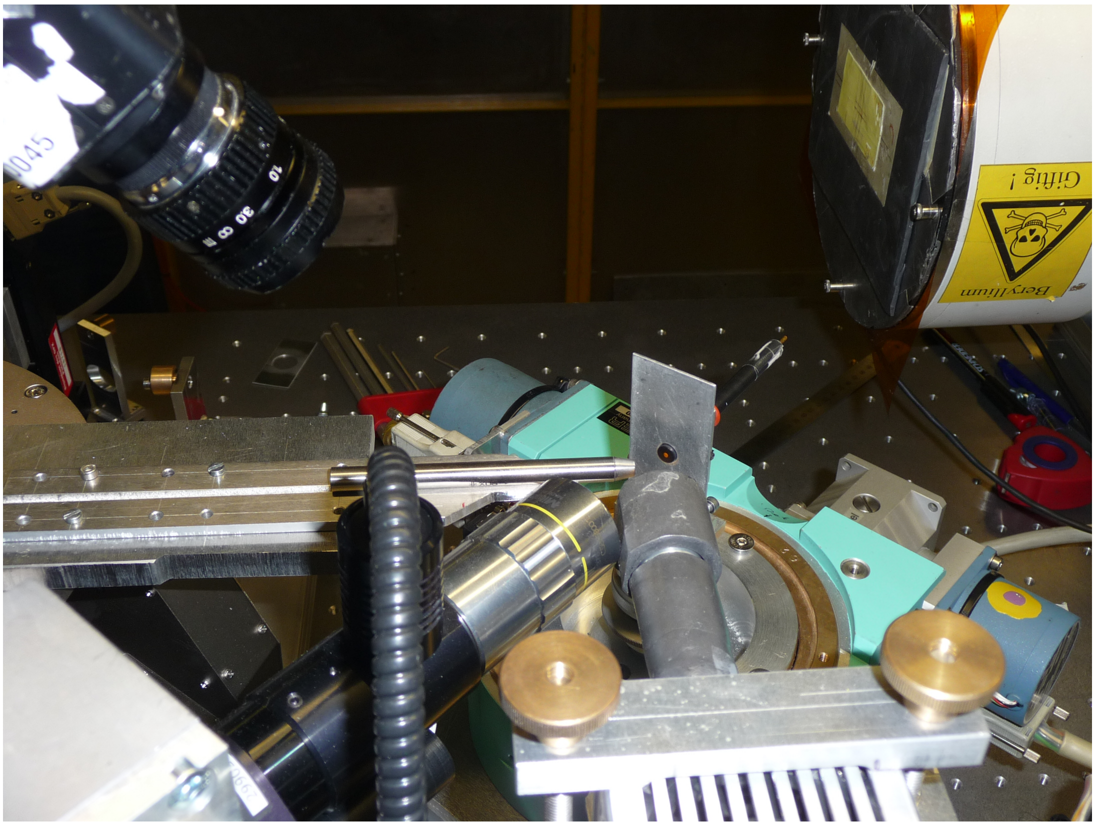

Figure 2.26: *Polycapillary used in front of the X-ray source at HASYLAB beamline L.*

Focusing mirrors

Another focusing optic based on the principle of total reflection concerns the use of mirrors which operate under a very small incident angle (typically around 0.5 degrees and reducing for high energies) and provide the reflection of a broad energy band. The advantage of total reflection mirrors is their high reflectivity and achromatic focusing nature and therefore they can be used for the production of high intensity tunable synchrotron micro/nano-beams. The mirror acts as a low-pass filter, i.e. filtering out high energy X-rays. The focusing effect of the mirror is always depending on the way it is curved and two designs are commonly used: a toroidal or an ellipsoidal mirror. The ellipsoidal mirror avoids aberration problems which occur when using toroidal mirrors, however, the manufacturing of these ellipsoidal mirrors are exceedingly difficult due to the extreme accuracy needed to reproduce the double curved ellipsoidal shape. The use of two perpendicularly aligned elliptical total reflection mirrors in a so-called Kirkpatrick-Baez geometry circumvents these problems [5].

Total reflection mirrors can also be used for low energetic radiation, for example, for energies lower then 1 keV. In that case, also larger incident angles are accepted which offers the possibility for highly curved mirrors. Total reflecting mirrors are produced from substrates with extremely low roughness. If they are used for beam shaping the bending radii must be very large to ensure that the incident angle is smaller than the critical angle of total reflection. To enlarge this angle they can be coated with heavy materials with a high density such as Au or even Re [22].

Fresnel zone plates

Fresnel zone plates are based on diffraction instead of total reflection to focus the X-ray beam. A zone plate consists of a set of radially symmetric rings, known as Fresnel zones, which alternate between opaque and transparent. X-rays hitting the zone plate will diffract around the opaque zones and the space between the zones can be chosen such that the diffracted X-rays constructively interfere at a desired focus on the sample as can be seen in ***Fig. 2.27***. Zone plates produce equivalent diffraction patterns no matter whether the central disk is opaque or transparent, as long as the zones alternate in opacity. It should be noted that unlike a standard lens for visible light, a zone plate produces subsidiary intensity maxima along the axis of the plate through higher order diffraction, although these are less intense than the principal focus [29].

In order to get complete constructive interference at the focus, the amplitude of the diffracted light waves from each zone in the zone plate must be the same (which means that for an evenly illuminated zone plate, the area of each zone is equal) and the width of the zones must decrease further from the center. Therefore, the maximum possible resolution of a zone plate depends on the smallest zone width and thus, the smallest size object which can be imaged, is limited by the accuracy of the zone plate fabrication. Zone plates are mostly manufactured using lithography and by improving this techniques, the size that can be manufactured will decrease and the possible resolution will improve [29]. Zone plates currently provide the best spatial resolution for two-dimensional X-ray focusing, but due to their low efficiency they are mainly used for soft X-ray applications and were not used in the scope of this work.

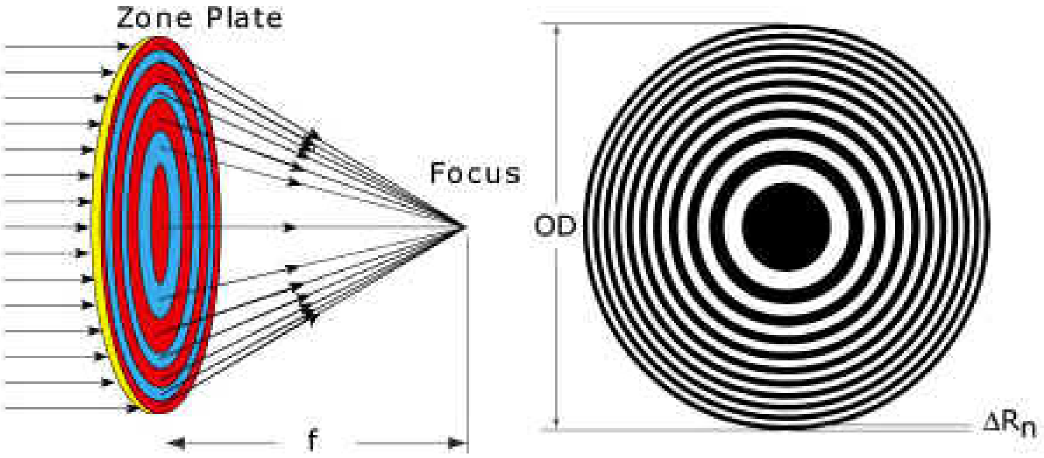

Figure 2.27: *Working principle of a Fresnel zone plate [22].*

2.3.3 X-ray detection

The first X-ray detector was discovered along with the discovery of the X-rays themselves by Wilhelm Conrad Röntgen. The X-rays were detected using a fluorescent screen, made of barium platinocyanide, which started to glow upon the accidental irradiation by X-rays generated by Rontgen's cathode-ray tube. In a sense, this fluorescent screen can be regarded as the first X-ray detector. This was soon followed by the use of photographic screens, which are still widely used in medical applications, and ionization chambers. These chambers consist of a gas filled enclosure between two conducting electrodes and when the gas is ionized by the incoming radiation, positively charged ions and electrons arise. When they move towards the electrodes of opposite polarity, an ionization current is created which can be measured by a galvanometer [6, 11, 30].

Such types of X-ray detectors are however not energy dispersive: only the presence of X-rays and the intensity of the ionizing radiation can be derived but their exact energy remains unknown. For use in energy dispersive X-ray fluorescence spectroscopy, the knowledge of the energy of the X-ray photons is required since the distinction between different elements can only be made based upon the X-ray photon energy. The first device designed to enable the measurement of the energy of ionizing radiation is the proportional counter, which has the advantage of being cheap, easy to operate, but comes with a low detection efficiency for high energy X-rays. An alternative is the scintillation detector which has a much higher detection efficiency for high energy photons and is very small in size. However, its poor energy resolution is its main disadvantage which decreases the capability of the system to distinguish photons closely separated in energy [13].

Semiconductor detectors

In the early 1960s, the introduction of semiconductor detectors led to a significantly better energy resolution [30]. The main advantage of the employed semiconductors is that the energy needed to create one primary elementary charge is only a few eVs compared to 20 to 30 eV needed needed when using gases, reducing the statistical fluctuations by about a factor 3 [5].

The working principle of an energy despersive semiconductor detector is shown schematically in ***Fig. 2.28***. Depending on the energy of the incoming X-rays, the detector material and the thickness of the material, X-rays entering the detector are mainly absorbed by photoeletric absorption. The interaction with the semiconductor detector material is analogous to the ionization chamber: the semiconductor material is ionized by the incoming photons either through the photoelectric effect or through inelastic scattering, depending on the energy of the photon and the detector material. If ionization occurs, the incoming X-ray photon will be converted into energetic photo- and Auger electrons through a series of interactions. The fastest electrons rapidly lose their energy by creating a large number of electron-hole pairs in the semiconductor material which can be collected on the electrodes of the device. The electrons accelerate along the high-voltage bias, and generate a measurable electric pulse which is recorded in a multichannel analyzer. Since the number of generated electron-hole pairs is proportional to the initial photon energy, the determined electric pulse height provides a measure of the original X-ray energy [11].

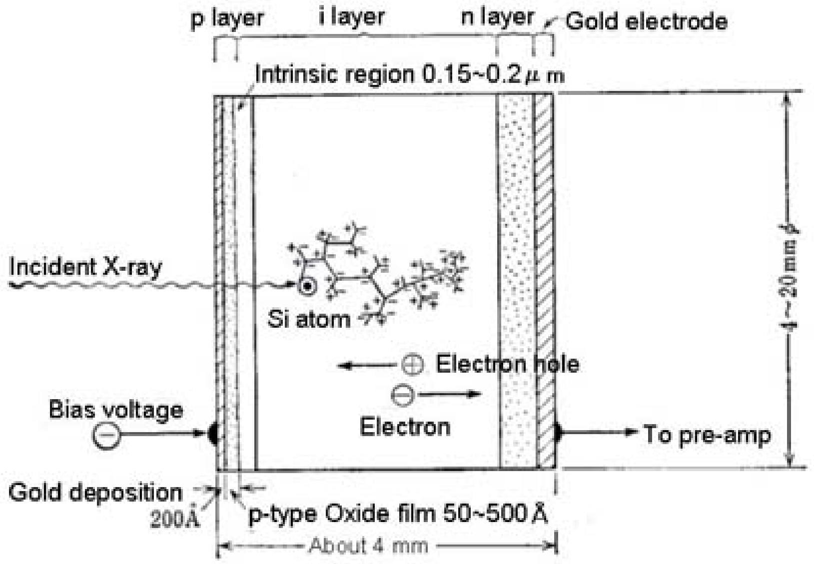

Figure 2.28: *Working principle of an energy dispersive semiconductor detector [6].*

Usually the semiconductor material is doped with acceptors (which provide free positive charged holes, p-type material) and donors (which introduce free electrons, n-type material) in order to increase the conductivity of the material. The Si(Li) detector is a semiconductor detector, made of Si and doped with Li atoms. When a voltage is applied to it, holes and free electrons will be formed: the holes will gather near the cathode and the free electrons will drift towards the anode. In between, an area will be formed without holes or electrons: the depletion region. When a photon enters the detector and is absorbed in the depletion region, it creates a number of electron-hole pairs, which is proportional to the X-ray energy. The average number of formed charge carriers is determined by the mean energy necessary for the production of a single electron-hole pair (e.g. 3.65 eV per electron-hole creation in Si). The production of these electron-hole pairs will generate a measurable voltage. As a disadvantage, a continuous charge flow is thermally generated within the bulk material (dark current) which is also collected on the detector electrodes, contributing to a statistical spread in the measurements of the charge signal. However, by suitably cooling the detector, the dark current value can be highly reduced . The need for liquid nitrogen cooling for a Si(Li) detector to produce spectroscopic data makes this detection system rather large and difficult to handle, as the detector requires hours to cool down to the operating temperature before it can be used. The next Si-based detector devices were Si-PIN-diodes which have the advantage that electric cooling is sufficient. Their disadvantages are the small sensitive area and the limited energy resolution against the Si(Li)s [22]. Another, more advanced alternative for ED-XRF detectors is represented by Si-drift detectors (SDDs), which are described below [18].

Silicon drift detectors

Although still widely used, Si(Li) detectors are nowadays being replaced by so-called Silicon Drift Detectors (SDD) [30]. The working principle of these devices is the same as that of other semiconductor detectors, however, the material is arranged in a different way compared to the Si(Li) detectors: a transversal field of ring sensitive electrodes causes charge carriers to drift towards a small collection electrode which allows for significantly higher count rates compared to Si(Li) or Si-PIN detectors. The collection electrodes are characterized by a very low capacitance, which allows the application of short shaping times, as well as low leakage current, removing the need for the inconvenient liquid nitrogen cooling. Electrical Peltier cooling is used instead, leading to a far more compact device. All these advantages explain the popularity of SDD devices for XRF experiments both at synchrotron facilities and in case of laboratory experiments [31].

Full-Field XRF detectors

A full-field X-ray fluorescence detector is an instrument capable of detecting X-rays in an energy dispersive manner, while spatial information is recorded at the same time. In this way, full-field XRF detectors can be used to take ‘pictures’ of fluorescence X-rays for entire samples at a time, much like a photo-camera takes pictures using visible light. In fact, the CCD chips registering the X-rays are basically the same chips one can find in any digital camera. The property of making almost photograph-like images is also the reason why this type of detector is sometimes referred to as a full-field camera [11].

Full-field detectors have been used since 2000 to perform μ-XRF measurements. Within the class of full-field detectors, a distinction can be made between Charged Coupled Device (CCD) detectors and Complementary Metal Oxide Semiconductor (CMOS) detectors [32–35]. The main difference between these two types, is the way in which they read out the collected signals. A CMOS detector will read out each pixel separately, whereas a CCD detector will transfer the photogenerated charge from pixel to pixel and convert this charge to a voltage at an output node. The detector chip is usually built up (out) of silicon, which absorbs incoming X-rays and converts them into electron clouds. In a CMOS detector every pixel has its own readout electronics, resulting in very fast signal readout. In fact, one could picture this CMOS full-field detector as a collection of many miniaturized Si(Li) detectors. A CCD detector reads out the signal in a somewhat more complex way. However, the production of a CCD chip is less complex than that of a CMOS chip, as the electron to volt conversion occurs on a separate circuit board [34, 35].

A full-field detector prototype, named SLcam, was used during the investigation of the majolica samples. This full-field device is based on the use of a 2D energy dispersive X-ray pnCCD detector, which acquires nearly 70,000 XRF spectra simultaneously, while the sample is illuminated with a broad X-ray beam enabling 2D elemental imaging without any need for sample manipulation. More information and research results corresponding to the use of the SLcam detector for full-field XRF imaging can be found in [36] and [37].

2.3.4 EDAX Eagle III micro-XRF spectrometer

Laboratory micro-XRF instruments are nowadays available in many laboratories worldwide and with different instrumental concepts, both as prototypes but also as commercially available instruments. This enables their use for a wide range of different applications.

Micro-XRF has experienced a strong development in the last decades. The high interest in this method for position dependent elemental analysis can be understood because of the increasing demands for analysis of composites of diverse materials. Another reason for the requirement to analyze a small sample area can be the size/shape of investigated materials. In case the sample surface of interest is not flat or the size of the object does not allow to position it in the chamber of the instrument, a section of the sample needs to be taken for the measurement, eventually damaging because of the physical sampling. However this may be avoided when small sample areas can be excited applying micro-XRF methodology: the microscopic distribution of elements across the sample area of investigation can then be studied by simply positioning the analyzing x-ray beam at the positions of interest on the sample. The obtained results can vary from simple single point measurements to 1-dimensional line scans or 2-dimensional area maps, to ultimately 3-dimensional elemental distribution. This analytical performance is available combined with an easy sample handling and a straight forward sample preparation [22].

Micro-XRF is based on concentrating the x-ray radiation from the laboratory source onto a selected microscopic small area of the sample. The introduction of capillary optics allowed the excitation of such small sample areas resulting in fluorescence intensities high enough to be useful for micro-XRF mapping by the laboratory instrument. In case of heterogeneous samples, using a microscopic x-ray beam, there is the need for correct positioning of the sample into the analyzing beam. Next, its microscopic size gives also the need of a dedicated optical viewing system that helps to guide the user when moving the points of interest of the sample into the beam. Finally, a detection system of the characteristic x-rays delivers the spectroscopic spectral data that can be further processed by the computing system. High acceptance angle, good energy resolution, and high count rates are necessary when investigating a broad range of sample types [22].

The EDAX Eagle III, as shown in ***Fig. 2.29*** is the laboratory micro-XRF spectrometer of the X-ray Microspectroscopy and Imaging (XMI) Group. This instrument was used in this dissertation to study Antwerp majolica (chapter 3 section 3.3) and to investigate insects trapped in amber (chapter 7 section 7.3.1 and 7.3.2). The spectrometer consist of an air cooled Rh X-ray tube with polycapillary optics attached to it, and a liquid nitrogen cooled Si(Li) detector with an active area of 80 mm^2 as main components. The incidence angle of the X-rays on the sample is 60° and a beryllium window separates the detector crystal from the rest of the device. Also, two cameras are present with 10 and 100 times magnification for sample positioning to set up the scanning micro-XRF experiments. Samples are placed in the sample stage which can be moved in the X-, Y- and Z-direction, and the stage motors can move with minimun step sizes of 5 μm. This enables performing point, line as well as area scan measurements. ***Fig. 2.30*** shows the set-up of the instrument. The instrument can be operated under vacuum, making the detection of low energy X-rays possible as attenuation by air is eliminated, making low-Z element analysis possible down to Na.

Figure 2.29: *Front view of the EDAX Eagle III micro-XRF spectrometer.*

Figure 2.30: *Inside view of the EDAX Eagle III micro-XRF spectrometer.*

In operation, the X-ray tube work typically at a voltage of 40 kV and the applied current is then adjusted to obtain a maximal detector dead time of 30 %. A real advantage of the EagleIII compared to other commercially available instruments is that the x-ray beam is focused by polycapillary optics using the so-called varispot system that allows to vary the beam size to the need of the experiment. ***Fig. 2.31*** shows the operation principle of the varispot: by moving the polycapillary away from the sample compared to the ideal working (focal) distance, the divergent beam covers an area on the sample varying from 25 to 300 μm where the beam size is slightly out of focus. The spot size is inversely proportional to the X-ray energy because the critical angle of total reflection within the glass channels of the polycapillary scales according to 1/E, where E is the X-ray energy.

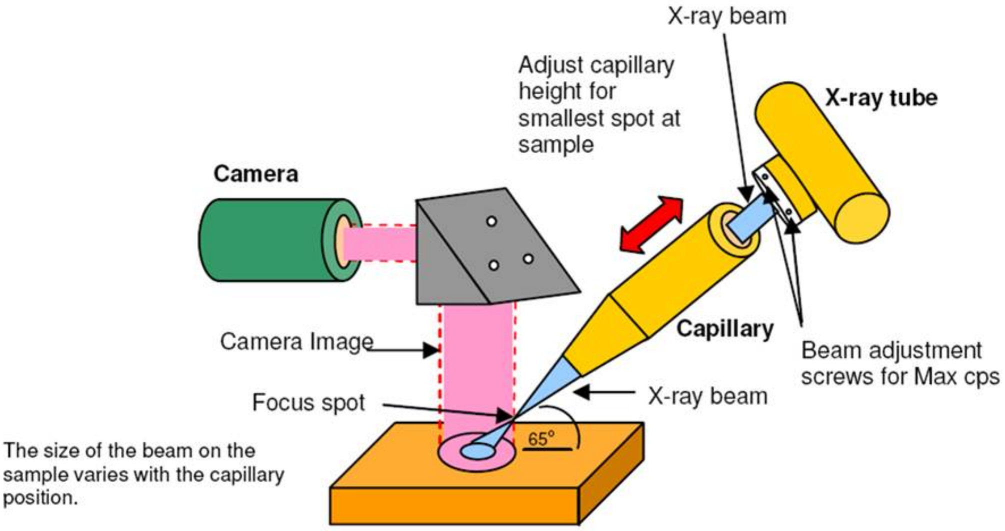

Figure 2.31: *EagleIII: Working principle of the varispot system [18].*

2.3.5 Handheld XRF spectrometer

XRF has the advantage of being a non-destructive, multi-elemental method of quantitative analysis that allows the examination of a variety of material types down to the ppm level of concentration. As already mentioned above, a number of commercial μ-XRF instruments are currently available but all these instruments are of the table-top (laboratory) type, where objects or samples need to be brought to the instrument for examination [3].

A μ-XRF instrument suitable for *in situ* analyses (i.e. allowing the analyses at the location where the objects/materials are normally resides, e.g. in museum or customs warehouse) requires a compact, light-weight and easy-to-handle design. The portable XRF instrument has to provide an intense x-ray beam with a small diameter so that relatively small samples or sub-millimetre details on larger objects can readily be analysed coming from air-cooled, low-power x-ray tubes. For the (energy-dispersive) detection of the fluorescent radiation, the use of compact, liquid nitrogen free devices appears to be appropriate as an energy-dispersive (ED) detector. Currently, several types of compact ED detectors with significantly different resolution and maximum processing count rates are commercially available [38–40]. The portable XRF spectrometer used during this PhD work was the Olympus InnovX Delta handheld XRF (hXRF) spectrometer. ***Fig. 2.32*** shows a picture of the instrument.

Figure 2.32: *The handheld Olympus Innovx Delta XRF spectrometer. Its rugged design suggests use in harsh environments on the field. The operation should be as simple as aiming, "shooting" and getting results. Source: http://www.olympus-ims.com (17/05/2015).*

The Olympus InnovX Delta handheld XRF (hXRF) spectrometer has a pistol-like shape with 26.0 cm x 24.0 cm x 9.0 mm size and total weight of 1.5 kg (without battery) and is a highly performing instrument for fast *in situ* and non-destructive elemental analysis. The instrument consists of a 4 W x-ray tube based on a Rh anode with a spot size of 5 mm^2 and a SDD detector. The operation of the instrument can be controlled by the touch screen available at the back of the instrument or by using a USB-USB cable connection between the hXRF and a portable PC, on certain distance of the instrument. The latter is preferred because of reasons of safety. The power of the hXRF is delivered by one battery which has an active lifetime of approximately 5 hours (two batteries are available). Also an extra docking station is included (external power necessary) where the battery can be loaded and which is needed to calibrate the instrument by connecting the hXRF into the docking stage, before a measuring day can start. The positioning of the x-ray beam is done using markers on the probe head or a cross-shaped slider system when using a tripod stand. The correct positioning of the probe head is achieved when the markers on the instrument overlap with markers on a transparent polyester melinex sheet that is put in place for this purpose and removed prior to the actual XRF measurement.

Fig. 2.33 shows limits of detection (LOD) for the Innovx Delta hXRF instrument, together with values obtained with the laboratory micro-XRF spectrometer EDAX EagleIII when performing measurements on the NIST SRM 1412 glass standard. The standard was measured under the optimum conditions of each instrument. These LOD values were determined to get knowledge about the performance of the instruments. The obtained LOD_i for a given element i is calculated as follows:

$$C_{LOD_i} = 3\frac{\sqrt{N_{B_i}}}{N_{N_i}} \times C_i \qquad (2.8)$$

with N_{B_i} the number of background counts, N_{N_i} the net number of counts and C_i the concentration of element i in the standard reference material. For both instruments, a point measurement was performed on the NIST SRM 1412 glass standard by measuring at 40 kV (maximum voltage) for 300 s (measuring time). For the EDAX Eagle III micro-XRF spectrometer, the current was adjusted to reach a dead time rate of 30 % (150 μA) and a maximum beam size of 300μm. Two measurements were performed: the first one in vacuum (best performance) and the second in air in order to be able to compare with the hXRF spectrometer where there is no choice between vacuum or air.

Working in vacuum, the EagleIII performs better for the low Z elements. Operation in air, the hXRF shows better LOD values than EagleIII which can be explained by the lower number of geometrical constraints of the hXRF. The probe head can be placed at a much smaller distance from the sample's surface, and the spectrometer uses a broad beam instead of a micro-beam. However, hXRF will not allow long measurement times when operated by hand. The major advantages of EDAX Eagle-III are, that all instrumental parameters are optimized in order to acquire data in optimal conditions and that there is the possibility of measuring in vacuum to obtain the best LOD for low Z elements at microscopic spatial resolution. The handheld XRF instrument emits a broad beam and analyzes areas which are 3-4 orders of magnitude larger.

2.3.6 XRF Spectral data interpretation: pitfalls

The areas mentioned in equation 2.8 were derived by converting spectral data (see next paragraph 2.3.7) that were obtained using XRF instruments described in previous paragraphs. ***Fig. 2.34*** is the XRF spectrum of the NIST SRM 1412 glass standard acquired with the EDAX EagleIII micro-XRF spectrometer (300 μm beam size, 40 kV, vacuum conditions, 1000 sec). The X-ray peaks can be related to elements of the sample (energies are given in the literature [7, 41]) and are superimposed on a background signal [42]. The height of the peaks, more precisely the area under a peak, is proportional to the concentration of the elements. Next to the peaks, one needs to possibly take into account several artifacts in order to correctly interpret XRF spectral data as explained in the following.

A first artifact is a sum peak, which appears at an energy that corresponds to the sum of two or more other peak energies. A sum peak occurs from the summing of the electrical pulses at high-count rates because the individual events occur within a time period that is less than the resolving time of the detector electronics. Therefore one count is lost from each peak and is added to the sum peak. This phenomenon logically occurs mostly with the most intense peaks of the spectrum [42]. Another artifact are escape peaks, related to the escape of the K or L X-ray photons of the detector material from the detector active volume. In the case of the Si detector (in most cases in this PhD work), the

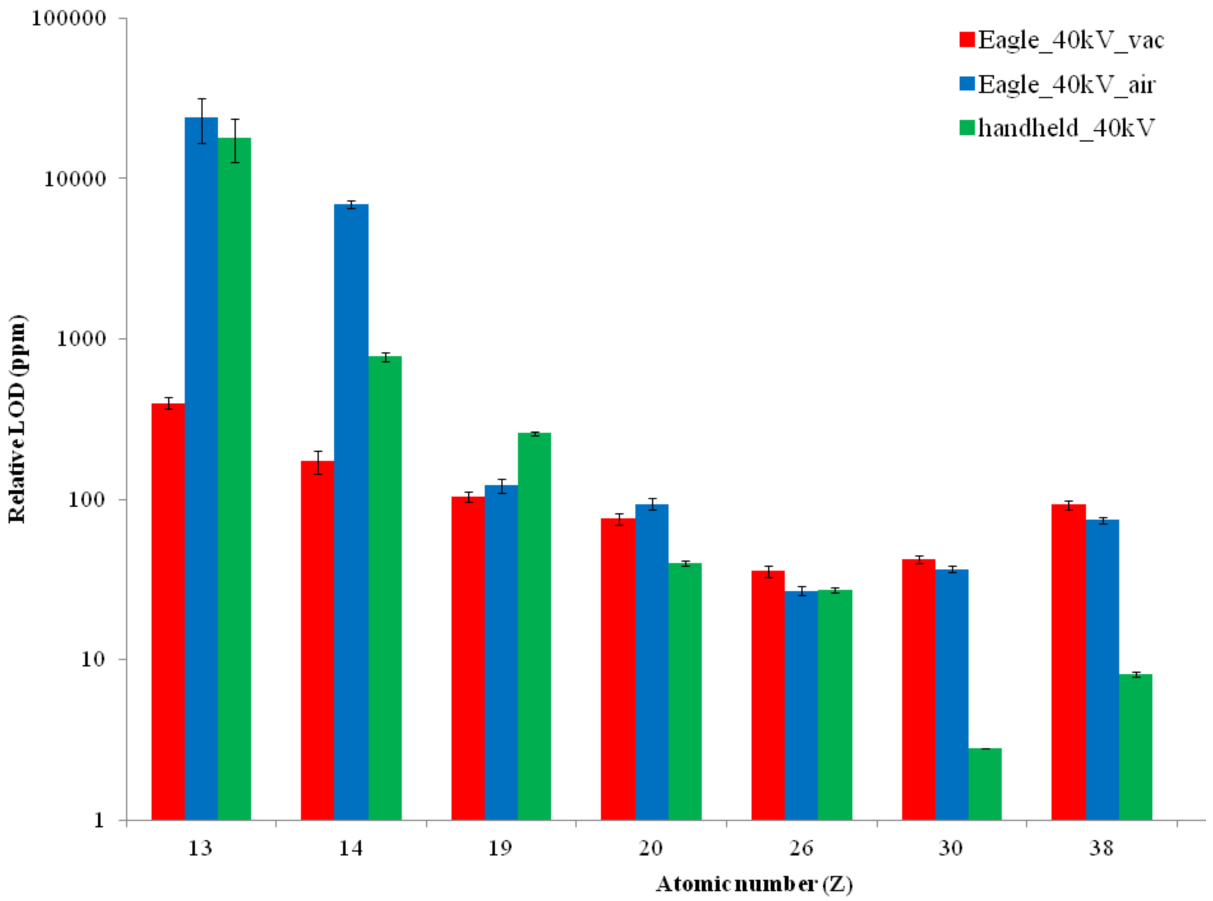

Figure 2.33: *Comparison of the LOD of the EDAX Eagle III micro-XRF spectrometer and the handheld XRF spectrometer (voltage of 40 kV, 300 s measuring time).*

position of the escape peaks are expected 1.742 keV (Si-K_α) below the parent peak. In practice they only are noticeable when they are connected to intense peaks in the spectrum [42]. The researcher may be mislead when small peaks of interest are positioned near escape peaks.

2.3.7 Spectrum evaluation by AXIL

Owing to the presence of the above described artefacts in the collected spectra with ED-XRF based instruments, the evaluation of these spectra requires dedicated software. Therefore, a software package was employed for the fitting of the collected XRF spectra: AXIL (Analysis of X-ray Spectra by Iterative Least Squares) which uses a non-linear least squares fitting strategy to fit a mathematical function to experimental data [43, 44]. A modified Marquardt algorithm was used to minimize the weighted sum of differences χ^2 between the experimental data y and a mathematical fitting function y_{fit}:

$$\chi^2 = \frac{1}{n-m} \sum_i \frac{[y_i - y_{fit}(i)]^2}{y_i} \tag{2.9}$$

where y_i is the observed value in channel i of the spectrum and $y_{fit}(i)$ the calculated value of

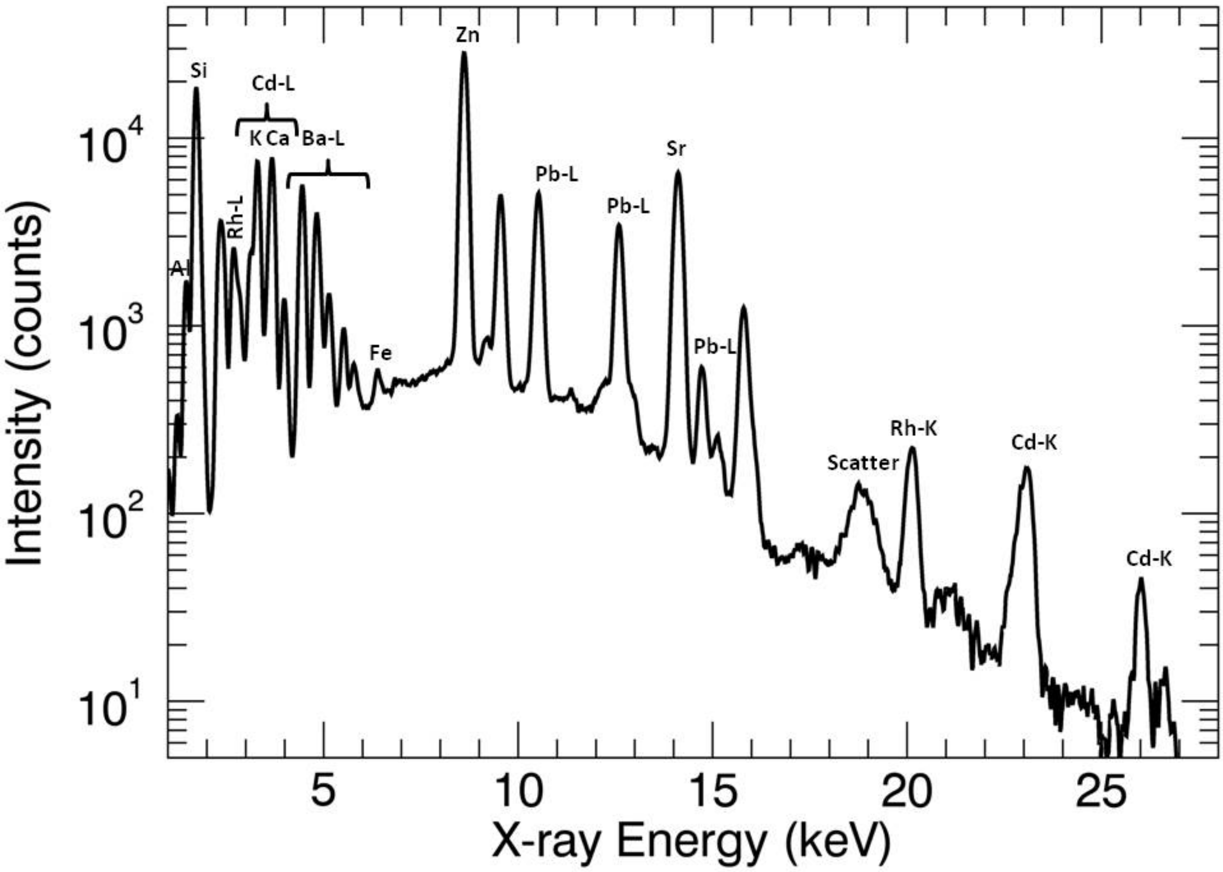

Figure 2.34: *Typical X-ray fluorescence spectrum of NIST SRM 1412, identified using AXIL [43, 44]. The height of the peaks, more precisely the area under a peak, is proportional to the concentration of the element in the specimen.*

the fitting function in this channel; n is the total number of channels in the fitting window while m represents the number of parameters of the fitting function that are estimated during the fitting process. The fitting function is the sum of the spectral background and the fluorescence peaks:

$$\begin{aligned} y_{fit}(i) &= y_{back}(i) + y_{peak}(i) \\ &= y_{back}(i) + \textstyle\sum_j y_j i \end{aligned} \tag{2.10}$$

where the first term represents the spectral background and the second term corresponds to the fluorescence peaks included in the model. The index j runs over all characteristic line groups. For each line group j, (e.g. Ca K, Pb L), the contribution $y_j(i)$ to the i^{th} channel content is calculated as:

$$y_i(i) = A_j(\sum_{k=1}^{N_j} R_{jk} G_{jk}(E_{jk}, i) t(E_{jk})) \tag{2.11}$$

where A_j represents the total area of all photopeaks (e.g. Ca–K$_\alpha$ and Ca–K$_\beta$) belonging to this group and being optimizable parameters in the least squares fitting process. The index k runs over all lines in group j, each line having a relative abundance R_{jk} with $\sum R_{jk} = 1$. G_{jk} represents a

Gaussian function centered around the energy E_{jk} which optionally also accounts for escape peaks. $t(E_{jk})$ denotes the total attenuation factor for X-rays with energy E_{jk} as defined by absorption of radiation in the detector, in absorbers placed between sample and detector and in the sample itself. During the iterative process, the parameters are optimized to obtain the best match between the model and the spectral data. Another parameter to be optimized during the fitting process is the background model function which represents the background shape by a mathematical function [45].

Every energy dispersive detector that is used for collecting the XRF spectra has a certain energy resolution. The energy resolution expresses how accurately X-ray photons can be distinguished in terms of energy [5]. Because of certain statistical fluctuations affecting the measurement of a photon energy, the received signal will not be a "narrow" line at a certain energy E_0. Instead, the signal will be broadened around this value E_0 resulting in a Gaussian-like peak. The energy resolution of a detector can be expressed as the Full Width at Half Maximum (FWHM) of this Gaussian peak at a certain energy E_0. A higher FWHM value means that it is harder to distinguish between closely spaced XRF-lines of e.g. neighboring elements. In X-ray fluorescence spectroscopy, the energy resolution is a function of the energy: as the energy increases, the X-ray photon must be converted into more charge carriers in the detector crystal. There is a statistical uncertainty on this photon-to-charge conversion process, which results in an increasing FWHM [5, 6].

2.3.8 Principal Component Analysis (PCA) of XRF data sets

Performing experiments with the EDAX EagleIII spectrometer, it is possible to obtain quantitative data applying the standardless quantification procedure that was provided with the instrument [46]. Prior to the actual quantification, the identification of the peaks are checked by means of the AXIL. The resulting quantitative data are then further explored using appropriate statistical data treatment methodology, which was applied on the majolica data to obtain evidence of the presence or absence of similarities between production methods. Very often principal component analysis (PCA) is used to detect similarities and hidden patterns in the multivariate data set [47–49]. As shown in ***Fig. 2.35***, the starting point for PCA is a matrix of data with N rows (observations) and K columns (variables), here denoted by X. The observations can be analytical samples, chemical compounds, biological specimens, and so on and in order to characterize the properties of the observations one measures variables. The most important use of PCA is representing a multivariate data table as a low-dimensional plane, usually consisting of 2 to 3 dimensions, so that a clear overview of the data is obtained. This overview may reveal groups of observations, trends and outliers and uncovers also the relationship (often hidden) between observations and the variables themselves [48].

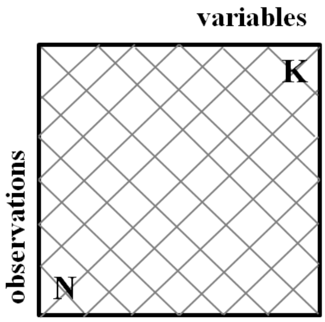

Figure 2.35: *Notation used in PCA [48].*

The method can be explained as follows. A dataset of spectra X can be written as a combination of signals from the constituents and some noise [47, 49].

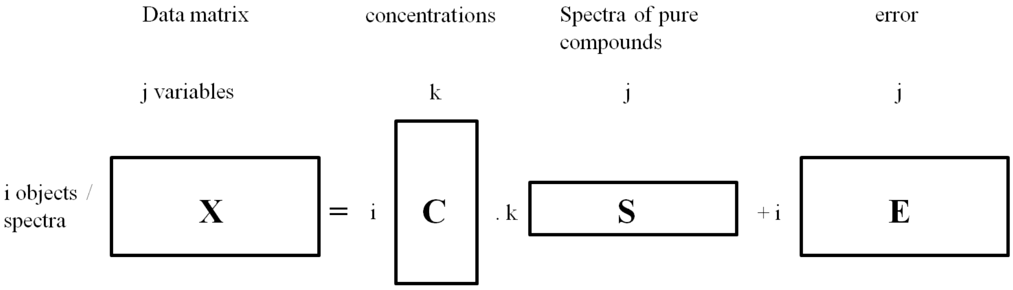

with **X** representing the original data (spectral) matrix (objects in rows, variables in columns), **C** the concentrations of each constituent in every object, **S** the matrix of pure compound spectra of each constituent and **E** corresponds to the matrix of spectra error. **C** and **S** could be predicted, but can never be observed directly and exactly. In order to observe the most important features and trends in the dataset, this can be reduced by PCA [47–49].

By using PCA the data table **X** is modelled as

$$X = 1 \times \overline{x'} + T \times P' + E \tag{2.12}$$

In these expression, the first term ($1\times\bar{x}'$), represents the variable averages and originates from the pre-processing step. The second term, the matrix product ($T\times P'$), models the structure, and the third term is the residual matrix E [48].

The principal component scores of the first, second, third, etc. components ($\mathbf{t}_1$**,** $\mathbf{t}_2$**,** $\mathbf{t}_3$, etc.) are columns of the score matrix **T**. These scores are the co-ordinates of the observations in the model (hyper-)plane. Alternatively, these scores may be seen as new variables which summarize the old ones (***Fig. 2.36***). In their derivation, the scores are sorted in descending importance [48].

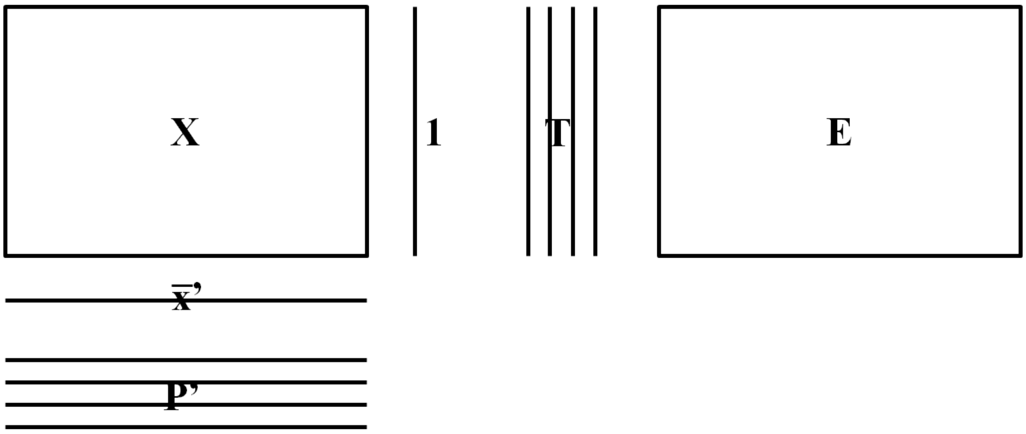

Figure 2.36: *A matrix representation of how a data table X is modelled by PCA [48].*

The meaning of the scores is given by the loadings. The loadings of the first, second, third, etc. components ($\mathbf{p}_1$, $\mathbf{p}_2$, $\mathbf{p}_3$, etc.) build up the loading matrix **P**. The loadings define the orientation of the PC plane with respect to the original X-variables. Algebraically, the loadings inform how the variables are linearly combined to form the scores [48].

Score and loading vectors are orthogonal, which means that the scalar (dot) product between any two loading and score vectors is zero. If the columns are mean centred, the correlation between any two scores or loading vectors is also zero. As our original dataset contained j variables, in theory the score matrix also contains j components. Each component contains a certain percentage of information (variability) of the dataset, which is expressed by the eigenvalue λ_j of the component j [47, 49]:

$$\lambda_j = \frac{S_j}{S_{total}} = \frac{\sum_{i=1}^{I} t_{ij}^2}{\sum_{i=1}^{I} \sum_{j=1}^{j} X_{ij}^2} \tag{2.13}$$

S_j being the sum of squares if the j^{th} PC (score vector) and S_{total} the sum of squares of the entire dataset. The first component has the highest eigenvalue and the further eigenvalues decrease with increasing number of the components. The dataset can now be reduced by retaining m principal components, where m is mostly determined by studying the eigenvalues. In this way, PCA has reduced the dataset (i,j) to a scores matrix (i,m) as can be seen in ***Fig. 2.37*** [47, 49].

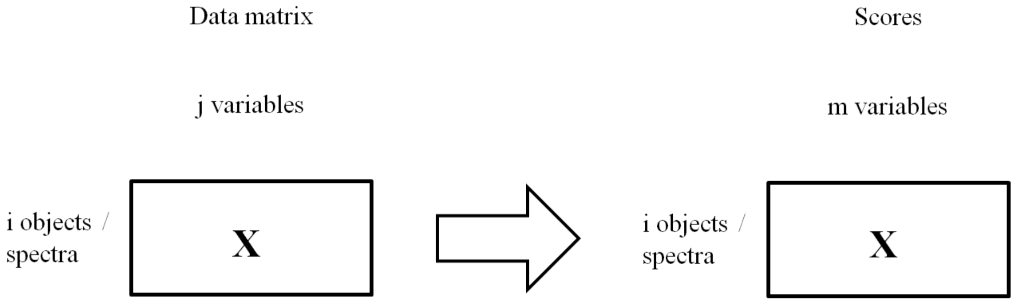

Figure 2.37: *Simplified representation of how PCA reduces a dataset X(i,j) to a scores matrix X'(i,m) [47, 49].*

A very helpful result of applying PCA is that data can be graphically presented using principal components that hold most significant information. The so-called score plots may show trends of objects (measurements, e.g. the quantification data of the measurements on the majolica body and further on the glaze layer), while loading plots can be used to reveal relations between variables (elements, e.g. the chemical elements detected in the X-ray spectra). From the comparison between the scores and loading plots, it can be deduced which variables are characteristic for certain objects and which variables are responsible for the differentiation between them [47–49].

2.4 X-ray diffraction

Techniques based on X-ray fluorescence provide information on the elemental composition of the analyzed samples, such as culturo-historical artefacts, however, in many cases also information about the crystal structure of the materials are required. Therefore, X-ray diffraction crystallography for powder samples is a well-established and widely used technique in the field of material characterization to obtain information on the atomic scale structure of various substances in a variety of states. The advances in this field since 1912 by Max von Laue [50] and in 1913 by W.L. Bragg and W.H. Bragg has eventually led to a commercially available portable XRF/XRD instrument distributed by the Assing company [51].

2.4.1 Crystalline State

The concepts of crystalline state and symmetry are about synonymous nowadays, although the general sense of symmetry is much older than the idea of symmetrical arrangement of atoms in the structures of crystalline solids. Matter usually exists in one of the three basic states: gaseous, liquid, or solid. At fixed temperature and pressure, only one of the states is typically stable for any given substance, except for some combinations of these thermodynamic variables, where two or all three states may coexist in equilibrium. By decreasing the temperature and/or increasing the pressure, transitions can occur from one state to another. Gases and liquid are formed by weakly interacting particles. For gases, these particles are not permanently linked together resulting in no fixed shape nor volume, while liquids, on the other hand, have a specific volume but no defined shape. Structures of liquids and gases, therefore, remain isotropic on a macroscopic scale. When attractive forces become so strong that the particles cannot easily move away from one another, matter becomes solid. Solids have both a defined shape and volume. Although particles in a solid can be distributed randomly in space, an ordered and repetitive pattern is more likely, as it corresponds to a lower energy state when compared with a random spatial distribution of strongly interacting atoms or molecules. The appearance of long-range order brings about structural anisotropy and is classified as a crystalline solid. It is important to recognize that not all solids are crystalline or ordered: in this case these classes of solids are often classified as amorphous, i.e. they are only characterized by short-range order and loss of long-range order. The boundary between amorphous and crystalline states is generally diffuse, and these intermediate cases are known as semicrystalline solids, in other words:

nearly ordered solids described by a lattice that is distorted to a greater or lesser degree. One of the most distinct properties of the crystalline state is, therefore, the presence of long-range order, or in other words, a regular and, in the simplest case, periodic repetition of atoms or molecules in space. In theory, periodic crystals are infinite, but in practice, their periodicity extends over a distance from $\sim 10^3$ to $\sim 10^{20}$ atomic or molecular dimensions. These limits occur because any crystal necessarily has a number of defects and may contain impurities without losing its crystallinity. Furthermore, a crystal is always finite, regardless of its size and since our surroundings are three-dimensional, we tend to assume that crystals are formed by periodic arrangements of atoms or molecules in three dimensions. [52].

The periodic structure of an ideal crystal is most easily described by a lattice. This lattice is build up by a small volume called unit cell, that can be identified and which is propagating (translating or shifting) along one, two, or three directions independently. If the distribution of atoms in one unit cell is known, the structure of the whole crystal, regardless of its physical size, can be reconstructed. Without the lattice, location of every atom in the crystal must be individually described [52, 53].

To fully describe three-dimensional lattice or its building block "the unit cell" a total of three non-co-planar vectors are required. These vectors (a,b,c) coincide with the three independent edges of the elementary parallelepiped, as shown schematically in ***Fig. 2.38***.

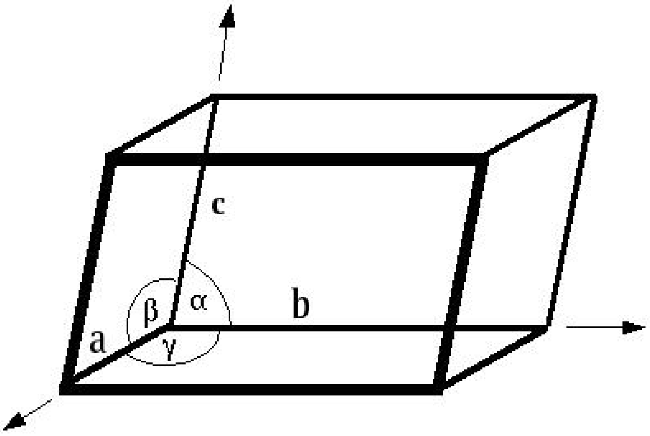

Figure 2.38: *Unit cell in three dimensions: α angle between b and c; β, angle between a and c; γ angle between a and b [52, 53].*

Therefore, any point in a three-dimensional lattice can be described by a vector, q, defined in equation 2.14, where u, v, and w are integer numbers

$$\mathbf{q} = u\mathbf{a} + v\mathbf{b} + w\mathbf{c} \tag{2.14}$$

The three basic vectors (a, b, c) and all derived vectors (q) represent translations in the lattice. They translate the unit cell, including every atom and/or molecule located inside the unit cell, in three dimensions, thus filling the entire space of a crystal. The point with u = v = w = 0 is taken as the origin of coordinates; positive and negative u, v, and w define positive and negative directions, respectively. Since the lattice is infinite, any point in the lattice can be chosen as the origin of coordinates. Instead of three noncoplanar vectors, the unit cell can be completely described by specifying a total of six scalar quantities, which are called the unit cell dimensions or lattice parameters. These are (see also ***Fig. 2.38***): a, b, c, α, β, γ. The first three parameters (a, b and c) represent the lengths of the unit cell edges, and the last three (α, β and γ) represent the angles between them [52].

2.4.2 Principles of X-ray diffraction

Since atoms are arranged in a regular three dimensional lattice, constructive interference of the scattered waves in a few directions will take place. This can be described mathematically by the Laue equations for diffraction:

$$\begin{aligned} a(cos\Psi_a - cos\Psi_{a,0}) &= h\lambda \\ b(cos\Psi_b - cos\Psi_{b,0}) &= k\lambda \\ c(cos\Psi_c - cos\Psi_{c,0}) &= l\lambda \end{aligned} \tag{2.15}$$

where a, b and c are lattice spacings, $cos\Psi_x$ is the direction cosines of the diffracted X-ray beam, $cos\Psi_{x,0}$ is the direction cosines of the incident X-ray beam, h, k and l are natural numbers and λ is the wavelength of the incident X-ray beam [52]. The Laue equations (2.15) are very difficult to implement because in total six angles, three lattice spacings and three natural numbers need to be defined. Further investigations of the scattered X-rays on the periodically structure of the crystals brought father and son Bragg to the recognition of their scattering law [53]:

$$n.\lambda = 2d.sin\theta \tag{2.16}$$

whereas λ is the wavelength of the radiation, d is the d-spacing of the scattering lattice and θ the scattering angle.

Bragg studied the diffraction in terms of reflection from crystal planes. This relation can be understood from ***Fig. 2.39***. Two identical beams in terms of wavelength and phase approach two layers of a crystalline solid. After interaction with two different atomic layers, they are scattered away. The beam that is scattered by the second crystal plane travels an extra length equal to 2dsinθ compared to the beam that is scattered by the upper crystal plane. If the path length is a multiple, n, of the wavelength λ the overlapping of the waves generates high intensity reflections at the scatter angle θ and produce constructive interference [53].

This diffraction of X-rays explained the nature of X-rays but opened also the opportunity for investigations of the structure of materials [22]. The Bragg correlation offers different possibilities for material investigation. It has three parameters, if one of them is fixed and another is measured, the third one can be calculated. The different techniques/methods for using that correlation for material analysis are summarized in ***Table 2.1***.

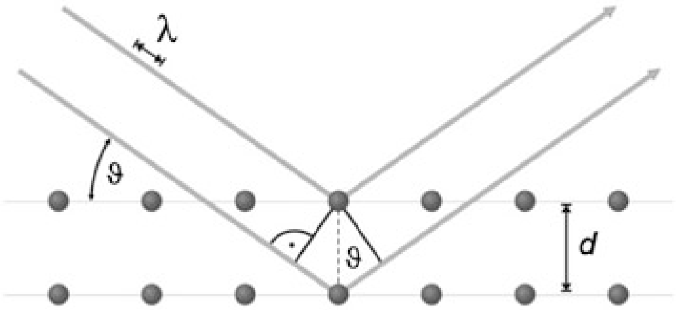

Figure 2.39: *Explanation of the Bragg law [53].*

Table 2.1: *Analytical methodologies based on Bragg's law*

Method	Fixed	Measured	Calculated
XRD	λ or E	θ	d
ED-XRD	θ	E	d
WDX	d	θ	λ

With XRD it is possible to examine the symmetry of single crystals, explain their structure and study the structure of crystal powders and polycrystalline materials to understand e.g. their mechanical behavior [22]. With ED-XRD it is possible to look up individual diffraction peaks and control fast changes of their intensities due to structural changes. With wavelength dispersive X-ray (WDX) spectroscopy the investigation of spectra is possible allowing, for example, the analysis of characteristic radiation of a material and in this way the determination of its elemental composition. In this work, only XRD combined with ED-XRF will be considered.

2.4.3 Surface Monitor: a portable XRF/XRD spectrometer

Within this work, a series of X-ray diffraction measurements were performed using the portable Surface Monitor of the S.p.Assing company (Italy), which has been purchased by the Department of Analytical Chemistry of Ghent University in 2012. By design it allows performing elemental analysis by XRF and XRD for the simultaneous analysis of mineral phases. An X-ray tube, a detector, a laser interferometer and an XRD goniometer (main components of the Surface Monitor) are assembled in a probe head that is mounted on a tripod (for easy positioning) as shown in ***Fig. 2.40***. More details and characterization of this instrument are given in chapter 6.

Fig. 2.41 shows the LOD values for the Surface Monitor, compared with the EagleIII and hXRF spectrometer (see also section 2.3.5) derived from the NIST SRM 1412 multicomponent glass standard. All devices were operated at their maximum performance for 300 s (measuring time). The LODs for the Surface Monitor are neer 100 ppm, except for Fe, for which a lower LOD was obtained. If these values are compared with the other two instruments, the LOD values for the Surface Monitor are comparable due to the optimal performance by which the LOD data were collected: there are

Figure 2.40: *Left: The Surface Monitor and its four main components, portable PC, control box, tripod and probe head. Right: Detailed probe head, consisting of X-ray tube (A), detector (C) and laser interferometer (B) attached to the XRD goniometer (D).*

no slits nor pinholes used, thus the maximum intensity can be measured. The higher LOD can be explained by the larger distance between sample and X-ray source/detector.

2.5 SEM-EDX

The Scanning Electron Microscope (SEM) is one of the most versatile instruments available for the examination and analysis of the microstructural characteristics of solid objects and also culturo-historical objects. Since its invention in the early 1960s, the SEM has moved out of the specialists laboratory, and became an every-day tool, used by many investigators. It opens a world of amazing three-dimensional structures, which are easily interpreted, even by users with little experience. A major reason for SEM's usefulness is the high resolution which can be obtained when bulk objects are examined; instrumental resolution on the order of 1 - 5 nm is now routinely quoted for commercial instruments [54, 55].

SEM is based on the interaction between an electron beam and the sample to be measured. One of the ways to create an electron beam is by thermionic emission via the electrically heating of a V-shaped metallic filament (most of the times a tungsten filament) to about 2700 K. The emitted electrons are accelerated through a potential difference. The beam is focused by an electromagnet which is produced using a coil enclosed in a cylindrical iron case supply with a small gap in the inner bore where the electrons pass. A single point of focus is only produced when all the electrons have the same energy. By changing the current through the coil the magnetic field strength changes and hence a change in the focal length of the lens occurs as well. The instrument is under vacuum to avoid enlargement of the beam size [54].

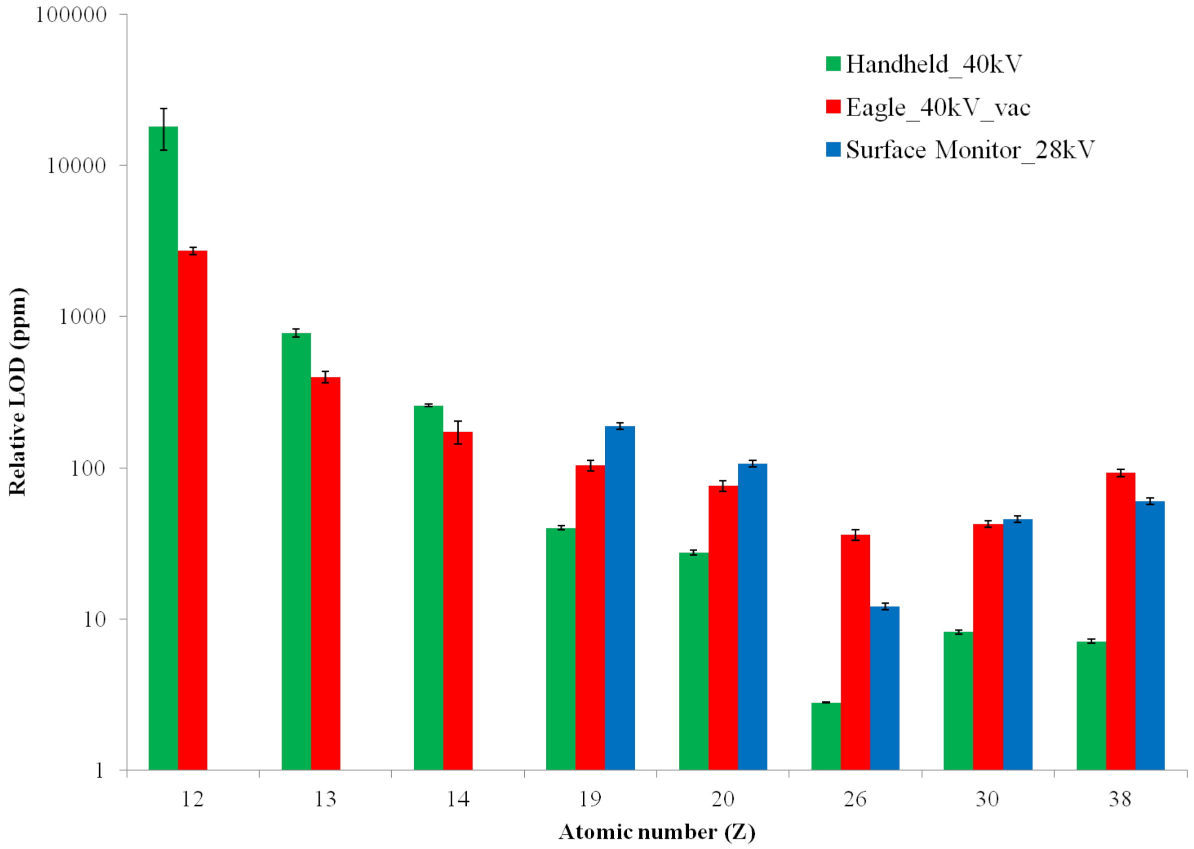

Figure 2.41: *Comparison of the LOD of the EDAX Eagle III, the hXRF and Surface Monitor spectrometers, all working at their maximum performance.*

In the SEM, a surface is viewed directly which limits the specimen size to the viewing section or to the specimen chamber volume. When the surface is hit by a beam of electrons, the emission of secondary and back-scattered electrons occurs as one of the secondary processes. The beam can be kept fixed in one position or swept in a raster across the surface of the specimen to form images. Secondary electrons have lower energy (< 50 eV) and provide information on the morphology of the sample. Back-scattered electrons are electrons that belong to the primary beam and that undergo an elastic collision with the nuclei of atoms present in the target and are scattered with energy close to the initial one. Back-scattered electrons give information about the nature of atoms because when a surface is rich in elements with high atomic number, more electrons will be back-scattered and this will correspond to brighter areas on the image [54–56].

In the SEM, characteristic X-rays are also emitted as a result of electron bombardment of the specimen. The analysis of the characteristic X-radiation emitted from samples can yield both quantitative identification and quantitative elemental information from regions of a specimen nominally with 1 μm diameter and 1 μm depth under normal operating conditions. Since basic X-ray microanalyzers are self-contained, any SEM can be fitted with independent instrumentation for collecting the X-rays, usually with little or no modification. To detect these X-rays a solid state X-ray energy dispersive detector was used which was described in section 2.3.3 [54].

The SEM measurements in this work were performed by means of a JEOL 6300 electron microprobe system equipped with a digital, thin-window energy dispersive Si(Li) X-ray detector of Princeton Gamma Tech (PGT), at the University of Antwerp, Department of Chemistry (see ***Fig. 2.42***) . The studied samples had to be coated with carbon to enhance conductivity.

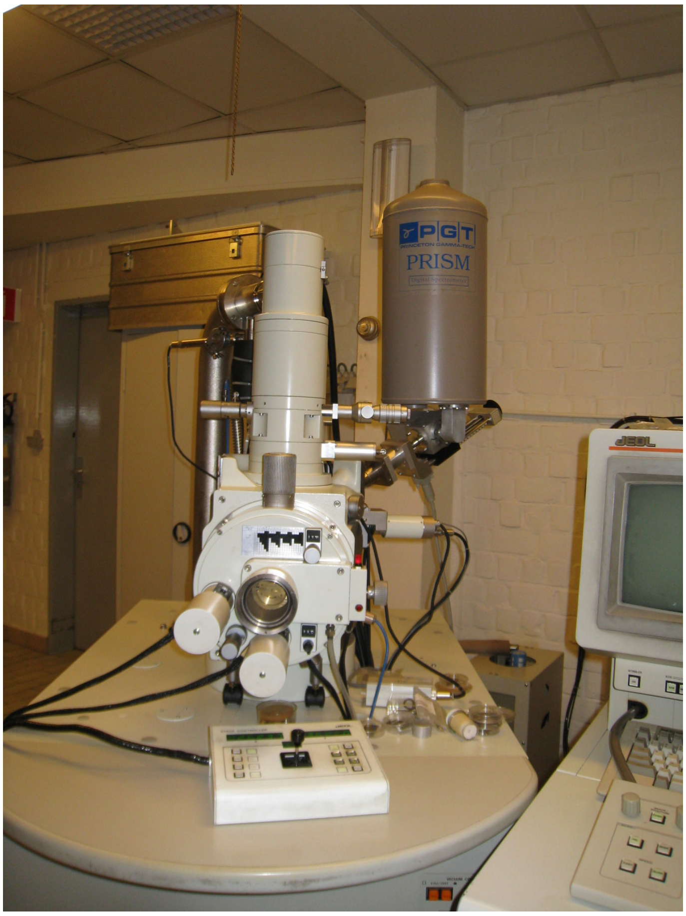

Figure 2.42: *Photograph of the used JEOL 6300 electron microprobe system equipped with a digital, thin-window energy dispersive Si(Li) X-ray detector of Princeton Gamma Tech (PGT), at the University of Antwerp, Department of Chemistry.*

2.6 Raman spectroscopy

The study of culturo-historical objects often needs a multi-method approach of non-destructive analytical techniques to obtain an as completely as possible characterization of an object. Next to the already presented XRF, XRD and SEM-EDX techniques, Raman spectroscopy will be described and is applied in the projects of Antwerp majolica (see chapter 4) and Mad Meg painting of Pieter Bruegel the Elder (see chapter 5).

Raman scattering or inelastic scattering of light was theoretically predicted by Smekal in 1923 and observed for the first time using solar irradiation by Raman and Krishnan in 1928 [57, 58]. Raman spectroscopy as an analytical technique became important with the invention of lasers in the 1960's and as a result of the development of better instrumentation in the 1980's (detector, fiber optics, miniaturization) [59]. Raman spectroscopy is a non-destructive and fast technique that requires only small sample volumes, has a high spatial resolution and the sample preparation and water interference is minimal. A disadvantage is the inherent weakness of the Raman effect, therefore the suppression and/or subtraction of interferences (e.g. fluorescence) and noise is important by choosing appropriate instrumental properties such as laser wavelength and spectrometer type. The wavelength of the laser is mostly chosen in the UV or near-IR region. In the latter case interference by fluorescence is suppressed, while in case of UV lasers higher Raman intensity is obtained at the expense of increased interference by fluorescence and higher probability of laser induced sample damage. Lasers in the near-IR region suppress also the effect of fluorescence but the sensitivity is lower [60]. A dispersive spectrometer (CCD detector) is more sensitive than a Fourier transform spectrometer, but it does not allow high laser wavelengths [61].

2.6.1 The Raman effect: quantum theory

The Raman effect is a light scattering effect and can be described according to the energy diagram in ***Fig. 2.43*** [62]. When monochromatic light interacts with a molecule, the latter can be excited to a virtual state (and not to an excited state as with fluorescence radiation), from which it will relax in several ways afterwards. Rayleigh or elastic scattering occurs when the molecule returns to its original state by emitting a photon of the same energy as the incident light. Inelastic scattering can also take place when the molecule returns to a higher vibrational state, resulting in a scattered photon with a lower energy than the incident light (Stokes scattering). Relaxation can also occur with a transition to a lower vibrational state compared to the original state, resulting in a scattered photon with higher energy. This process is referred to as anti-Stokes scattering. The energy associated to the wavenumber shift between the incident light and the Stokes and anti-Stokes scattering gives information about the vibrational states of a molecule. The intensity of both inelastic scattering processes is proportional to the number of molecules that can undergo these processes. According to the Boltzmann distribution, the number of molecules at thermal equilibrium in a lower vibrational state is always higher than in a higher vibrational state which explains the higher Stokes intensity compared with the anti-Stokes, therefore Stokes peaks are used more commonly in Raman spectroscopy.

2.6.2 Raman spectrum

A Raman spectrum is a plot of the Raman intensity versus the wavenumber or Raman shift in reciprocal centimeters. The relation between energy, wavelength, wavenumber and Raman shift is as follows [59]:

$$E = h\nu = \frac{hc}{\lambda} = hc\varpi \tag{2.17}$$

$$Raman\ shift(cm^{-1}) = (\frac{1}{\lambda_{inc}(nm)} - \frac{1}{\lambda_{stokes}(nm)})10^7 \tag{2.18}$$

with E, ν and c being respectively energy, frequency and speed of light, h is the Planck constant, λ

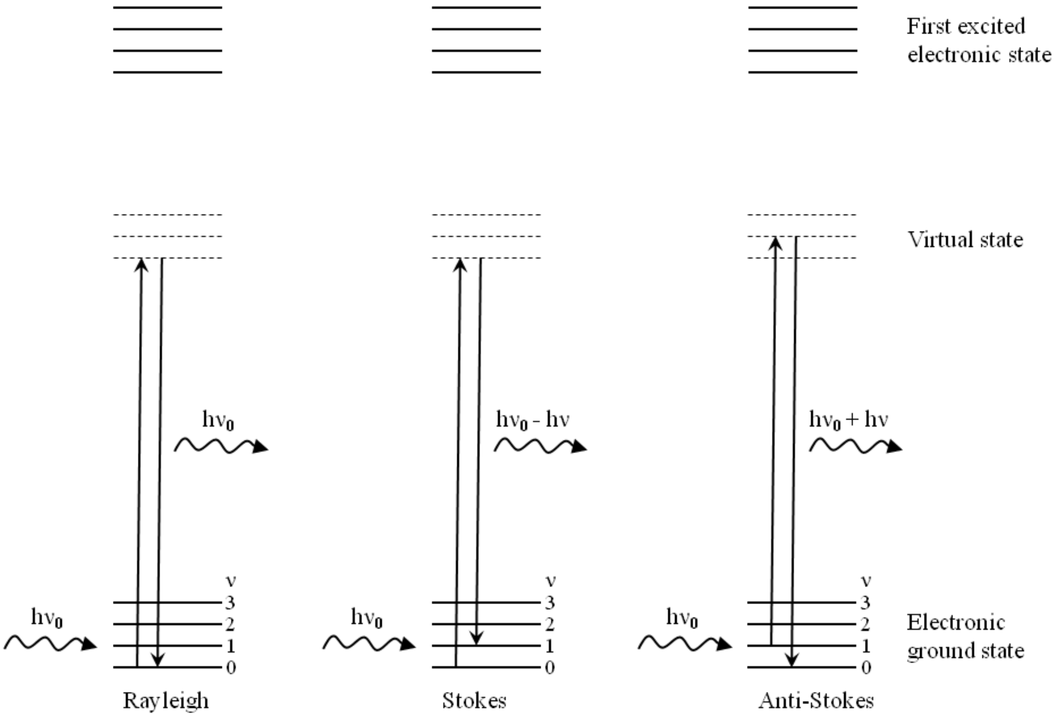

Figure 2.43: *Energy diagram that illustrates different types of scattering when a molecule is illuminated with light of energy $h\nu_0$. The vibrational states of the molecule are characterised by different ν values [60].*

the wavelength of light from incident light (inc) or Stokes scattering (stokes) and ϖ the wavenumber of light.

An expression for the intensity of Raman scattering was derived by Plac̄zek [59]:

$$I_R = \frac{2^4\pi^3}{45\ \ 3^2c^4}\frac{hI_LN(\nu_0-\nu)^4}{\mu_r\nu(1-e^{\frac{-h\nu}{kT}})}[45(\alpha'_a)^2+45(\gamma'_a)^2] \tag{2.19}$$

Where I_L = intensity of the incident light
N = number of molecules that scatter light
ν = molecular vibrational frequency (s^{-1})
ν_0 = frequency of the incident light (s^{-1})
k = Boltzmann constant
T = absolute temperature
α'_a = mean value of the invariant of the polarizability tensor
γ'_a = anisotropy invariant of the polarizability tensor

From this equation, it can be deduced that the intensity of the scattered light is proportional to the number of molecules (basis for quantitative analysis), the intensity of the incident light and $(\nu_0 - \nu)^4$ [59]. Higher laser intensity and higher laser frequency thus enhance the intensity of Raman scattering.

Some molecular factors that affect the intensity of a Raman band are:

- The Raman bands of vibrations of polar bonds are generally weak because their electron clouds are not easily distorted by light.
- The Raman intensity of stretching vibrations is generally stronger than that of bending vibrations.
- Double or triple bonds yield more intense stretching bands.
- The Raman intensity increases with the atomic number of the vibrating atoms.
- Symmetric vibrations generally cause more intense Raman bands.
- Crystalline materials cause stronger Raman bands.

2.6.3 MArtA

The instrument used for collecting molecular information, is the Mobile Art Analyser or MArta, a non-commercial portable Raman spectrometer produced at the UGent in 2004, see ***Fig. 2.44*** [63]. This spectrometer is often used in this work for investigating cultural heritage objects on their location to get not only the elemental information via XRF spectrometers but also information about the molecular structure of the used products and so a providing a better complete survey of the investigated artefact.

MArtA consists of a SpectraPro-150i 150-mm spectrometer and a thermo-electrically cooled charge-coupled device detector (Roper Scientific/Princeton Instruments). ***Fig. 2.45*** shows a general overview of the instrument. It is equipped with a 785 nm diode laser (near-IR) for excitation, which has a maximum output power of 300 mW at the source delivering up to ca.70 mW on the sample. When analyzing art objects, usually much lower laser powers have to be selected in order to avoid damaging the artefacts (typically a few mW on the sample). In the instrument, two diffraction gratings are available (600 and 1200 lines mm^{-1}). Single spectrum are captured over 2700 cm^{-1} and 1300 cm^{-1} respectively, for detailed studies. The spectral resolution in the latter case is about 4 cm^{-1}. The probe head is coupled with optical fibres to focus the laser beam on the sample and to collect the Raman scattered light. Using a probe head instead of a microscope allows performing direct analysis on larger works of art and on less accessible sample locations. The probe head is equipped with an infinity corrected objective lens (6x magnification), resulting in a laser spot size of ca. 25 μm. A digital colour camera, which captures bright-field images of the area under examination, is attached to the probe head and is used for focusing [63, 64].

Figure 2.44: *Left: Use of MArtA during investigation of the Mad Meg painting in Museum Mayer van den Bergh, Antwerp (see chapter 5). Right: impression of the compactness of MArtA.*

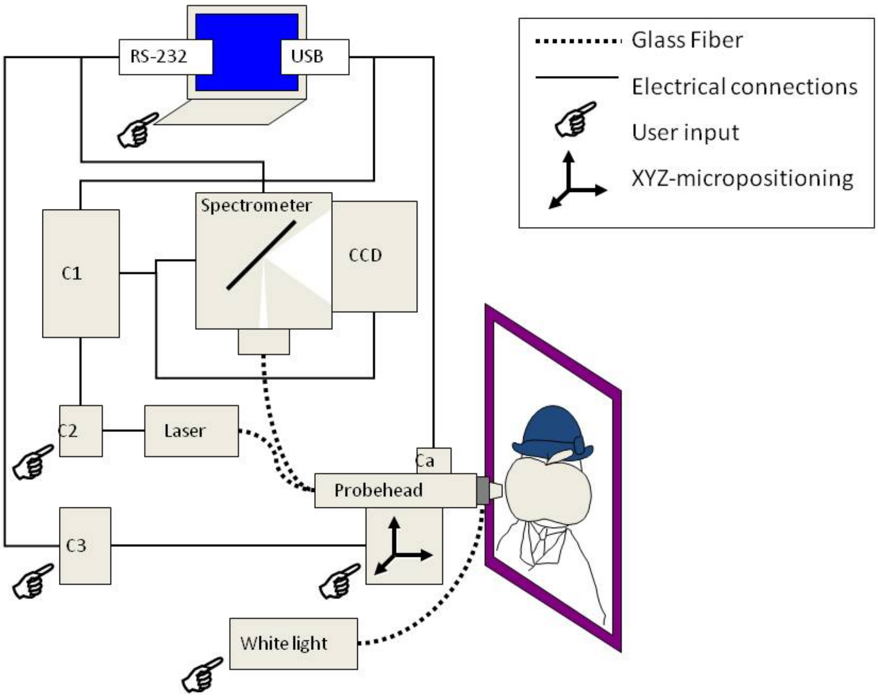

Figure 2.45: *Schematic overview of MArtA instrument [63].*

When performing micro-Raman spectroscopy, it is important that the probe head and area under examination are well aligned and focussing. This requires careful micro positioning and hence a system of posts and micro positioners is added to the instrument, as can be seen in ***Fig. 2.44***. These micro positioners are attached to a large travel range translation stage in order to be able to examine various selected areas of large cultural heritage objects. Prior to a measurement, first the large adjustment movements are performed (away from the object of investigation) by moving the carriage and, in a second step, focusing and positioning are done at the microstage level. A mobile instrument requires a certain degree of compactness, therefore its main components can be controlled through USB and serial (RS-232) connections which are compatible with portable computers. Measurements with the MArtA spectrometer always have to be performed in a dark place, so windows are often covered, or the measurements need to be performed during the night in order to avoid the interference of day light. During the last decade, a number of mobile instruments became available on the market aiming at diverse applications. Due to these developments, in 2013 the Raman research group of the Department of Analytical Chemistry (UGent) acquired a new mobile Raman spectrometer. This dual laser portable Raman instrument (EZRAMAN I-DUAL Raman system) has as main advantage the choice between two lasers (red diode laser (785 nm) and a green Nd:YAG laser (532 nm)) compared to the single laser of MArtA. This new instrument is even more compact than the previous. More information about this instrument can be found in [65, 66].

Bibliography

[1] T. Price and J. Burtin, *An introduction to archaeological chemistry.* Springer, 2011.

[2] J. Ambers and I. C. Freestone, "Introduction," in *Raman spectroscopy in archaeology and art history* (H. G. M. Edwards and J. Chalmers, eds.), ch. 1, pp. 3–16, The royal society of chemistry, 2005.

[3] K. Janssens, G. Vittiglio, I. Deraedt, A. Aerts, B. Vekemans, L. Vincze, F. Wei, I. Deryck, O. Schalm, F. Adams, A. Rindby, A. Kn, A. Simionovici, and A. Snigirev, "Use of Microscopic XRF for Non-destructive Analysis in Art and Archaeometry," *X-RAY SPECTROMETRY*, vol. 91, no. July 1999, pp. 73–82, 2000.

[4] K. Janssens and R. Van Grieken, *Non-destructive micro analysis of cultural heritage materials.* Elsevier, 2004.

[5] B. Beckhoff, B. Kanngieß er, N. Langhoff, R. Wedell, and H. Wolff, *Handbook of Practical X-Ray Fluorescence Analysis.* Springer Berlin Heidelberg, 2006.

[6] R. Van Grieken and A. Markowicz, *Handbook of X-Ray Spectrometry.* CRC Press; 2 edition, 2001.

[7] A. Thompson, D. Attwood, E. Gullikson, M. Howells, K.-J. Kim, J. Kirz, J. Kortright, I. Lindau, Y. Liu, P. Pianetta, A. Robinson, J. Scofield, J. Underwood, G. Williams, and H. Winick, *X-*

ray data booklet. Berkely: Center for X-ray Optics and Advanced Light Source: University of California, 2009.

[8] L. Vincze, K. Tsuji, J. Injuk, and R. Van Grieken, "Chapter 6: New computerisation Methods," in *X-Ray Spectrometry: Recent Technological Advances*, ch. 6, p. 616, Wiley, 2004.

[9] I. Szalóki, A. Somogyi, M. Braun, and A. Tóth, "Investigation of geochemical composition of lake sediments using ED-XRF and ICP-AES techniques," *X-Ray Spectrom.*, vol. 28, pp. 399–405, 1999.

[10] T. Schoonjans, A. Brunetti, B. Golosio, M. Sanchez Del Rio, V. A. Solé, C. Ferrero, and L. Vincze, "The xraylib library for X-ray-matter interactions. Recent developments," *Spectrochimica Acta - Part B Atomic Spectroscopy*, vol. 66, no. 11-12, pp. 776–784, 2011.

[11] P. Tack, *Full-field vs scanning -XRF: Optimazation and characterization. Thesis.* 2012.

[12] J. Garrevoet, *Development of full-field and scanning X-ray fluorescence microspectroscopy.* 2015.

[13] T. Schoonjans, *Three dimensional quantitative X-ray fluorescence at the micro- and nanoscopic level: methodological development and application. PhD thesis.* 2012.

[14] N. Langhoff and A. Simionovici, "X-ray sources," in *Handbook of Practical X-ray Fluorescence Analysis* (B. Beckhoff, B. Kanngiesser, N. Langhoff, R. Wedell, and H. Wolff, eds.), ch. X-ray sour, Springer Berlin Heidelberg, 2006.

[15] B. Ertural, G. Apaydin, U. Çevik, M. Erturul, and a. I. Kobya, "Kβ/Kα X-ray intensity ratios for elements in the range 16Z92 excited by 5.9, 59.5 and 123.6 keV photons," *Radiation Physics and Chemistry*, vol. 76, pp. 15–22, 2007.

[16] T. He, R. P. Gardner, and K. Verghese, "An Improved Si(Li) detector response function," *Nucl.Instrum.Meth.*, vol. A299, pp. 354–366, 1990.

[17] Http://www.scienceclarified.com/Vi-Z/X-Ray.html, "XRF X-ray tubes," 2014.

[18] B. De Samber, *Spatially Resolved X-Ray Micro/Nano-Spectroscopy and Imaging on the Model Organism Daphnia Magna Using Laboratory and Synchrotron Sources. PhD thesis.* 2010.

[19] J. Als-Nielsen and D. McMorrow, *Elements of Modern X-ray Physics.* Wiley, second ed., 2011.

[20] K. W. Jones, "Synchrotron Radiation-induced X-ray emission," in *Handbook of X-Ray Spectrometry* (R. Van Grieken and A. Markowicz, eds.), p. 1016, CRC Press; 2 edition, second ed., 2001.

[21] F. R. Elder, A. M. Gurewitsch, R. V. Langmuir, and H. C. Pollock, "Radiation from Electrons in a Synchrotron," *Physical Review*, vol. 71, no. 11, pp. 829–830, 1947.

[22] M. Haschke, *Laboratory Micro-X-Ray Fluorescence Spectroscopy. Instrumentation and Applications.* Springer, volume 55 ed., 214.

[23] N. Gao and K. Janssens, "Polycapillary X-ray optics," in *X-Ray Spectrometry: Recent Technological Advances* (K. Tsuji, J. Injuk, and R. Van Grieken, eds.), ch. 3.3, pp. 89–110, Wiley&Sons Ltd., 2004.

[24] L. Vincze, B. Vekemans, F. E. Brenker, G. Falkenberg, K. Rickers, A. Somogyi, M. Kersten, and F. Adams, "Three-dimensional trace element analysis by confocal X-ray microfluorescence imaging," *Analytical Chemistry*, vol. 76, no. 22, pp. 6786–6791, 2004.

[25] F. E. Brenker, L. Vincze, B. Vekemans, L. Nasdala, T. Stachel, C. Vollmer, M. Kersten, A. Somogyi, F. Adams, W. Joswig, and J. W. Harris, "Detection of a Ca-rich lithology in the Earth's deep (¿ 300 km) convecting mantle," *Earth and Planetary Science Letters*, vol. 236, pp. 579–587, 2005.

[26] B. De Samber, G. Silversmit, K. De Schamphelaere, R. Evens, T. Schoonjans, B. Vekemans, C. Janssen, B. Masschaele, L. Van Hoorebeke, I. Szalóki, F. Vanhaecke, K. Rickers, G. Falkenberg, and L. Vincze, "Element-to-tissue correlation in biological samples determined by three-dimensional X-ray imaging methods," *Journal of Analytical Atomic Spectrometry*, vol. 25, p. 544, 2010.

[27] G. Silversmit, B. Vekemans, S. Nikitenko, S. Schmitz, T. Schoonjans, F. E. Brenker, and L. Vincze, "Spatially resolved 3D micro-XANES by a confocal detection scheme," *Physical chemistry chemical physics : PCCP*, vol. 12, no. 21, pp. 5653–5659, 2010.

[28] A. J. Westphal, R. M. Stroud, H. A. Bechtel, F. E. Brenker, A. L. Butterworth, G. J. Flynn, D. R. Frank, Z. Gainsforth, J. K. Hillier, F. Postberg, A. S. Simionovici, V. J. Sterken, L. R. Nittler, C. Allen, D. Anderson, A. Ansari, S. Bajt, R. K. Bastien, N. Bassim, J. Bridges, D. E. Brownlee, M. Burchell, M. Burghammer, H. Changela, P. Cloetens, A. M. Davis, R. Doll, C. Floss, E. Grun, P. R. Heck, P. Hoppe, B. Hudson, J. Huth, A. Kearsley, A. J. King, B. Lai, J. Leitner, L. Lemelle, A. Leonard, H. Leroux, R. Lettieri, W. Marchant, R. Ogliore, W. J. Ong, M. C. Price, S. A. Sandford, J.-A. S. Tresseras, S. Schmitz, T. Schoonjans, K. Schreiber, G. Silversmit, V. A. Sole, R. Srama, F. Stadermann, T. Stephan, J. Stodolna, S. Sutton, M. Trieloff, P. Tsou, T. Tyliszczak, B. Vekemans, L. Vincze, J. Von Korff, N. Wordsworth, D. Zevin, and M. E. Zolensky, "Evidence for interstellar origin of seven dust particles collected by the Stardust spacecraft," *Science*, vol. 345, pp. 786–791, 2014.

[29] B. Kaulich, J. Susini, and R. Barrett, "High-efficiency multilevel zone plates for keV X-rays," *Nature*, vol. 401, no. October, pp. 895–898, 1999.

[30] F. Scholze, A. Longoni, and C. Fiorini, "x-ray detectors and XRF detection channels," in *Handbook of Practical X-Ray Fluorescence Analysis* (B. Beckhoff, K. Birgit, N. Langhoff, R. Wedell, and H. Wolff, eds.), Springer, 2006.

[31] G. Knol, *Radiation Detection and Measurement.* John & Wiley and Sons Ltd., 4th ed., 2010.

[32] X. Llopart, M. Campbell, R. Dinapoli, D. S. Segundo, and E. Pemigotti, "Medipix2: a 64-k pixel readout chip with 55 mu m square elements working in single photon counting mode," *IEEE transactions on nuclear science*, vol. 49, pp. 2279–2283, Oct. 2002.

[33] J. Jakubek, S. Pospisil, D. Vavrik, and J. L. Visschers, "Resolution and stability tests of a Medipix-1 pixel detector for X-ray dynamic defectoscopy," *Nuclear Instruments and Methods in Physics Research section A-accelerators spectrometers, detectors and associated equipment*, vol. 509, pp. 294–301, Aug. 2003.

[34] D. Litwiller, "CCD vs. CMOS: The battle cools off," *Photonics spectra*, vol. 36, pp. 102–103, Jan. 2002.

[35] D. Litwiller, "CMOs vs. CCD: Maturing technologies, maturing markets," *Photonics spectra*, vol. 39, pp. 54+, Aug. 2005.

[36] P. Tack, J. Garrevoet, S. Bauters, B. Vekemans, B. Laforce, E. V. Ranst, D. Banerjee, A. Longo, W. Bras, and L. Vincze, "Full-Field Fluorescence Mode Micro-XANES Imaging Using a Unique Energy Dispersive CCD Detector," *Analytical chemistry*, vol. 86, p. 87918797, 2014.

[37] J. Garrevoet, B. Vekemans, P. Tack, B. D. Samber, S. Schmitz, F. E. Brenker, G. Falkenberg, and L. Vincze, "Methodology toward 3D Micro X-ray Fluorescence Imaging Using an Energy Dispersive Charge-Coupled Device Detector," *Analytical chemistry*, vol. 06, 2014.

[38] G. Vittiglio, K. Janssens, B. Vekemans, F. Adams, and a. Oost, "Compact small-beam XRF instrument for in-situ analysis of objects of historical and/or artistic value," *Spectrochimica acta, Part B: Atomic spectroscopy*, vol. 54, pp. 1697–1710, 1999.

[39] S. Bichlmeier, K. Janssens, J. Heckel, D. Gibson, P. Hoffmann, and H. M. Ortner, "Component selection for a compact micro-XRF spectrometer," *X-Ray Spectrometry*, vol. 30, pp. 8–14, 2001.

[40] C. Zarkadas and a. G. Karydas, "A portable semi-micro-x-ray fluorescence spectrometer for archaeometrical studies," *Spectrochimica Acta - Part B Atomic Spectroscopy*, vol. 59, pp. 1611–1618, 2004.

[41] J. Mayer and E. Rimini, *Ion beam handbook for material analysis.* Academic Press, 1977.

[42] A. Ide-Ektessabi, *Applications of synchrotron radiation.* New York: Springer, 2007.

[43] B. Vekemans, K. Janssens, L. Vincze, F. Adams, and P. Vanespen, "Analysis of X-Ray-spectra by iterative least-squares (AXIL) - New developments," *X-Ray spectrometry*, vol. 23, no. 6, pp. 278–285, 1994.

[44] P. Van Espen, K. Janssens, and J. Nobels, "AXIL-PC: software for the analysis of complex X-ray spectra," *Chemometrics Intell. Lab. Syst.*, vol. 1, pp. 109–114, Nov. 1986.

[45] B. Vekemans, K. Janssens, L. Vincze, F. Adams, and P. Van Espen, "Comparison of several background compensation methods useful for evaluation of energy-dispersive X-ray fluorescence spectra," *Spectrochimica Acta Part B: Atomic Spectroscopy*, vol. 50, no. 2, pp. 149–169, 1995.

[46] W. T. Elam, R. B. Shen, B. Scruggs, and J. Nicolosi, "Accuracy of Standardless FP Analysis of Bulk and Thin Film Samples Using a New Atomic Database," *Advances in X-ray analysis*, vol. 47, pp. 104–109, 2004.

[47] R. Brereton, "Pattern recognition," in *Chemometrics: Data anlysis for the laboratory and chemical plant*, ch. 4, pp. 183–270, Chichester,: John & Wiley and Sons Ltd., 2003.

[48] L. Eriksson, E. Johansson, N. Kettaneh-Wold, J. Trygg, C. Wikström, and S. Wold, "PCA," in *Multi- and megavariate data analysis, Part I: Basic principles and enlarged edition*, pp. 39–62, Umetrics Academy, 2006.

[49] R. Brereton, "Pattern recognition," in *Applied chemometrics for scientists* (J. . W. Ltd and Sons, eds.), ch. 5, pp. 145–190, Chichester: Wiley, 2007.

[50] W. Friedrich, P. Knipping, and M. Von Laue, "Interferenz-Erscheinungen bei Röntgenstrahlen," *Bayerische Akademie der Wissenschaften*, p. 303, 1912.

[51] W. Bragg and W. Bragg, "The Reflexion of X-rays by Crystals," *Proceedings of the Royal Society of London*, vol. 88, no. 605, pp. 428–438, 1913.

[52] V. K. Pecharsky and P. Y. Zavalij, *Fundamentals of Powder Diffraction and Structural Characterization of Materials.* Springer, second edi ed., 2009.

[53] Y. Waseda, E. Matsubara, and K. Shinoda, *X-Ray Diffraction Crystallography.* Springer, 2011.

[54] G. Lawes, *Scanning electron microscopy and X-ray microanalysis.* London: John Wiley and Sons Ltd., 1987.

[55] J. I. Goldstein, D. E. Newbury, P. Echlin, D. C. Joy, C. E. Lyman, E. Lifshin, L. Sawyer, and J. R. Michael, *Scanning Electron Microscopy and X-ray Microanalysis.* Springer US, third ed., 2003.

[56] L. E. Murr, *Electron and ion microscopy and microanalysis. Principles and applications.* CRC Press, 1982.

[57] A. Smekal, “Zur quantentheorie der dispersion,” tech. rep., Naturwissenschaften, 1923.

[58] C. Raman and K. Krishnan, “A new type of secondary radiation,” *Nature*, vol. 121, pp. 501–502, 1928.

[59] M. Pelletier, “Introduction to applied Raman spectroscopy,” in *Analytical applications of Raman spectroscopy*, ch. 1, pp. 1–52, Oxford: Blackwell Science Ltd, 1999.

[60] J. Grasselli, “The Raman effect: an introduction,” in *Analytical Raman Spectroscopy*, pp. 1–19, New York: John Wiley and Sons Ltd., 1991.

[61] R. McCreery, “Instrumentation overview and spectrometer performance,” in *Raman spectroscopy for chemical analysis*, ch. 5, pp. 73–94, New York: John Wiley and Sons Ltd., 2000.

[62] R. McCreery, “Introduction and scope,” in *Raman spectroscopy for chemical analysis*, ch. 1, pp. 1–14, New York: John Wiley and Sons Ltd., 2000.

[63] P. Vandenabeele, T. L. Weis, E. R. Grant, and L. J. Moens, “A new instrument adapted to in situ Raman analysis of objects of art.,” *Analytical and bioanalytical chemistry*, vol. 379, pp. 137–42, May 2004.

[64] P. Vandenabeele, K. Castro, M. Hargreaves, L. Moens, J. M. Madariaga, and H. G. M. Edwards, “Comparative study of mobile Raman instrumentation for art analysis.,” *Analytica chimica acta*, vol. 588, pp. 108–16, Apr. 2007.

[65] D. Lauwers, A. G. Hutado, V. Tanevska, L. Moens, D. Bersani, and P. Vandenabeele, “Characterisation of a portable Raman spectrometer for in situ analysis of art objects,” *Spectrochimica Acta - Part A: Molecular and Biomolecular Spectroscopy*, vol. 118, pp. 294–301, 2014.

[66] D. Lauwers, V. Cattersel, L. Vandamme, A. Van Eester, K. De Langhe, L. Moens, and P. Vandenabeele, “Pigment identification of an illuminated mediaeval manuscript De Civitate Dei by means of a portable Raman equipment,” *Journal of Raman Spectroscopy*, vol. 45, no. April, pp. 1266–1271, 2014.

Chapter 3: Analytical characterization of Antwerp majolica (Belgium) from 16th to 17th century using X-ray fluorescence and scanning electron microscopy

This chapter presents the analytical results obtained by micro X-ray fluorescence (laboratory and synchrotron) and Scanning Electron Microscopy with Energy Dispersive X-ray spectrometer (SEM-EDX) on original Antwerp majolica tiles produced during the 16th and 17th century. The investigated material, majolica, is a type of ceramics, which fascinated many people and potters throughout history by its beauty and colourful appearance. The microstructure and chemical composition of majolica provides valuable information on the used materials and on the technological skills of the manufactures living in the 16th and 17th century. This information enables historians and conservators to gain knowledge about the historical and technological background behind these objects: they want to know how these objects were made and used, their historical context and the changes or degradations they have undergone since they were used and much more to reach in this way information about how people lived, ate, slept, etc. This chapter illustrates how chemistry and conservation science can join forces with the potential to obtain extra information compared to what is available in the historical literature.

3.1 Introduction

Although a lot of studies on glazed ceramics can be found in the international scientific literature, none of these studies focus on majolica production in Antwerp (Belgium) and its influence on the production techniques. There were already some studies which use Antwerp majolica tiles to enlarge the number of samples, however, non of these researches was pursued on the majolica subject itself, even though Antwerp was an important production center of majolica in the 16th and 17th century, together with the production of the *façon de Venise* glass [1–7].

The scientific work presented in this chapter was aiming to identify the used materials (earthenware body, glaze and pigments), the structure as well as to investigate the similarity in a majolica collection, consisting of 30 archaeological tiles from the 16th and 17th century, originating from four different historical production sites in the city of Antwerp (Belgium). The fragments were examined using micro-XRF and SEM to obtain their chemical makeup and to assess the influence of the production sites by comparing Antwerp majolica with majolica from Italy, Spain, etc. Based on the detailed chemical microanalysis, we aim to establish consistent scientific criteria to define a group of glazed ceramics, produced in Antwerp in the 16th and 17th century.

3.1.1 Composition of Majolica

Majolica refers to a type of earthenware covered by a thin layer of white opaque glaze. On the surface of the white primary glaze, bright colored glazes were applied in order to create appealing decorations. The artists had only a limited palette of colors: blue (Co^{2+} ions dissolved in the glaze), yellow ($Pb_3(SbO_4)_2$ particles not fused in the glaze), orange/brown (Fe_2O_3 particles in the glaze), green (Cu^{2+} ions dissolved in the glaze) and purple (Mn^{3+} ions dissolved in the glaze). To opacify the glaze, cassiterite was added (SnO_2 particles) in the glaze [2, 4, 8]. Written historical sources concerning material preparation of majolica are rare. A very important manuscript is that of Cipriano Piccolpasso, "*Li tre Libri Dell'Arte Del Vasaio*" written in 1557 AD or "*The three books of the potter's Art*", about the Italian majolica production [9].

Majolica is built up by a layered structure of three layers due to the different production stages, associated with the production of the earthenware body, apllication of primary white glaze and application of pigments. It should be mentioned that a fourth transparent lead glaze layer (named coperta) is sometimes present on the pigment layer. As the first step of the manufacturing process, the clay layer was prepared, shaped and then fired at around 1000 °C, forming the body (called "biscuit"). The white glaze is applied on the already fired porous body containing lead as primary component and tin is added to opacify the glaze. Eventually, a decorated pigment layer was applied. During the second baking cycle, the pigment layer probably fused with the white glaze layer which was applied in the previous stage. In some cases, a final thin transparent and homogeneous layer (coperta) was added on the surface of the white glaze/pigment layer fused during a third baking period.

The fabrication of majolica is clearly a complex process which was accompanied by experiments of the potters, often with trials and errors [6]. The potters made specific technological choices in order to facilitate the production and to enhance the quality of the final product. Traditionally, majolica was made from chalky, high lime clay, because of the favorable properties of the raw material in terms of fusibility, whiteness after firing, being lighter in weight, requiring less tin glaze and better attachment of the glaze [10, 11]. However, lime clays and chalky deposits were not always available where people wished to make pottery. The potters therefore had to blend their local clays with lime clays also called "marl" originating from places in Europe (Tournai, Belgium or even from Boyton in Northern Ireland) [12, 13]. Manufacturing techniques experienced changes in relation with the quality of the available raw materials. The earliest tiles were thick (20-25 mm) with a coarse structure where the glaze was well attached to the body. Tiles from a later period became thinner (10-20 mm), finer and more friable [11]. Besides the changes in tile thickness, also variations in colors were observed. After ca. 1500, the color of the ceramic bodies changed from intense red-brown to pinkish and later to whitish [14].

More details about the preparation of the glaze reveal that first a *marzacotto*, or transparent fusible glass frit containing fused lead, soda or potash and silica, was prepared. Each workshop had its own recipe for its standard *marzacotto*, which was, besides the main ingredient for the white tin glaze, also a flux for pigments. To make tin glaze, tin and lead ashes were added to the standard *marzacotto* and the whole mixture was calcined and reground. To enhance the brilliance and brighten up the colors, a layer of colorless glaze could be applied on top of the decoration. This layer is known in Italian as "coperta" [12] or as "kwaart" in Dutch [15]. The multilayer structure of the white tin glaze, colored decoration and coperta was fired in one step at ca. 900 °C [16]. The glaze firing was achieved, as already mentioned above, on the already fired earthenware body.

3.1.2 History of Antwerp Majolica

There have been many historical studies conducted in the 20^{th} century on Antwerp majolica which offer information on the biography of the potters (periods of activity and family alliance), as well as on their properties and workshops (location, size, organisation and products themselves). M. Laurent, H. Nicaise, B. Rackham and A. Groneman have produced essential historical and stylistic reports [17–19]. However, the history of Antwerp majolica has recently been pursued through a systematic research on documentary records, the extensive collection of majolica from Antwerp excavations as well as through typological and iconographic analyses of the products [20, 21]. These approaches have revealed that this ceramic product spread across Europe, and have provided the link between the majolica of Italy and the tin-glazed pottery of the northern regions, especially that made in the Netherlands, Germany and in England [22].

The first potters of Italian origin who settled in Antwerp were Janne Maria De Capua, Jan Francisco de Bress (or Jan Frans) and Guido Andries [18]. Janne Maria de Capua only lived for a few years in Antwerp having a lot of debts to Nicolas Sete (a Venetian merchant), possibly linked to his return to Italy after the request by the Duke of Milan. To pay back his debts, he sold majolica vessels to Jan Frans and to Guido Andries. Franchois Frans, the nephew of Jan Frans, played the most important role: he married the widow of Guide Andries in 1543 [23]. Guido di Savino, otherwise known as Andries, and his sons dominated the majolica production mainly in the sixteenth century. He had settled in Antwerp before 1508 and in 1520 he bought the house called Den Salm in the Cammerstreet, which became the seat of the factory and belonged to the Andries family until 1622. When he died (before 1541), his widow married with potter Jan Frans, who ran the workshop until 1562. Five of his sons took up the potter's trade e.g., Lucas owned a workshop on the Antwerp Steenhouwersvest, Frans was active in Sevilla, Joris owned two workshops: one in the Oever and another in Sint-Jansvliet [22, 24, 25]. The Andries family workshops were run in the same way as the Italian factories. The same type of kiln was used, as well as manufacturing techniques similar to those used in Italy.

However, also other potters were active in Antwerp between the 16^{th} century and the beginning of the 17^{th} century. In fact, there were more than 80 potters all together. Religious wars decreased the production of majolica in Antwerp and potters left Antwerp (temporarily or permanently) but after the separation of the northern and the southern parts of the Netherlands, the production of Antwerp majolica was carried on and even new factories were built [22]. The importance of the ceramic production in Antwerp is well documented, however, in most of the cases it is difficult to combine documentary and material information due to the fact that most of the documents correspond to unassigned pieces. With our research, we tried to get more reliable information on the production of Antwerp majolica.

3.1.3 Research on Antwerp Majolica

A set of 30 representative majolica tiles, covering a period of one century (1550-1650), were selected from the vast amount of excavated majolica artifacts found in Antwerp, constituting the collection of the Archaeological department of the City of Antwerp (see ***Fig. 2.2***). The 30 Antwerp majolica tiles were selected from four archaeological production centers located in Antwerp which ensures with a high degree of certainty that the analyzed tiles were manufactured in Antwerp. These representative tiles are named after the streets where they were found: Aalmoezenierstraat, Schoyestraat, Steenhouwersvest and Sint-Jansvliet (see ***Fig. 3.1***) [26]. ***Table3.1*** gives all details about each tile in terms of street names of origin, manufacturing period and tile thickness.

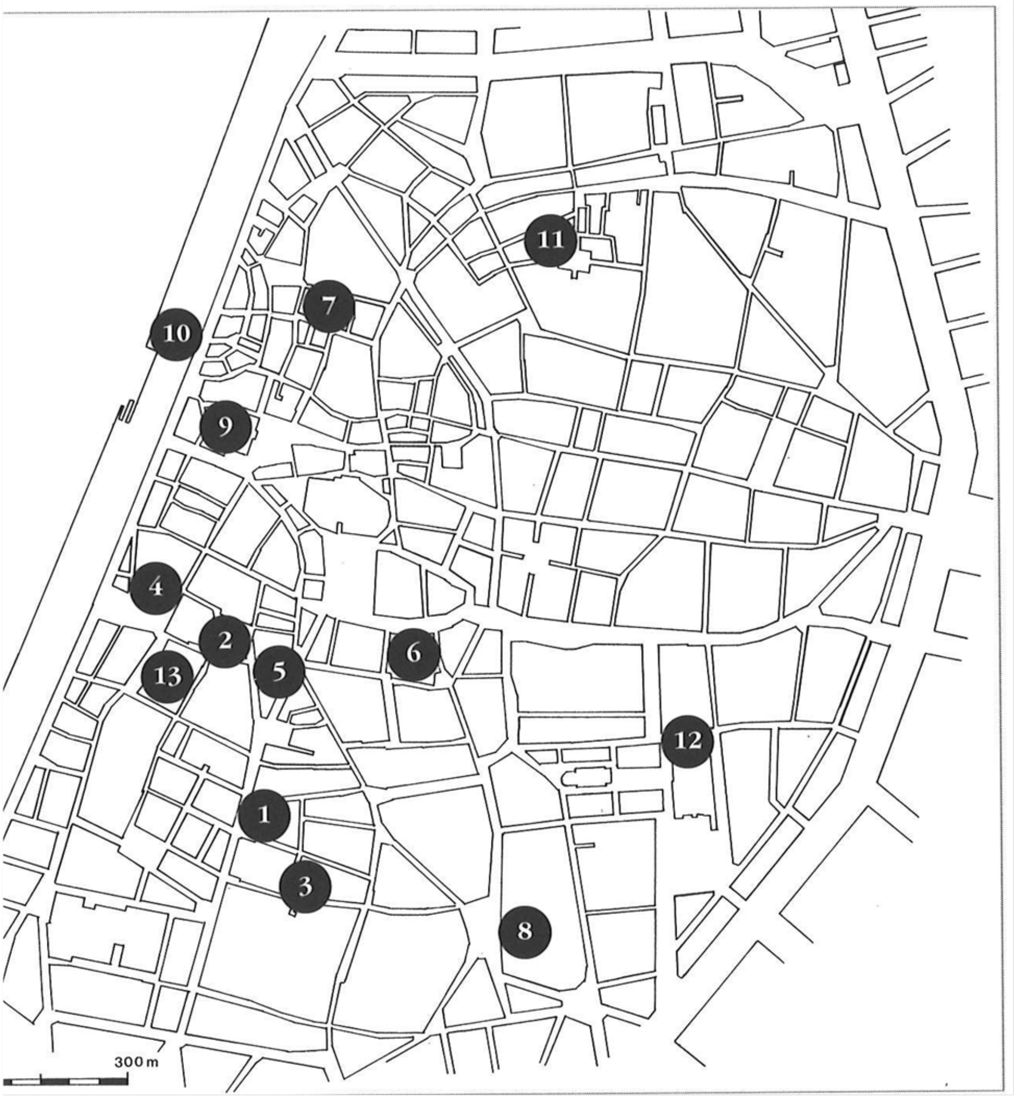

Figure 3.1: *Historical map of Antwerp indicating the sites mentioned in the text: 1) Schoytestraat, 2) Steenhouwersvest, 3) Aalmoezenierstraat, 4) Sint-Jansvliet, 5-13) Other production sites in Antwerp but not included in our research [26].*

Table 3.1: *Description of the analysed samples*

Archaeological ID	Street	Period	Thickness (mm)
A152-6-mx	Schoytestraat	1610-1640	15.00
A152-6-m7	Schoytestraat	1620-1650	12.67
A104-17-m152	Schoytestraat	1549-1616	12.83
A104-17-m51	Schoytestraat	1580-1600	19.00
A104-17-m50	Schoytestraat	1580-1600	19.00
A104-1-m274	Schoytestraat	1600-1630	12.33
A104-1-m272	Schoytestraat	1620-1650	13.67
A104-0-m19	Schoytestraat	1600-1630	12.00
A187-t1	Aalmoezenierstraat	1580-1600	19.33
A187-t2	Aalmoezenierstraat	1600-1625	18.00
A117-7-t1	Steenhouwersvest	1580-1600	15.33
A117-7-t2	Steenhouwersvest	1570-1600	21.00
A117-7-t3	Steenhouwersvest	1570-1600	20.83
A117-7-t4	Steenhouwersvest	1556-1562	19.00
A117-7-t5	Steenhouwersvest	1580-1610	16.83
A117-7-t6	Steenhouwersvest	1570-1600	21.17
A218-0-m1	Steenhouwersvest	1610-1650	11.67
A218-0-m2	Steenhouwersvest	1580-1610	23.83
A218-0-m3	Steenhouwersvest	1580-1610	22.83
A218-0-m4	Steenhouwersvest	1600-1625	18.67
A218-0-m5	Steenhouwersvest	1600-1625	18.67
A218-0-m6	Steenhouwersvest	1610-1650	17.00
A218-0-m7	Steenhouwersvest	1600-1625	|
AJB-ma1	Sint-Jansvliet	1610-1650	19.67
AJB-ma2	Sint-Jansvliet	1570-1600	18.33
AJB-ma3	Sint-Jansvliet	1570-1600	17.17
AJB-ma4	Sint-Jansvliet	1570-1600	18.50
AJB-ma5	Sint-Jansvliet	1570-1600	19.67
AJB-ma6	Sint-Jansvliet	1570-1600	17.00
AV-1466	|	1550	|

The investigation of the above mentioned set of tiles was possible after obtaining permission to remove small fragments from the edges of the tiles, typically a few mm in size (max. 1 x 1 cm^2), as can be seen in ***Fig. 2.3***. Whenever possible, fragments were removed from already damaged areas at the edges using a small diamond saw and/or scalpel. The fragments were embedded in epoxy resin and polished afterwards to provide flat surfaces necessary for scanning micro-XRF measurements. The polishing took place in two steps starting using silicon carbide papers for removing redundant resin on top of the fragment, followed by polishing using diamond pastes with grain sizes down to 3 μm in the second step, in order to obtain a high quality surface for analysis. The orientation of the samples in the resin was such that a cross-section perpendicular to the original glaze surface, could be studied as can be seen in ***Fig. 3.2***. The investigation of the cross-section of the tiles gave us the opportunity to obtain information on its layered structure. We studied the small embedded fragments to get information on the heterogeneous nature of the composition, the layered micro-structure, the used pigments and to obtain quantitative elemental information by using XRF spectroscopy. In parallel, we also performed *in situ* analysis on the unique and only known 16th century Antwerp majolica tile floor in Belgium, which is situated in a tower of the Rameyenhof castle (Gestel, Belgium). More information about this research can be found in chapter 4

Figure 3.2: *Embedded sample of fragment A218-0-M3.*

3.2 Experimental

We used different non-destructive analytical techniques based on X-rays, including laboratory source based and synchrotron radiation (SR) induced XRF spectroscopy. A scanning μ-XRF spectrometer (EDAX Eagle-III) and a SEM-EDX (JEOL 6300) were used as laboratory instrumentation combined with SR-XRF measurements performed at beamline P06 of PETRA III (DESY, Hamburg, Germany). The measurements allowed to obtain (quantitative) information on (1) the elemental composition and (2) the homogeneity of materials constituting Antwerp majolica tiles.

The operating conditions of the EDAX Eagle-III spectrometer were as follows: X-ray tube voltage 40 kV (Rh-anode), current $\backsim$ 150 μA, beam size 25 μm and scanning step size 20 μm for mapping and line scans through the different layers. The measurements on the prepared cross-sections were performed in vacuum in order to enable the detection of elements with lower atomic numbers (down to Na). The used measuring time was 15 s per scan point for the 2D maps and 1000 s per scan point for the line scans. Standardless fundamental parameter analysis of these measurements was possible using the software of the EDAX Eagle-III laboratory spectrometer [27]. From the XRF spectra, the chemical composition (in oxide weight %) was calculated and normalized to 100% so that the average composition of the material could be derived. Due to the heterogeneous nature of the material and the uncertainties associated with the low-Z-matrix the results are considered semi-quantitative. All collected XRF spectra were processed using the dedicated XRF spectrum evaluation software AXIL, as explained in chapter 2, section 2.3.6.

In case of the SEM-EDX measurements, the embedded samples were coated with carbon to enhance conductivity and analyzed by means of a JEOL 6300 electron microprobe at the University of Antwerp, Department of Chemistry (more information is found in chapter 2, section 2.5). Yhe SEM-EDX maps were recorded using a 20 kV acceleration voltage and current between 15 nA and 20 nA and a live time of about 3600 s. The conditions were adjusted to get the highest possible signal.

To be able to obtain additional information on the used pigments, the studied archaeological fragments were also investigated using synchrotron based full-field XRF imaging. This technique is based on the use of a 2D energy dispersive pnCCD X-ray detector (SLcam) [28], which acquires nearly 70,000 XRF spectra simultaneously, while the sample is illuminated with a broad X-ray beam enabling 2D elemental imaging without the need of scanning the sample. The measurements were performed at the Microprobe endstation of beamline P06 at the 6GeV synchrotron storage ring PETRA III at DESY (Hamburg, Germany) operated with a current of 100 mA.

The SLcam consists of a large 12.7 x 12.7 mm^2 Si based chip with an active thickness of 450 μm and comprises 264 x 264 pixels of 48 μm. The obtained spatial resolution, with a maximum of 8 μm, depends on the used optics which can be mounted in front of the SLcam, such as pinhole or polycapillary optics. The full-field technique allows 3D elemental imaging when the sample is illuminated with a sheet beam, and 2D X-ray absorption near edge structure (XANES) spectroscopy imaging in a much shorter time frame than it was previously possible using conventional scanning techniques. This is described elsewhere [29, 30].

3.3 Results

3.3.1 Pigment identification and layered structure

As mentioned in the introduction, majolica is a ceramic earthenware covered by an opaque white tin glaze and decorated with colored pigments. These beautiful objects fascinated people in the past by their beauty and colourful appearance. For the study of these objects, the use of the scanning methodology was important because majolica is a very heterogeneous material with a lot of inclusions in the body and glaze.

The choice of pigments is limited to blue, yellow, orange/brown, green and purple. As can be seen in the selection of the 30 tiles shown in ***Fig. 2.2***, yellow and blue are the most frequently used colors in Antwerp majolica while orange and purple are rather uncommon. As a result of working with small embedded fragments of the tiles, we could only analyze the blue and yellow pigments, as these were the only colors available on the edge of the tiles that could be sampled. Therefore, we could not analyze the uncommon orange and purple pigments. However, simultaneously with these measurements, we had the opportunity to analyze the floor in the chapel of the Rameyenhof castle, located in Gestel (Belgium), which possesses a majolica tile floor that can be considered as a magnificent representation of the 16^{th} - 17^{th} century Antwerp majolica production (see chapter 4). The study gave information about the used Antwerp pigments blue, green, orange, red, yellow and purple in terms of average composition. The green pigment could be characterized using an extra tile AV-1466 (see ***Table3.1***) which was known to be Antwerp majolica, but which could not be unambiguously assigned to one of the four streets mentioned above. It is a majolica façade tile from 1550 from the workshop "Den Salm" (Antwerp, Franchois Frans).

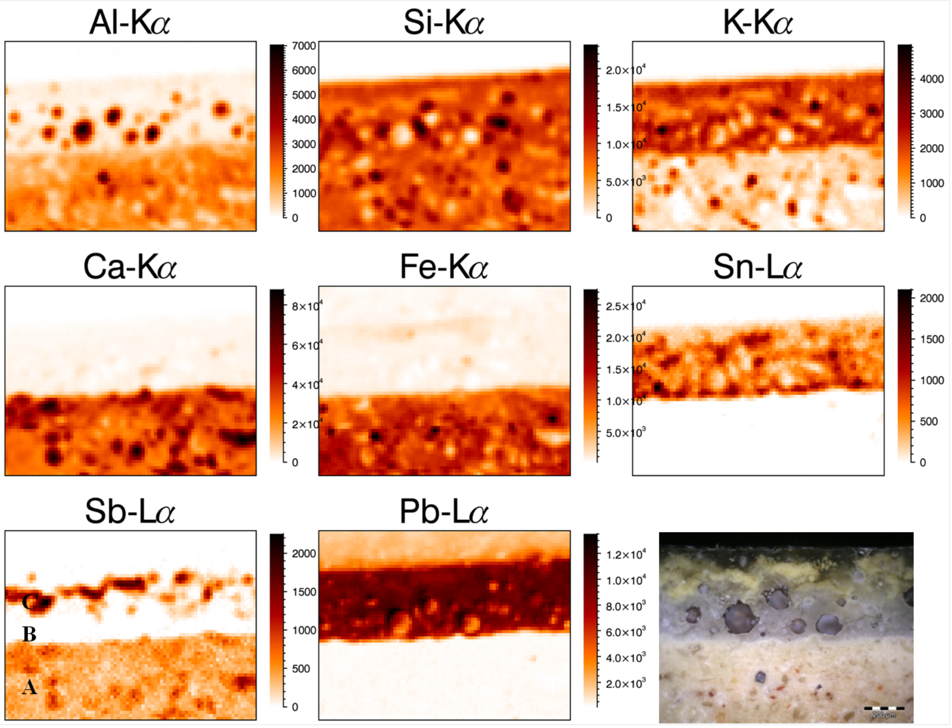

Figure 3.3: *2D mapping performed using the EDAX Eagle-III μ-XRF spectrometer, showing the layered structure of an embedded majolica fragment of tile A187-t1. The elemental maps correspond to a scanning area of 1.6 x 1.2 mm^2, obtained using a live-time of 15 s per scan point. Labels in Sb-map: A = body layer, B = primary white glaze layer, C = pigment layer + transparent lead glaze.*

Fig. 3.3 and ***Fig. 3.4*** show elemental distributions corresponding to cross-sectional mappings of embedded fragments of majolica tiles A187-t1 (yellow pigment) and AV-1466 (green pigment). In both cases, a layered structure of three layers can be seen, by which majolica is built up as a result of the different production stages: earthenware body, primary white glaze and pigments, as indicated with letters A, B and C in the elemental map of Sb-L (***Fig. 3.3***). In these elemental maps it can be seen that the body layer is rich in Ca and Fe, with inclusions exhibiting high Si and K signals. These originate from quartz and feldspar, which were probably added into the clay to modify the clay properties. Al and Sb are also present in this body layer but with significantly lower intensities (darker tones correspond to higher intensity of the concerned element). The Pb-L_α elemental map has the highest intensity on the upper part of the body, which can be assigned to the glaze layer. Sn is added to opacify this glaze layer as can be seen in the Sn-L_α elemental map having a significantly lower intensity than Pb which is the main component of this glaze layer. Again, also K and Si rich inclusions (feldspar, quartz) are present next to gas bubbles. These inclusions exhibit a lower intensity in terms of Pb L-lines, giving a heterogeneous character to the layer. In the last production step, a decorative pigment layer was added to the surface. In this case, this layer exhibits Sb signal, typically used for yellow pigments, and is surrounded by the glaze layer consisting of Sn and Pb. These results confirm the theory that during a second baking cycle, the pigment layer probably fused with the white glaze layer applied in the previous stage.

Fig. 3.4 shows the elemental maps from tile AV-1466 to determine the coloring substances in the green glaze. The general body and glaze composition of this Antwerp majolica were the same as in tile A187-t1 (***Fig. 3.3***). The earthenware body layer consists of quartz and feldspar mixed with clay, as can be seen in the high intensity maps of Ca and Fe, low intensity of Al and inclusions of Si and K. The upper glaze layer has Pb as main component with Sn as opacifier. In contrast with the yellow pigment, there is no Sb signal detected in this decorative green surface layer. However, high XRF intensities of Cu and Zn are observed, and even the typical Ni constituent for green pigment, albeit with low intensity, could be detected.

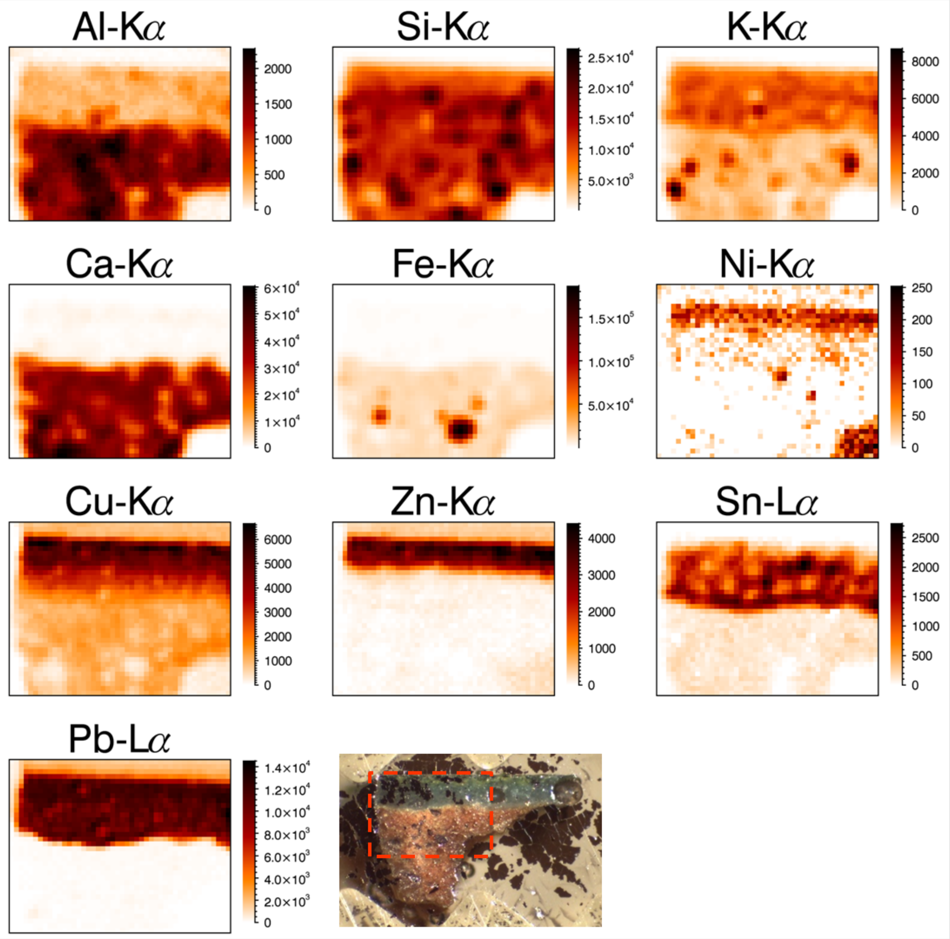

Figure 3.4: *2D mapping performed using the EDAX Eagle-III μ-XRF spectrometer for the embedded majolica fragment of tile AV-1466. The elemental maps correspond to a scanning area of 0.9 x 0.7 mm^2, obtained using a live-time of 25 s per scan point.*

As mentioned during the introduction, in some cases, a final thin transparent and homogeneous layer (coperta) was added on the surface of the white glaze/pigment layer, which fused during a third baking stage. However, this is not conclusive because due to the spatial resolution limitations of the instrument one cannot differentiate sufficiently between the pigment and the coperta layer. However, when comparing the elemental maps of Si and K in ***Fig. 3.3***, it can be seen that a very thin layer is present above the K rich region, which is perhaps the coperta layer with Si as main component.

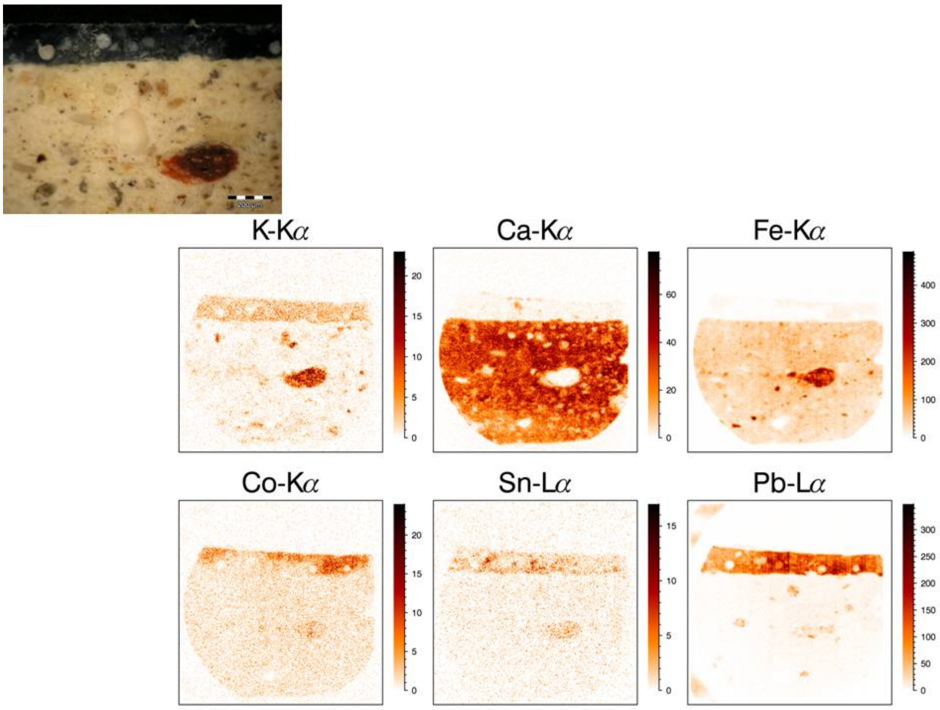

Figure 3.5: *2D elemental imaging performed using the SLcam at beamline P06 at PETRA III of tile A218-0-m4. The elemental maps correspond to an illuminated area of 2.1 x 2.1 mm^2 of 264 x 264 pixels, obtained using a measuring time of 90 min and a count rate of approximately 1000 cps.*

The used blue pigment was identified via synchrotron full-field XRF using the SLcam detector and a line scan through the whole embedded fragment of tile A187-t2. The synchrotron measurements were used to demonstrate the advantage of this full-field XRF in cultural heritage studies. Using the SLcam, it is possible to perform 2D XRF imaging in a direct way and to image areas of 2.1 mm by 2.1 mm with a microscopic resolution of 8 μm. In this way, one extracts the same information,albeit with higher spatial resolution, as with the scanning mode EDAX Eagle-III spectrometer but in much shorter time: data acquisition time 2 hours in case of the SLcam, compared to at least 30 hours using the Eagle-III. The drawback of the full-field XRF technique is the necessary combination with synchrotron facilities which are not available routinely, like a laboratory μ-XRF spectrometer. ***Fig. 3.5*** shows the results of imaging the embedded fragment of tile A218-0-m4 with the SLcam at beamline P06 of PETRA III. Based on these elemental maps, it is possible to identify the general Antwerp majolica body and glaze layer components (K, Ca and Fe presence in the body, Sn and Pb in the glaze layer) and Co as specific coloring agent associated with the blue pigment.

Fig. 3.6 and ***Fig. 3.7*** show the results of a line scan through the embedded fragment of tile

A187-t2, starting in the resin, passing first through the blue colored glaze layer, then the body and ending up again in the resin. These line scans were mainly carried out to get more information about the layered structure in the whole glaze layer where we found that it contains a mixture of Pb, Sn and a coloring agent at the top of the earthenware body, as described above. The glaze layer is approximately 200 μm thick as can been seen from ***Fig. 3.6***: The intensity of Pb (main constituent in the glaze layer) is decreasing whereas the intensity of Ca and Fe are increasing. The transition of the glaze layer to the bulk is not sudden but rather gradual. This can be explained by the porous property of the body through which, during the second glaze baking period, compounds from the glaze diffused in the upper part of the body.

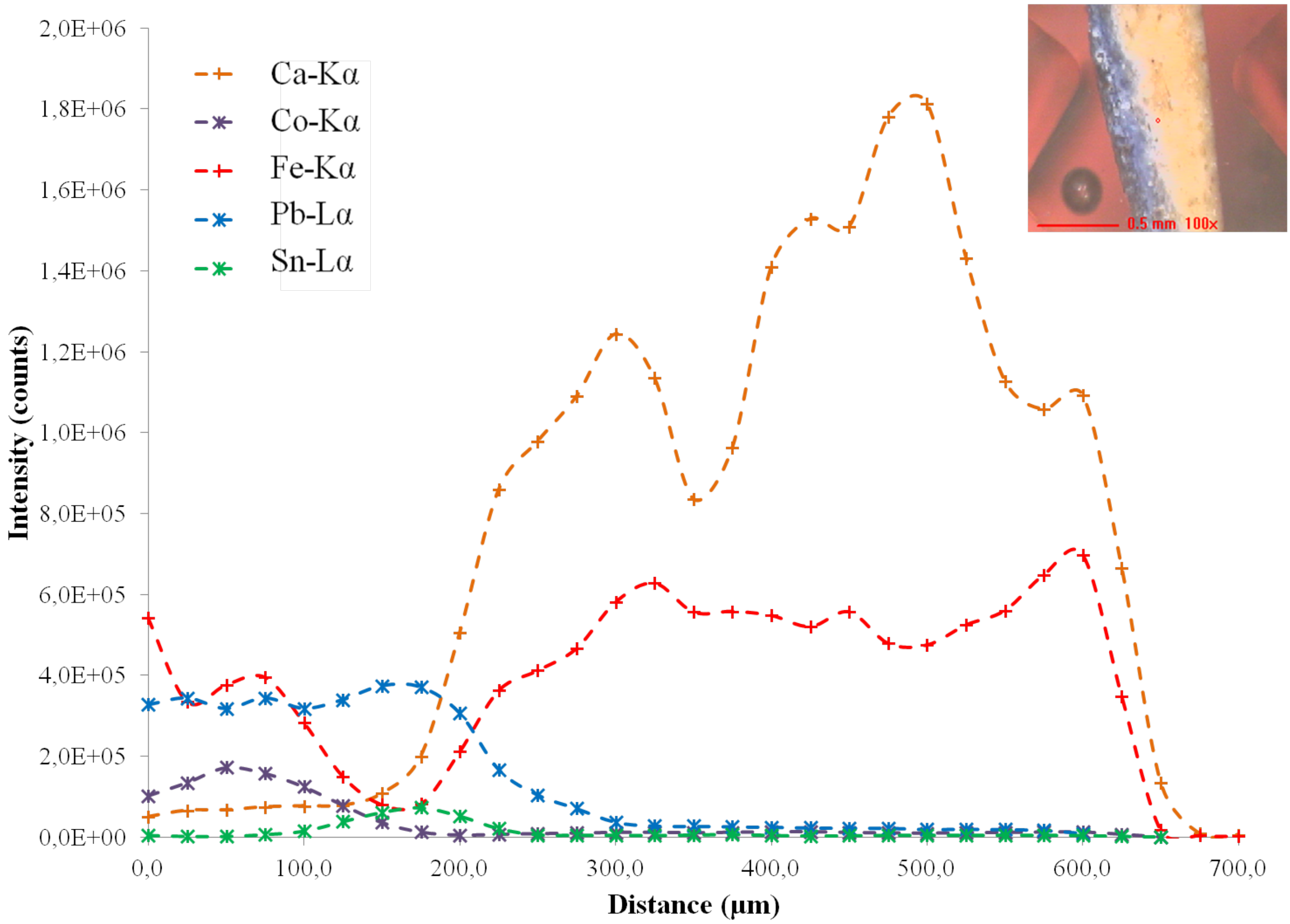

Figure 3.6: *Line scan (dimension: 700 μm with step size of 25 μm and 1000 s live-time per point) through the fragment originating from tile a187-t2 using the EDAX Eagle-III spectrometer: scan through the entire tile. The inserted optical image (top right) shows the fragment with a red dot representing the center of the performed line scan.*

More details about the layer build-up in the glaze layer can be gathered from ***Fig. 3.7***. As mentioned above, the glaze layer displays a high concentration of Pb, Sn and pigment specific elements, and also inclusions of body components. This is in contrast with some accounts in the literature which describe a more elaborate layered structure, consisting of a Pb rich glaze layer with high concentration of Sn observed on its surface, or in the transition zone glaze - body and the pigment layer on top of the glaze layer. ***Fig. 3.7*** zooms in on the first 200 μm of ***Fig. 3.6*** and the intensities of the Co and Sn signal are multiplied by two. We can see that the K_α signal of the pigment specific element Co (blue color) reaches its maximum intensity in the upper region of the glaze layer, whereas the Sn-L_α peak reaches its maximum intensity in a deeper region of the glaze layer. This can be observed in case of all selected tiles of Antwerp majolica which allow concluding that the Pb-based glaze layer is comprised of two layers: a top pigment layer with a Sn-rich layer underneath. We summarize the characteristic elemental composition (expressed weight percentages of oxides) used for the production of the coloring agents of Antwerp majolica in ***Table3.2***. Typical for the blue pigment is the high concentration of CoO and the detection of As_2O_3. For the green and yellow pigment: presence of Sb_2O_3 and, specific for the green pigment, which is a mixture of yellow and blue, a low amount of CoO and high concentration of CuO. Our measurements confirm the findings of the literature with respect to the used pigments in this period.

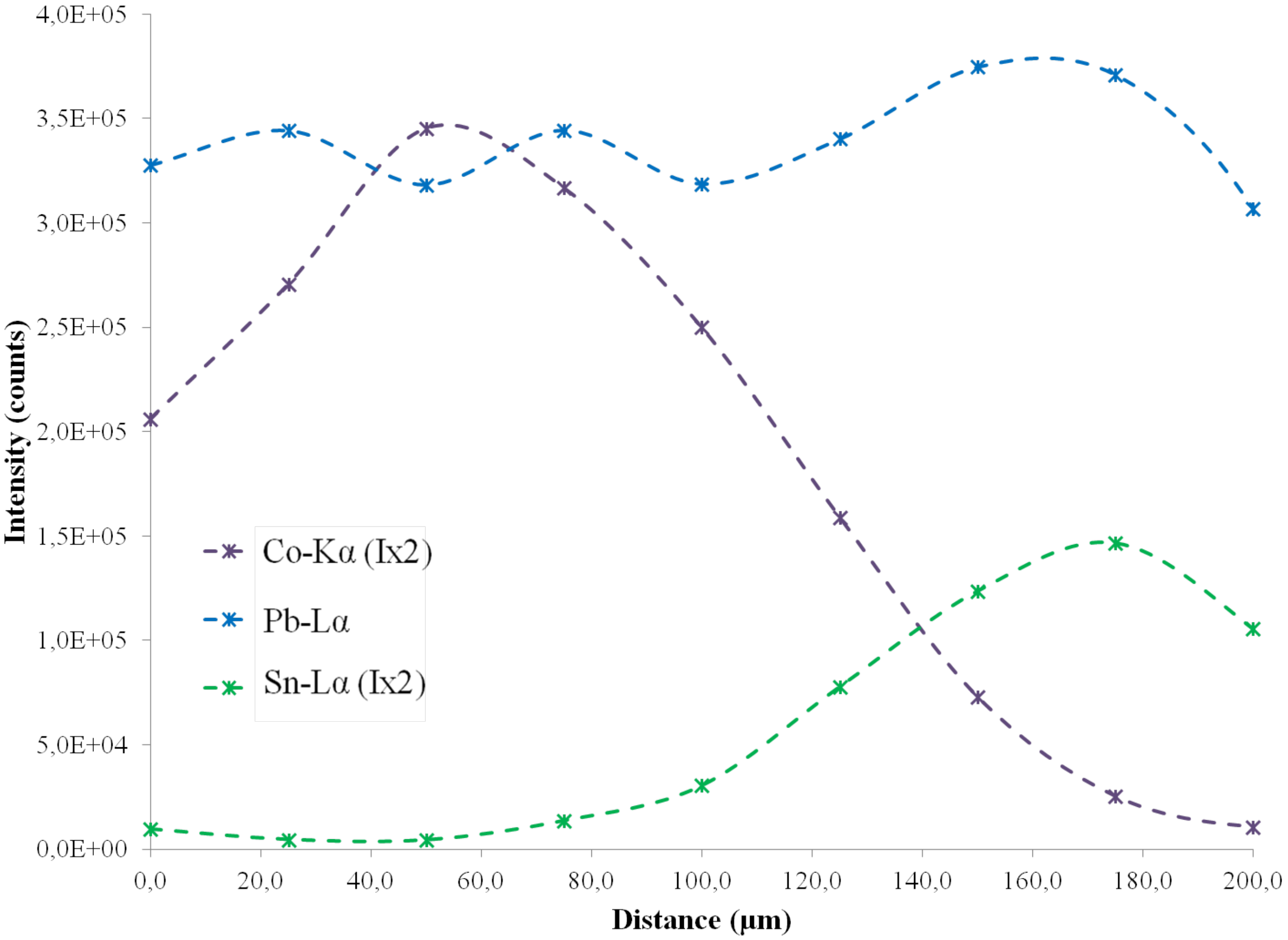

Figure 3.7: *Zoom of the pigment layer scan shown in **Fig. 3.6**: The Intensities of Co-K_α and Sn-L_α signals are multiplied by 2 for clarity.*

Table 3.2: *Quantitative results corresponding to the used coloring agents obtained from the analyzed samples. Oxide concentrations are given in weight percentages.*

	Al_2O_3	SiO_2	P_2O_5	K_2O	CaO	TiO_2	MnO	Fe_2O_3
Blue - A218-0-m4	4.51	39.48	4.39	10.00	6.12	0.09	0.08	1.77
Green - AV1466	3.24	35.89		6.60	1.95	0.17	0.11	0.72
Yellow - A117-7-t6	1.76	48.31		6.57	2.15	0.11	0.07	5.22

	CoO	NiO	CuO	ZnO	As_2O_3	SnO_2	Sb_2O_3	PbO
Blue - A218-0-m4	0.82	0.17	0.04	0.04	0.01	4.46		28.19
Green - AV1466	0.02	0.04	2.92	1.93		1.13	1.74	39.93
Yellow - A117-7-t6			0.15	0.13		0.40	0.32	34.56

3.3.2 Similarities in the Antwerp majolica collection

All 30 embedded fragments of the different Antwerp majolica tiles from the four different streets were measured using the EDAX Eagle-III spectrometer in line scan mode, with two or more line scans performed on each fragment. The line scans start in the resin, passing first through the glaze layer and then through the body. Depending on the thickness of the body, the scan either stops in the resin behind the body, or in the body itself. The line scan was performed using a measuring (live) time of 1000 s per point, with a beam size of 25 μm and a step size of 25 μm which gives detailed information on each layer and allows using the standardless quantification scheme provided by the software package of the instrument. The latter calculates the oxide concentration in weight percentages based on the measured XRF spectra. The line scan data was divided into subsets corresponding to glaze and body, based on the lead (Pb) signal because this element is typical for the glaze. These results deliver information about the similarity of the production processes used by the four different workshops situated in the four different streets in the city center of Antwerp.

When we quantify the 624 point measurements in the body of all 30 embedded fragments of the Antwerp majolica tiles originating from the four production sites and when the average of the quantification data of the body is taken for each tile, the results can be used to learn more about the similarities of the production process of the earthenware body applied by the potters settled in Antwerp. Plotting the weight percentage of CaO (as x-axis) against the weight percentage of Fe_2O_3, the two main components of the body, the graph of ***Fig. 3.8*** is obtained. In this figure, no obvious difference can be observed between the four production sites for the oxides used for the production of the earthenware body.

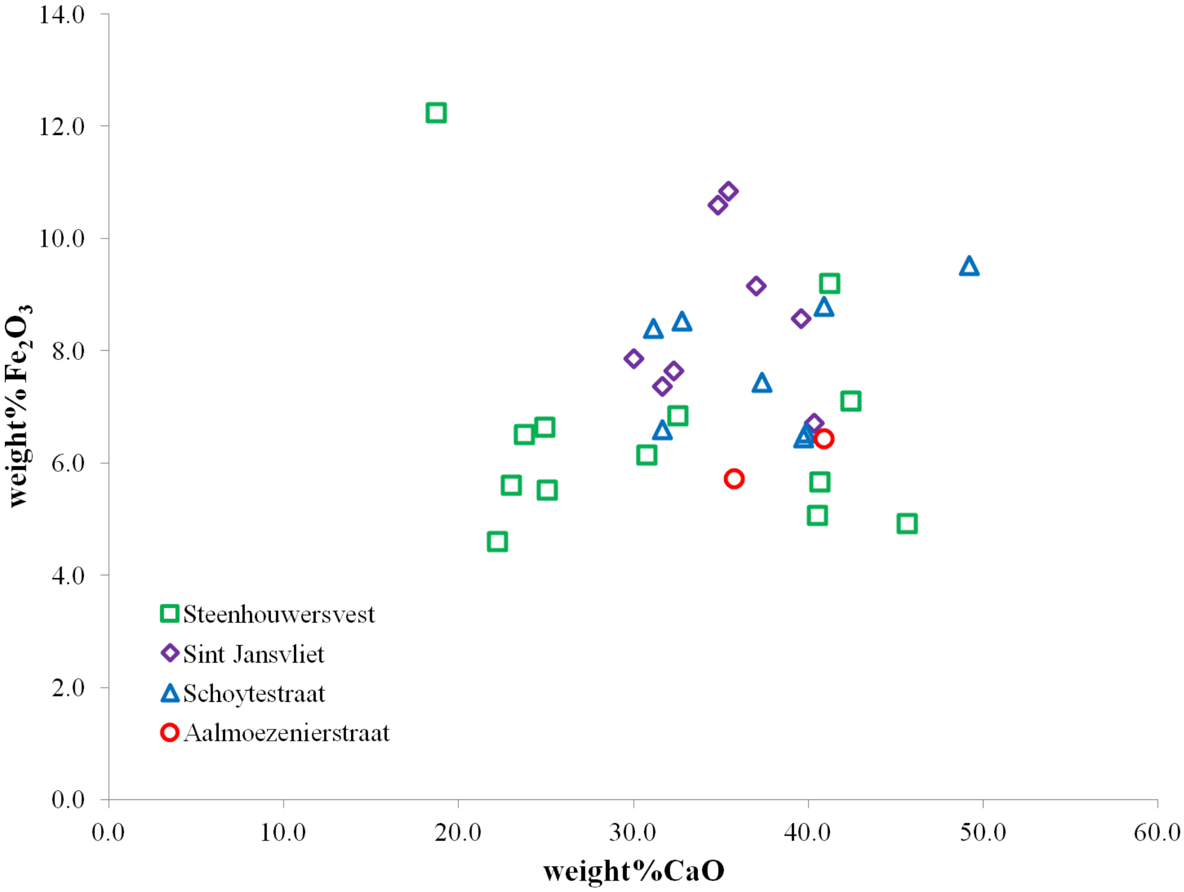

Figure 3.8: *Correlation plot of weight percentage of CaO and Fe_2O_3 (main components of body) of the averages per tile.*

Result of PCA processing on XRF data from the body layer

Confirmation of the above conclusion needs an appropriate statistical data processing method to get clear evidence about the presence or absence of similarities between the production methods used by the Antwerp potters. Principal component analysis (PCA) is such a multivariate statistical method which allows unsupervised pattern recognition aiming to detect similarities and for which no prior knowledge is used as explained in chapter 2, section 2.3.8. In what follows, this type of multivariate statistical method will be applied on the original data of all 30 majolica fragments. These original data consist of 624 point measurements in the body layer and 938 point measurements in the glaze layer which were quantified using the standardless fundamental parameter analysis available in the software of the EDAX Eagle-III micro-XRF spectrometer (see 3.2). Before applying PCA, the data were scaled and mean-centered as part of a standard pre-processing procedure, in order to improve the interpretation of the model [31].

As could be seen in ***Fig. 3.8***, by plotting the weight percentages of the two main components of the earthenware body, the average body composition did not show distinct groups of tiles but rather one consistent set of data. When applying PCA on the 624 point measurements in the body layer, the obtained score plot of PC1 versus PC2 (see ***Fig. 3.9***) confirm this result by showing no possible classification of the objects based on the (quantitative) XRF dataset. All the objects in the score plot are centered in the middle and mixed, without defining any distinct groups based on the determined compositional/elemental signatures. In summary, by using PCA on our quantitative XRF data-set, one can see that there are no classifiable differences in the elemental fingerprints in case of the samples originating from the different workshops, which in its turn is an indication that similar production processes were applied by the different potters working at various production sites in Antwerp.

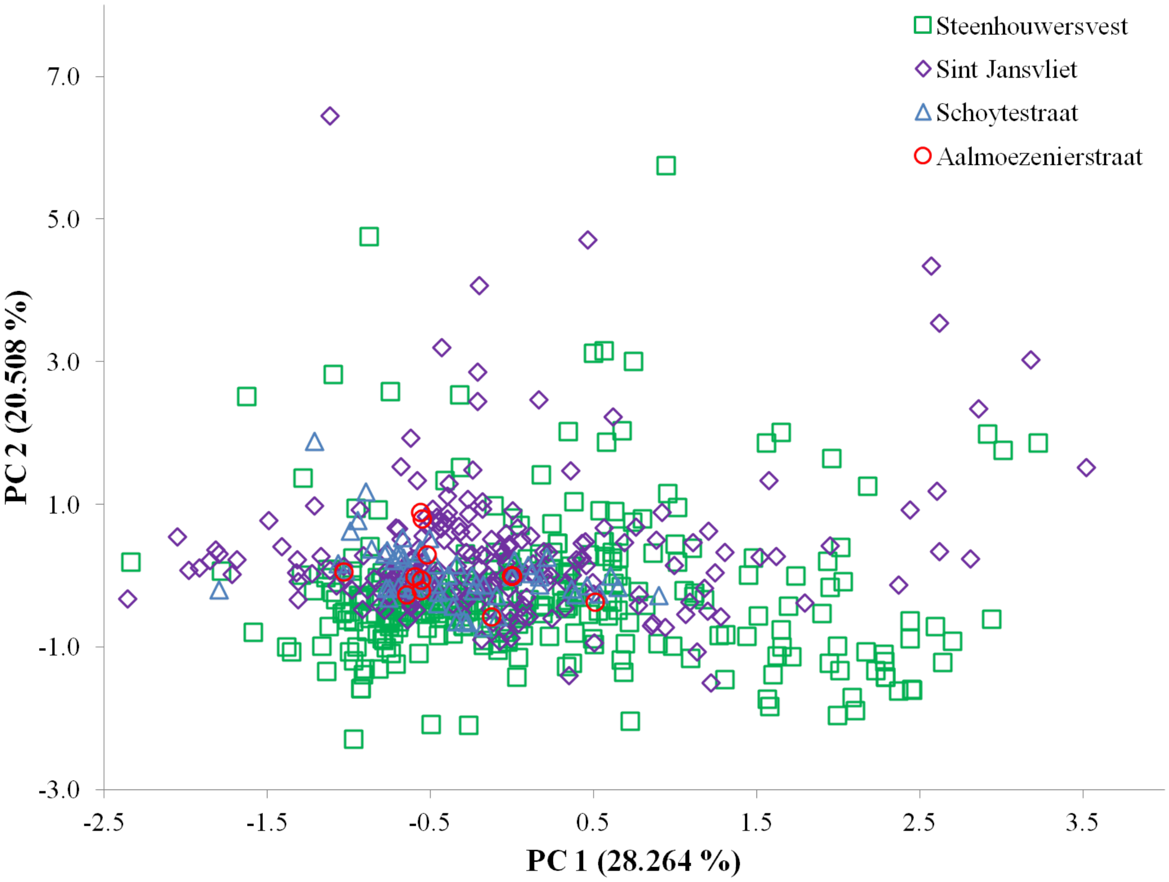

Figure 3.9: *Confirmation of the similarities in the body composition of majolica originating from the different production sites in Antwerp, indicating a similar production process, based on the score plot of PC1 (28.3 % of variation is present in this component) vs PC2 (20.5 % of variation is present in this second component) on the 624 point measurements of the body layer.*

Result of PCA processing on XRF data from the pigment layer

The same strategy was followed to examine the similarity in the composition (indicating similar production processes used) of the glaze layer. ***Fig. 3.10*** shows the quantification data of 938 point measurements in the glaze layer, which are plotted using the weight percentage of the two main components of the glaze layer (SnO_2 and PbO). In the presented correlation plot, no identifyable trends can be observed corresponding to the Steenhouwersvest, Sint-Jansvliet, Schoytestraat and Aalmoezenierstraat production sites: all the data are mixed and spread out over the entire area of the graph. Confirmation is acquired using PCA on these original glaze layer measurements by constructing a score plot of PC1 versus PC2 (***Fig. 3.11***) where no different groups can be distinguished.

Another confirmation that the production process for the glaze layer of Antwerp majolica likely to be the same, can be found in ***Fig. 3.12*** where the score plot is given of all the measurements in the blue pigment (color frequently used in Antwerp majolica tiles). Again, all objects are mixed and centralized in the middle of the plot, therefore no significant differentiation is possible among the four Antwerp workshops based on the quantitative XRF data.

The results presented above give a strong indication of an equivalent production process for Antwerp majolica used in the different workshops present in the city center of Antwerp in the 16^{th} and 17^{th} century. This is an interesting finding in the light of the fact that in the available literature and by conservators it has been assumed that at least two different production processes existed, and not just one community of potters who worked very close together. A very interesting historical question about Antwerp majolica concerns the influence of foreign potters settled in Antwerp. Therefore, we compared the average quantitative data obtained from the analysis of the earthenware body of the 30 tiles with data available in literature for majolica from Portugal [4], Spain [1], and Italy [6, 32]. ***Fig. 3.13*** shows the results of this comparison and from this figure we can conclude that the Antwerp majolica manufacturers are mainly influenced by the Italian potters, however, they also chose their own specific Antwerp majolica production process. This is indicated by the fact, that there is no complete overlap between the data from Antwerp and the Italian data.

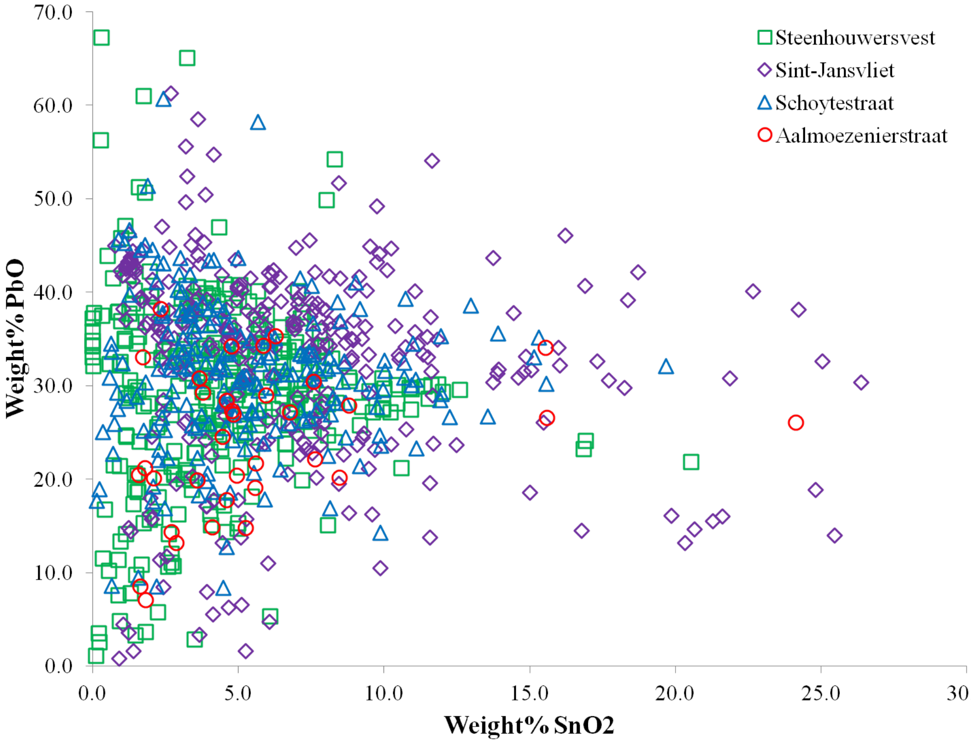

Figure 3.10: *Quantification data corresponding to 938 point measurements in the glaze layer of all embedded fragments obtained using the EDAX Eagle-III spectrometer, visualized as correlation plots of weight percentages of SnO_2 and PbO (main components of glaze) of all tiles.*

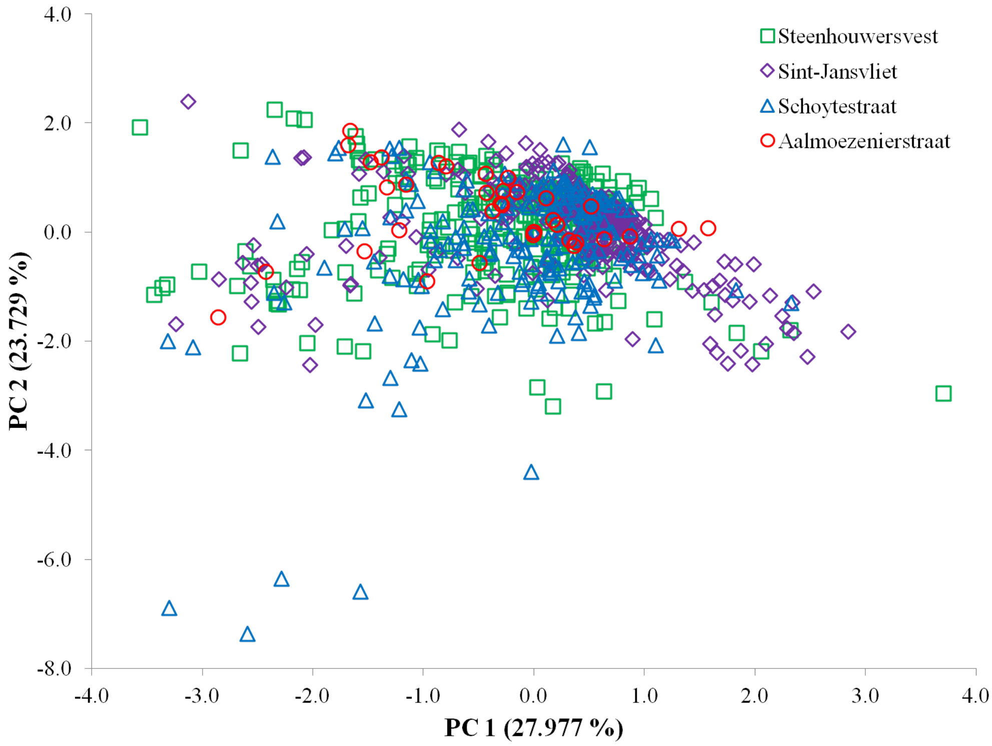

Figure 3.11: *Confirmation of the production equivalence in the glaze production process by using PCA.*

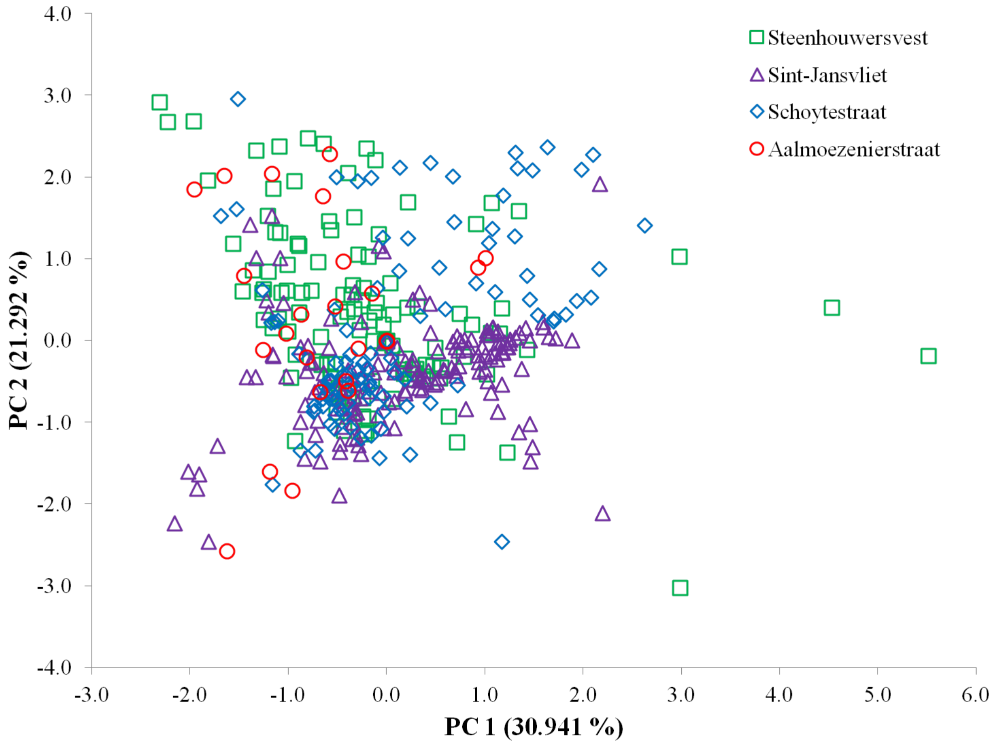

Figure 3.12: *Similar equivalence can be found in the compositional properties of the blue pigment by using PCA on the derived quantitative data corresponding to the blue pigment top layer. This is another indication of the similarities between the applied raw materials and production processes.*

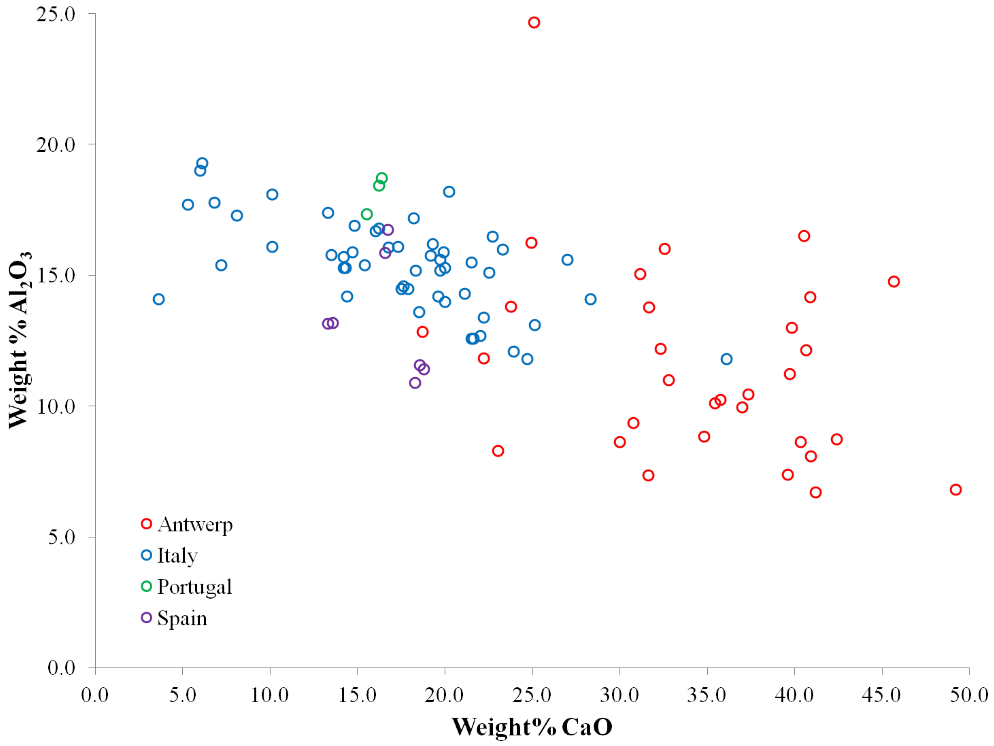

Figure 3.13: *Correlation scatter plot of the weight percentages of CaO and Al_2O_3 (components of body) of the averages for each Antwerp majolica tile compared with quantification data from the literature, corresponding to majolica from Spain, Portugal and Italy.*

3.3.3 SEM analysis

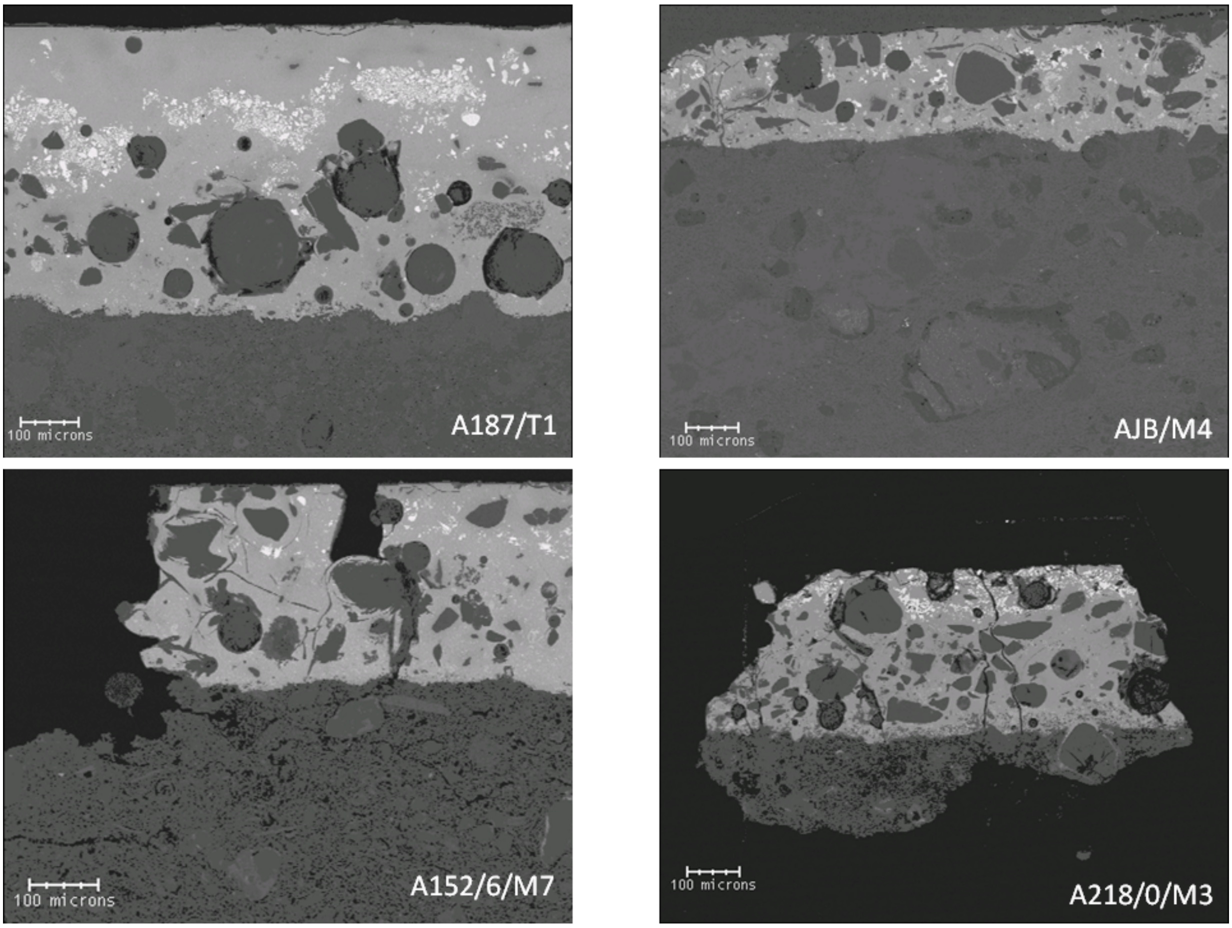

Figure 3.14: *SEM images of embedded cross-sections of Antwerp majolica samples corresponding to the four production sites.*

As explained in the literature [6], SEM analyses can in certain cases confirm the period in which the majolica was produced, beside providing information on the glaze type. ***Fig. 3.14*** shows the results of SEM analysis, indicating a double layer glaze type which is typical for Antwerp majolica produced in the 16^{th}-17^{th} century. Indeed, Antwerp majolica fragments show distinct properties of the double layered glaze (as also discerned from the XRF line scans) where the inner opaque glaze layer contains fine tin oxide particles (white) and angular shaped quartz and potassium feldspar particles (dark), whereas the outer transparent glaze layer is more or less devoid of such particular crystalline phases. This layer can correspond to the coperta layer described by Piccolpasso. This two-layer glaze type has been first used during the early 15^{th} century and its use was continued until the early 17^{th} century, covering the whole production period of Antwerp majolica.

3.4 Conclusion

By using a combination of non-destructive laboratory scanning micro-XRF spectrometry, full-field XRF imaging at a synchrotron facility and SEM analysis it was possible to investigate archaeological majolica tiles produced in Antwerp, Belgium. For this study, a set of 30 Antwerp majolica tiles produced in the period 1550-1660 in four different production sites in the city center of Antwerp were investigated to determine the characteristics of the earthenware body, the glaze layer and the used coloring agent in order to obtain information on their characteristic elemental signature. In order to achieve this goal, fragments of the tiles were sampled and embedded in resin to be able to obtain elemental information on the layered structure of these heterogeneous materials. The use of quantitative XRF data evaluation methods enabled us to examine the compositional characteristics of the majolica originating from the four production centra and, based on the similarities between the samples in terms of their elemental fingerprints, one can conclude that the production methods (and the used raw materials) were likely to be very similar. The obtained elemental analysis data also allowed us to discover features which are characteristic to Antwerp majolica production, together with indications regarding the influence of Italian production methods. All these results are very useful for comparison with historical manufacturing recipes described in literature.

When studying the embedded fragments, the micro-XRF based techniques proved extremely valuable providing elemental information and providing elemental information (i.e. elemental fingerprints) on the earthenware body, the glaze layer on the surface of this body and the used pigments. Ca and Fe are the main components of the body originating from quartz and feldspar, which were probably added to the clay to modify its properties. The glaze layer contains Pb and Sn as main elements, with Sn oxide particles added to opacify the glaze layer. As a result of micro-XRF line scans, it was found that this glaze layer was a two-layered glaze type. Above this Pb-Sn mixture, a layer with coloring agent was added to get the unique paintings on the tiles. Our research identifies the used pigments for this coloring agent: for blue Co^{2+} ions were dissolved in the glaze, for yellow Sb was detected corresponding to $Pb_3(SbO_4)_2$ particles and for green a high Cu intensity and weight percentage was detected. The layered structure was also confirmed by the results of the SEM measurements.

Based on the quantitative XRF data of each tile, it was possible to compare the compositional characteristics of the tiles: the similarities of their elemental fingerprints indicate that equivalent or very similar production methods were used in the four production centra of Antwerp majolica. When comparing the weight percentages of the main components of the body and the glaze layer, no difference can be seen between the workshops. Statistically, it is confirmed by using PCA which did not identify distinct groups based on the compositional data. When focusing on the components of the blue pigment, the same conclusions can be reached.

Bibliography

[1] J. Molera, M. Vendrell-Saz, and J. Pérez-Arantegui, “Chemical and Textural Characterization of Tin Glazes in Islamic Ceramics from Eastern Spain,” *Journal of Archaeological Science*, vol. 28, pp. 331–340, Mar. 2001.

[2] R. Padilla, O. Schalm, K. Janssens, R. Arrazcaeta, and P. Van Espen, “Microanalytical characterization of surface decoration in Majolica pottery,” *Analytica Chimica Acta*, vol. 535, pp. 201–211, Apr. 2005.

[3] I. Catalano, A. Genga, C. Laganara, R. Laviano, A. Mangone, D. Marano, and A. Traini, “Lapis lazuli usage for blue decoration of polychrome painted glazed pottery: a recurrent technology during the Middle Ages in Apulia (Southern Italy),” *Journal of Archaeological Science*, vol. 34, pp. 503–511, Apr. 2007.

[4] A. Guilherme, J. Coroado, and M. L. Carvalho, “Chemical and mineralogical characterization on glazes of ceramics from Coimbra (Portugal) from the sixteenth to nineteenth centuries.,” *Analytical and bioanalytical chemistry*, vol. 395, pp. 2051–9, Dec. 2009.

[5] J. G. Iña nez, R. J. Speakman, J. Buxeda i garrigos, and M. D. Glascock, “Chemical Characterization of Tin-Lead Glazed Pottery From the Iberian Peninsula and the Canary Islands: Initial Steps Toward a Better Understanding of Spanish Colonial Pottery in the Americas,” *Archaeometry*, vol. 51, pp. 546–567, Aug. 2009.

[6] M. Tite, “The production technology of Italian maiolica: a reassessment,” *Journal of Archaeological Science*, vol. 36, pp. 2065–2080, Oct. 2009.

[7] A. Guilherme, J. Coroado, J. dos Santos, L. Lühl, T. Wolff, B. Kanngieß er, and M. Carvalho, “X-ray fluorescence (conventional and 3D) and scanning electron microscopy for the investigation of Portuguese polychrome glazed ceramics: Advances in the knowledge of the manufacturing techniques,” *Spectrochimica Acta Part B: Atomic Spectroscopy*, vol. 66, pp. 297–307, May 2011.

[8] C. Viti, I. Borgia, B. Brunetti, A. Sgamellotti, and M. Mellini, “Microtexture and microchemistry of glaze and pigments in Italian Renaissance pottery from Gubbio and Deruta,” *Journal of Cultural Heritage*, vol. 4, pp. 199–210, July 2003.

[9] C. Piccolpasso, R. Lightbown, and A. Caiger-Smith, *The three books of the potters art: a facsimile of the manuscript in the Victoria and Albert Museum, London.* London: Scolar Press, 1980.

[10] J. D. Van Dam, “The Difference Between Dry and Wet Clay Mixing and the Effect on the Deterioration of Dutch Tiles,” in *The Conservation of Glass and Ceramics: Research, Practice and Training*, p. 293, London: James & James, 1999.

[11] D. Korf, *Tegels*. Haarlem: W. De Haan, 1969.

[12] A. Caiger-Smith, *Tin Glaze Pottery in Europe and the Islamic World: The Tradition of 1000 Years in Maiolica, Faience and Delftware*. Faber & Faber, first edit ed., 1973.

[13] M. J. Hughes and D. Gaimster, “Neutron activation analyses of maiolica from London, Norwich, The Low Countries and Italy,” in *Maiolica in the North, the archaeology of tin-glazed earthenware in North-West Europe c. 1500-1600* (D. Gaimster, ed.), British Museum Press Occasional Paper Nr. 122, 1999.

[14] C. Dumortier, *Céramique de la Renaissance à Anvers. De venise à Delft*. Racine Lannoo, 2002.

[15] C. H. De Jonge, *Nederlandse tegels*. Amsterdam: J. H. De Bussy N. V., 1971.

[16] B. Rackham and A. Van de Put, *The three books of the potters art*. London: Victoria and Albert museum, 1934.

[17] M. Laurent, “Guido di Savino & the Earthenware of Antwerp,” *The Burlington Magazine for Connoisseurs*, vol. 41, no. 237, pp. 288–297, 1922.

[18] H. Nicaise, *Les Origines italiennes des faïenceries d’Anvers et des Pays-Bas au XVIe siecle*. 1934.

[19] B. Rackham, *Early Netherlands Maiolica with special reference to the tiles at the Vyne in Hampshire*. London: Geoffrey Bles, 1926.

[20] T. Oost, “Produkten van Antwerpse tegelbakkers,” *Cultureel jaarboek Stad Antwerpen IV*, pp. 26–28, 1986.

[21] J. Veeckman, “Van ’Craywyck’ tot Guldenberg. Archeologisch onderzoek op de Guldenberg,” *Blik in de bodem*, pp. 55–62, 1992.

[22] D. Gaimster, *Maiolica in the North. The Archaeology of tin-glazed earthenware in north-west Europe c.1500-1600*. London: British Museum Press Occasional Paper Nr. 122, 1999.

[23] C. Dumortier, “Les faïenciers italiens à Anvers au 16ème siècle, Aspects historiques,” *Faenza*, vol. 73, no. 4-6, pp. 161–172, 1987.

[24] C. Dumortier, “Les ateliers de majolique à Anvers (1508-1585),” *Bulletin van de Antwerpse Vereniging voor Bodem-en Grotonderzoek*, vol. 1, pp. 23–28, 1988.

[25] C. Dumortier and T. Oost, “Un atelier de majoliques installé à Anvers vers 1600,” *Bulletin des Musées Royaux d’Art et d’Histoire*, vol. 60, pp. 203–216, 1989.

[26] J. Veeckman and (ed.), *Majolica and glass from Italy to Antwerp and beyond. The transfer of technology in the 16th-early 17th century*. Antwerp: stad Antwerpen afdeling archeologie, 2002.

[27] W. T. Elam, R. B. Shen, B. Scruggs, and J. Nicolosi, "Accuracy of Standardless FP Analysis of Bulk and Thin Film Samples Using a New Atomic Database," *Advances in X-ray analysis*, vol. 47, pp. 104–109, 2004.

[28] O. Scharf, S. Ihle, I. Ordavo, V. Arkadiev, A. Bjeoumikhov, S. Bjeoumikhova, G. Buzanich, R. Gubzhokov, A. Günther, R. Hartmann, M. Kühbacher, M. Lang, N. Langhoff, A. Liebel, M. Radtke, U. Reinholz, H. Riesemeier, H. Soltau, L. Strüder, A. F. Thünemann, and R. Wedell, "Compact pnCCD-based X-ray camera with high spatial and energy resolution: A color X-ray camera," *Analytical Chemistry*, vol. 83, pp. 2532–2538, 2011.

[29] J. Garrevoet, B. Vekemans, P. Tack, B. D. Samber, S. Schmitz, F. E. Brenker, G. Falkenberg, and L. Vincze, "Methodology toward 3D Micro X-ray Fluorescence Imaging Using an Energy Dispersive Charge-Coupled Device Detector," *Analytical chemistry*, vol. 06, 2014.

[30] P. Tack, J. Garrevoet, S. Bauters, B. Vekemans, B. Laforce, E. V. Ranst, D. Banerjee, A. Longo, W. Bras, and L. Vincze, "Full-Field Fluorescence Mode Micro-XANES Imaging Using a Unique Energy Dispersive CCD Detector," *Analytical chemistry*, vol. 86, p. 87918797, 2014.

[31] L. Eriksson, E. Johansson, N. Kettaneh-Wold, J. Trygg, C. Wikström, and S. Wold, "PCA," in *Multi- and megavariate data analysis, Part I: Basic principles and enlarged edition*, pp. 39–62, Umetrics Academy, 2006.

[32] C. Ricci, I. Borgia, B. G. Brunetti, A. Sgamellotti, B. Fabbri, M. C. Burla, and G. Polidori, "A study on late medieval transparent-glazed pottery and archaic majolica from orvieta (central Italy)," *Archaeometry*, vol. 3, no. July 2004, pp. 557–570, 2005.

Chapter 4: Study of a unique 16th century Antwerp majolica floor in the chapel of the Rameyenhof castle by means of X-ray fluorescence and portable Raman analytical instrumentation

Lien Van de Voorde, Melissa Vandevijvere, Bart Vekemans, Jolien Van Pevenage,
Joost Caen, Peter Vandenabeele, Piet Van Espen, Laszlo Vincze

Spectrochimica Acta Part B, 102, 28-35 (2014)

In the previous chapter, we presented results on the average elemental signatures of the various materials found in 16th-17th century Antwerp majolica tiles. Here, we describe our in situ investigations of a unique and only known majolica tile floor found in Belgium, in a chapel of the Rameyenhof castle (Gestel, Belgium), originating from the 16th century. Next to the detailed investigation of the tiles, the central medallion of the chapel's floor is compared to a similar one, stored in the Rubens House museum in Antwerp (Belgium). This chapter reports on the results of the analyses based on a combination of non-destructive and portable instrumentation described in chapter 2. The characteristic major/minor and trace element signature of 16th century Antwerp majolica is determined in situ and valuable information about the originality of the chapel floor and the two central medallions is obtained.

4.1 Introduction

The chapel of the Rameyenhof castle, which is located in Gestel (Belgium) on a private domain, possesses a majolica tile floor that can be considered as a magnificent representation of majolica production that was once so popular during the 16th - 17th century in Antwerp (***Fig. 4.1***). The castle dates probably from the 13th century, built by the bishop of Liege as an outpost from their area around the Belgian city Mechelen. In this period, the castle was a locked rectangular building without turrets, only with a tower at the entrance. During the 16th century, the Rameyenhof castle was transferred to Nicolaas Rubens (the son of the famous Flemish painter Peter Paul Rubens) who built three turrets from which one turret served as a chapel decorated with a unique Antwerp majolica tile floor [1]. At the time, the majolica technique was often used to make tiles as well as other types of ceramic art, such as sculptures and tableware [2]. As discussed in chapter 3, majolica refers to earthenware covered with a white opaque glaze (tin glaze) and decorated with various metal oxides based pigments to obtain a multi-coloured painting [3]. In earlier studies, researchers investigated majolica from an archaeological, (art) historical or chemical point of view [4–6].

Figure 4.1: *Left: Photograph of castle of Rameyenhof, Gestel, Belgium , Right: the majolica floor.*

This study aims at the detailed analysis based on a novel combination of non-destructive and portable instrumentation, including a handheld XRF spectrometer for obtaining elemental information and a mobile Raman spectrometer for retrieving structural and molecular information on the floor tiles in the Rameyenhof castle and on a second, similar medallion, which is stored in the Rubens House museum in Antwerp (Belgium). The investigated majolica tile floor in the Rameyenhof castle has a specific hexagonal form, which indicates that it was specially designed for the chapel, where the tiles are set in six triangular zones converging to a central medallion. The tiles in the zones can be divided into smaller (green area) and larger tiles (yellow area), on the basis of size, and reddish border tiles, which separate the six zones and surround the whole floor (***Fig. 4.2***). The decoration of the floor is an appealing overall painting with typical Renaissance motifs and coats of arms. The floor was most likely made in Antwerp at the beginning of the 16th century (1526-1528) in the workshop of Guido di Savino, also known as Guido Andries, who was a prominent figure in the majolica industry in that period [1, 7].

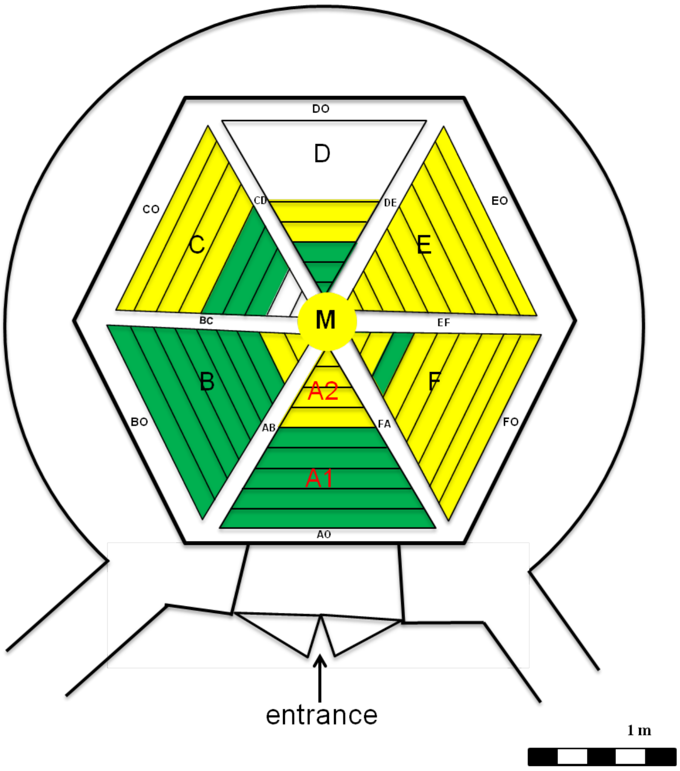

Figure 4.2: *Schematic overview of the floor with indication of small tiles (green coloured) and large tiles (yellow coloured), the six triangular zones named A to F, the central medallion (named M) and the reddish border tiles, named AB to FA and AO to FO. Tiles themselves are named starting with the letter of the zone, followed by the number of the row (counted from outside to the central medallion) and ending with their position in the row (counted from left to right).*

On the attic of the Rameyenhof chapel, another central medallion had been kept for a long time until it was moved in the year 2000 to the Rubens House museum, (Antwerp, Belgium) where it is still preserved (***Fig. 4.3***). The floor itself has a stylistically similar medallion. The fact that there are two allied medallions is curious and rather unusual from an art historical point of view [8]. It can be seen that compared with the chapel medallion (***Fig. 4.3***), the quality of the tiles in the Rubens House museum is clearly different and they show an inaccurate iconography. After almost

500 years, the floor was in a relative bad condition and therefore it was restored and conserved in 2009. During this intervention all tiles were removed, individually restored and the floor was rebuilt in the chapel whilst missing tile zones were filled with lime mortar [1]. During this intervention, a few fragments were studied by Neutron Activation Analysis (NAA) and Inductively Coupled Plasma Mass Spectroscopy (ICP-MS) [9], which are unfortunately destructive methods. For that reason, this approach is no longer allowed for the analysis of additional tiles or glazes, which represent the important pictorial layers of the artefacts.

Figure 4.3: *Detail images of the central medallion (both have 4 x 4 full tiles with dimensions of a single tile of 144 mm x 144 mm). Left: medallion preserved in the Rubens House museum (Antwerp, Belgium) where it was not possible to use colour corrected photography. Right: Medallion present in the floor of the Rameyenhof castle (Gestel, Belgium).*

This project aims at identifying the used materials (glaze and pigments), studying the structure and the impact of wear and degradation on the chemical characteristics, as well as comparing the chemical makeup of the two medallions in order to verify their authenticity and in this way to provide a scientific confirmation of the (art) historical assumption of their similar provenance.

In this type of cultural heritage studies, there is a special need for *in situ* non-destructive and portable techniques, as the floor tiles cannot be moved. Also, special precautions concerning the portable instrumentation must be taken to protect the analysed objects. Tiles of interest and the analysed points are selected based on (colour corrected) photographic documentation and by using portable digital microscopy, in order to know precisely where the molecular and elemental information is retrieved from using a mobile Raman spectrometer (MArtA) and a handheld XRF spectrometer respectively [10, 11].

4.2 Experimental

We used a multi-method approach comprising currently available state of the art portable and non-destructive analytical instrumentation, including the MArtA (see 2.6.3) and the hXRF spectrometer (see 2.3.5) to obtain respectively molecular and elemental information on the majolica floor tiles. In

Fig. 4.4 , snapshots of the instruments installed for the *in situ* analysis of the Rameyenhof floor or the medallion in the Rubens House museum are shown: the Olympus Innovx Delta handheld X-ray fluorescence spectrometer and the MArtA instrument. Performing the on-site experiments required six days in the castle's chapel (private location) over a period of 1.5 months, and two days in the depot of the Rubens House museum.

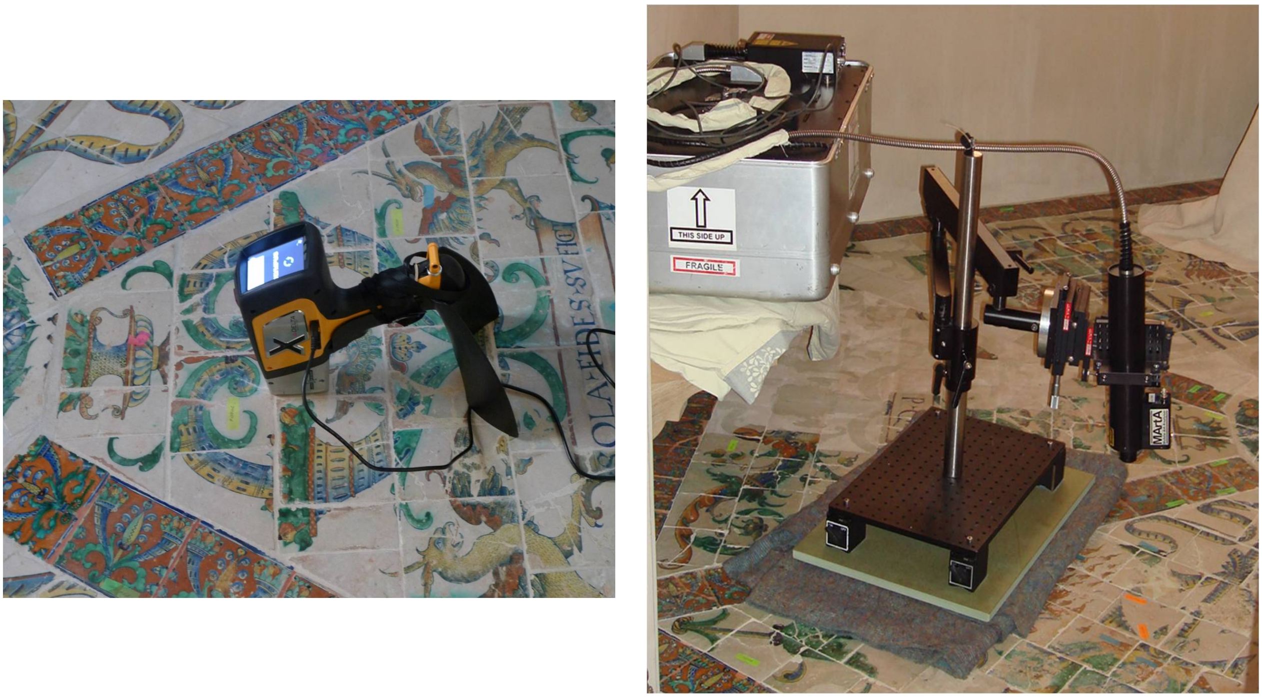

Figure 4.4: *in situ analysis using a set of mobile scientific instruments. Left: Olympus Innovx-Delta hXRF spectrometer on the Rameyenhof floor, right: MArtA Raman spectrometer.*

A preliminary investigation at the Rameyenhof castle was performed by colour corrected photography, documenting each tile, and calibrating the images in terms of colours using a colour card. A 5 Mpixel Dino-Lite digital microscope (Dino-Lite Europe, The Netherlands) was used to get high resolution digital images of different details from several tiles. Setting the magnification to 50x, a field view of interest of 8 mm by 6 mm was obtained, which was compatible with the macroscopic nature of analysis by the X-ray based instrumentation.

The hXRF measurements were performed using the commercial Olympus InnovX Delta instrument (for more details see 2.3.5), working with the following fixed settings: atmospheric conditions, tube voltage of 40 kV, tube current 79 μA, beam size of 5x5 mm^2 and measuring time of 300 sec (***Fig. 4.4***). The option of using the X-ray source in connection with a portable PC was used to allow controlling and monitoring the actual XRF measurements remotely. To position the probe head on the point of interest on the tile, special marks on the probe head and on a transparent polyester sheet were aligned, which was placed on the tile. After positioning the polyester sheet was removed. The collected XRF spectra were processed using the dedicated XRF spectrum evaluation software AXIL [12, 13].

The measurements of the tiles using the MArtA were performed using a 785 nm diode laser source with a spot size of 50 μm. The measuring time ranged between 3 and 20 seconds with accumulations ranging between 30 and 225 times. A laser power of 19 to 47 mW was applied. Because of the exclusive nature of the floor, the instrument was placed on a wooden board to distribute the pressure of the instrument over a larger surface. Furthermore, extra protection was provided by soft cover materials as can be seen in ***Fig. 4.4***. During the Raman measurements, the probe head and the analyzed region were covered using a black cloth in order to avoid interference caused by the ambient light. Raman measurements were only performed on the tiles of the Rameyenhof floor and not on the medallion of the Rubens House museum, due to the limited access time offered by the museum.

The EDAX Eagle-III laboratory scanning μ-XRF spectrometer was used to obtain information of the 30 archaeological majolica tiles (excavated from local production centers in Antwerp) described in chapter 3 by measuring embedded fragments of the tiles, to get cross section information of each separate layer. In contrast with these previous measurements, the XRF measurements on the floor tiles in the Rameyenhof castle in Gestel and on the medallion in the Rubens House museum can only be performed perpendicularly to the surface using the hXRF spectrometer. The obtained information in this case represents an average compositional information on the different layers from the majolica, integrated over the element-dependent information depth values. To have the possibility to compare the *in situ* measurements with the data corresponding to the 30 archaeological majolica tiles, also five of the archaeological majolica fragments were measured in the same way using the handheld instrument.

In all cases (Rameyenhof floor, medallion preserved in the Rubens House museum and archaeological tiles), measurements were also performed on the filler materials, the white opaque glaze, colouring agents and the clay body. The latter was possible in cases when the top layer had been removed by wear and tear. During the selection of the measuring points, larger areas were selected on the white glaze and pigments, taking the spot size of the instruments into account.

4.3 Results

4.3.1 Material and technical aspects of majolica in the chapel floor

As already described above, the *in situ* measurements with the hXRF instrument had a restriction that only measurements perpendicular to the floor's surface were possible, which implies that an element dependent information depth was probed across several layers, providing average elemental information from the probed depths. Therefore, it is important to interpret correctly what can be seen in the XRF spectra, measured perpendicularly to the floor providing multilayer information, and what can be learned about the materials used for the manufacturing of majolica compared with what we already learned about majolica described in chapter 3.

Fig. 4.5 and ***Fig. 4.6*** show typical XRF spectra obtained when performing direct *in situ* measurements on the floor with the hXRF instrument as shown in the photos (***Fig. 4.4***). Although the wear and tear/preservation conditions varied for the different archaeological fragments, ***Fig. 4.5***

shows a lot of similarities between the different spectra, all of which were obtained by measuring on the white pigment on different places. This can be deduced from the similar fingerprint that all spectra have, with the difference that Zn is present or absent.

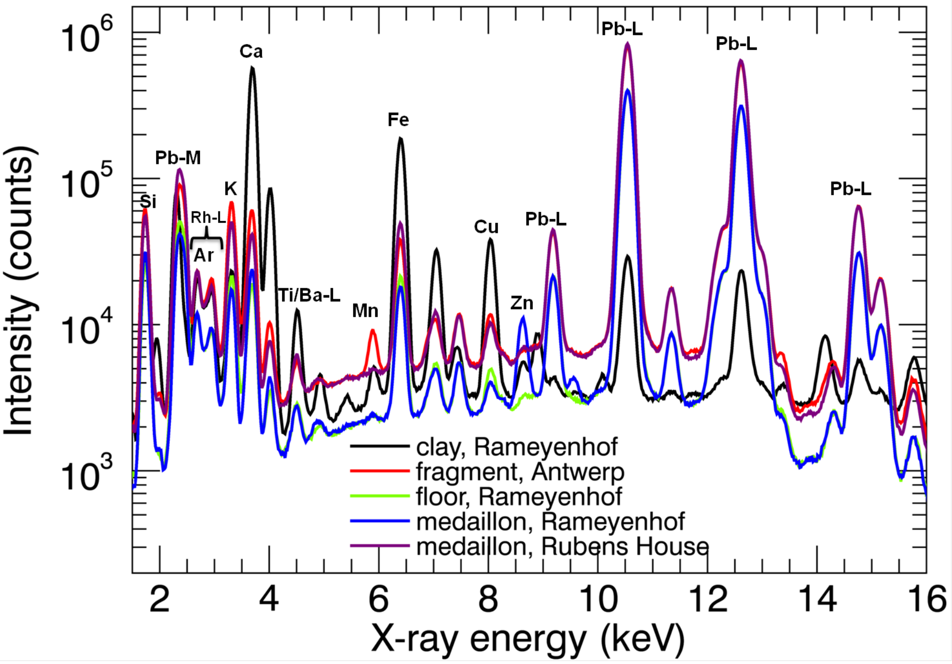

Figure 4.5: *XRF based spectral fingerprints obtained with the handheld XRF spectrometer to characterize Antwerp majolica: similarity between the spectral response of the white pigments is present in all cases.*

Beside the spectral features typically expected from the Rh anode based XRF instrument, such as Rh–K/L scatter peaks, Ar (due to operation in air), the XRF spectral data are dominated by the Pb lines. In the spectral region of the Pb-L lines (9.0-16.2 keV), it is difficult to extract information on elements of which the peaks are expected in that region, for example arsenic in the spectrum measured on the blue pigment. The most intense K_α line of arsenic is totally overlapping with one of the Pb-L peaks. Nevertheless, arsenic is still detected based on the presence of its K_β line. Also, because the detector dead-time cannot be controlled (i.e. tube settings are fixed at 40 kV and 79 μA), so-called sum or pile-up peaks are to be expected from the Pb-L lines, including combinations with other elemental peaks that may appear prominently (***Fig. 4.6***). On the other hand, the detection of Sn and Sb could still be performed on the basis of their K-lines, and the presence or absence of the corresponding L-lines for these elements may provide extra information on the depth of origin of these lines, and indirectly on the layered structure of the majolica floor tiles. For example, compared to measurements on the orange and yellow pigment, the red pigment only shows Sb-K lines indicating that antimony is present in a layer underneath a surface layer(s) to such an extent that the characteristic Sb-L lines could not be detected (***Fig. 4.6*** and ***Fig. 4.7***) [3][14–16].

All above XRF spectra shown in ***Fig. 4.5*** and ***Fig. 4.6*** were processed using an accurate XRF spectrum evaluation software which is crucial to reliably estimate the peak intensities as well as the corresponding background areas besides the correct identification of elements (e.g. distinguishing Ba-L_α or Ti-K_α in clay layer) and to resolve peak overlap, e.g. in case of the blue pigment where

Co-K$_\alpha$ partially overlaps with Fe-K$_\beta$ [12, 13]. Based on the measurements of the tile spectra and the associated discussion above, and combining the obtained results with information available from the literature [17], we can summarize the characteristic elemental constituents and the corresponding probable materials used for the production of the investigated Antwerp majolica floor in ***Table4.1***.

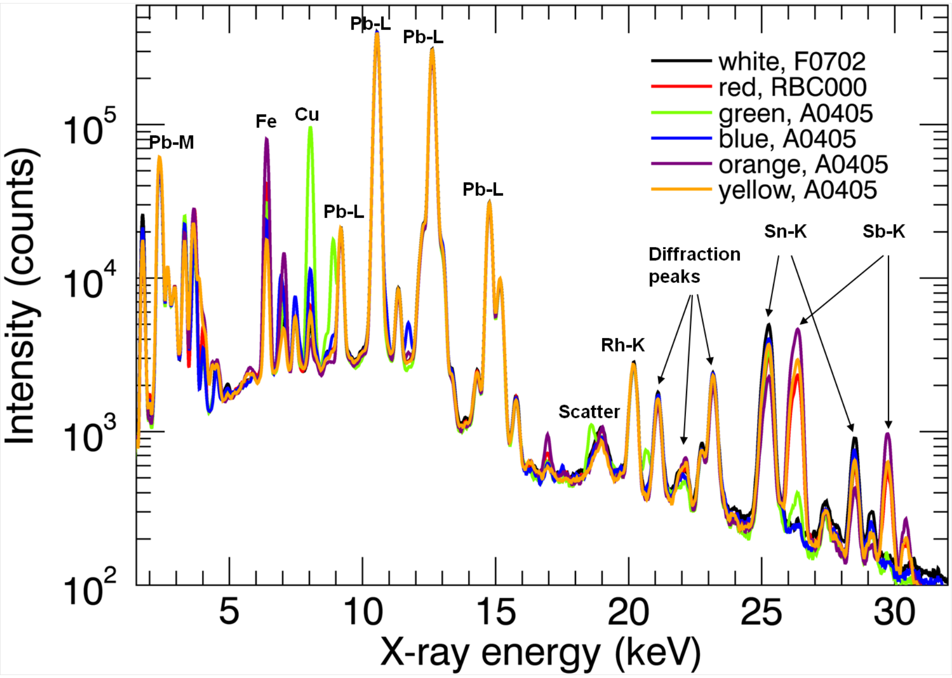

Figure 4.6: *XRF spectra corresponding to different coloured regions, showing the presence or absence of tin and antimony K and/or L lines.*

Table 4.1: *Identification of main characteristic elements based on the XRF measurements and their assignment to the probable materials used.*

Element	Indicated material
Al	Present in feldspars minerals
Si	Quartz added to the *marzacotto* (basis for the white glaze and flux for pigments)
P	Unpurified ashes give a higher content of phosphor
K	Potassium rich deposit in wine casks used as flux in the glaze
Ca	Present in feldspars minerals
Sn	*Flanders tin*: ingredient to opacify the glaze
Pb	Base ingredient to prepare the *marzacotto* (litharge)

4.3.2 Characterization of the used pigments

The pigment layer is made of general components of Antwerp majolica used for the production of the glaze mixed with components to obtain a specific colour. To perform the chemical characterization of the used pigments corresponding to the various colours on the Rameyenhof floor, different small

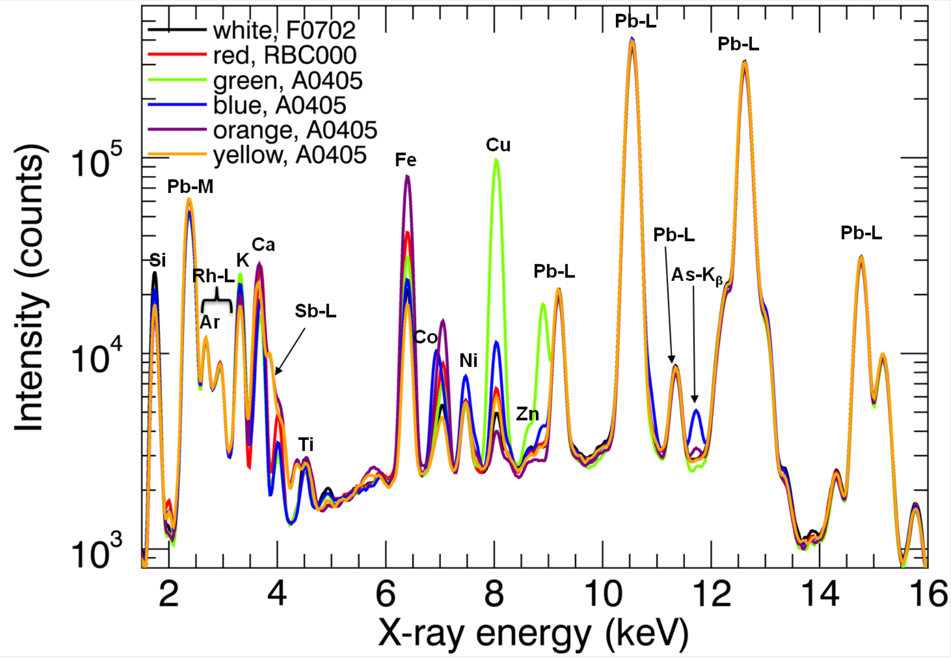

Figure 4.7: *Detail of **Fig. 4.6** to illustrate the difficulties encountered during the identification of certain elemental constituents based on the measured XRF spectra, hampering the characterization of the used coloured pigments.*

areas were analyzed using the hXRF spectrometer and the MArtA instrument. ***Fig. 4.8*** shows a photograph of tile A0405 from the Rameyenhof floor, located in region A, together with detailed optical microscope images. This tile was used for the characterization of the used blue, orange, green and yellow pigments, respectively. For the yellow and orange pigments, both XRF (white stars) as well as the Raman spectrometer (black circle) were used on the same spot, whereas for the blue and green pigments various spots on the same tile were compared to get complete information on these pigments. All XRF spectra of the different pigments were compared with the fingerprint of the white pigment (***Fig. 4.7***) so that the specific elements for a given pigment could easily be identified.

Figure 4.8: *Left: optical image of Tile A0405 (dimension: 127 mm x 128 mm), indicating the places where the handheld XRF (white stars) and MArtA measurements were done (black circles). Right: optical microscope images of the analyzed area in the orange pigment (dimension: 8 mm x 6 mm).*

From the XRF spectra corresponding to the yellow and orange pigments, it is clear that antimony is a characteristic element for both pigments (***Fig. 4.6***). ***Fig. 4.9*** shows the Raman result of the yellow pigment which confirms the use of lead antimonite (spectrum b) in the pigment. In this spectrum, also a small Raman band of SiO_2 (spectrum c) around 484 cm^{-1}, originating from quartz, is present. At a higher wavenumber, around 1400 cm^{-1}, broad features similar to those obtained when recording a spectrum of Paraloïd B72 (spectrum d) can be seen. Paraloïd B72 is an acrylic medium which is a commonly used product for the consolidation and fixation during restoration, and it is likely that the entire floor was covered with this product during an earlier restoration.

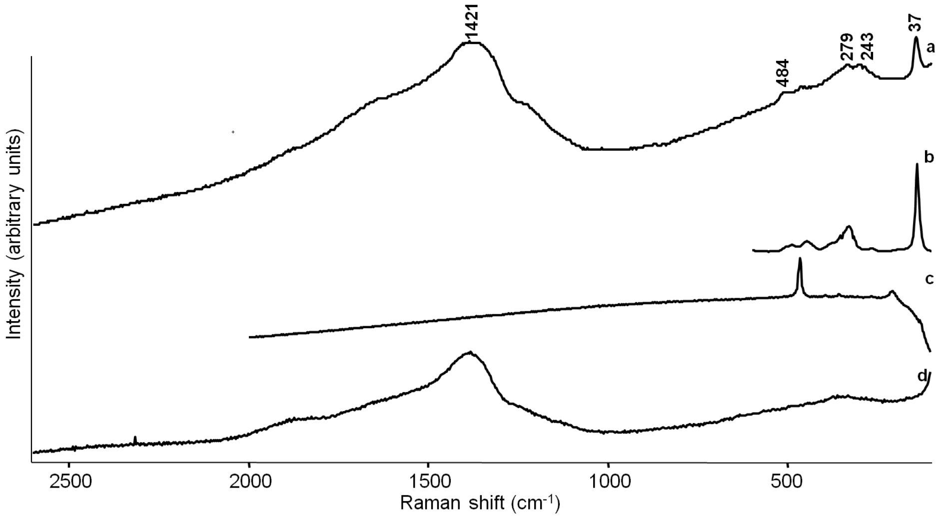

Figure 4.9: *Result of the Raman measurements on the yellow colour (spectrum a) of tile A0405: identification of lead antimonate (spectrum b),* SiO_2 *(spectrum c) and Paraloïd B72 (spectrum d).*

The orange pigment could not be identified with Raman spectroscopy. It is likely that the strong signal of Paraloïd B72 is masking the signal of the orange pigment so that it is not detectable, while the pigment itself is a weak Raman scatterer. Some weak Raman bands are observed at low wavenumbers, but we were not able to identify all Raman bands ***Fig. 4.10***.

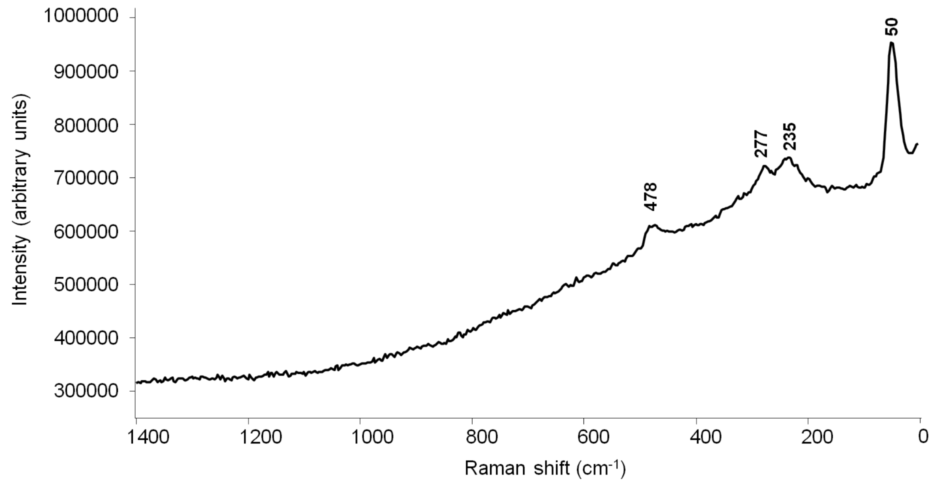

Figure 4.10: *Raman spectrum of the orange colour for which no identification was possible.*

Cobalt, nickel and arsenic are strikingly present in the XRF fingerprints corresponding to the measurements on the blue pigment but the Raman measurements (***Fig. 4.11***) could not confirm these results. The bands at 148 cm^{-1}, 285 cm^{-1} and 333 cm^{-1} originate possibly from PbO, probably from the glaze. The band at 464 cm^{-1} can be related to $CoO.nSiO_2$, but as a band around 917 cm^{-1} is missing, it is more likely that the band indicates the presence of SiO_2. Characteristic for the green pigment is the high intensity of copper and the presence of zinc in the XRF spectra but no confirmation with Raman spectroscopy is possible, mainly due to absorption of the red laser by the green and blue colour. This can be avoided if a second laser with different wavelength is available. Unfortunately this is not the case for the MArtA instrument. The purple pigment, which is measured on another tile (not shown here), located in the C region (C0102), has manganese, arsenic and barium as specific elements. An overview of all characteristic elements present in the different coloured regions together with possible historical pigments is given in ***Table4.2***.

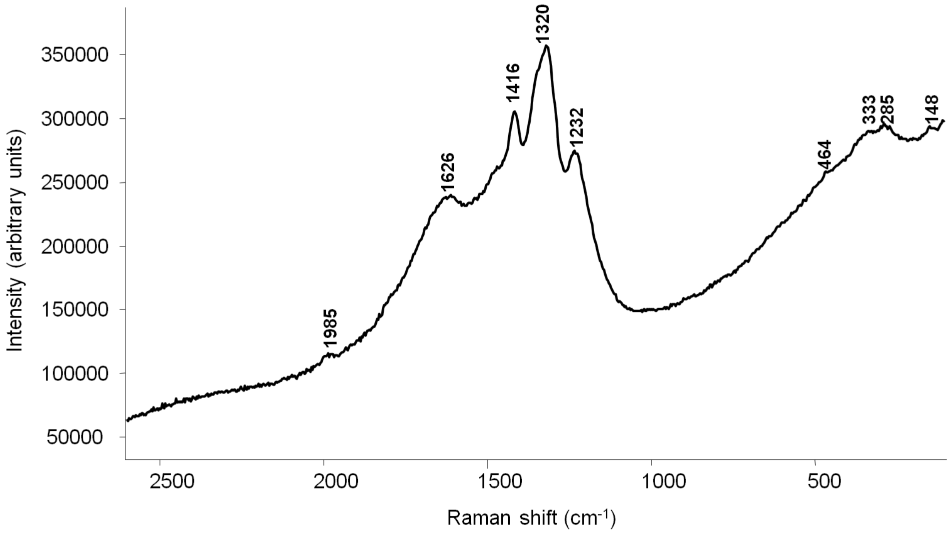

Figure 4.11: *Raman spectrum of the blue colour.*

4.3.3 Comparison between different white glazes

The tiles of the Rameyenhof floor contain several relatively large zones of white pigment. As the handheld instrument has a beam size of ca. 5 mm diameter, it is relatively easy to record spectra of these large zones, without interference of the pigments from adjacent areas. Different white areas were analyzed on the Rameyenhof floor as well as on the medallion kept in the Rubens House museum, and on the archaeological fragments. ***Fig. 4.5*** gives the fingerprints of the white pigments with a high degree of similarity between all spectra with the exception related to the presence or absence of zinc (see ***Fig. 4.12*** until ***Fig. 4.14***, with error bars representing 99% confidence interval). In ***Fig. 4.12***, all the measurements of the white glazes are summarized in a graph, using lead (more specificly Pb-L_α) as an internal standard since lead is the main component of the white glaze layer for all cases. The x-axis refers to the intensities of zinc relative to lead and the y-axis to the ratio of silicon to lead. In this figure, a clear difference between the chapel medallion and the other tiles

Table 4.2: *Summary of the chemical characterization of the colouring agents based on fingerprint studies using the handheld XRF and the MArtA instrument*

Pigment	Characteristic colouring agents (XRF)	Characteristic colouring agents (Raman)	Historical literature
Blue	Co, Ni, Cu, As	Cobalt silicate	Zaffre: an impure ore of cobalt
Green	Cu, Zn	No identification	Ramina or calcined copper
Orange	Sb	Lead antimonite + magnetite	Oxides of iron
Purple	Mn, As, Ba	No identification	Manganese earth or pyrolusite
Red	Fe, Cu, Sb	No identification	Armenian bole
Yellow	Sb	Lead antimonite + magnetite	Lead antimony silicate or naples yellow

in the chapel floor can be observed: the medallion exhibits a much higher relative intensity of zinc. This can be explained by the fact that the medallion in the chapel is made in a later period, probably in the 19th century, when zinc was used as a primary component for the white pigment.

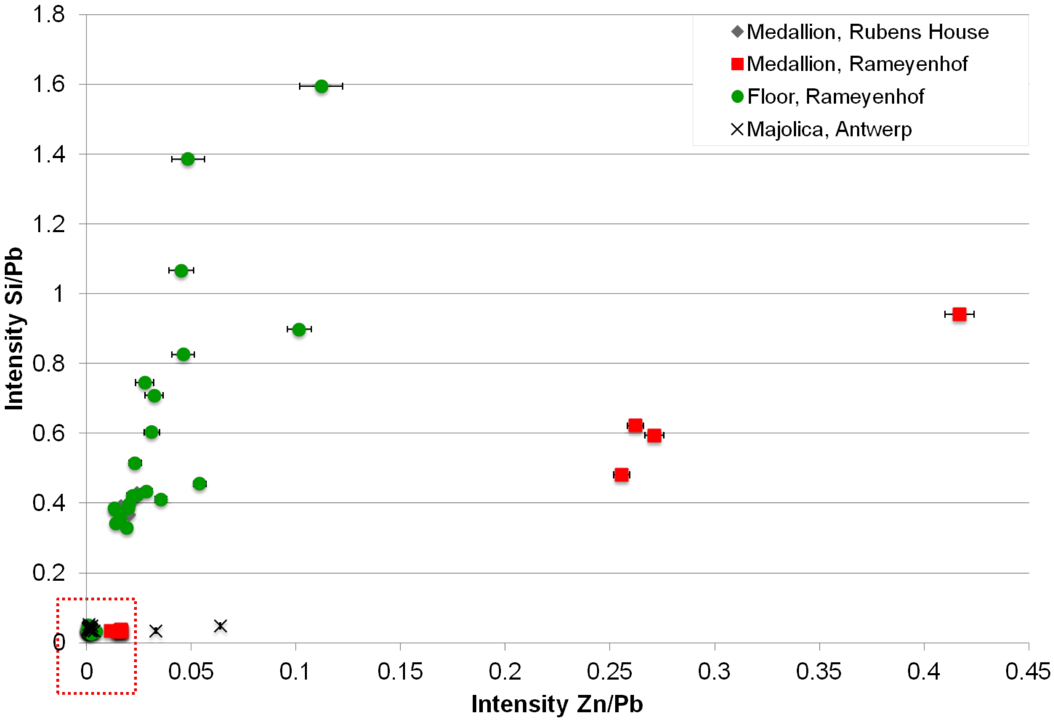

Figure 4.12: *Correlation scatter plots of* Zn_α *and* Si_α *normalized by Pb-*L_α *for all measurements in the white pigment, present in all cases (error bars: 99% confidence interval): The differences in relative elemental intensities between the chapel medallion and all other tiles (except for tile A0902) can be clearly observed.*

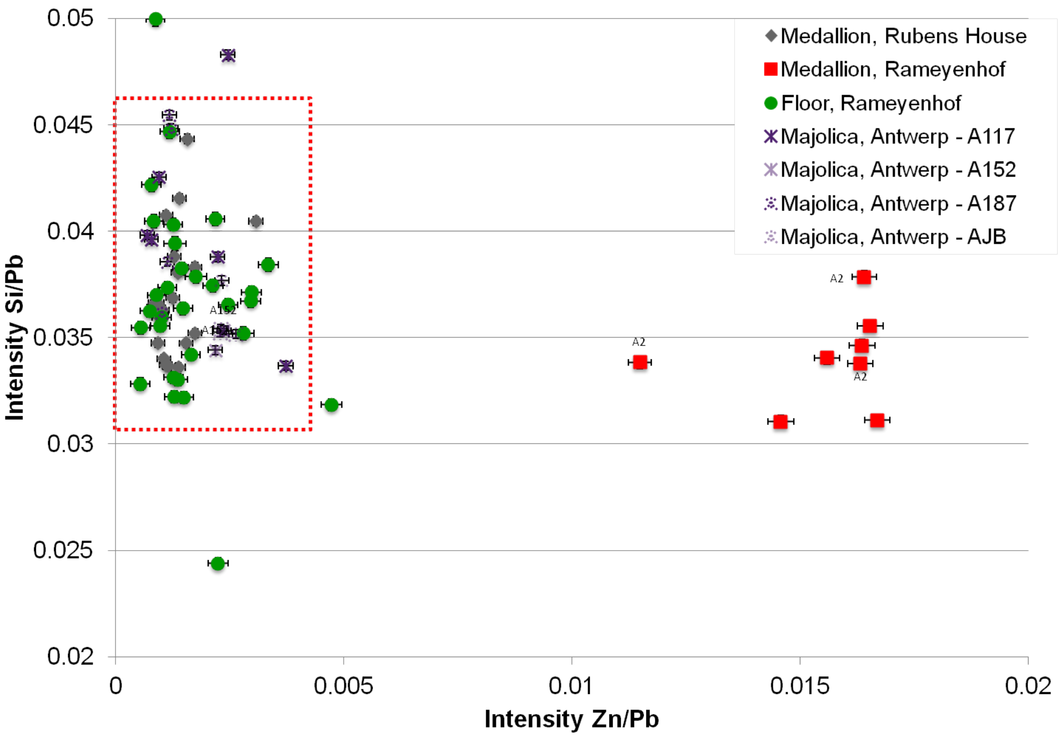

Figure 4.13: *Magnified region corresponding to the red square indicated in* ***Fig. 4.12****.*

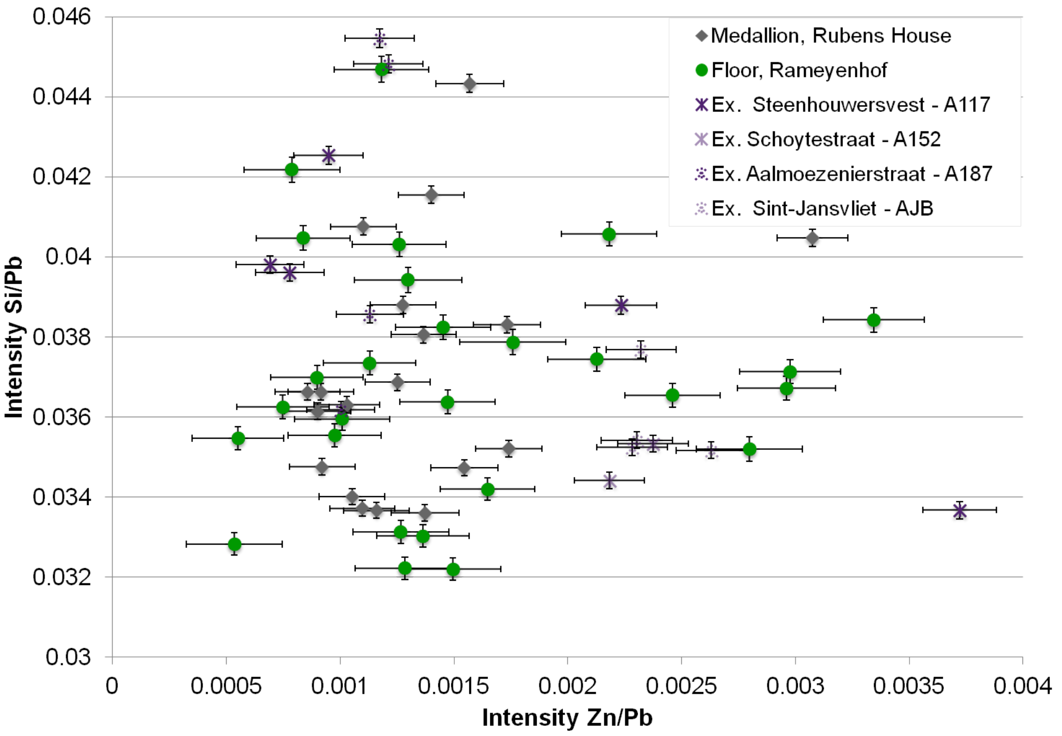

Figure 4.14: *Magnified region corresponding to the red square indicated in* ***Fig. 4.13****.*

Looking more in detail to the data (***Fig. 4.13***) with a Zn/Pb ratio ranging up to 0.02 and Si/Pb ratio up to 0.05, it is possible to see that there is also a difference in the amount of quartz used in the medallion of the Rameyenhof castle compared to the other tiles of the floor, and also compared to the probably original medallion preserved in the Rubens House museum. A remarkable finding suggested by the data obtained from one of the tiles located in region A2, tile A0902 (tile of a row connected to the medallion, see ***Fig. 4.3***), is that this tile has a similar elemental signature as that of the medallion and not the generally different result obtained from the rest of floor. Probably, when removing the chapel medallion, tile A0902 was used as a starting element. This tile is also reconstructed and it has the characteristics of a replica medallion of the Rameyenhof castle. By looking at even more the details in the graph (***Fig. 4.14***), one can hypothesize that the floor in the Rameyenhof castle was manufactured in Antwerp because the data of the archeological fragments overlap with the data of the floor and also with the medallion kept in the Rubens House museum. These findings suggest that the preserved medallion is most likely original, having an Antwerp origin.

4.4 Conclusion

By using a novel combination of portable non-destructive handheld XRF and a mobile Raman spectrometer it was possible to investigate a unique 16^{th} century Antwerp majolica floor located in the Rameyenhof castle (Gestel, Belgium). Based on the XRF measurements, which were acquired using an orthogonal illumination of the majolica floor, we were able to obtain an average elemental signature of the Antwerp majolica tiles from which, combined with the Raman results, it was possible to get information on the pigments used for the decoration of the floor. All these results are very useful for comparisons with historical accounts describing manufacturing details found in the literature. The floor was restored in 2009 and the Raman results indicate that Paraloïd B72 was used to consolidate and fix the floor during the restoration in that period.

In addition to the measurements on the Rameyenhof floor tiles and medallion, another medallion was analyzed (originating from the castle and currently preserved in the Rubens House museum) together with a number of comparable archaeological majolica fragments for comparison. At the floor in the Rameyenhof castle in Gestel and at the medallion in the Rubens House museum, the XRF measurements were always performed perpendicularly to the surface, due to the geometrical constraints involved. From a methodological point of view, this is not a perfect way to retrieve information from a layered sample, since the obtained information represents an integrated signal from the element dependent information depth, originating from different layers. Therefore, the XRF measurements were also performed on the archaeological fragments using the same geometry. On the other hand, these fragments could also be analyzed across their cross-section using scanning micro-XRF instrumentation, and the comparison of these results could be used to validate the XRF measurements.

Based on our experiments, it was possible to compare the measurements performed using XRF on the floor tiles and Antwerp majolica fragments and to investigate if the floor was manufactured according to production methods used to produce traditional Antwerp majolica. When using the intensity of lead as an internal standard, and plotting the intensity of zinc relative to the intensity of silicon, a difference between the Chapel medallion and the rest of the measurements can be seen.

This can be explained by the use of a remake of the medallion for the Rameyenhof floor in which zinc is a main elemental constituent in case of the white pigment, and not as a substitute as in case of 16^{th} century Antwerp majolica. Our results also show a difference in the use of quartz: the chapel medallion exhibits less quartz compared to the floor and to the Rubens House medallion. Finally, it is observed that the investigated castle floor tiles and Rubens House medallion have essentially identical elemental fingerprint to that of the Antwerp majolica fragments, therefore the medallion stored in the Rubens House museum can be regarded as the original one.

Bibliography

[1] F. Caignie, *De majolica tegelvloer in de kapel van kasteel Rameyenhof te Gestel.* Caignie, Frans, 2009.

[2] A. Zucchiatti and I. Katona, "The 'Della Robbia blue': a case study for the use of cobalt pigments in ceramics during the Italian Renaissance," *Archaeometry*, vol. 1, no. May 2005, pp. 131–152, 2006.

[3] M. Tite, "The production technology of Italian maiolica: a reassessment," *Journal of Archaeological Science*, vol. 36, pp. 2065–2080, Oct. 2009.

[4] R. Padilla, O. Schalm, K. Janssens, R. Arrazcaeta, and P. Van Espen, "Microanalytical characterization of surface decoration in Majolica pottery," *Analytica Chimica Acta*, vol. 535, pp. 201–211, Apr. 2005.

[5] A. Guilherme, S. Pessanha, M. Carvalho, J. dos Santos, and J. Coroado, "Micro energy dispersive X-ray fluorescence analysis of polychrome lead-glazed Portuguese faiences," *Spectrochimica Acta Part B: Atomic Spectroscopy*, vol. 65, pp. 328–333, Apr. 2010.

[6] A. Caiger-Smith, *Tin Glaze Pottery in Europe and the Islamic World: The Tradition of 1000 Years in Maiolica, Faience and Delftware.* Faber & Faber, first edit ed., 1973.

[7] C. Dumortier, *Céramique de la Renaissance à Anvers. De venise à Delft.* Racine Lannoo, 2002.

[8] H. Niçaise, "XVIIe eeuwsche Antwerpsche of Nederlandsche tegels," in *Jaarboek van Antwerpens oudheidkundige kring*, pp. 36–42, Het Rijksarchief in België, deel 10 ed., 1934.

[9] M. J. Hughes and D. Gaimster, "Neutron activation analyses of maiolica from London, Norwich, The Low Countries and Italy," in *Maiolica in the North, the archaeology of tin-glazed earthenware in North-West Europe c. 1500-1600* (D. Gaimster, ed.), British Museum Press Occasional Paper Nr. 122, 1999.

[10] K. Janssens, G. Vittiglio, I. Deraedt, A. Aerts, B. Vekemans, L. Vincze, F. Wei, I. Deryck, O. Schalm, F. Adams, A. Rindby, A. Kn, A. Simionovici, and A. Snigirev, "Use of Microscopic

XRF for Non-destructive Analysis in Art and Archaeometry," *X-RAY SPECTROMETRY*, vol. 91, no. July 1999, pp. 73–82, 2000.

[11] P. Vandenabeele, T. L. Weis, E. R. Grant, and L. J. Moens, "A new instrument adapted to in situ Raman analysis of objects of art.," *Analytical and bioanalytical chemistry*, vol. 379, pp. 137–42, May 2004.

[12] P. Van Espen, K. Janssens, and J. Nobels, "AXIL-PC: software for the analysis of complex X-ray spectra," *Chemometrics Intell. Lab. Syst.*, vol. 1, pp. 109–114, Nov. 1986.

[13] B. Vekemans, K. Janssens, L. Vincze, F. Adams, and P. Vanespen, "Analysis of X-Ray-spectra by iterative least-squares (AXIL) - New developments," *X-Ray spectrometry*, vol. 23, no. 6, pp. 278–285, 1994.

[14] G. Padeletti and P. Fermo, "Italian Renaissance and Hispano-Moresque lustre-decorated majolicas: imitation cases of Hispano-Moresque style in central Italy," *Applied Physics A: Materials Science & Processing*, vol. 77, pp. 125–133, June 2003.

[15] K. Yu and J. Miao, "Characterization of blue and white porcelains using the Mn/Fe ratio from EDXRF, with particular reference to porcelains of the Xuande period (1426 to 1435 A.D.)," *Applied Radiation and Isotopes*, vol. 51, pp. 279–283, Sept. 1999.

[16] C. Fortina, I. Memmi Turbanti, and F. Grassi, "Glazed Ceramic Manufacturing in Southern Tuscany (Italy): Evidence of Technological Continuity Throughout the Medieval Period (10Th14Th Centuries)," *Archaeometry*, vol. 1, pp. 071024000902003–???, Oct. 2007.

[17] C. Piccolpasso, R. Lightbown, and A. Caiger-Smith, *The three books of the potters art: a facsimile of the manuscript in the Victoria and Albert Museum, London.* London: Scolar Press, 1980.

Chapter 5: Non-destructive in situ study of “Mad Meg” by Pieter Bruegel the Elder using mobile XRF/XRD and Raman spectrometers

Lien Van de Voorde, Jolien Van Pevenage, Kaat De Langhe, Robin De Wolf,
Bart Vekemans, Laszlo Vincze, Peter Vandenabeele, Maximiliaan Martens

Spectrochimica Acta Part B, 97, 1-6 (2014)

The two foregoing chapters (chapters 3 & 4) demonstrate the usefulness of a multi-method approach based on the application of various analytical techniques for the study of ceramic based cultural heritage objects. The obtained data in all these cases correspond to the use of different types of analytical instruments which, in combination with appropriate data treatment, help us revealing up to now hidden details regarding the studied materials. In this chapter, another type of cultural heritage object, namely a painting exhibited in a museum, is examined using also a combination of non-destructive portable instrumentation. "Mad Meg", a figure of Flemish folklore, is the subject of a famous oil-on-panel painting by the Flemish renaissance artist Pieter Bruegel the Elder, exhibited in the Museum Mayer van den Bergh (Antwerp, Belgium). This chapter reports on the in situ chemical characterization of this masterpiece and the verification of two important historical iconographic hypotheses concerning the economic way of painting by Brueghel.

5.1 Introduction

The analysis of artworks and cultural heritage artifacts benefits significantly from recent technological developments and increased access to portable or mobile analytical scientific instrumentation allows the *in situ*, non-destructive chemical analysis of precious objects of art due to the flexible nature of such instruments. When analyzing precious easel paintings, it is typically requested to obtain as much information on the artwork as possible using non-invasive spectroscopic methods, without any physical contact with the object to be analyzed and without their displacement. As a direct consequence of this, mobile analytical instruments can be used for *in situ* and non-destructive analysis of the object. Obviously, it is favorable to combine the results from different, complementary analytical techniques. This is a typical approach that was used to investigate important artworks, during extended research campaigns[1–6]. In some cases it is sufficient to apply two analytical methods in a combined fashion, such as Raman spectroscopy and X-ray fluorescence analysis [7] or Raman spectroscopy and laser-induced breakdown spectroscopy [8].

This work describes the investigation of Mad Meg ("Dulle Griet") by Pieter Bruegel the Elder (1561) performed in the Museum Mayer van den Bergh (Antwerp, Belgium), using currently available state-of-the-art portable analytical instrumentation. The instrumentation included the transportable MArtA (Raman) spectrometer, the hXRF spectrometer and a portable X-ray fluorescence/X-ray diffraction or XRF/XRD instrument (Assing, Surface Monitor). The novelty of the latter portable XRF/XRD instrumentation is represented by the combination of energy-dispersive XRF spectroscopy with goniometer based X-ray diffraction (XRD) data collection. This is different from most of the commercially available systems, which are based on CCD-based non-dispersive XRD methodology. During this PhD work, the overall characterization of this instrument was done and more details about these results and the application of this portable XRF/XRD instrument can be found in chapter 6.

The use of each of these instruments represents a specialized analytical approach or methodology, enabling the retrieval of specific types of analytical information from the investigated material, including atomic, molecular and structural data. Beside the differences in the type of information obtained by each instrument, this combination allows multi-scale analysis of the areas of interest ranging from 50 μm^2 until 50 mm^2. This set of instrumentation enables a multi-methodological approach that has, , as already mentioned earlier, the definite advantage of confirming and/or complementing individual analytical results obtained by the separate techniques and therefore enhancing the data interpretation. Although each of the portable equipment may differ in terms of practical handling and typically offer somewhat reduced analytical performance compared to its laboratory equivalent used under optimized conditions, in most cases precious and delicate works of art demand investigation on-the-field, requiring the scientific equipment to be transported to the location where the artwork resides.

The study of Mad Meg in the Museum Mayer van den Bergh required a detailed planning for the application of the suite of spectrometers described above. This chapter provides a thorough description and evaluation of the applied multi-spectroscopic methodology, characterized by specific working methods for each instrument which were used to retrieve chemical information from various positions of interest on the artwork. The obtained information could be linked to art technical, art historical and conservation related questions.

Earlier research on the Mad Meg painting with high resolution macrophotography and the study of the painting through visual inspection combined with digital infrared reflectography (to visualise the underdrawings of the painting) and UV-fluorescence photography (to study overpaintings or retouchings) gives general information about the stylistic composition of the panel, layer build-up of the painting, the used painting techniques, as well as the preliminary drawing underneath the paint layers. The remarkable use of colours (e.g. faded blue zones in the dress of Mad Meg and in the rest of the painting) raised questions related to the use of pigments. Another interesting question is whether the preliminary compositional lay-out re-appears in the final painting as can be seen by the visitors of the museum. [9]. However, the above described methods used in earlier investigations did not allow to draw solid conclusions concerning the nature of the applied paint layers, as the portable techniques for pigment analyses were not available yet. The study described in this chapter has been set up with the specific goal to obtain elemental/molecular information on the pigments in order to be able to identify this pigments. From a technical point of view, Pieter Bruegel the Elder made the preliminary drawing and the subsequent light-dark distribution in such a way that he was able to finish the painting in a very economical manner. This led to a number of research questions, such as: what are the consequences with respect to the type of pigments used, the thickness of the layers and the difference in type of pigments applied for the same colour in different areas of the painting. One central question was why the central Mad Meg figure was painted using pigments that quickly deteriorated, which had a major shift in the colour balance of the painting as a consequence.

5.2 Experimental

The panel painting representing Mad Meg is exhibited in the Museum Mayer van den Bergh in Antwerp (Belgium), hanging at a wall in an acclimatized room, approximately 1.5 m behind a knee-high fence that prevents visitors to approach it too closely. It spans over a height starting approximately from 1.4 m up to 2.6 m, inclining ca. 8° forward. As any repositioning of the artwork within the museum was discouraged, the *in situ* investigation of this artwork required specific adaptations and additions to the mounting elements of the portable analytical instrumentation in order to be able to safely position the probe heads in the proximity of the surface of the painting. The used mobile analytical instrumentation were as follows: Dino-Lite digital microscope, hXRF spectrometer, XRF/XRD Surface Monitor, and the MArtA spectrometer. ***Fig. 5.1*** show (respectively) snapshots of the hXRF spectrometer and the MArtA probe installed for the *in situ* analysis. The flexible design of special tripods/stands for each of the four devices allowed easy and safe positioning of the device probe-heads aiming at the positions of interest on the artwork, covering a suitable height range and easily compensating for the 8° inclination angle of the painting, and as such, allowed real *in situ* measurements (i.e. without any repositioning of the artwork as requested by the museum). In all cases the forward motion of a probe head towards the painting surface was the last physical movement when positioning for the next point of interest (POI).

Figure 5.1: *Photographs illustrating the in situ analysis using a set of portable scientific instruments. Left: the Olympus Innovx-Delta handheld XRF spectrometer mounted on a dedicated positioning system. Right: Mobile Art Analyser (MArtA) Raman-spectrometer (also shown is the extra shielding for darkening to avoid interference of ambient light with the Raman signal).*

All experiments related to this work were performed during the weekly closing day of the museum, i.e. on Monday, over a period of 6 weeks. As a first step of the applied methodology, based on results of the previous research (macrophotography, digital infrared reflectography and visual inspection), high resolution digital images of the regions of interest were taken to establish a roadmap with a number of points of interests (POIs). These POIs were used as preparation for the investigation by a group of specialists using the above mentioned analytical instrumentation (***Fig. 5.2***). Next to the limitation in available time per measuring session, other reasons for not using different equipment at the same time were as follows: (i) each instrument needs careful positioning in front of the painting and is operated by different scientists, (ii) the use of X-ray methods limits the access to the artwork during the measurements (in time and space) due to reasons of radiation safety regulations, (iii) Raman equipment needs a darkening of the surrounding area inhibiting safe management of other equipment.

Figure 5.2: *Establishment of the roadmap that guided the measurements using the different portable analytical instrumentation. POIs a-d illustrate specific pigment analysis cases given in Table 2: three POIs "a" related to white colour (bag and dress of Mad Megs dress, and the eggshell at the top of the painting), two POIs "b" to study the flesh tone colour (nose Mad Meg and the "milk soup eater" on the left bottom corner, two POIs "c" showing pink colour(shield on the right bottom and the bag just below the boat), and POIs "d" to illustrate the use of different colours to represent water.*

The high resolution digital images were taken using a 5 Mpixel Dino-Lite digital microscope (Dino-Lite Europe, The Netherlands, see ***Fig. 5.3***). The magnification was set to 50x in order to obtain a field of view of 8 mm by 6 mm, compatible with the macroscopic nature of analysis by the X-ray based instrumentation. ***Fig. 5.3, right*** illustrates a resulting field of view which reveals features that could not be seen by the naked eye, i.e., showing the brush strokes and craquelure pattern in detail. One disadvantage of the applied digital microscope is that a colour correction strategy based on the use of a calibration colour card (as used in conventional photography) is not available in a sub-centimeter format. Nevertheless, combined with the information from the first investigations [9], our research questions could be formulated and consequently, the areas for the analyses could be determined with sufficient accuracy.

The XRF measurements were performed using the commercial hXRF Olympus InnovX Delta instrument, described in detail in 2.3.5, attached to a positioning system on a tripod (***Fig. 5.1***).

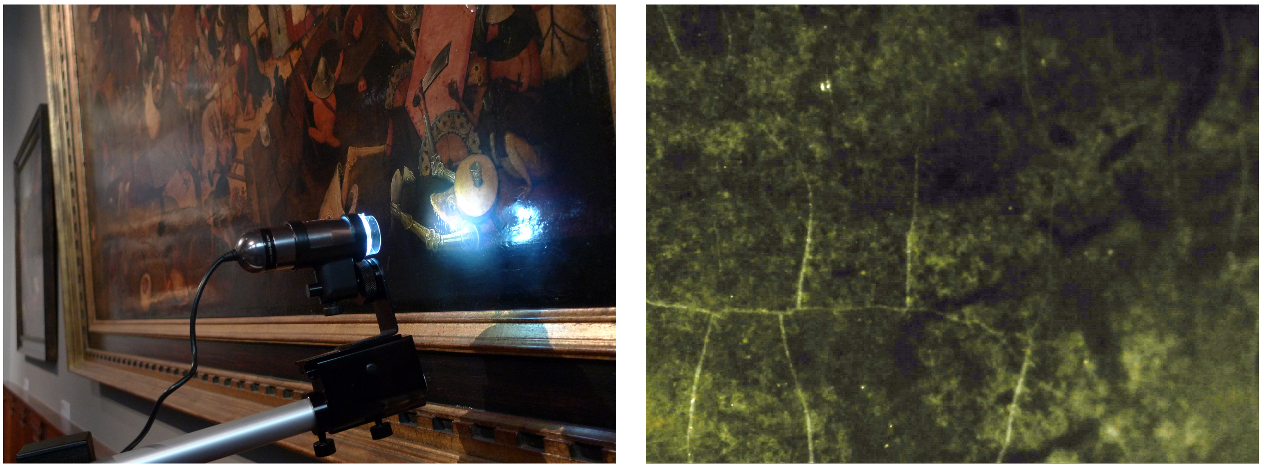

Figure 5.3: *Left: The Dino-Lite digital microscope. Right: analyzed area (POI 2 in* ***Fig. 5.2****) on the blue dress of the central figure "Mad Meg".*

The experiments were performed in air with each POI measured for 300 s (life time), tube voltage of 40 kV and current of 79 μA. To position the probe head relative to the point of interest, visible marks indicating the position of the beam on the probe head were used. Because it was not allowed to touch the painting, we were not able to use the extra transparent polyester sheet with marks to have the best alignment fit between marks of the instrument head and the examined POI. So only centering of the probe head marks on the spot of the painting that had to be analyzed was applied, achieving a satisfactory level of positioning. During these measurements, we made use of a remote connection to a portable PC which allowed to control and to monitor the actual XRF measurement from safe distance. The collected spectra were processed using the dedicated XRF spectrum evaluation software AXIL (see 2.3.6 for more detailed working principles of this software).

Combined XRF/XRD experiments were performed by using Assing's Surface Monitor. This instrument uses the Bragg-Brentano θ:θ methodology [10, 11] and was equipped with a Cu anode based X-ray tube set to 28 kV and 250 μA in combination with an Amptek X-123 Si-Pin diode detector. In order to establish the XRD calibration, a NIST SRM 660b LaB_6 powder sample, sandwiched between two thin ultralene membranes (Premier, Lab Supply company) stretched over a polymer cup was measured. The XRD measurements were performed on POIs following the pre-determined roadmap. The applied diffraction angle varied from 40° (the minimum angle was always verified in order to avoid touching the painting) until 90° in steps of 0.2°, measuring 5 s per step with detector slits of 2 mm × 0.5 mm and, on the x-ray source, pinholes of 2 mm × 1 mm providing information from a sample area of 13 mm wide 3.5 mm height. The probe head was positioned by adjusting the tripod using the laser interferometer in order to place the probe head ca. 94.5 mm away from the painting. The measurements were aided by a webcamera mounted on a flexible arm, delivering an inclined top-view of the probe head and the sample, so that also all movements could be monitored by means of the controlling portable PC at a safe distance from the instrument. The data were processed by means of the XRF/XRD software package delivered with the instrument (XRD match with International Centre for Diffraction Data (ICDD) database) [12]. While acquiring an XRD pattern using the Surface Monitor, an integrated XRF sum-spectrum (at the end of the measurement) was simultaneously retrieved to constrain the search in the ICDD databank. These XRF sum-spectra were not used for the final elemental analysis of the measured pigment. For the elemental analysis, additional XRF information was collected by the hXRF instrument because of the higher quality of the XRF spectra due to its optimized X-ray tube (Rh-tube for handheld compared with Cu-tube in the Surface Monitor) and detector (SDD as opposed to Si-PIN diod detector) characteristics.

The Raman measurements, using the MArtA spectrometer, were executed using a 785 nm diode laser source, having a spot size of 50 μm at the painting surface, using a measuring time between 3 and 20 seconds and accumulations between 20 and 360 using a laser power of 19 mW (***Fig. 5.1***).

Table5.1 gives an overview of the number of POIs analyzed using the three instruments, together with the estimated penetration/information depth values. Also given are the size/weight of each instrument used in the multi-technique methodology.

Table 5.1: *Overview of specifications (amount of measured POIs, penetration depth and the size/weight) of the instruments used in the multi-technique methodology.*

	Handheld XRF	Surface Monitor	MArtA
# measured POIs	25	4	10
Size of the instrument	26.0 cm x 24.0 cm x 9.0 cm	/	67.0 cm x 47.0 cm x 35.0 cm
	1.5 kg	1.84 kg	27.5 kg
Penetration depth	± 100 μm	± 100 μm	surface layer

5.3 Results: Analyses of pigments applied

Previous research on this painting essentially focused on the surface layer (the visible painting) and on the underdrawing (using infrared reflectography) without obtaining information about the used pigments in underlying layers. With the combined use of X-ray based techniques, characterized by large information-depth values, and Raman technique it was possible to unwrap hidden information on the pigments used in the underlying layers as well. In the following, a discussion concerning used pigments and painting style is shown, based on a specific selection of all measured POIs described in the roadmap and indicated with numbers in ***Fig. 5.2***

5.3.1 Blue pigments

Fig. 5.4 shows the XRF response (sum spectrum) corresponding to the measurements on POIs 1 and 2 (***Fig. 5.2***), using the handheld XRF-spectrometer, providing an elemental fingerprint of the blue pigment present in the measured areas. The spectral fingerprint of the blue pigment contains a high intensity Co-signal indicating the use of potential pigments, such as smalt (65% SiO_2 + 15%

K_2O + 10% CoO + 5% Al_2O_3), cerulean ($CoO.nSnO_2$) or cobalt blue ($CoO.Al_2O_3$) for the blue colour. Combined with the available historical information and results from previous research [9], the use of smalt is more reliable then the use of one of the other suggested blue pigments. Raman spectroscopy in principle should be able to help with ultimate identification of the used blue pigment, but due to the presence of a thick varnish layer, the Raman signals were overwhelmed by fluorescence and no clear Raman bands are detectable. This can be seen in ***Fig. 5.5*** measured in the blue dress of "Mad Meg".

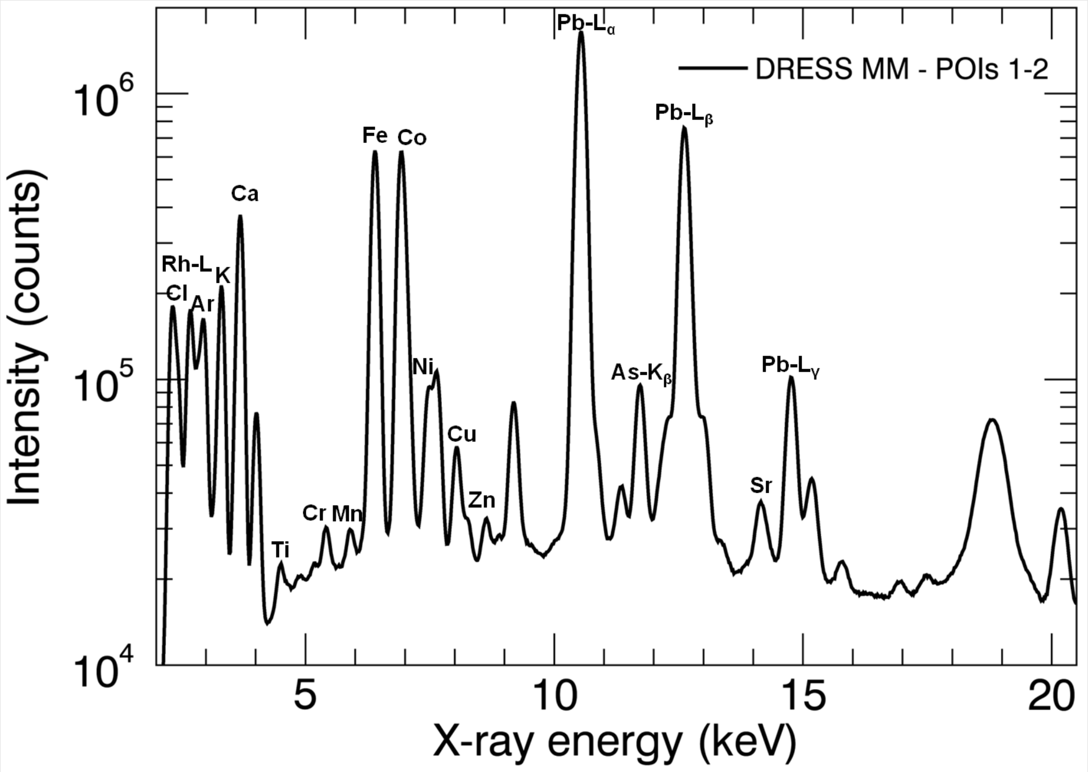

Figure 5.4: *Obtained XRF fingerprint related to blue areas of the painting: summed spectrum of POI 1 and POI 2 (see **Fig. 5.2**).*

An important historical iconographic assumption, which can be confirmed based on these measurements, is related to the hypothesized economical manner of painting by Brueghel. ***Fig. 5.6*** compares the XRF spectral response of the blue pigment present on the central "Mad Meg" figure and on the blue dress worn by the woman indicated by POI 3 (***Fig. 5.2***). POIs 1-3 are chosen because of the high importance of the central figure in order to verify the assumption that this central figure is painted using more expensive pigments than those detectable from other blue areas of the painting. ***Fig. 5.6*** shows four XRF spectra which are essentially the same: all show the strong presence of Co, which can be linked to the use of a cheaper smalt blue pigment instead of, for example, a more expensive ultramarine ($Na_8 - 10Al_6Si_6O_24S_2 - 4$) pigment, that would be expected for a painter of Bruegels calibre. This is a clear indication of the economical style of painting by Pieter Bruegel.

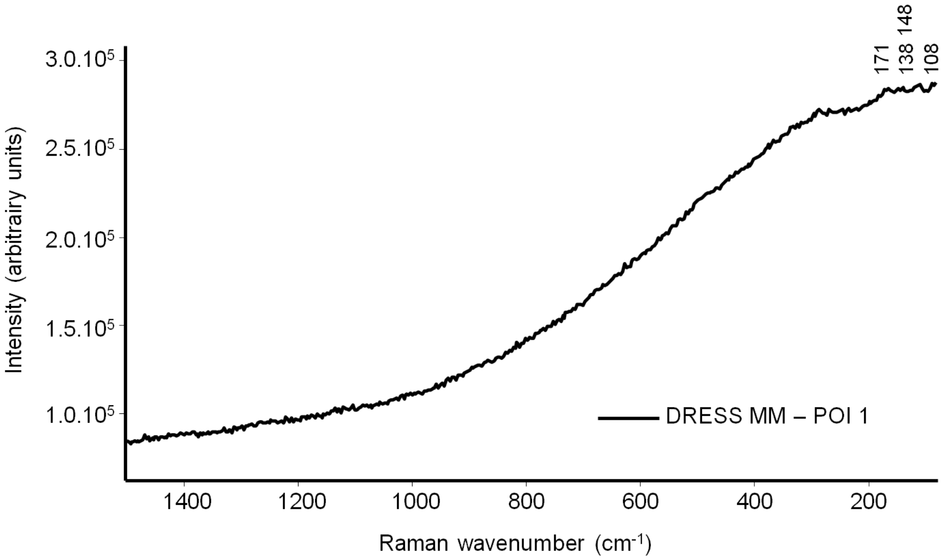

Figure 5.5: *Obtained RAMAN fingerprint related to blue areas of the painting which is overwhelmed by fluorescence background, resulting in insufficiently detected Raman bands. Only some very small bands are observed in the region of 108-171 cm^{-1}, based on which pigment identification is nearly impossible.*

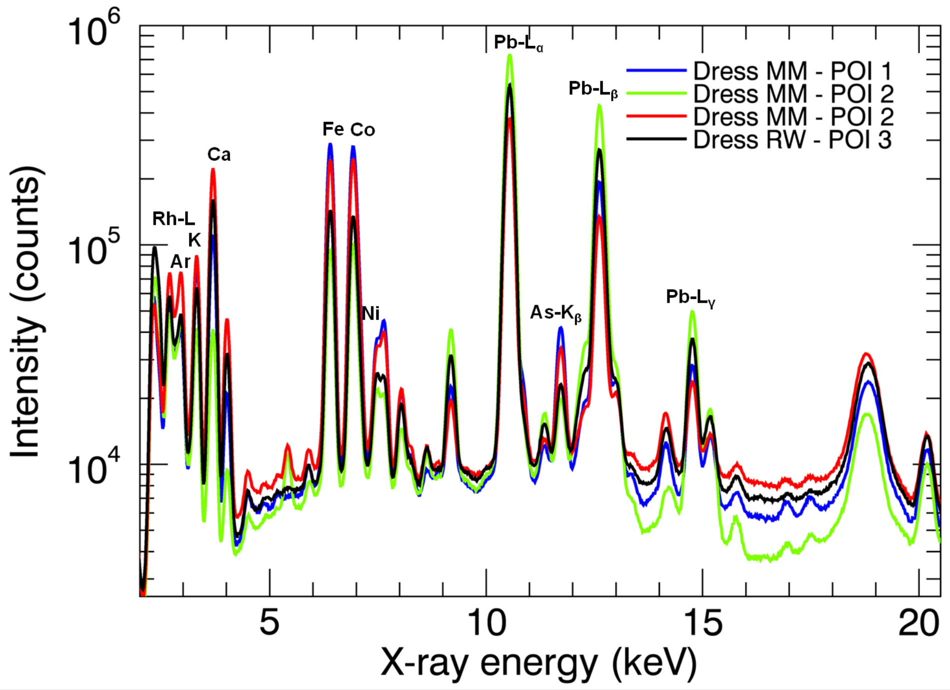

Figure 5.6: *XRF spectra obtained from the dress of Mad Meg (POIs 1, 2 in **Fig. 5.2**) and the dress of the woman in a crowd of people on the right (POI 3 in **Fig. 5.2**).*

5.3.2 Red pigments

For evaluating the red coloured areas using X-ray based techniques, POIs 4-6 (***Fig. 5.2***) were selected for further investigation. Using Raman spectroscopy, we were not able to measure on these POIs, because of the presence of the varnish layer. Fortunately, another POI with red colour present had less varnish cover (POI 7, ***Fig. 5.2***), which provided valuable Raman results. Detailed information on these red coloured areas could be obtained using the results of the red pigment measurements with the different techniques. The results of the XRF measurements (see (***Fig. 5.7***) indicate the presence of calcium (that probably originates from the preparation layers) and lead (lead white in the imprimatura or from red lead minium pigment), as well as mercury and sulfur that are typical for red pigments. The latter suggests the use of vermillion. These XRF results could be easily confirmed by the Raman technique because the peaks present in the Raman spectrum, originating from the surface layer, are typical for vermillion (see ***Fig. 5.8***).

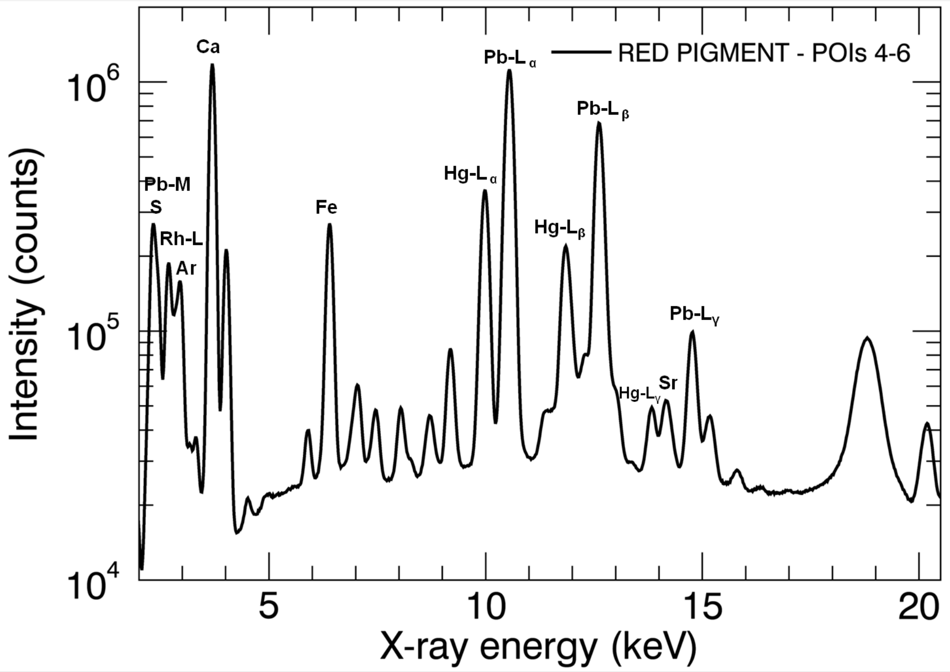

Figure 5.7: *Identification of red pigment using the XRF sum-spectrum corresponding to measurements on the sleeves of "Mad Meg" (POIs 4 and 5) and on the helmeted creature climbing the bridge (POI 6).*

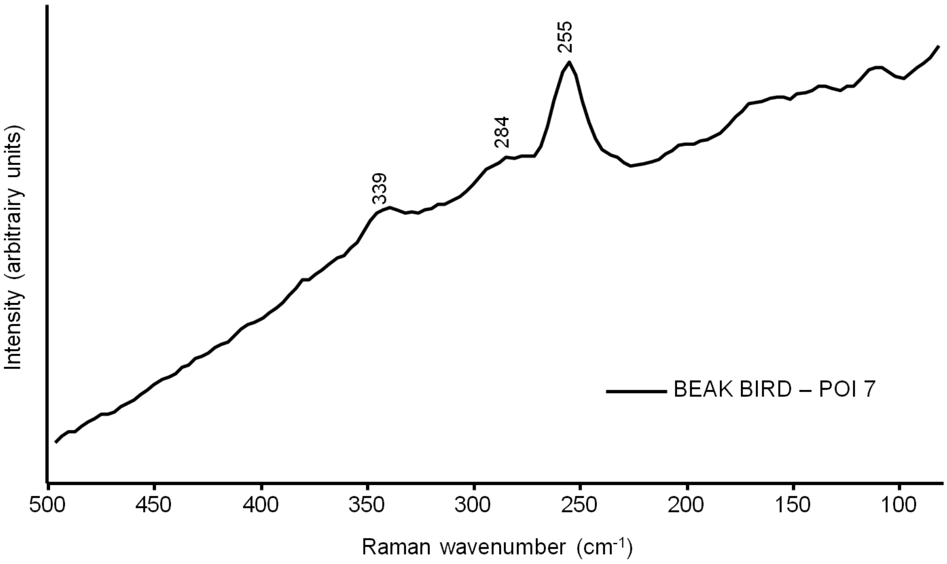

Figure 5.8: *Confirmation of the XRF result on the red pigment by Raman spectroscopy obtained from the red beak of the bird (POI 7), corresponding to vermillion.*

5.3.3 Green pigments

Fig. 5.9 shows the difference between the XRF measurements on the boat (POI 8), on the blue pigment of the dress of the “Mad Meg” figure and on green pigments from different areas on the painting. The motivation for this comparison is related to another important historical iconographic hypothesis concerning Mad Meg, suggesting that the boat (POI 8, ***Fig. 5.2***) that appears towards the top of the painting also looks as if it was painted using the cheaper blue glaze (probably smalt). If it turns out to be a blue pigment by the XRF-fingerprint, it could be a reference to the “blauwe schuit”, the blue boat, which is a known concept in the literature of the time as being the “ship of fools” [13]. As shown in ***Fig. 5.9***, by the XRF elemental fingerprint corresponding to the measured points on the boat, the used pigment here is not the same as the blue smalt pigment used in the other areas of the painting. Its chemical signature is more related to the elemental fingerprint of the green pigment used in other areas of the painting, so the boat was not meant to be painted blue, and therefore it probably does not symbolize the “blauwe schuit”.

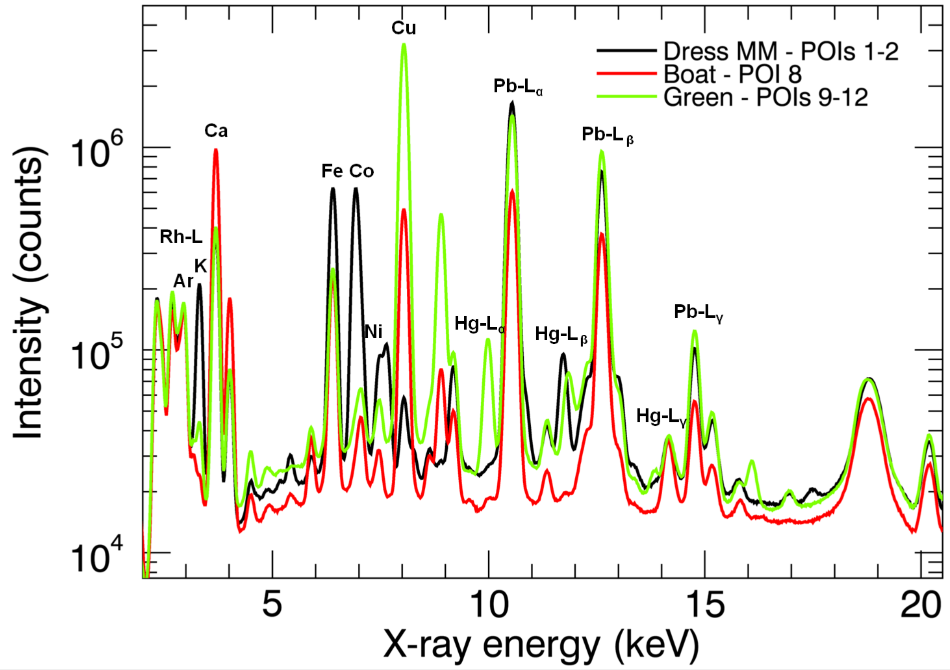

Figure 5.9: *Comparison of XRF fingerprints of the boat, the dress of “Mad Meg”, and the summed fingerprint of green pigments used (boat: POI 8 in **Fig. 5.2**).*

To characterize this green pigment, and thus also the pigment used for painting the boat, different POIs containing green pigments are measured using the handheld XRF instrument (POIs 9-12, ***Fig. 5.2***). The obtained XRF spectra are shown in ***Fig. 5.10***, exhibiting high K and L-line intensities for Cu and Pb: the lead signal originates from the lead white containing imprimatura layer which Pieter Bruegel used as an overall binding coloured ground on the preparation, while the copper XRF signal, combined with information of previous research [9], is linked to the green copper resinate pigment. The latter means that the “blue” boat is probably painted using a green copper resinate pigment instead of the blue smalt pigment. The presence of azurite ($Cu_3(CO_3)_2(OH)_2$) as blue pigment cannot be totally excluded, but is unlikely as this pigment was not detected in any other blue area of the painting. The Raman results should be able to exclude this, but due to the presence of the varnish layer on all green areas, all Raman signals in this zone were overwhelmed by fluorescence background.

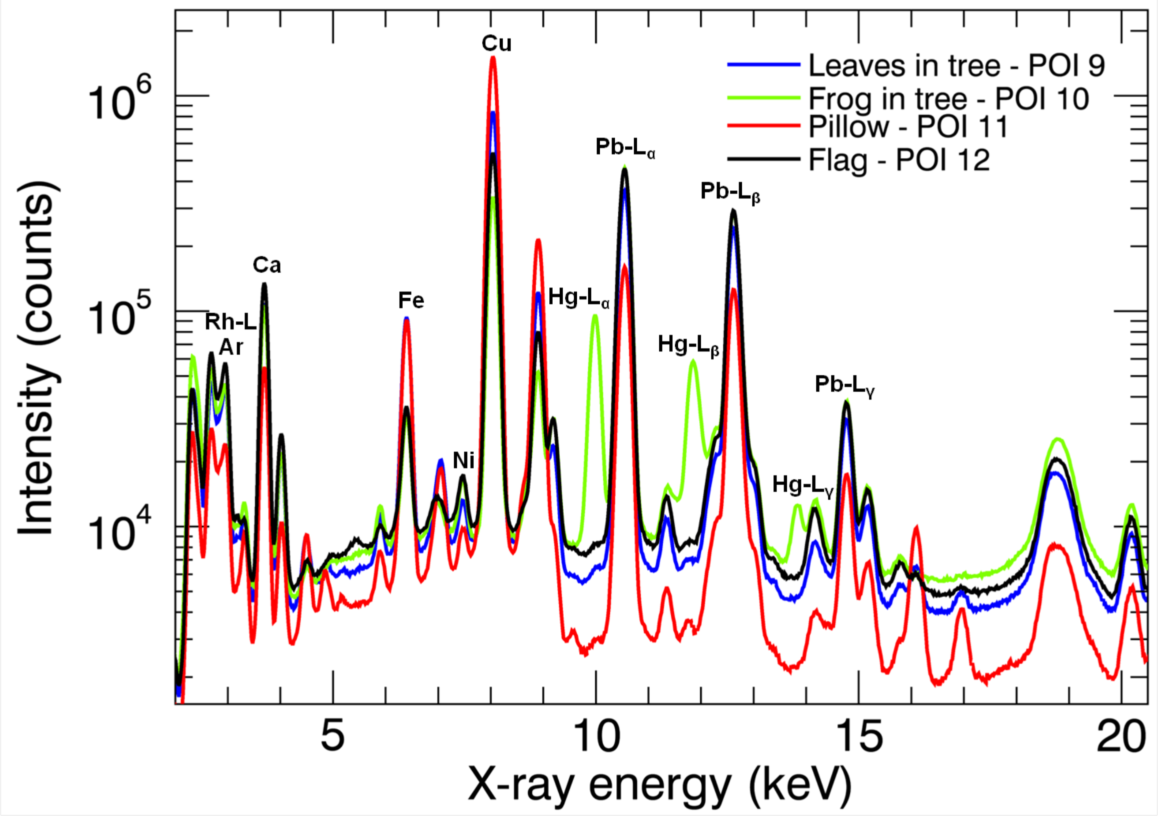

Figure 5.10: *Overlay plot of XRF spectra obtained from green areas of the painting (POIs 9-12 in* ***Fig. 5.2****) to identify the used green pigment.*

5.3.4 Preparation layer

A novel commercially available XRF/XRD instrument was used for the *in situ* analysis of a limited number of POIs on the Mad Meg painting. The restricted time of investigation (one day of 8 hours) combined with a measuring time and set-up time of approximately 45 minutes limited the amount of available results. Together with the fact that the instrument was bought a very short period before the Mad Meg project started (only preliminary characterization of the instrument could be performed and building up some experience on field was not possible) results in almost all cases too noisy XRD patterns to confirm suggested models.

The analysis of POI 13 (***Fig. 5.2***) using the XRD method give, however, very valuable information about the underlying layer used, as shown in ***Fig. 5.11***: the XRD fingerprint matches very well with calcite of which the calcium signal could be confirmed in the simultaneously acquired XRF spectrum, as shown in ***Fig. 5.11***. Because the XRD pattern gives value data about the preparation layer, the information deriving from the simultaneous recorded XRF spectra can verify our suggestions about these layers. Here the presence of iron may indicate the use of an earth-pigment, not excluding the hypothesis that a mixture of lead white with an earth-pigment is used as an imprimatura on a calcite containing preparation layer.

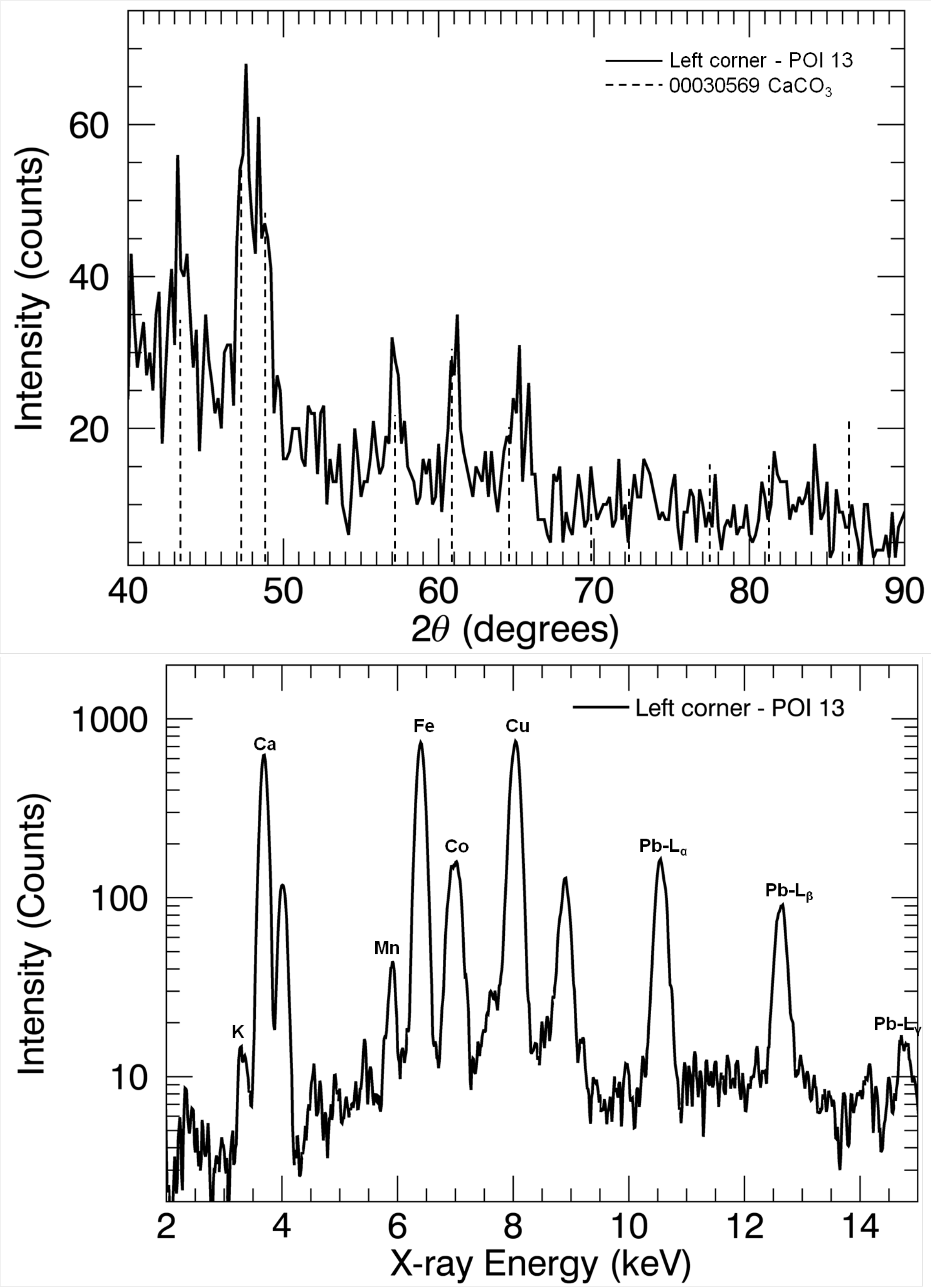

Figure 5.11: *Top: XRD result of the measurement on POI 13 using the XRF/XRD Surface Monitor: the measured pattern shows a match with calcite diffraction pattern of the ICDD databank. Bottom: Simultaneously acquired XRF spectrum.*

5.3.5 Other pigments

Above we focused on the blue, green and red pigments which were successfully identified by the use of the XRF technique and on the confirmation by the Raman technique for the red pigment. During the experimental session using the hXRF, more points in different pigments were measured. ***Fig. 5.2*** (letters) gives an overview on the measurements corresponding to the white, fleshtone, pink pigments and the pigments used for painting the water. ***Table5.2*** summarizes the results of these elemental analyses, providing extra information on the palette of pigments used in this painting.

Table 5.2: *Summary of the chemical characterization of the pigments of interest analyzed in situ on the painting "Mad Meg" based on fingerprint studies using the handheld XRF spectrometer.*

colour	# measured points	Letter or number in *Fig. 5.2*	Characteristic chemical elements	Possible pigments
White	3	a	Ca, Fe, Pb-L	Lead white
Fleshtone	2	b	Ca, Fe, Pb-L, Hg-L	Mixer of lead white and red vermillion pigments
Pink	2	c	Ca, Fe, Pb-L	Conspicuous: suspected that the used pink was a tint of red but no Hg present so no mixer white and red to get pink. Typical pink colours (from quercitron or Persian berries or ultramarine pink) can not be confirm by using above instruments
Pigments in water	3	d	Ca, Fe, Cu, Pb-L	Cu-resinate (green pigment) which recolour after period of time
Dark blue	1	POI 13	Ca, Fe, As, Pb-L	

5.4 Conclusion

A combined working method involving different and specialized portable techniques (optical imaging by digital microscopy, XRF and XRD spectroscopy, Raman spectroscopy) has been applied for the *in situ* investigation of the famous painting, Mad Meg, by Pieter Bruegel the Elder. An essential step in this methodology was the establishment of a roadmap with points of interest of the artwork specified by the experimentalists together with art historians. This information could then be shared amongst the specialized scientific teams in preparation for the actual experiments.

When studying Mad Meg by Pieter Bruegel the Elder, the hXRF instrumentation proved extremely valuable providing elemental information and fingerprinting about the (most likely) smalt pigments for the blue colour, probably copper-resinate for the green pigments, accompanied by lead white and vermillion pigments, and confirming the economical way of painting by the artist. The XRF technique benefits from the fact that information of several sample layers can be obtained, but without clear distinction from which layer(s) the recorded element-specific signals are originating. Raman spectroscopy confirmed the use of a vermillion pigment, though the presence of the varnish layer made it challenging to obtain information with this technique in general. With the portable XRF/XRD instrument, it was possible to retrieve XRF and XRD data simultaneously. A particular example given in this work illustrated its potential of retrieving structural information from deeply buried layers (limited by X-ray absorption length values), while delivering elemental information of the multi-layered sample as explained before, giving the indication that a mixture of lead white and earth-pigment could have been used as an imprimatura.

Future improvements of the applied experimental procedure will take into account specific demands and/or constraints as was listed in this work: (a) although the manual positioning of the probe heads could be done perfectly by the flexible designs of the different stands, motorized positioning could improve systematic investigation when coupled with a monitoring system (e.g. optical system with direct view on the investigated area) and will enable to perform automated imaging; (b) concerning the digital imaging capturing the true colour of the different sample features may enhance the quality of the roadmap; (c) improvements of instrumentation such as beam size (in case of X-ray instrumentation) and specific constraints regarding safety in general are necessary in order to apply different techniques simultaneously.

Bibliography

[1] P. Vandenabeele, R. Garcia-Moreno, F. Mathis, K. Leterme, E. Van Elslande, F.-P. Hocquet, S. Rakkaa, D. Laboury, L. Moens, D. Strivay, and M. Hartwig, “Multi-disciplinary investigation of the tomb of Menna (TT69), Theban Necropolis, Egypt.,” *Spectrochimica acta. Part A, Molecular and biomolecular spectroscopy*, vol. 73, pp. 546–52, Aug. 2009.

[2] Molab, “http://www.charismaproject.eu/,” 2014.

[3] M. Gil, C. Araujo, M. Carvalho, S. Longelin, L. Dias, S. Valadas, C. Souto, J. Frade, I. Ribeiro, J. Mirão, and a. Candeias, “Microanalytical study of the fresco the good and the bad judge in the medieval village of Monsaraz (Southern Portugal),” *X-Ray Spectrometry*, vol. 42, pp. 242–250, July 2013.

[4] S. Pessanha, a. LeGac, T. I. Madeira, a. Guilherme, M. Manso, and M. L. Carvalho, “Characterization of a Namban folding screen from the Edo period by means of EDXRF, SEM-EDS and Raman spectroscopy,” *X-Ray Spectrometry*, vol. 42, pp. 128–133, May 2013.

[5] A. Le Gac, R. Estrompa, J. C. Frade, S. Pessanha, T. I. Madeira, A. Cardoso, L. Piorro, L. Dias, J. Mirão, A. Candeias, and M. L. Carvalho, “Multianalytical approach for the authenticity of an eighteenth-century Pascal Taskin harpsichord,” *Journal of Analytical Atomic Spectrometry*, vol. 27, p. 626, 2012.

[6] K. Castro, N. Proietti, E. Princi, S. Pessanha, M. L. Carvalho, S. Vicini, D. Capitani, and J. M. Madariaga, "Analysis of a coloured Dutch map from the eighteenth century: the need for a multi-analytical spectroscopic approach using portable instrumentation.," *Analytica chimica acta*, vol. 623, pp. 187–94, Aug. 2008.

[7] A. Deneckere, F.-P. Hocquet, A. Born, P. Klein, S. Rakkaa, S. Lycke, K. De Langhe, M. P. J. Martens, D. Strivay, P. Vandenabeele, and L. Moens, "Direct analysis of the central panel of the so-called Wyts triptych after Jan van Eyck," *Journal of Raman Spectroscopy*, vol. 41, pp. 1500 – 1509, Nov. 2010.

[8] A. Giakoumaki, I. Osticioli, and D. Anglos, "Spectroscopic analysis using a hybrid LIBS-Raman system," *Applied Physics A*, vol. 83, pp. 537–541, Feb. 2006.

[9] M. P. Martens, "Het Realisatieproces in Dulle Griet en de Twaalf Spreuken van Pieter Bruegel de Oude," in *Pieter Bruegel Ongezien! De verborgen Antwerpse collecties* (M. Sellink, ed.), pp. 26–59, Museum Mayer van den Bergh, Antwerpen: Davidsfonds, 2012.

[10] D. Blake, C. Bryson, and F. Freund, "Design of an X-Ray Diffraction/X-Ray Fluorescence Instrument for Planetary Applications," *Abstracts of the Lunar and Planetary Science Conference*, vol. 23, pp. 117–118, 1992.

[11] A. Pifferi, G. Campi, C. Giacovazzo, and E. Gobbi, "A New Portable XRD / XRF Instrument for Non-destructive Analysis," *CROATICA CHEMICA ACTA*, vol. 82, no. 2, pp. 449–454, 2009.

[12] S. Assing, "http://www.assing-group.it/index_eng.html," 2014.

[13] J. V. Oestvoren, *De blauwe schuit.* Muiderberg: Dick Coutinho, 1979.

Chapter 6: Analytical characterization of a new mobile X-ray fluorescence and X-ray diffraction instrument combined with a pigment identification case study

Lien Van de Voorde, Bart Vekemans, Eddy Verhaeven, Pieter Tack,
Robin De Wolf, Jan Garrevoet, Peter Vandenabeele, Laszlo Vincze

Spectrochimica Acta Part B, 110, 14-19 (2015)

The benefit of using different analytical techniques in the investigations of culturo-historical objects and answering material specific and in some cases historical questions of conservators/historians, which could not be answered using only historical literature, is demonstrated in chapters 3, 4 & 5. A related topic was the evaluation evaluation of a new, commercially available, mobile system combining X-ray diffraction and X-ray fluorescence enabling both elemental analysis and phase identification simultaneously. This chapter focuses on the characterization of this instrument, combined with a study of its potential in pigment identification. The chapter is concluded with an application example concerning the analysis of so-called printing letters.

6.1 Introduction

Analysis of cultural heritage objects and their environment with the application of archaeometry can teach us not only much about the objects themselves, but also about history as well as past behaviour and interactions of people. Archaeometric studies often involve the analysis of unique and vulnerable, fragile objects that must be preserved without any damage as a result of the analysis. Therefore, *in situ* non-destructive qualitative and quantitative elemental/structural analyses are often required [1–3]. Currently, there is a large number of commercial portable instruments available allowing the analysis of objects on site. Hence, analytical measurements are not restricted to investigations during which researchers have to get the permission to relocate the cultural heritage objects to the lab, and to objects which are sufficiently small to fit into the analytical instruments [4–6]. Among currently used mainstream methods, analytical techniques based on X-ray fluorescence (XRF) are among the most appropriate to examine the elemental composition. In most cases, however, not only elemental information is required, but also structural data on the detectable crystalline phases [7, 8]. X-ray (powder) diffraction has proven to be a powerful tool for identifying crystal structures with very useful applications in the analysis of objects of art or archaeological artefacts containing crystalline materials [9–14]. Starting from the early 1990s, the first prototypes of mobile XRD instruments were developed at NASA. A few commercial companies (e.g. CHEMIN and MOXTEK) started manufacturing portable X-ray fluorescence/X-ray diffraction (XRF/XRD) instruments starting from 2000 and the development of their own, improved, instruments is still ongoing [15–17]. Recently, a number of companies (e.g. OLYMPUS, ASSING) made mobile instruments available combining XRF and XRD, providing powerful tools for the comprehensive in situ characterization of materials in several research fields. However, until now, almost no information on these commercially available instruments can be found in the literature. Concerning non-commercial XRF/XRD instruments, the latest developments on such instrumentation can be found in e.g.[14, 18].

In this chapter, the commercially available mobile X-ray fluorescence/X-ray diffraction instrument (Surface Monitor, Assing S.p.A, Italy) is characterised [19]. It is a new mobile device for simultaneous determination of the elemental constituents by XRF and of the mineral phases by XRD. The Surface Monitor works on a broad range of surfaces, without the need of any sample preparation. The instrument adopts an innovative data acquisition strategy allowing the exploitation of the entire energy range provided by the X-ray sources. The novelty of this mobile XRF/XRD instrumentation is due to a combination of energy-dispersive XRF spectroscopy with goniometry based XRD data collection. This is different from most other commercially available systems, which rely on a Charge Coupled Device based non-dispersive XRD methodology. Also, the very low weight of the entire instrument is unique and allows a straightforward way of working on site. Besides, the characterization of the instrument, also some application examples are discussed demonstrating the applicability of the mobile XRF/XRD instrument.

6.2 Experimental

The Surface Monitor is equipped with a Cu (maximum voltage 30 kV/current 500 μA) or Mo (maximum voltage 30 kV/current 300 μA) anode based X-ray tube in combination with an Amptek X-123 Si-Pin diode detector (260 eV energy resolution at 5.9 keV, 6 - 25 mm^2 detector area depending on collimation conditions and 25 μm Be window thickness). Both the X-ray tube and the detector are mounted on an XRD goniometer applying the Bragg-Brentano $\theta : \theta$ geometry [15, 20]. The $\theta : \theta$ goniometer is integrated in a motorized probe head which is equipped with a laser interferometer for beam positioning as shown in ***Fig. 6.1***. The tube and the detector can be respectively equipped with (pairs of) pinholes or vertical slits, with internal diameters ranging from 0.5 mm to 2.0 mm (in steps of 0.5 mm, see ***Fig. 2.23***). Furthermore, the Surface Monitor is equipped with a control unit to manage the measurements performed, which is connected to a portable PC running the control software.

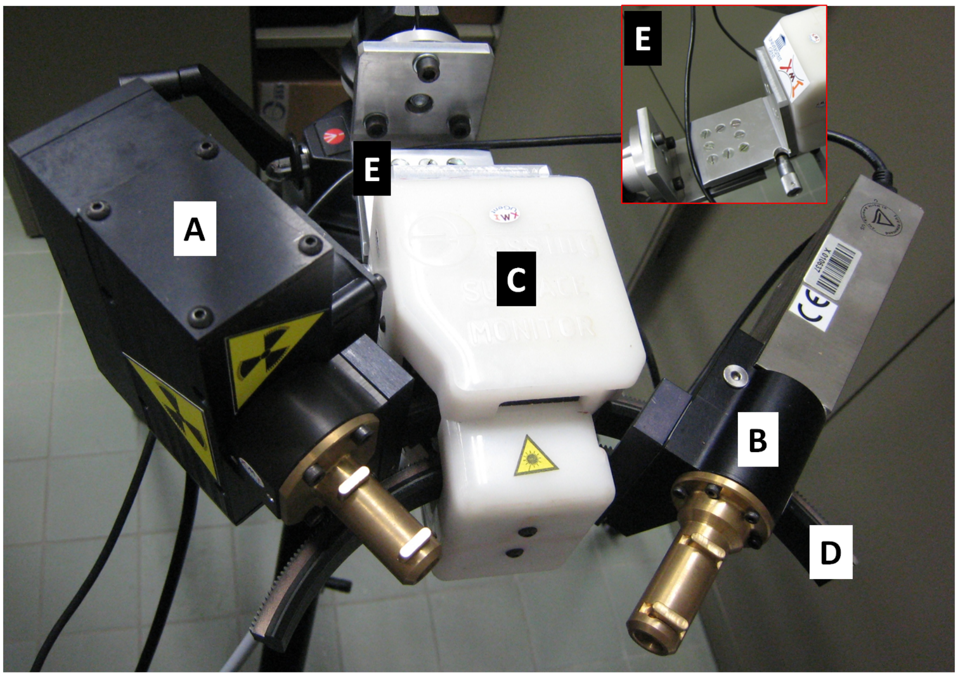

Figure 6.1: *Photograph of the Surface Monitor, a mobile XRF/XRD system: (A) X-ray tube, (B) detector, (C) laser interferometer, (D) goniometer for Bragg-Brentano $\theta : \theta$ methodology (see further), (E) micromanipulator for the (last) fine adjusting step relative to the sample surface, zoom out in small photograph right top.*

The X-ray tube and detector attached to the XRD goniometer, applying the Bragg-Brentano $\theta : \theta$ acquisition mode, is a popular set-up for recording an XRD spectrum. The sample that needs to be analyzed is placed in a static sample holder. Both, X-ray tube and detector axes make an angle θ with the surface plane of the sample. Also the distances between the sample and the tube, and the sample and the detector are identical. During the measurement both X-ray tube and detector move simultaneously over a given angular range, defined at the beginning of the experiment, see ***Fig. 6.2*** [19].

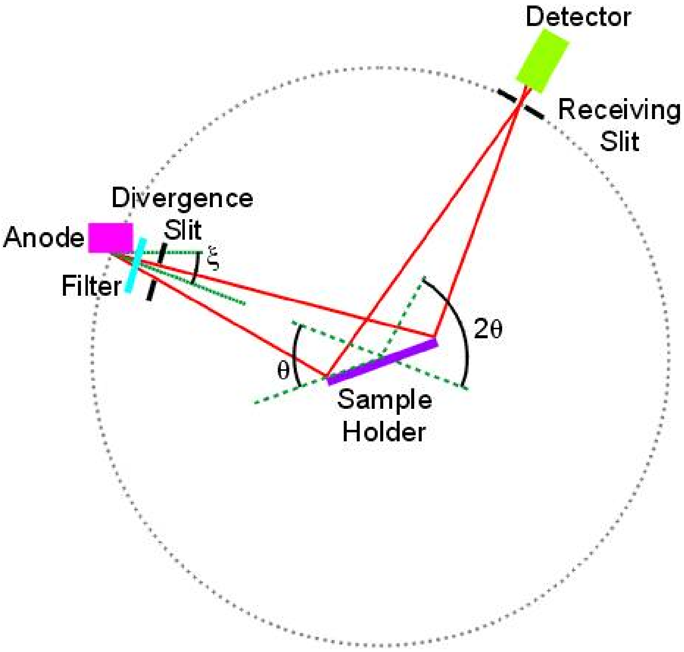

Figure 6.2: *Bragg-Brentano $\theta : \theta$ set-up, with on the left the X-ray tube (anode) and on the right the X-ray detector. The sample is placed in between. Detector and X-ray tube move with the same angle θ with respect to the sample plane in order to detect the diffracted X-ray beams. Source: http://pd.chem.ucl.ac.uk/pdnn/inst1/optics1.htm (15/09/2015).*

The entire systems weighs only 3.5 kg, which is a considerable improvement compared to other mobile instruments available from the early 2010s [14]. During analysis, the instrument is installed on a tripod which allows easy and safe positioning of the device probe-head at the position of interest, covering a suitable height range and, if needed, compensating for the inclination angle to the artefacts surface (see ***Fig. 2.40***). This allows for *in situ* measurements without a need for repositioning the artwork, as typically requested by the museum. A camera, mounted on a flexible arm, was added to provide an inclined top-view of the probe head and the sample to monitor all movements (by means of a controlling portable PC) so that the operator can work from a safe distance (at least two meters) with the X-ray instrument.

In the experiments described below, the Cu X-ray tube was used for the characterization and application of the instrument. The Cu anode, providing lower energy characteristic lines, is preferable for X-ray diffraction experiments compared to Mo. In general, the procedure for swapping the available X-ray tubes (Mo, Cu) is not straightforward. In case of a tube replacement, the entire procedure of calibration and characterization needs to be repeated. The Mo tube is preferable when

XRF measurements have priority over XRD due to the higher excitation energy represented by its characteristic lines. X-ray tubes with targets of lower characteristic energy allow to carry out diffraction analysis with larger diffraction angles, resulting in a better separation of diffraction peaks. For most measurements described below, a start angle ($2\theta_i$) of 20° was used with an end angle ($2\theta_f$) of 70° or 90° (which is below the instrumental limit of 92.1°), with a step size of either 0.1° or 0.2°. The detector dwell (live) time per angular step was 5 s or 30 s. In all cases, the exact parameters of data acquisition are given in the text or figure.

The Cu X-ray tube of the Surface Monitor is typically operated at a voltage of 28 kV but because of unknown electrical problems of this tube, the mean part of the measurements showing in this PhD work where only execute on a current of 18 kV. ***Fig. 6.3*** is giving the difference in LOD (limit of detection) between the two voltages, using a NIST SRM 1412 glass standard, corresponding to optimum excitation/detection conditions (i.e. without slits/pinholes, with the X-ray tube and detector positioned at an angle of 45°) using a dwell time of LT = 500 s. The LOD values are between 50 ppm and 1000 ppm, except for Fe for which a lower LOD was obtained (10 ppm). The narrow higher LOD using the Surface Monitor with Cu tube only on 18 kV can be solved by extending the measuring time to get the same information as when the X-ray tube was working on maximum performance.

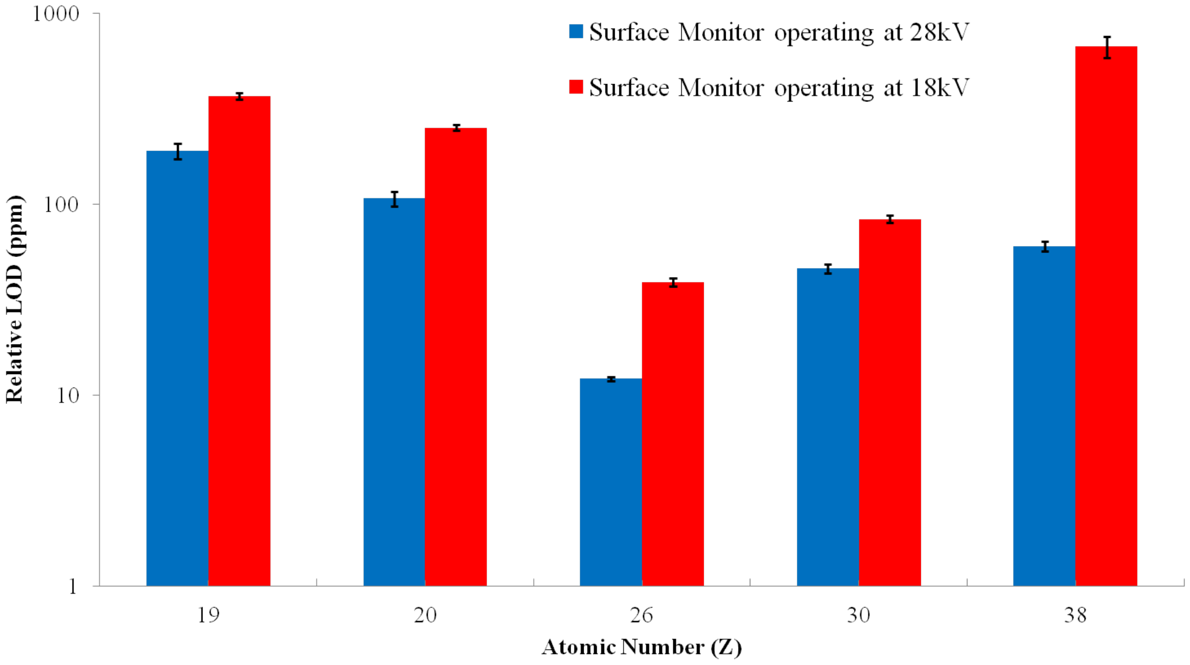

Figure 6.3: *Difference in LOD of the Surface Monitor spectrometer working on 18 kV or 28 kV*

6.3 Characterization of the mobile Surface Monitor

When installing the Surface Monitor in front of the investigated object, we start with positioning the tripod at the approximate height for the analysis. When the tripod is placed in a stable position, the instrument head is fixed on the tripod and the cables, connecting the instrument head with the control box, are plugged in. Once the connection with the computer is made and the initialization of the instrument is completed, the Surface Monitor is switched on and the laser interferometer is automatically lighting up. The final step of setting up the instrument, before starting the analysis, is to measure and adjust the distance between the surface of the sample and the analytical head. To obtain XRD patterns with optimal quality, the Surface Monitor has to be positioned with the main axis perpendicular towards the sample and the distance between the instrument head and the sample should be between 94.5 mm and 95.0 mm. Therefore, a laser interferometer is built in the analytical head (between the X-ray tube and detector) to measure the sample distance and to ensure the correct positioning of the X-ray beam on the area of interest (C on ***Fig. 6.1***). A micromanipulator has been added by ourselves (to the commercial components of the Surface Monitor), between the mounting points of the tripod and the Surface Monitor in order to enhance the accuracy of the longitudinal positioning of the analytical head in the direction of the sample (E on ***Fig. 6.1***). Next to monitoring the distance, the laser beam is also used to position the sample area to be analyzed to the impact point of the X-ray beam. In this way, it is also providing us a very useful tool to position the X-ray beam in the two other directions on the sample area of interest.

6.3.1 Performance of the laser interferometer

As mentioned above, the laser interferometer is an important component in defining the performance of the Surface Monitor contributing significantly to the quality of the obtained XRD spectra. As a result, the characterization of the performance of this laser is an important part of the characterization of the whole instrument. A first element which is tested, is the read-out precision of the laser and therefore an experiment was set up where the laser was pointing perpendicular on a flat surface, i.e. a paper taped on a holder as can be seen in ***Fig. 6.4***. The probe head was then moving with the micromanipulator in steps of 50 ± 1 μm, where the micromanipulator has an own reading accuracy of 5 μm.

Fig. 6.5 shows the difference between the manually set 50 μm and read-out of the interferometer at a working distance between ca 98.0 mm and ca 88.0 mm (distance between flat surface and instrument head) where we can conclude that the precision of the laser interferometer is ± 0.11 mm.

During this chapter, the distances 94.5 mm and 95 mm are already mentioned a few times when we write about the distance between sample and the head of the Surface Monitor. This distance is not arbitrary chosen by ourselves but is also part of the characterization of the laser and the best performance distance between Surface Monitor head and sample. When the Surface Monitor was delivered, the distance to acquire XRF and XRD spectra was set in the control software by the company Assing S.p.A. between 91.80mm and 92.20 mm. However, it was quickly clear that the proposed distance of 92.0 mm was not the optimal distance for the instrument (recorded spectra had only maximum counts per peak of 1 count, so probably only background signal was measured).

It was thus of utmost importance to know the optimal distance between the object and the sensor

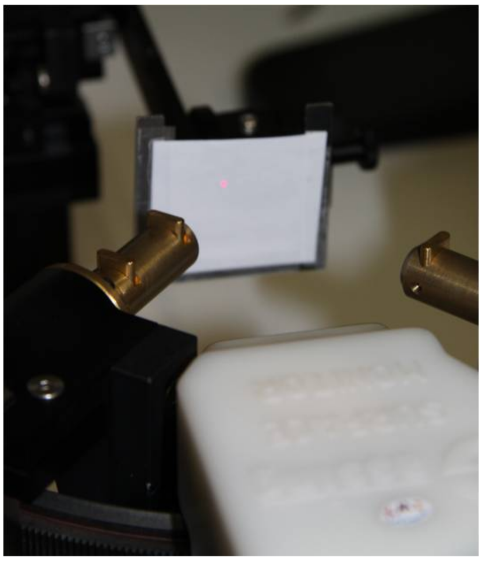

Figure 6.4: *Experiment to test the read-out precision of the laser interferometer.*

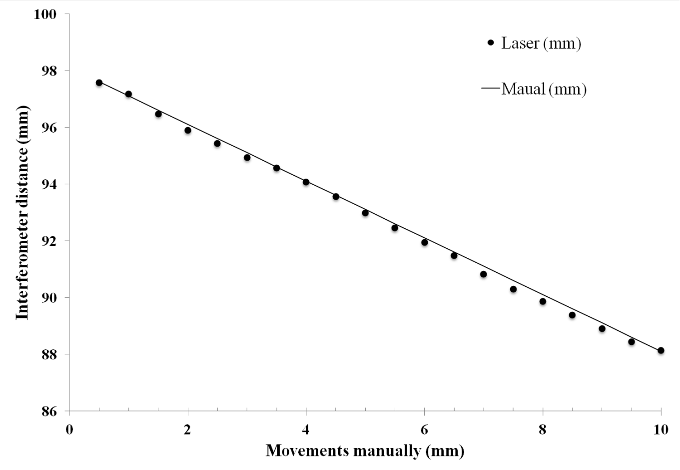

Figure 6.5: *Performance characterization of the laser interferometer, showing the difference between the 50 μm sample positioning steps adjusted manually and the corresponding read-out of the interferometer.*

of the probe head. This was determined by measuring a NIST SRM 660b lanthanum hexaboride (LaB_6) powder diffraction standard between 20° (start-angle = $2\theta_i$) and 90° (end-angle = $2\theta_f$), using a step size of 0.2° and measuring time of 5 s LT/step. ***Fig. 6.6*** is showing the recorded XRD pattern where the most intense peak at approximately 30° helps us in the characterization of the best distance.

When varying the distance between the probe head and the standard from 92.0 to 98.0 mm and thus actually varying the corresponding interferometer read-out values, we expect to find the optimal distance between Surface Monitor and sample. ***Table6.1*** shows the area under the most intense diffraction peak and the difference in the 2θ-angle between this peak and the corresponding certified value (30.385° - [110]). Based on these results, the optimal distance is reached when maximal intensity and minimal angular deviation is obtained. This optimum is observed in the distance read-out range of 94.5 - 95.0 mm.

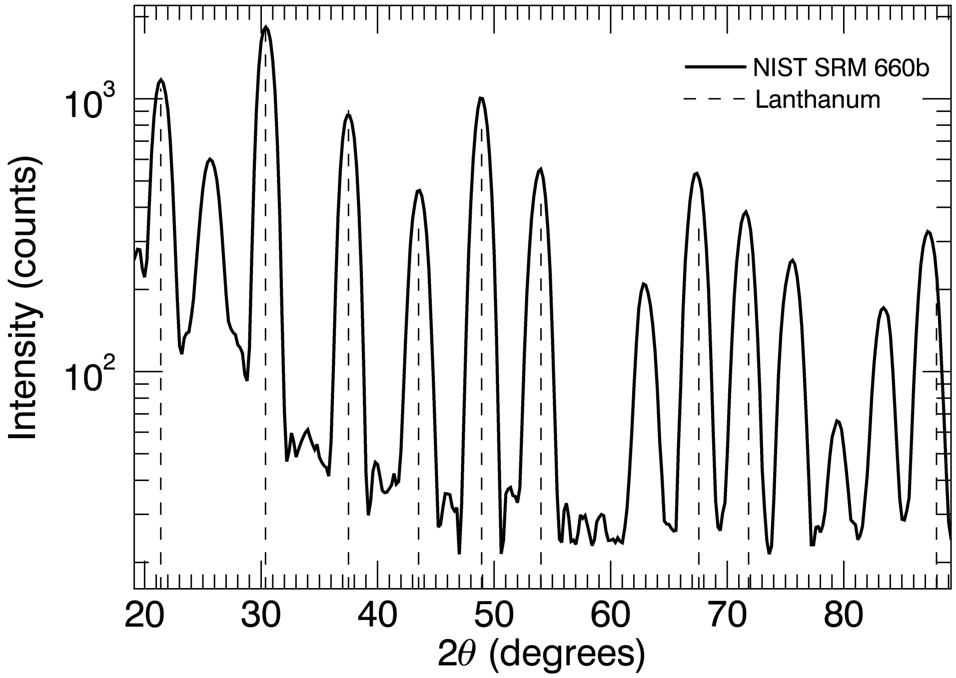

Figure 6.6: *Diffraction spectrum of the NIST SRM 660b powder-XRD standard, also indicating the La powder diffraction peaks in the recorded pattern.*

6.3.2 Selection of slits and pinholes

The X-ray tube and detector can be equipped with respectively pairs of pinholes and vertical slits, having different internal diameters/widths, which can be used to improve the resolution at the expense of the signal intensity of the acquired XRD patterns. When performing *in situ* experiments with limited access time to the artifact, one has to find a balanced trade-off between the number of acquired XRD spectra and the data quality. Therefore, it is important to evaluate the performance of the different combinations of pinholes and slits to verify how their choice can affect the quality of XRD patterns. To limit the experiment to a realistic situation, only pairs of pinholes in front of the X-ray tube of same size and pairs of vertical slits of same size at the detector were used in a sequence of measurements using the NIST SRM 660b diffraction standard. ***Table6.2*** and ***Table6.3*** show the results of the measurements combining three different pinhole sizes (same size for the pair of pinholes) with four different slit sizes (same size for the pair of slits). The smallest pinholes provided, having diameters of 0.5 mm, could not be combined with the Cu-tube because of the too low signal intensity that reaches the detector. The obtained XRD spectra of the standard were fitted with Gaussians in order to determine the intensity and full width at half maximum (FWHM) of the diffraction peaks. These parameters represent important figures of merit regarding the performance of the instrument, defining respectively the necessary measuring time and achievable resolution of the diffraction peaks. ***Table6.2*** shows the relative intensity of the [110] peak corresponding to the results obtained with 1.0 mm pinholes, combined with detector slits having widths of 0.5 mm. ***Table6.3*** presents the

FWHM of the [110] peak of the LaB_6 standard for the different pinhole and slit combinations. It can be concluded that the FWHM is mainly influenced by the detector slit size and in a minor way by the pinhole size.

Table 6.1: *Numerical values defining the optimal distance of the Surface Monitor with respect to the sample surface using a NIST standard (SRM 660b - LaB_6), obtained by measuring the intensity and the deviation from the certified value ($2\theta = 30.385°$) of the most intense diffraction [110] peak*

Distance (mm)	Counts	Deviation (°)
92.80	832	3.613
94.04	1727	1.618
94.56	1807	0.612
94.95	1683	0.215
96.03	894	-1.385
97.03	139	-3.185
98.07		

Table 6.2: *Characterization for the use of pinholes (in front of X-ray tube, to define the primary beam) and slits (in front of the detector) in terms of* ***intensity*** *of the [110] peak of the NIST SRM 660b standard. The intensities are expressed in terms of relative values compared to the intensity (I) obtained with a pair of 1.0 mm pinholes in front of the source combined with a pair of 0.5 mm detector slits.*

		Slit size (detector) in mm			
		0.5	1.0	1.5	2.0
Pinhole size	1.0	I	1.7xI	2.9xI	3.6xI
in mm	1.5	1.7xI	3.7xI	5.0xI	6.7xI
(X-ray tube)	2.0	2.4xI	4.7xI	8.0xI	10.3xI

Table 6.3: *Characterization for the use of pinholes (in front of X-ray tube) and slits (in front of the detector) in terms of* ***resolution as FWHM*** *of the [110] peak of the NIST SRM 660b standard*

		Slit size (detector) in mm			
		0.5	1.0	1.5	2.0
Pinhole size	1.0	0.07 Å	0.11 Å	0.15 Å	0.16 Å
in mm	1.5	0.08 Å	0.13 Å	0.13 Å	0.16 Å
(X-ray tube)	2.0	0.09 Å	0.16 Å	0.20 Å	0.24 Å

6.3.3 Beam size and scan size

When using 0.5 mm pinholes with the Cu-tube the detected X-ray beam intensity proved to be insufficient for analysis, so to determine the minimum practical beam size of the Surface Monitor pinholes with a diameter of 1.0 mm were used. By placing a radiochromic film (GAFChromic RQTA2) in the sample position of the Surface Monitor, adjusting the X-ray tube and detector at an angle of 45°, the beam footprint of this setup defines an elliptical illuminated area of approximately 4 mm^2, with a major (horizontal) axis of 4 mm and minor (vertical) axis of 1 mm. Since the Surface Monitor has been used most of the time for XRD measurements with $2\theta_i$ of approximately 20°, $2\theta_f$ approximately 90°, also the evolution of the footprint/size during a scan was determined using a radiochromic film. When using the 1.0 mm pinholes, the scanning area has an elliptical shape with dimension 16.0 (w) x 3.0 (h) mm. When using the 1.5 mm pinholes, the area is again elliptical but with dimension of 21.0 (w) x 4.0 (h) mm. When combining these results with the results corresponding to the intensity and FWHM of different pinhole-slit combinations, when a large homogeneous area needs to be analyzed, a large pinhole and slit size is recommended which results in a shorter acquisition time but broader XRD peaks. In other situations, when high resolution is required for the XRD spectrum or small measurement area, slit and pinhole combination of 1.0 mm are preferable.

6.3.4 Sensitivity of the Surface Monitor to angular uncertainties

An important source of uncertainty associated with the use of the surface monitor originates from alignment errors with respect to its orientation relative to the sample surface. This is especially so, as the tripod on which the surface monitor is mounted can easily deviate ± 2° relative to the ideal orientation, and because X-ray diffraction is based on angles this can have a huge influence on the results. In order to test the sensitivity of the instrument to angular uncertainties of its orientation, a cinnabar pigment sample was measured while the angle of the sample was changed in 3 steps of 5° to the right. The results can be seen in ***Fig. 6.7*** and we can see that a change of 5° results in no change in the detected XRD pattern (intensity and resolution are essentially the same). The apparent change starts from angles more then 10° while the intensities of the diffraction peaks remain comparable, large differences can be observed in the XRD resolution.

An idea to correct for this is to attach a crossbar to the mounting point of the surface monitor on the tripod, and to equip this crossbar with 2 laser interferometers which can measure the distance between the laser and the sample surface. After determining the potential offset between the readout values of the interferometers, a calibrated equal distance value measured on both sides from a flat reference plane (sample surface) should represent an ideal orientation of the instrument. These lasers do not have to be expensive interferometers, because a rotational misalignment of e.g. 7° will result in a change in distance of 31 mm between original distances (black) and new distances (red) (see ***Fig. 6.8***) so laser positioning devices from common do-it-yourself stores with a read out sensitivity of 1 mm are sufficient. This element is not added yet but can be done in the future.

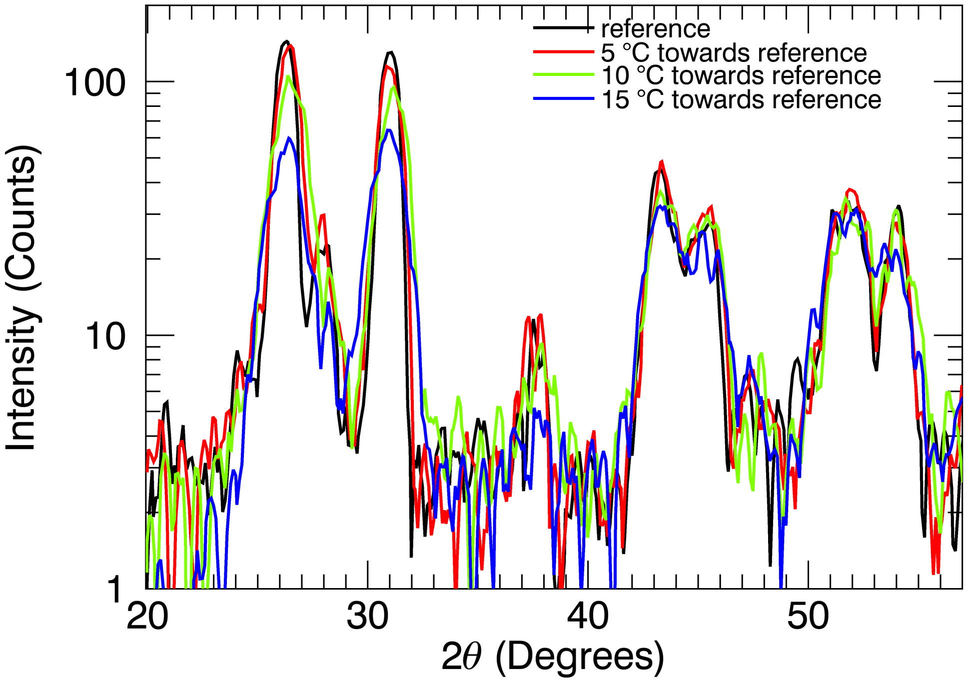

Figure 6.7: *Sensitivity of the Surface Monitor to changes in angular orientation: measuring a cinnabar pigment with the Surface Monitor and changing the angles of the sample in steps of 5°, XRD results.Cu-tube on 18 kV, 250* μ*A, slits & pinholes: 2 x 1 mm,* $2\theta_i$*:20°,* $2\theta_f$*:57°, stepsize of 0.1°, 30 s/step LT.*

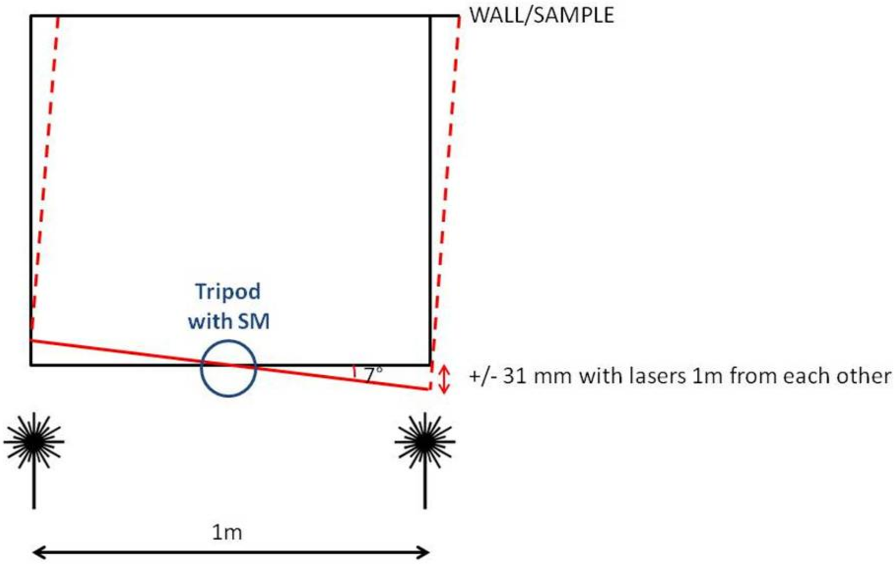

Figure 6.8: *Possible setup for getting always equal positions of the Surface Monitor towards different samples on different places.*

6.4 Data acquisition and analysis

The X-ray tube and detector attached to the motorized goniometer (goniometer) can be controlled can be controlled using the supplied Windows-based software, available on the portable control PC. The Surface Monitor can operate in two main modes: either in XRF mode only, or in both XRD and XRF mode where the XRF sum spectrum is simultaneously retrieved while acquiring an XRD pattern. The experimental parameters which can be supplied for the data collection include: angles (tube/detector), acquisition time, preheating time, voltage and current through the X-ray tube and nomenclature (file name, name of the operator, etc.).

In the XRF mode, detector and tube remain stationary at a chosen angle (***Fig. 6.9***). Changing the angle gives the possibility to affect the penetration depth of the X-rays, thus measuring different layers of multilayered samples [21, 22]. The fluorescence signal is plotted in real-time as counts versus energy (keV) and leads to the creation of a flo-extension file. The qualitative analysis of the XRF spectra is possible with the same software delivered with the Surface Monitor which allows identifying the detected elemental constituents in a manual or semi-automatic way. AXIL (see 2.3.6 for more detailed working principles of this software) was used to obtain a more reliable identification (compared to the included software) of elements present by converting the flo-extension files to spe-extension files with an *in-house* made developed conversion software. [23, 24]. The included software gives also the possibility to evaluate the XRF spectra in a semi-quantitative way by the standard based method or by a method based on linear regression. In both case of methods, it is essential to measure a standard or a sample with well defined elemental composition.

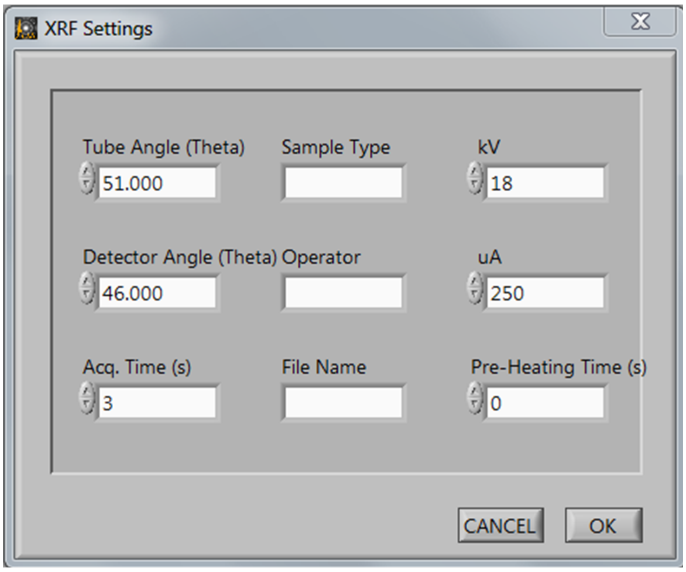

Tube Angle (Theta): 51.000
Sample Type:
kV: 18
Detector Angle (Theta): 46.000
Operator:
uA: 250
Acq. Time (s): 3
File Name:
Pre-Heating Time (s): 0

Figure 6.9: *Graphical user interface to set-up the experimental parameters for an XRF acquisition*

In XRF/XRD mode, while acquiring an XRD pattern, XRF spectra are simultaneously recorded and after the final scanning step, a sum of the (angle dependent) fluorescence spectra is obtained. The interface of the XRD acquisition set-up (***Fig. 6.10***) is similar to the interface for XRF measurements but some additional parameters need to be defined such as the start and stop angle. Hereby the tube and detector (which are moving symmetrically on the goniometer) have to be positioned with respect to the sample, at an angle equal to the set start and stop angles divided by 2 (2θ). Also, the angular step size and the XRD energy value have to be defined in the XRD mode. The XRD energy value is defined by the main emission line energy of the anode material of the used X-ray tube.

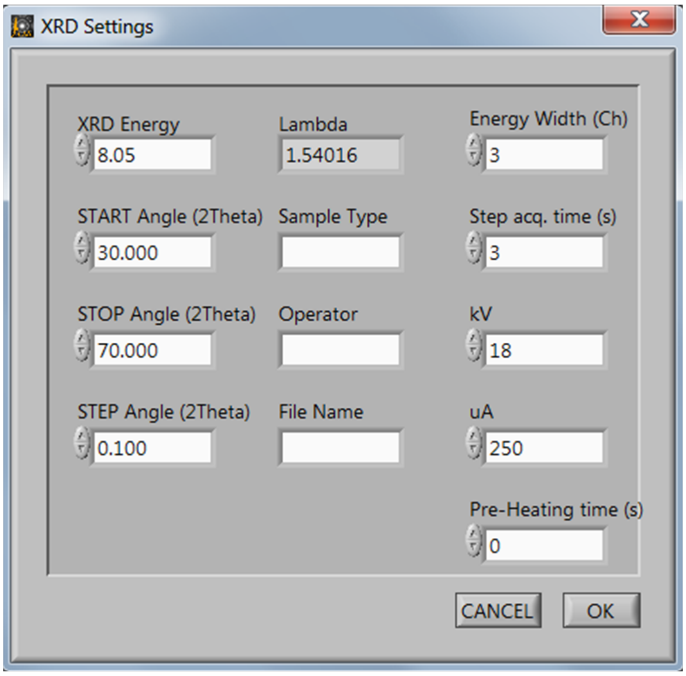

XRD Energy 8.05
Lambda 1.54016
Energy Width (Ch) 3
START Angle (2Theta) 30.000
Sample Type
Step acq. time (s) 3
STOP Angle (2Theta) 70.000
Operator
kV 18
STEP Angle (2Theta) 0.100
File Name
uA 250
Pre-Heating time (s) 0

Figure 6.10: *Graphical user interface to set-up the experimental parameters for the XRD acquisition*

After collecting the XRD patterns, the data can be processed by the same software package which is delivered with the International Centre for Diffraction Data (ICDD) database [19]. There are two main modes to interpret the XRD pattern using the ICDD databank: search match mode and free search mode. When performing the search match mode, one starts from the measured XRD pattern, assuming an unknown phase, and the software will suggest several phases which match with one or more peaks, preferably with all peaks. ***Fig. 6.11*** shows the snapshot of the first step in the search match mode. By selecting the right database as a function of sample type (choice between 20 types: e.g. mineral, organic, metals alloys, inorganic,$\cdots$), and defining the chemical elements which are present (based on the XRF sum-spectrum) one can constrain the search in the ICDD database. Indicating the most significant XRD peaks in a second step (see ***Fig. 6.12***), increases the quality of matching. When using the free search mode, the software uses the database independently of the measured pattern, which is useful if the composition of the sample is known.

In the last step of the search match mode (see ***Fig. 6.12***), it is also possible to activated a noise filter or a Gaussian fit around the selected peaks to get a better phase fit. These options have been often tested during the different measurements explained in the following parts, however, no significant improvements in the performance of data analysis could be obtained.. This can partly be explained by the lack of insight on how these options are working (no in-depth information is available in the user's manual of the Surface Monitor). Hopefully, further work with this instrument and software can help to find out the details about this part of the software. As can be seen in ***Fig.***

6.6, the identification of an XRD pattern is possible for the LaB_6 standard (NIST SRM 660b).

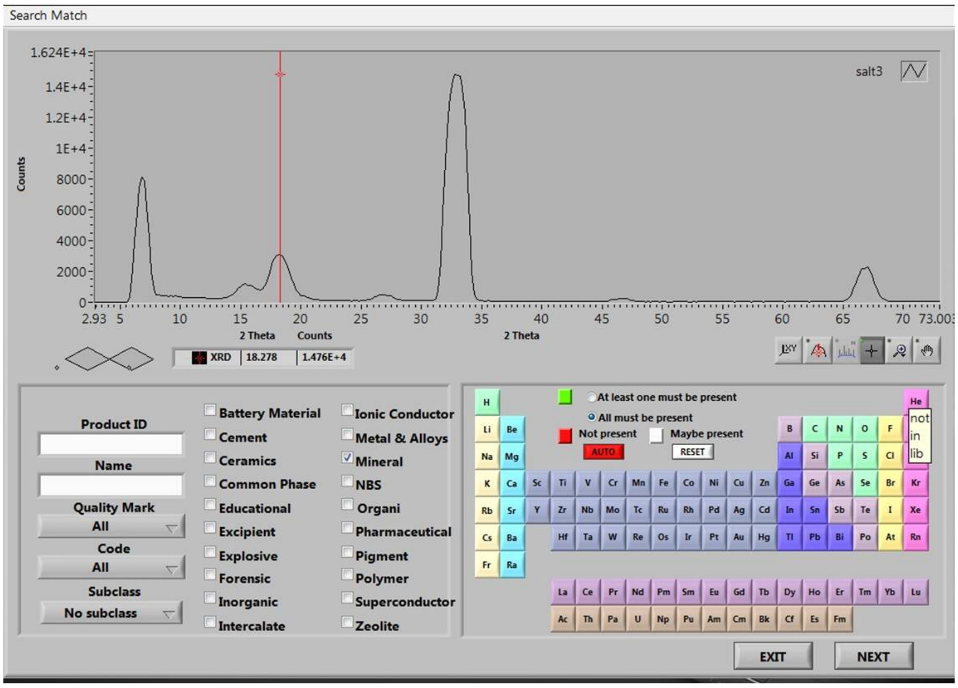

XRD | 18.278 | 1.476E+4

Product ID:

Name:

Quality Mark: All

Code: All

Subclass: No subclass

☐ Battery Material
☐ Cement
☐ Ceramics
☐ Common Phase
☐ Educational
☐ Excipient
☐ Explosive
☐ Forensic
☐ Inorganic
☐ Intercalate
☐ Ionic Conductor
☐ Metal & Alloys
☑ Mineral
☐ NBS
☐ Organi
☐ Pharmaceutical
☐ Pigment
☐ Polymer
☐ Superconductor
☐ Zeolite

🟩 ○ At least one must be present
● All must be present
🟥 Not present
☐ Maybe present

Figure 6.11: *Parameters which can be chosen in the first step of search match mode data acquisition of the XRD spectrum.*

6.5 Using the Surface Monitor for pigment identification

Prior to *in situ* applications using the XRF/XRD Surface Monitor, a number of test measurements were performed on known pigments mounted on tape to verify if one can detect the XRD patterns with sufficient resolution and intensity to be able to identify the pigment reliably based on the ICDD database. Since paintings are typically multilayer systems consisting of a preparation layer (calcite, gypsum, lead white, etc.) overpainted with several pigment layers (sometimes wet layers on each other can give rise to mixtures), a simulation of these situations was also made. All these intermediate steps were carried out to make a model painting and on the one hand, to get familiar with the possibilities of the Surface Monitor and to test the identification of the measured phases using the available ICDD database. The measurement on the model painting (specifically made for testing the surface monitor), on the other hand, was also useful to acquire experience concerning the use of the instrument for the analysis of real-life paintings. This is likely to increase significantly the chance of success for future projects aiming at the XRF/XRD analysis of unique paintings, such as “Mad Meg” (see chapter 5). All examinations above were done to make the Surface Monitor available for all those with interesting research questions on all types of cultural heritage objects and, that research with the Surface Monitor will help these people to unwrap the unknown facts and this with expertise about the performance of the Surface Monitor on paintings. In case of all previous analysis performed in the framework of this Ph.D. work, pigments were always investigated as part of a larger

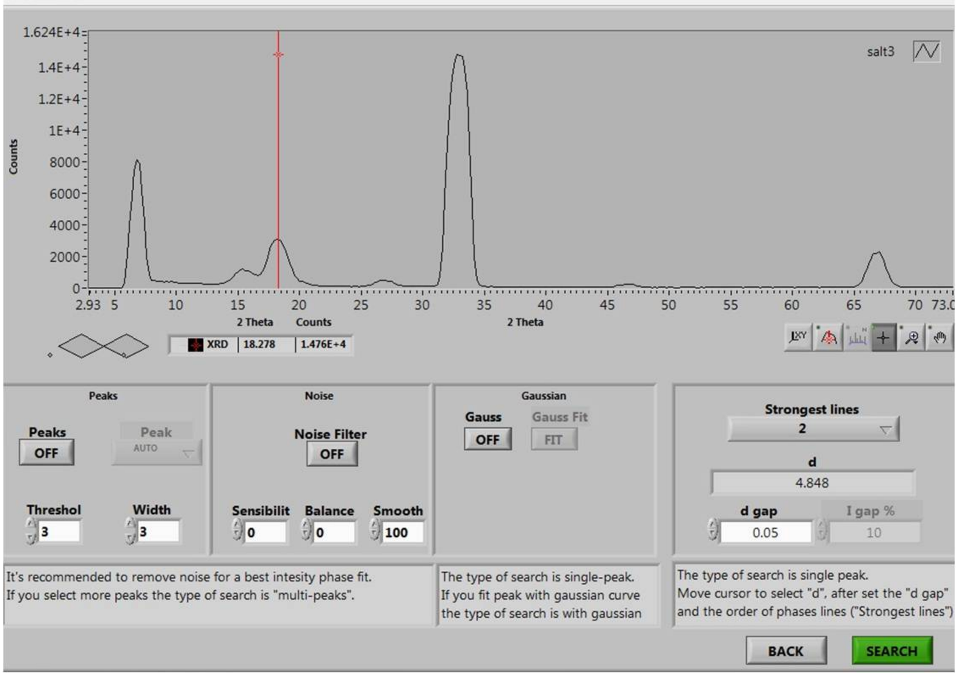

2 Theta | Counts
XRD | 18.278 | 1.476E+4

Peaks: OFF
Peak: AUTO
Threshol: 3
Width: 3

Noise Filter: OFF
Sensibilit: 0
Balance: 0
Smooth: 100

Gauss: OFF
Gauss Fit: FIT

Strongest lines: 2
d: 4.848
d gap: 0.05
I gap %: 10

It's recommended to remove noise for a best intesity phase fit.
If you select more peaks the type of search is "multi-peaks".

The type of search is single-peak.
If you fit peak with gaussian curve
the type of search is with gaussian

The type of search is single peak.
Move cursor to select "d", after set the "d gap"
and the order of phases lines ("Strongest lines")

Figure 6.12: *Second step in search match data acquisition mode: indicating the XRD peaks of interest and optionally subtracting noise and defining Gaussian fits around selected peaks.*

examination of a unique cultural heritage object. In case of these tests, the pigments should be regarded as model samples, used as standards for determining the figures of merit of the instrument.

There are two possibilities to mount the pigments, either by fixing them between 2 ultralene films attached on a cup, or by attaching the pigment to an adhesive (Scotch) tape which itself is mounted on an appropriate holder. ***Fig. 6.13*** shows the XRD spectra corresponding to both mounting support types (ultralene film sandwich or adhesive tape) without the presence of a pigment. As can be seen, the ultralene film gives rise to two diffraction peaks in the small angle region of the XRD spectrum, whereas the tape produces only an elevated background signal. Together with the fact that on the tape, a lower amount of pigment is typically present which simulates much more the situation of a painting (compared with the large amount of pigment typically present between the ultralene films) and taking into account the possibility to start from narrower angles with the taped pigments, the decision was made to mount model pigments on tape instead of using ultralene films. This sample preparation method was applied to a selection of model pigments.

The protocol to fix the pigment on the tape is as follows: either the pigment is applied on a clean glass plate, crushed and then the tape is pressed on the powderized pigment after which the tape (with the pigment) is fixed on a holder. Or, the tape is first attached to an Al sample holder made for XRF/XRD analysis (see ***Fig. 6.14***), followed by mounting the pigment in the hole of the holder (on the tape (see ***Fig. 6.14***). By dispersing the pigment over the available area of the tape, the pigment will be fixed on the tape as can be seen in ***Fig. 6.14***. This figure shows the set-up when double-sided tape is used and when the pigment is mounted on both sides of the tape (see section 6.5.2). In the first test measurements, only single sided tape is used and so only one pigment layer is applied on the front side of the holder extending over the aperture of the Al frame (circle of 2.0

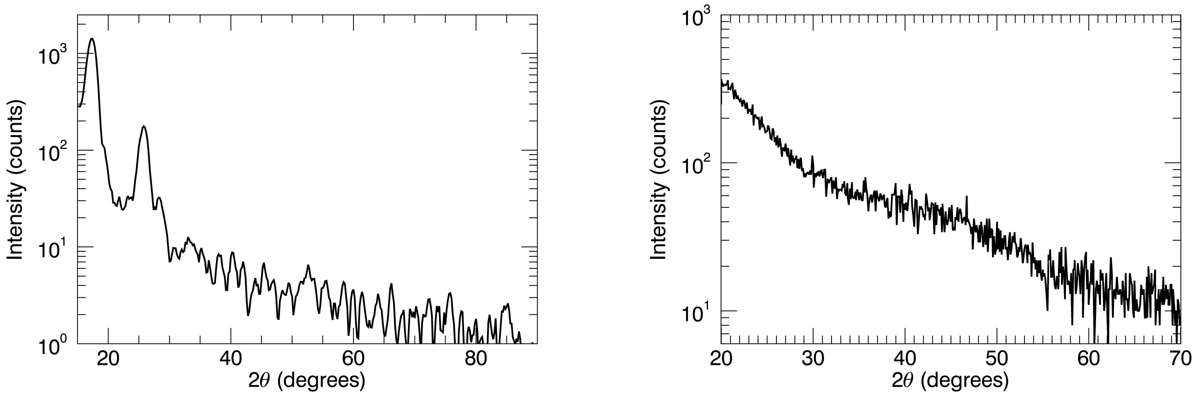

Figure 6.13: *XRD blank spectra corresponding to the two sample support solutions proposed for the XRD analysis of the pigment model samples used in this work, based on a) ultralene sandwich (left) and b) adhesive tape (right).*

cm x 2.0 cm) producing a reasonably uniform distribution over the full area.

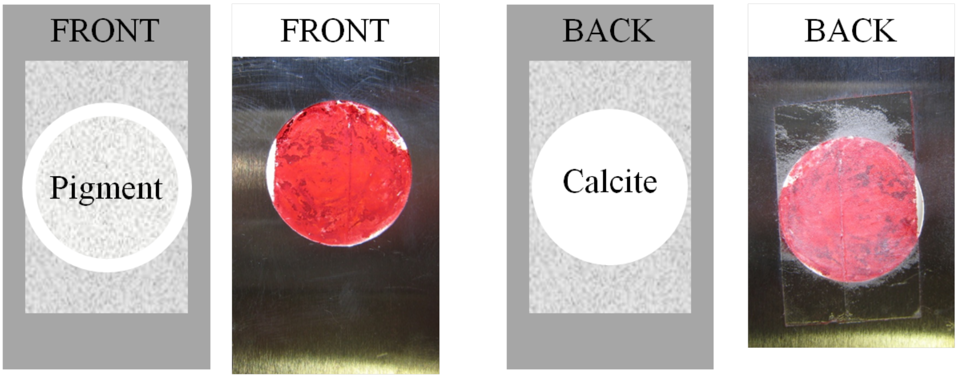

Figure 6.14: *Schematic drawing and a corresponding photograph of a used multilayer model sample, prepared using a double sided adhesive tape, with a pigment layer attached on the front side (here Cadmium red) and a calcite layer on the back.*

6.5.1 Pigment identification

A first model painting (20.0 cm x 15.0 cm x 0.5 cm) was made, coordinated by Eddy Verhaeven (UGent, previous Artesis), by using ten different pigments chosen on the basis of their importance in the era of the Flemish Primitives. This painting was in the first place made to support bachelor projects and to evaluate the quantification performance of the different mobile instruments available in the Department of Analytical Chemistry (UGent). Information about the applied amount of pigment and preparation layer was available. The use of this first model painting with the Surface Monitor had the drawback that measurements on the painting itself can only start at an angle of 40° (because at lower angles the X-ray tube and detector housing would touch the surface of the painting) and from the ten pigments, only four of them (azurite, carmin red, cinnabar and malachite) where available in a sufficient amount to produce detectable signals for these (pre-research) studies. In order to establish a practical database of diffraction patterns of pigments measured with the surface monitor and to get acquainted with the handling of the XRD matching software, 12 more pigments, made available by the Raman group, were selected and measured. ***Table6.4*** gives an overview of the selection of in total sixteen pigments, all measured with the Surface Monitor with the following settings: Cu-tube voltage 18 kV, current 250 μA, slits & pinholes: 2 x 1 mm, angular range $2\theta_i$:20° and $2\theta_f$:70°, stepsize of 0.1°, 30 s/step LT.

Table 6.4: *Pigment selection*

Pigment	Chemical formula	colour	match between XRD spectrum and ICDD database?
Atacamite	$Cu_2Cl(OH)_3$	green	No good match
Azurite	$Cu_3(CO_3)_2(OH)_2$	blue	Match
Cadmium red	CdSe	red	Good match
Cadmium yellow	CdS	yellow	Good match
Carmin red	$PbFe_2^{3+}(AsO_4)_2(OH)_2$	red	No XRD peaks detectable
Chrome yellow	$PbCrO_4$	yellow	Match
Cinnabar	HgS	red	Good match
Cobalt blue	$CoO.Al_2O_3$	blue	Very low intensities, so no match could be founded
Leadtinyellow	Pb_2SnO_4 or $Pb(Sn,Si)O_3$	yellow	Not available in ICDD database
Lead white	$PbCO_3$	white	Good match
Madder	$C_{14}H_8O_4$	red	Organic pigment almost no intensity so no good match
Malachite	$Cu_2CO_3(OH)_2$	green	Match
Naples yellow	$Pb(SbO_3)_2$ or $Pb(SbO_4)_2$	yellow	No good match
Titanium white	TiO_2	white	Good match
Ultramarine	Lapis lazuli (Na-Ca-Al-Si-S)	blue	Very low intensities, so no match could be founded
Zinc white	ZnO	white	Good match

The table shows, next to the chosen pigments, also their corresponding chemical formulas and specifies the colour of the pigment together with the possibility to get an XRD spectrum and match with the ICDD database. As one can expect, not all pigments produce an XRD spectrum with identifiable diffraction peaks or a good match with the patterns available in the database. All diffraction spectra without a good match with the database can be found back in **appendix A**. The six residual pigments (cadmium yellow and red, cinnabar, leadwhite, titanium white and zinc white) provide a diffraction spectrum which can be identified with the corresponding pigment available in the database.

Fig. 6.15 shows the results for the cinnabar and lead white pigment. For the cinnabar pigment, the found phase match with the most intense peaks, but unfortunately not with all peaks (some less intense peaks are unknown). The lead white pigment is matching with (hydro)cerussite, a mineral consisting of lead carbonate which is another name for lead white pigment. Here almost all peaks are assigned, only not the peaks above 55°. ***Fig. 6.16*** shows the complete match (all diffraction peaks can be assigned) between two white pigments, namely titanium white and zinc white, and the minerals available in the database, respectively anatase and zincite which have the same chemical formulas as the matched pigments. Same results are found for cadmium based pigments, as can be seen in ***Fig. 6.17***.

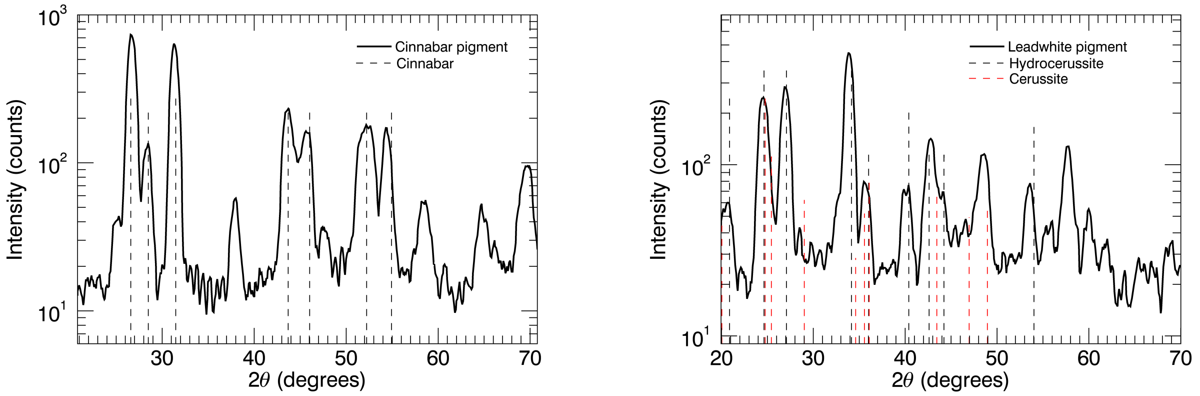

Figure 6.15: *Fit between single pigments measured with the Surface Monitor (XRD results) and the ICDD database. Left: Cinnabar pigment. Right: Lead white pigment.*

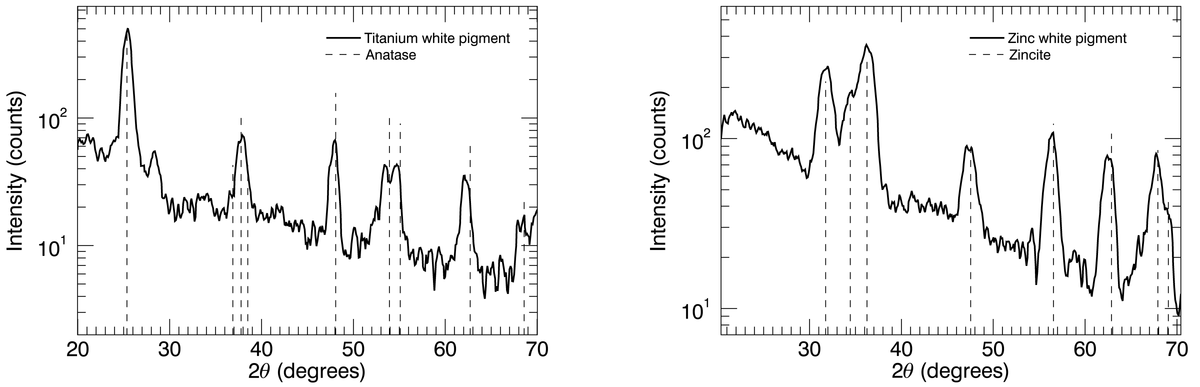

Figure 6.16: *Fit between single pigments measured with the Surface Monitor (XRD results) and the ICDD database. Left: Titanium white pigment. Right: Zinc white pigment.*

Previous results prove that for most pigments acceptable diffraction spectra could be obtained and the majority of these spectra could be identified by their corresponding measured pigment available as a mineral in the ICDD database. Without the possibility to select pigment as a sample type to find back the right phase in the database, most matching phases are found as mineral type and not as pigment. We also have to realize that the Surface Monitor instrument is a mobile equipment, so resolution available with laboratory instruments on pressed powder samples is not achievable, nevertheless, our identification objective of a selection of pigments was mostly accomplished. Now, the basis of diffraction analysis with the θ:θ based Surface Monitor, is that during the measurement, the angles are changed in small steps (most of the time 0.1°) and in theory, other layers will be

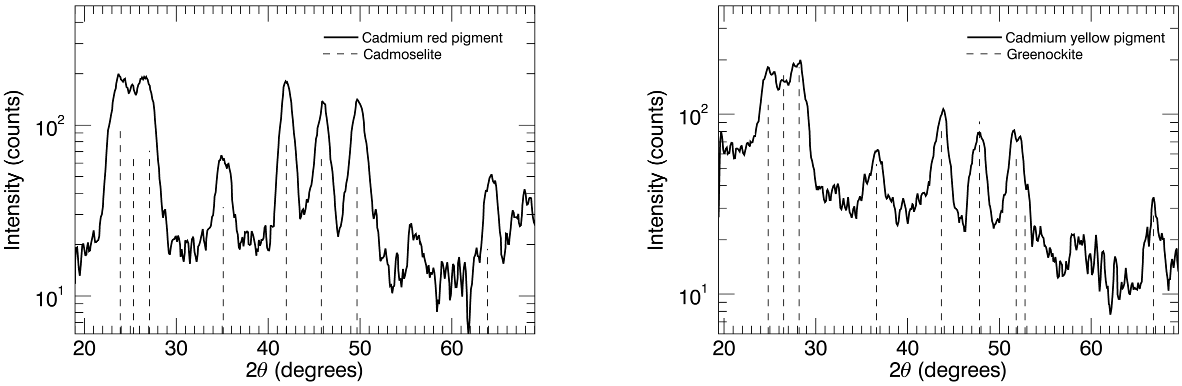

Figure 6.17: *Fit between single pigments measured with the Surface Monitor (XRD results) and the ICDD database. Left: Cadmium red pigment. Right: Cadmium yellow pigment.*

irradiated with X-rays. Therefore, in the next part, more research will be done on layered systems instead of the single pigment layer case presented here..

6.5.2 Identification in layered pigment systems

A first two layered system that has been examined, was built up using cinnabar (in hole) and azurite (back) pigment, using pigments linked to the initial selection based our first model painting. The pigments were dispersed on each side of a double sided tape and the tape is attached to a holder (see ***Fig. 6.14***). ***Fig. 6.18*** shows the result of measuring the double layered cinnabar-azurite system with first the azurite side oriented towards the Surface Monitor. The resulting diffraction spectrum was already quite satisfactory in terms of quality because the cinnabar underlayer (matched as metacinnabar by the ICDD database) could be identified (see ***Fig. 6.18*, left**). In a second measurement steps, the sample was reoriented so that the cinnabar side was directed towards the Surface Monitor but in this situation only information of the cinnabar toplayer was detectable with two unknown peaks (see ***Fig. 6.18*, right**).

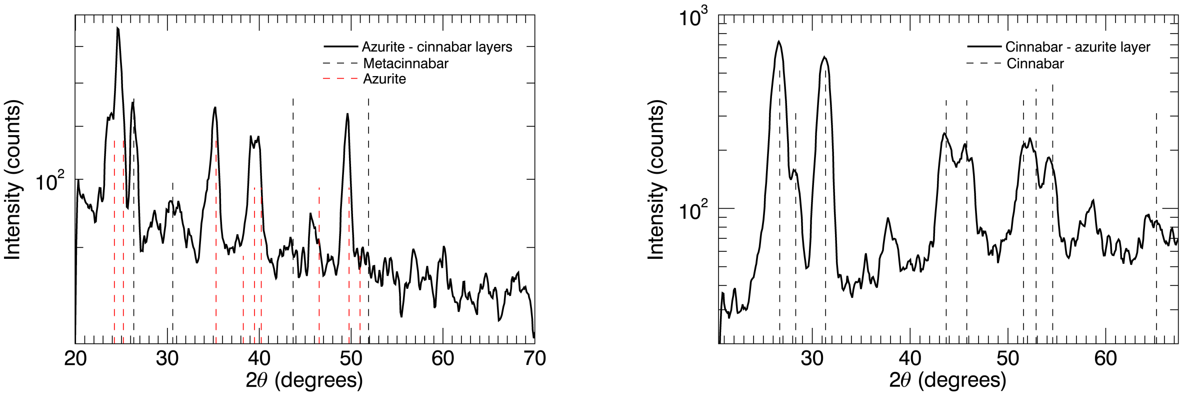

Figure 6.18: *Cinnabar (hole) - azurite (back) pigment double layered system. Left: Azurite pigment as top layer. Right: Cinnabar pigment as top layer.*

During these analyses, several questions emerged concerning the efficient use of experimental time. For example, is it really necessary to measure with a stepsize of 0.1°, resulting in a total measuring time of 4 hours, or if larger stepsizes are used (with shorter total measuring time), could we still obtain acceptable results so that both layers can still be distinguished? While trying to obtain answers to these questions, measurements on a different cinnabar-azurite double-layer sample and even a repeated experiment on the original sample - of which the results are shown in ***Fig. 6.18*** - produced unrepeatable results. This probably indicates that a very high accuracy is required to position the analyte layers in the center of rotation of the tube/detector goniometer assembly.

After the initial experiments on the cinnabar-azurite double-layer system, the even more relevant combination of pigment-calcite double layers (or more precisely, a triple layer of pigment-tape-calcite) was investigated. This choice is motivated by the fact, that paintings are typically multilayer systems consisting of a preparation layer (calcite, gypsum, lead white, etc.) overpainted with several pigment layers (sometimes wet layers on each other that can give rise to mixtures). As a result, during the following measurements, the calcite (typically used in preparation layer of paintings) layer is applied on the back of the double tape and a selection of the six pigments which gave good match with the ICDD database (see ***Table6.4***), are applied on the hole side of the double tape.

The first measurements that were performed with this strategy of combining pigments with calcite, was a (single-layer) mixture of calcite and cinnabar with corresponding results shown in ***Fig. 6.19*** shows the results of this measurement. Both components of the mixture could be identified by the software, except the peak at 58°, however, no other phase can be assigned to this peak in combination with the other peaks. This figure also shows the possibility of presenting a diffraction spectrum and how the diffraction peaks are identified by the database. In this thesis, the use of lines underneath the identified peaks is preferable instead of using symbols above the peaks, because the lines also give information about the expected heights of the matched peaks. In case of a correct match with the database, the lengths of the lines correspond approximately to the detected peak heights, which is the case in most XRD spectra shown earlier. However, this is not always the case. When this happens, we have to be critical regarding the identification of the non-matching peak.

Fig. 6.20 to ***Fig. 6.22*** show the results of a series of double layer model samples, analysed using the Surface Monitor. In ***Fig. 6.20***, the XRF sum-spectrum, which is automatically generated by the Surface Monitor at the end of an XRD measurement, is presented allowing the presence of mercury and sulfur associated with the cinnabar layer which was positioned facing to the Surface Monitor while no presence of calcium assigned to the calcite layer. The presence of Cu in the XRF spectrum originates from the Cu anode of the X-ray tube and the Ar peak is due to the fact that the measurements took place in air and not in vacuum. In the resulting diffraction pattern (the right figure), both layers can be identified by the database: the cinnabar top layer, as well as the calcite substrate layer.

The previous result was repeatable and already quite satisfying regarding the detection of different layers using the obtained diffraction spectra with the positive identification by the ICDD database. We investigated also the five other pigments (which show a good match with the database when

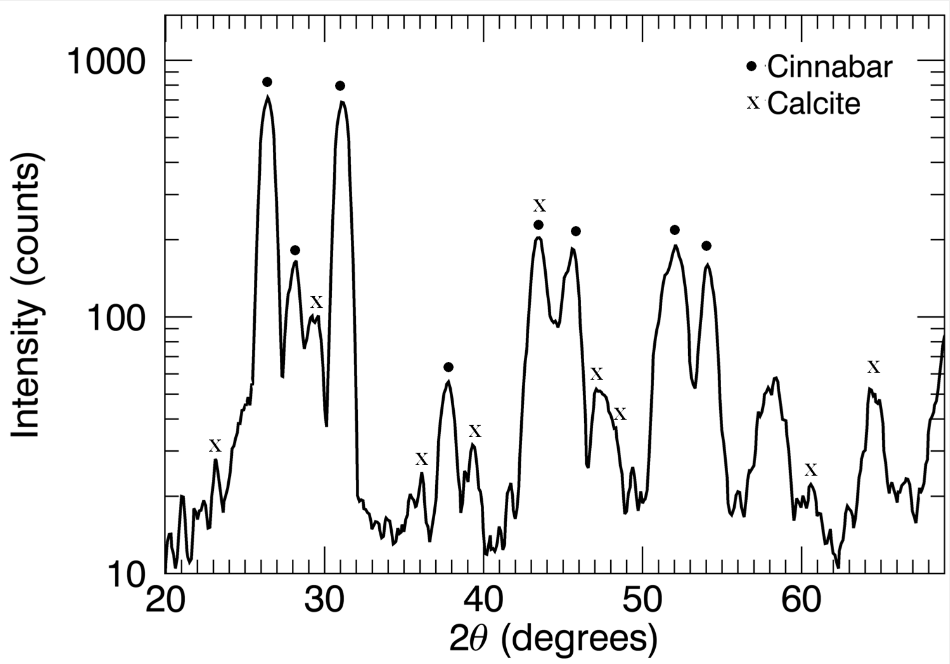

Figure 6.19: *XRD results corresponding to the measurements on the (single-layer) mixture of calcite and cinnabar pigments mounted on an adhesive tape. Diffraction scan range: $2\theta_i$=20°, $2\theta_f$=70°, stepsize of 0.1°, 30 s/step acquisition live time, 1.0 mm primary beam pinholes and 1.0 mm detector slits. The identification of both pigments present in mixture was possible.*

measured separately: cadmium red and cadmium yellow, lead white, titanium white and zinc white) or as double layered systems with the pigment side oriented towards the Surface Monitor and the calcite layer at the back. We expected to be able to identify both layers in all cases, but this was not possible for certain pigment/calcite combinations. For cadmium yellow and red, titanium white and zinc white only the identification of the top pigment layer was possible and where the identification of the calcite under layer was not self-evident (not all cases are shown). As can be seen in ***Fig. 6.21*** the identification of the top layer is possible in case of a specific type of yellow pigment (Greenockite) but the identification of the calcite preparation layer was more challenging. There are diffraction peaks which can be assigned to calcite but they always overlap with peaks of the pigment or exhibit peaks which are almost indistinguishable from the background noise. When these measurements were performed, in all cases, also the opposite orientation (calcite layer oriented towards the Surface Monitor) was tested to see if identification in this orientation was possible. ***Fig. 6.21*** also shows a diffraction spectrum obtained from these measurements and as can be seen, the identification of both layers was possible. These measurements had less significance in the context of modeling a real painting (as calcite is typically not used in a cover layer) but it proves the possibility to identify multiple layers by the XRD technique using the surface monitor. However, in some cases paintings are composed of different repainted layers, in which case it is possible that calcite is present as a cover layer above a pigment layer.

When measuring the lead white pigment ($PbCO_3$), calcite double layer with the pigment layer facing the Surface Monitor, both layers can be identified using the most intense peaks, as can be seen in ***Fig. 6.22***. This is probably due to the lower absorption in case of the white pigments compared

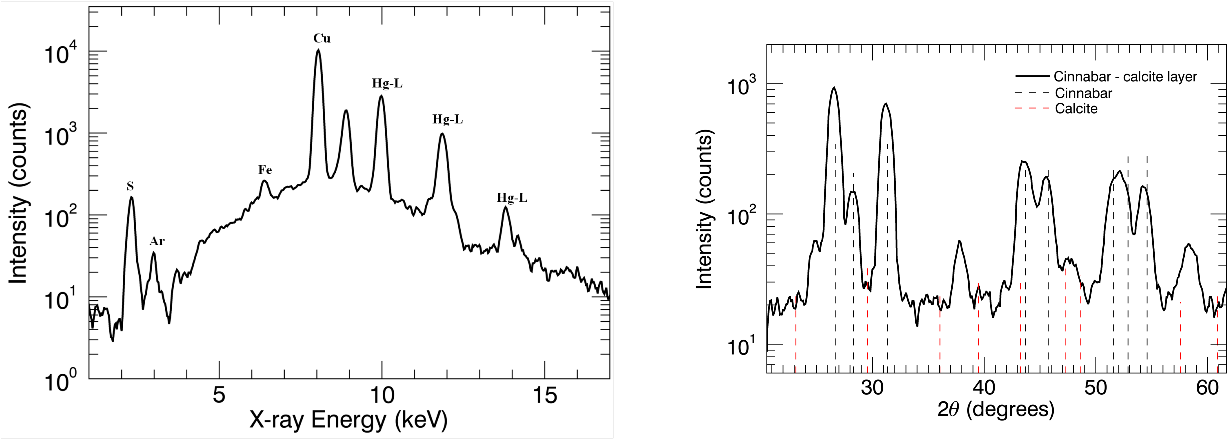

Figure 6.20: *Cinnabar-calcite double layer measured with the cinnabar layer oriented towards the Surface Monitor. Left: Simultaneously recorded XRF spectrum. Right: XRD result corresponding to a tube voltage of 18 kV, current 250 μA, slits & pinholes: 2 x 1 mm, angular range $2\theta_i$:20°, $2\theta_f$:70°, stepsize of 0.1°, 30 s/step LT.*

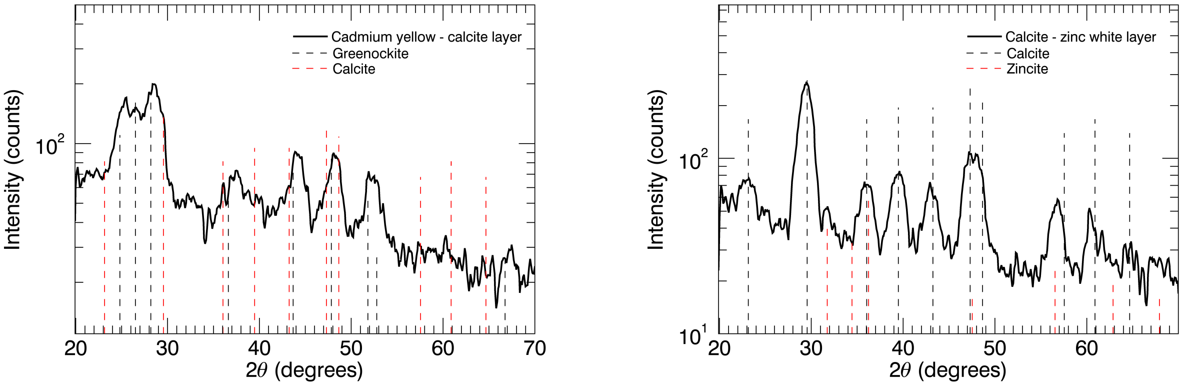

Figure 6.21: *XRD results of double layered systems measured with the Surface Monitor corresponding to a tube voltage of 18 kV, current 250 μA, slits & pinholes: 2 x 1 mm, angular range $2\theta_i$:20°, $2\theta_f$:70°, stepsize of 0.1°, 30 s/step LT. Left: Cadmium - yellow - calcite double layer where the pigment layer is oriented towards the Surface Monitor. Right: Zinc white - calcite double layer; here the calcite layer is oriented towards the Surface Monitor.*

to other pigments, which can block the X-ray signals originating from the preparation layer.

6.5.3 Model painting

Previous results demonstrate the possibilities in the identification of multilayered systems by collecting XRD spectra on test samples. In order to evaluate the surface monitor in a more realistic situation, an optimized model painting was made for analysis, as described earlier. In case of the earliest model painting, only a start angle ($2\theta_i$) of 50° could be set to measure in a safe way with no risk to touch the painting. In this way, one can see that most intense characteristic diffraction peaks are lost to identify the pigments in the painting measurements. The new, second model painting is realized on a narrow wooden oak board (which is suitable for the Surface Monitor enabling us to measure at small diffraction angles, below 20°), having colored patterns using (selected combinations

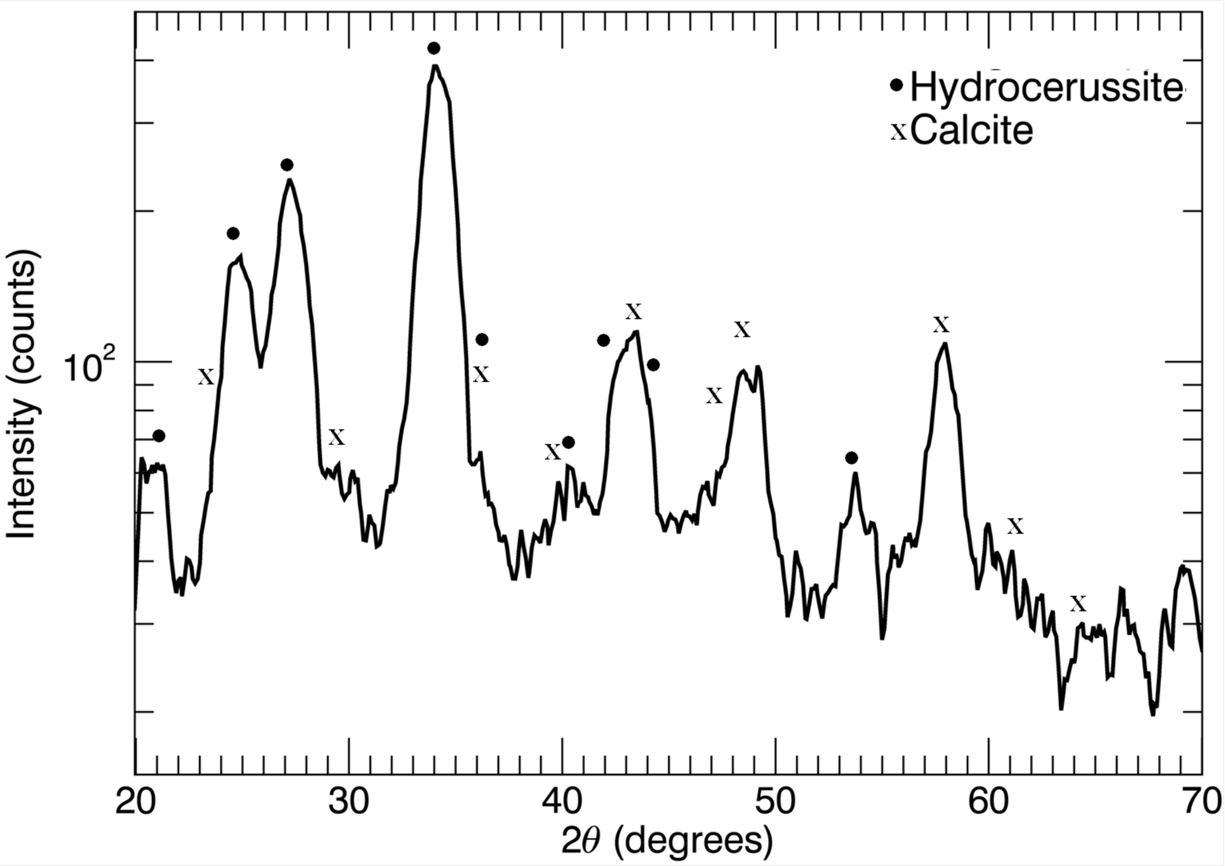

Figure 6.22: *Lead white - Calcite double tape system (with pigment in front of the instrument): identification of both layers was possible.*

of) all pigments with a detectable XRD response, including those having XRD patterns that could not be identified using the ICDD database (see ***Table6.4***). In contrast with the first model painting, no a priori knowledge about the amount of applied pigment was available in case of the second model painting. This posed no problem with respect to evaluating the surface monitor, because we were only interested in the possibilities of identifying the various paint layers. In the future, more research needs to be done to evaluate the quantification possibilities of the Surface Monitor which could not be studied systematically during this Ph.D. work.

Fig. 6.23 and ***Fig. 6.24*** presents some of the results regarding the measurements of pigments on the model painting. ***Fig. 6.23*** shows the result of the measurement corresponding to a cadmium yellow pigment, where identification of the top layer was possible, but the unambiguous identification of the calcite preparation layer was challenging. Only three small XRD peaks could be identified as calcite and the question is, if this is enough to define that calcite is also present. ***Fig. 6.24*** shows the result of a measurement corresponding to a white TiO_2 pigment, in which case clear identification of both layers was possible.

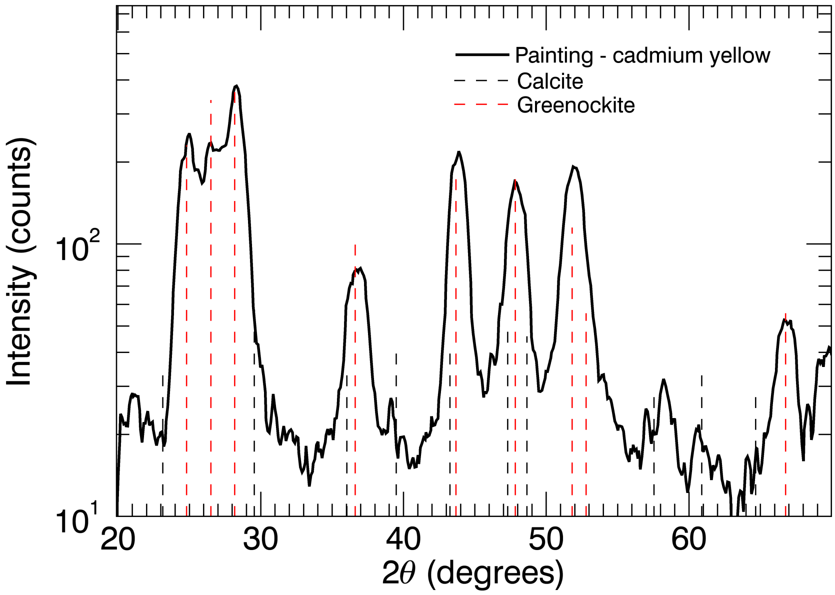

Figure 6.23: *Model painting analysis showing an XRD spectrum measured from a cadmium yellow layer (Greenockite) on a calcite layer. While matching the XRD response of the Cd yellow (top layer) with the ICDD database is straightforward, the unambiguous identification of the covered calcite layer is problematic. Experimental settings: Cu-tube voltage 18 kV, current 250 μA, slits & pinholes: 2 x 1 mm, angular range $2\theta_i$:20°, $2\theta_f$:70°, stepsize of 0.1°, 30 s/step LT.*

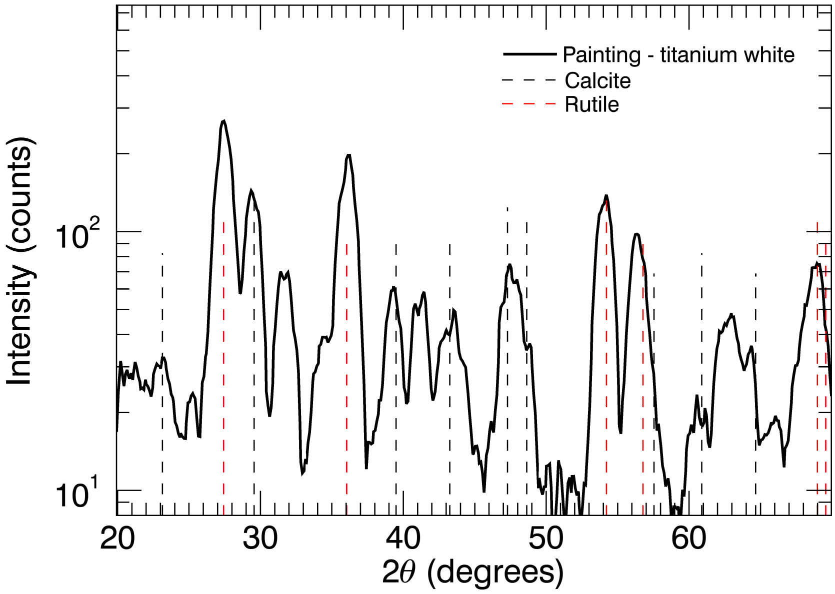

Figure 6.24: *Model painting analysis showing an XRD spectrum measured from a titanium white layer (rutile) on a calcite layer. In this case both phases could be identified unambiguously using the ICDD database. Experimental settings: Cu-tube voltage 18 kV, current 250 μA, slits & pinholes: 2 x 1 mm, angular range $2\theta_i$:20°, $2\theta_f$:70°, stepsize of 0.1°, 30 s/step LT.*

6.6 Research of lead alloyed printing letters

As a final illustrative example on the use of the surface monitor, more in line with studies on real life cultural heritage objects, lead alloyed printing letters collected in the Museum Plantin-Moretus (Antwerp, Belgium) are analyzed. This site encompasses the original workshop, presses, library and the family houses of Plantin and Moretus. The exhibition in this museum covers a printing history from the 16^{th} century until the 19^{th} century [25]. The lead alloyed printing letters show exceptional corrosion problems, including severe expansion and decomposing of the metal alloy. Previous research on powdered corrosion samples showed that a range of lead corrosion products such as cerussite ($PbCO_3$), hydrocerussite ($2PbCO_3.Pb(OH)_2$), lead acetate oxide hydrate ($Pb_3(CH_3CO_2)_2Pb.H_2O$), lead formate ($PbC_2H_2O_4$) and a crystalline phase with a structure of Sb could be identified [25]. One of the questions regarding these corroded artifacts - provided by P. Storme (UA, Antwerp) - was whether the corrosion products found in the powdered samples could be directly identified by *in situ* XRD analysis of the printing letters themselves, without any sample preparation. ***Fig. 6.25*** shows the XRD results of the measurements on one letter, where the successful identification of cerussite, lead formate and antimony oxide was possible. Further details on this research can be found in [26].

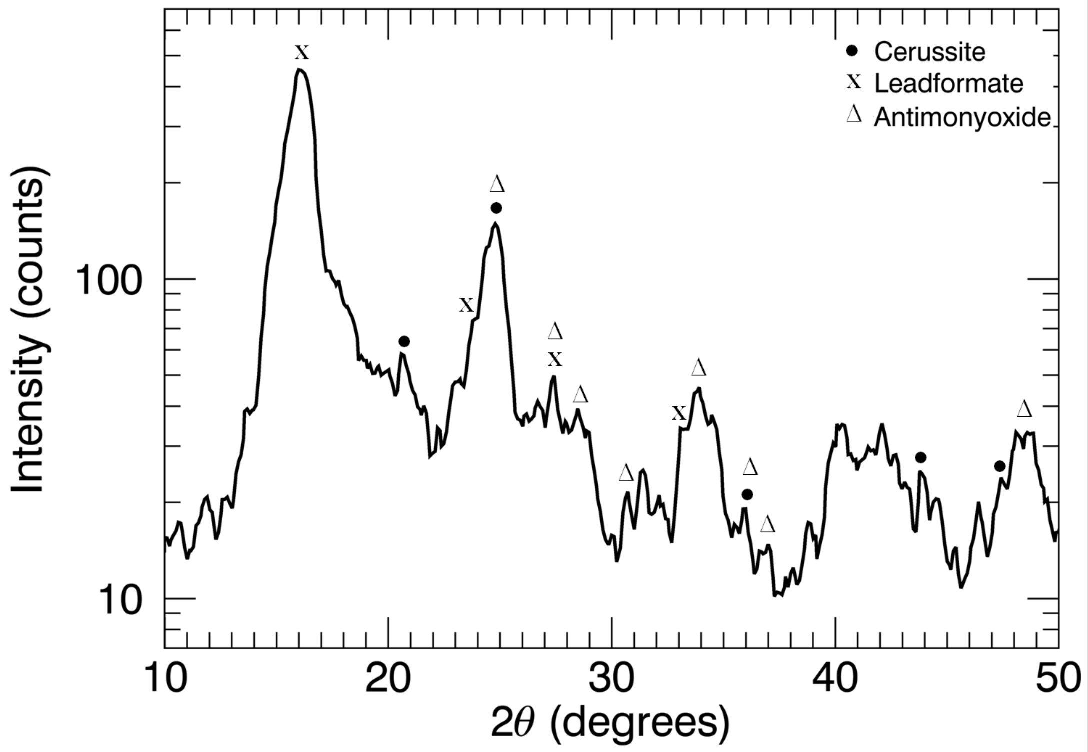

Figure 6.25: *XRD result of the measurements on lead alloyed printing letters, experimental settings: Cu-tube voltage 18 kV, current 250 μA, slits & pinholes: 2 x 1 mm, angular range $2\theta_i$:20°, $2\theta_f$:90°, stepsize of 0.1°, 30 s/step LT.*

6.7 Conclusion

This chapter focussed on the characterization of a new, commercially available, mobile instrument for simultaneous XRD/XRF measurements, which is one of the lightest of its kind (3.5 kg). The main features of the so-called Surface Monitor were described, including the choice of optimal measuring conditions and its main figures of merit. The instrument has the choice of a Cu or a Mo X-ray tube to be used in conjunction with a Si-pin diode (ED) detector, mounted on a XRD goniometer using the Bragg-Brentano θ:θ geometry. The delivered software allows to operate the instrument in a simple way and to perform data analysis by using its graphical user interface to find matching XRD patterns based on the installed ICDD databank. The use of the instrument for *in situ* analysis was demonstrated by test measurements performed on standards and model samples. As shown by the illustrative examples on layered pigment samples, a model painting and lead alloyed printing letters, the identification of the main phases were possible, and in some cases even the underlying layer could be identified in case of double layer systems. The instrument combines XRD data acquisition with XRF data collection, the latter achieving minimum detection limits in the 50-1000 ppm in the atomic number range of 12 to 82. A clear advantage of the combined XRF-XRD mode is the possibility to obtain both elemental and crystal structural information simultaneously from a single measurement. This, next to providing extra chemical information, also aids the unambiguous identification of the detected crystalline phases based on their elemental signature.

Bibliography

[1] G. E. Gigante and S. Sciuti, “A multipurpose energy dispersive x-ray spectrometer for low, medium and high-Z materials analysis,” *The International Journal of Applied Radiation and Isotopes*, vol. 35, pp. 481–488, June 1984.

[2] A. Adriaens, “Non-destructive analysis and testing of museum objects: An overview of 5 years of research,” *Spectrochimica Acta Part B: Atomic Spectroscopy*, vol. 60, pp. 1503–1516, Dec. 2005.

[3] P. Vandenabeele, “Archaeometry, an interdisciplinary approach.,” in *Analytical and bioanalytical chemistry*, vol. 387, p. 735, Springer, Feb. 2007.

[4] R. Cesareo, G. Gigante, P. Canegallo, A. Castellano, J. Iwanczyk, and A. Dabrowski, “Applications of non-cryogenic portable EDXRF systems in archaeometry,” *Nuclear Instruments and Methods in Physics Research Section A, Accelerators, Spectrometers, Detectors and Associated Equipment*, vol. 380, pp. 440–445, Oct. 1996.

[5] A. Longoni, C. Fiorini, P. Leutenegger, S. Sciuti, G. Fronterotta, L. Stru, and P. Lechner, “A portable XRF spectrometer for non-destructive analyses in archaeometry,” *Nuclear Instruments and Methods in Physics Research A*, vol. 409, pp. 407–409, 1998.

[6] P. Vandenabeele, K. Castro, M. Hargreaves, L. Moens, J. M. Madariaga, and H. G. M. Edwards, "Comparative study of mobile Raman instrumentation for art analysis.," *Analytica chimica acta*, vol. 588, pp. 108–16, Apr. 2007.

[7] G. Artioli, "Science for the cultural heritage: the contribution of X-ray diffraction," *Rendiconti Lincei*, vol. 24, pp. 55–62, Oct. 2012.

[8] A. Mendoza Cuevas and H. Perez Gravie, "Portable energy dispersive X-ray fluorescence and X-ray diffraction and radiography system for archaeometry," *Nuclear Instruments and Methods in Physics Research Section A, Accelerators, Spectrometers, Detectors and Associated Equipment*, vol. 633, pp. 72–78, Mar. 2011.

[9] M. Uda, "In situ characterization of ancient plaster and pigments on tomb walls in Egypt using energy dispersive X-ray diffraction and fluorescence," *Nuclear Instruments and Methods in Physics Research Section B, Beam Interactions with Materials and Atoms*, vol. 226, pp. 75–82, Nov. 2004.

[10] M. Uda, A. Ishizaki, R. Satoh, K. Okada, Y. Nakajima, D. Yamashita, K. Ohashi, Y. Sakuraba, A. Shimono, and D. Kojima, "Portable X-ray diffractometer equipped with XRF for archaeometry," *Nuclear Instruments and Methods in Physics Research Section B, Beam Interactions with Materials and Atoms*, vol. 239, pp. 77–84, Sept. 2005.

[11] J. Salomon, P. Walter, A. Gianoncelli, J. Castaing, L. Ortega, E. Dooryh, J. Hodeau, and P. Bordet, "A portable instrument for in situ determination of the chemical and phase compositions of cultural heritage objects," *X-RAY SPECTROMETRY*, no. March, pp. 418–423, 2008.

[12] a. Duran, J. L. Perez-Rodriguez, T. Espejo, M. L. Franquelo, J. Castaing, and P. Walter, "Characterization of illuminated manuscripts by laboratory-made portable XRD and micro-XRD systems.," *Analytical and bioanalytical chemistry*, vol. 395, pp. 1997–2004, Dec. 2009.

[13] G. Gatto Rotondo, F. Romano, G. Pappalardo, L. Pappalardo, and F. Rizzo, "Non-destructive characterization of fifty various species of pigments of archaeological and artistic interest by using the portable X-ray diffraction system of the LANDIS laboratory of Catania (Italy)," *Microchemical Journal*, vol. 96, pp. 252–258, Nov. 2010.

[14] I. Nakai and Y. Abe, "Portable X-ray powder diffractometer for the analysis of art and archaeological materials," *Applied Physics A*, vol. 106, pp. 279–293, Dec. 2011.

[15] D. Blake, C. Bryson, and F. Freund, "Design of an X-Ray Diffraction/X-Ray Fluorescence Instrument for Planetary Applications," *Abstracts of the Lunar and Planetary Science Conference*, vol. 23, pp. 117–118, 1992.

[16] D. F. Blake, C. Bryson, and F. Freund, "X-ray diffraction apparatus," 1993.

[17] S. Cornaby, A. Reyes-Mena, H. K. Pew, P. W. Moody, T. Hughes, A. Stradling, D. Turner, and L. Knight, "An XRD / XRF instrument for the microanalysis of rocks and minerals," *Measurements Science and Technology*, vol. 12, pp. 676–683, 2001.

[18] G. Van der Snickt, C. Miliani, K. Janssens, B. G. Brunetti, A. Romani, F. Rosi, P. Walter, J. Castaing, W. De Nolf, L. Klaassen, I. Labarque, and R. Wittermann, "Material analyses of Christ with singing and music-making Angels, a late 15th-C panel painting attributed to Hans Memling and assistants: Part I. non-invasive in situ investigations," *Journal of Analytical Atomic Spectrometry*, vol. 26, no. 11, p. 2216, 2011.

[19] S. Assing, "http://www.assing-group.it/index_eng.html," 2014.

[20] A. Pifferi, G. Campi, C. Giacovazzo, and E. Gobbi, "A New Portable XRD / XRF Instrument for Non-destructive Analysis," *CROATICA CHEMICA ACTA*, vol. 82, no. 2, pp. 449–454, 2009.

[21] V. K. Pecharsky and P. Y. Zavalij, *Fundamentals of Powder Diffraction and Structural Characterization of Materials.* Springer, second edi ed., 2009.

[22] Y. Waseda, E. Matsubara, and K. Shinoda, *X-Ray Diffraction Crystallography.* Springer, 2011.

[23] B. Vekemans, K. Janssens, L. Vincze, F. Adams, and P. Vanespen, "Analysis of X-Ray-spectra by iterative least-squares (AXIL) - New developments," *X-Ray spectrometry*, vol. 23, no. 6, pp. 278–285, 1994.

[24] P. Vanespen, K. Janssens, and J. Nobels, "AXIL-PC, software for the analysis of complex-X-Ray spectra," *Chemometrics and intelligent laboratory systems*, vol. 1, pp. 109–114, Nov. 1986.

[25] P. Storme, M. Jacobs, and E. Lieten, "Research on Corrosion of Lead Printing Letters from the Museum Plantin-Moretus, Antwerp," *Procedia Chemistry*, vol. 8, pp. 307–316, Jan. 2013.

[26] P. Storme, A. Selucká, K. Rapouch, M. Mazík, F. Vanmeert, K. Janssens, L. Van de Voorde, B. Vekemans, L. Vincze, J. Caen, and K. De Wael, "Composition and Corrosion Forms on Archaeological and Non-Archaeological Historic Printing Letters from the Moravian Museum, Memorial of Kralice Bible, the Czech Republic and the Museum Plantin Moretus Antwerp, Belgium," 2015.

Chapter 7: Confocal micro-XRF/XANES analysis on insects trapped in amber

Chapter 7 provides on outlook towards more advanced three-dimensional elemental and chemical-state analysis methods using confocal X-ray microbeam techniques for potential future applications in the field of palaeontology. Unique samples from this field can be regarded as 'heritage from nature' as opposed to cultural heritage materials created by earlier generations of humanity.

7.1 Introduction

Amber is a light, organic substance that is usually yellow or orange in colour and often transparent. It is easy to carve and polish, which makes it a popular material for jewellery. Amber is fossilized resin that exuded out of the bark of trees protecting a tree by blocking gaps in its bark. It has antiseptic properties that protect the tree from diseases and it is also very sticky and can trap insects that come in contact with this material. Different types of trees produce different types of resin in different amounts but not all tree resins can form amber, as most gets broken down by decay. Nowadays, only two types of plants produce stable resins that could, in time, fossilize into amber, namely the Kauri pine of New Zealand and species of the legume *Hymenae* in East-Africa and South and Central-America. Amber can be found in many parts of the world, but most of the deposits are small and localized [1].

Often, when resin from the bark of a tree, insects become trapped and engulfed in the sticky material. When the resin falls to the ground and becomes incorporated into the soil and sediments, it fossilizes into amber over a period of millions of years. Any insects and other organisms that have been trapped in it are well preserved. The amber acts actually as a protective container for the insects and any other organism that it may include, turning it into an interesting subject for further investigations. ***Fig.7.1*** shows a progressive scheme how this capturing of insects in amber takes place. After exuding the resin, trapping the insect and fossilizing, one can see that the insects are preserved with remarkable detail [1]. The production of amber from resin is called amberization and several factors affect the production. Resin contains liquids such as oils, acids and alcohols, including aromatic compounds that produce the distinctive resinous smell. The liquids are volatile and they could dissipate and evaporate from the resin by which polymerization will occur. Hardened resin is known as copal and when this copal becomes incorporated into soil and sediments, it continues to polymerize and lose volatiles until the resultant amber is completely polymerized, which has no volatile liquids and which become inert [1].

The study of elemental composition of insects is a way to obtain data about environmental conditions in certain regions and about characteristics of insect remote migrations. Previous studies show the possibilities of examining insects whether or not trapped in amber using mostly Raman spectroscopy or phase contrast X-ray synchrotron radiation (SR) tomography [2–6]. Our goal was to obtain chemical information of the trapped insects without extracting the organisms from the amber using the EDAX eagle (laboratory micro-XRF spectrometer), to execute preliminary investigation, and SR confocal micro-XRF equipment (Beamline L, Hasylab, DESY, Hamburg, Germany). ***Fig.2.7*** in chapter 2 shows pictures of the investigated insects trapped in amber samples where the

Figure 7.1: *Progressive scheme how the capturing of insects in amber works: From exuded resin from bark of trees, to enveloping the trapped insect by resin and ending with the fossilizing (in quite some time: up to millions of years) when the resin falls into the ground.*

obtained chemical information consists of elemental information and local chemical-state information of a specific element of interest in the sample.

7.2 Experimental

Because of the limited access to SR facilities, preliminary measurements using routinely available laboratory instrumentation can be used to perform the initial characterization of the samples, which also helps to reject uninteresting samples, to detect and tackle potential elemental interference problems and gives the possibility to optimize sample mounting. In case of these studies, the EDAX Eagle III scanning micro-XRF instrument was used to perform the preliminary investigations. More detailed information about this instrument is already given in chapter 2 (see section 2.3.4). The confocal SR micro-XRF/XAS measurements, to obtain elemental and chemical-state information, were performed at beamline L of HASYLAB, DESY, a SR facility located in Hamburg, Germany.

Synchrotron Radiation induced X-ray fluorescence spectroscopy is a non-destructive method for the qualitative and quantitative determination of elements with detection limits down to the sub-ppm level. The examination of the insects (trapped in amber) at this SR facility made use of a confocal set-up which is obtained by the mounting of a polycapillary halflens in front of the detector. The collected XRF signal is produced in the intersection volume, defined by the incoming beam and the acceptance of the polycapillary. In this way it is possible to acquire direct information from the specified microscopic volume within a sample body. ***Fig. 7.2*** provides an overview on the employed confocal set-up used for the measurements of the amber samples. As can be seen in this figure, the polycapillary optic is used as a focusing element for the primary beam (here SR, coming from the bottom left on the photo, see black arrow) and as a “smart” collimator in front of the detector. Polycapillaries in front of the sample are used to increase the flux density of the beam on a microscopic spot on the surface of a sample ((see section 2.3.2 to know more about the working principles of this X-ray focusing optic). By mounting the polycapillary in front of the detector, using it as a detector collimator, one confines the detection volume to the coinciding foci of the two polycapillaries, allowing depth resolved two- and three-dimensional XRF analysis on the microscopic scale. Due to its high-energy filtering, the detector polycapillary suppresses high-energy fluorescence lines and scatter peaks, progressively cutting down background intensity above 25 keV. It should be noted however, that this imposes a practical limit for the detection of high-energy XRF lines, limiting the usefulness of this method.

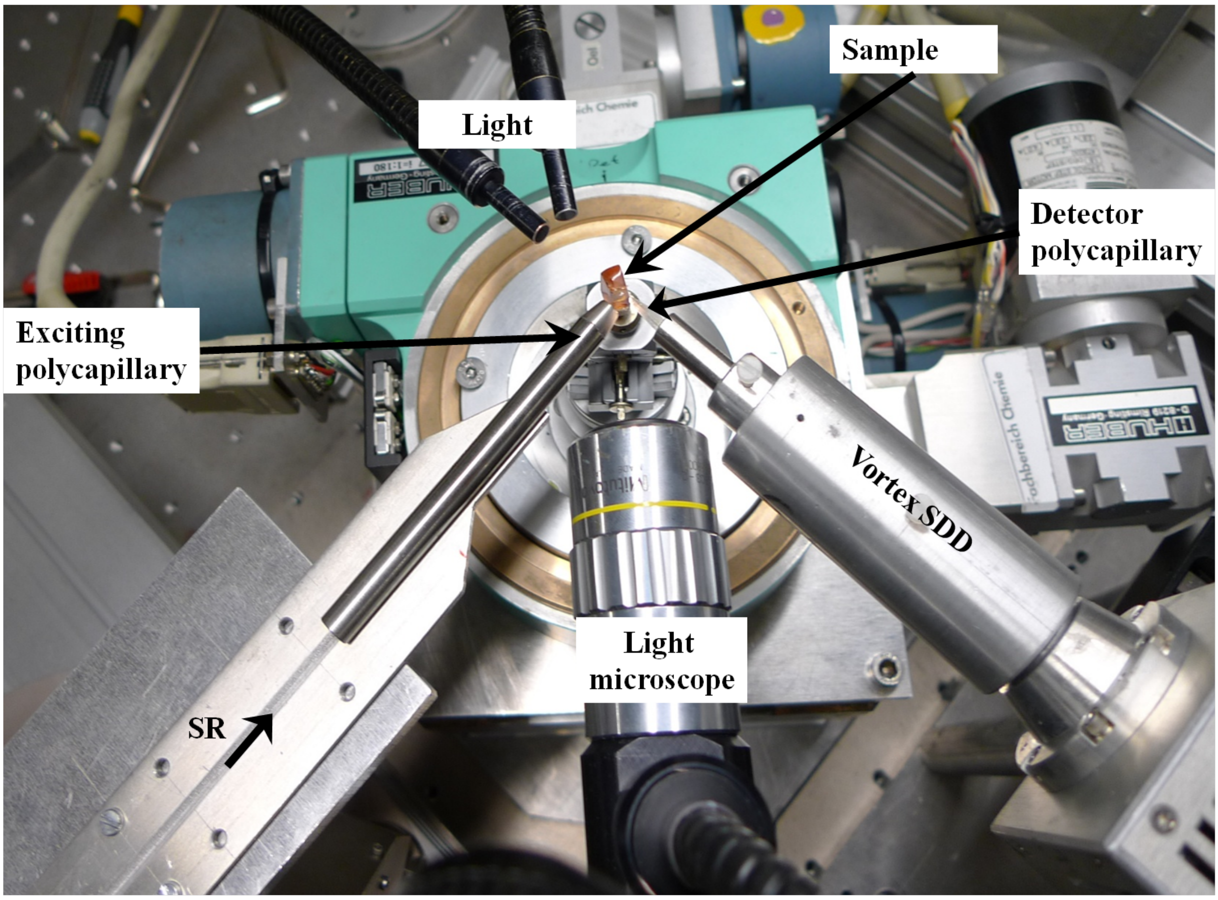

Figure 7.2: *Confocal SR micro-XRF set-up at beamline L of Hasylab (DESY, Hamburg, Germany).*

To obtain the local chemical, electronic and structural information on a specific element of interest in the sample, X-ray absorption spectroscopy (XAS) in fluorescence mode was used which is a complementary X-ray based technique. Both XRF and XAS techniques can be applied in the same confocal mode, which is described above. ***Fig. 7.3*** shows schematically incident X-rays of intensity I_0 and energy E, transmitted through a sample with absorption coefficient μ(E) having a thickness t. According to the Beer-Lambert Law, the transmitted intensity I_t is

$$I_t(t) = I_0 e^{-\mu(E)t} \tag{7.1}$$

Over large energy regions, μ(E), is a smooth function of the photon energy and decreases with increasing photon energy (E). If the latter equals or exceeds the binding energy of a core electron, a new absorption channel becomes available in which the photon is absorbed by ejecting an electron from its shell, thereby creating a photoelectron and a core-hole. This leads to a sharp increase in absorption coefficient as shown schematically in ***Fig.7.3***. Above the absorption edge, μ(E) continues to decrease with increasing photon energy until the next binding energy level (i.e. absorption edge energy) is reached. The core-hole is subsequently filled via an electron transition from a higher shell, coupled with the emission of either an X-ray fluorescence photon or Auger electron [7]. The corresponding energy difference is released mainly via fluorescence X-ray or Auger electron emission (see chapter 2, section 2.2.1).

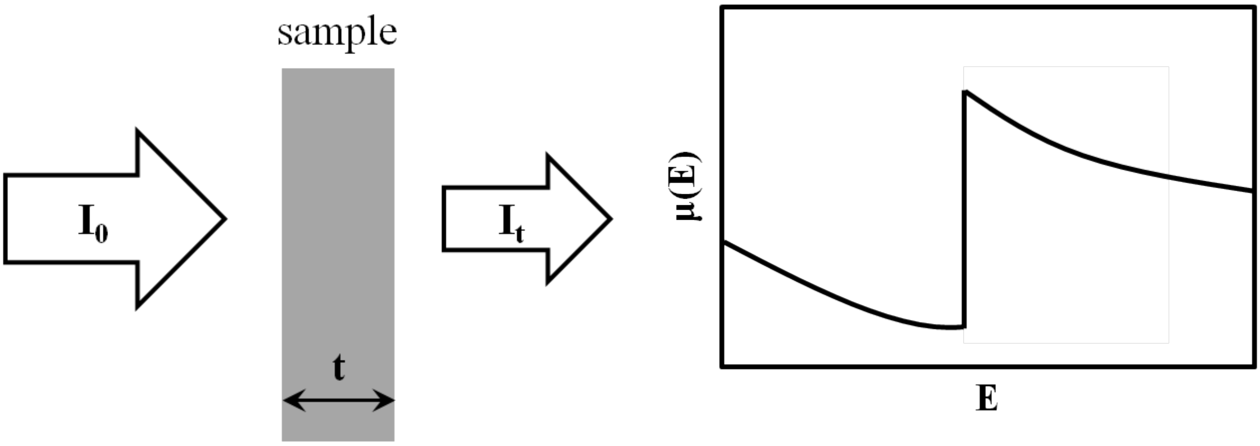

Figure 7.3: *Left: Scheme of incident and transmitted X-ray beam. Right: Absorption coefficient μ(E) versus photon energy E around an absorption edge [7].*

At the smallest X-ray energies for which the photon can be absorbed, a photoelectron will be excited to unoccupied bound states of the absorbing atom as shown schematically in ***Fig.7.4***. This can lead to a strong increase of the absorption coefficient (μ) at particular X-ray energies corresponding to the energy difference between the core level and the unoccupied states. For higher X-ray energies, the photoelectron is promoted to a free or continuum state and the created photoelectron wave propagates outwards and will be scattered by neighboring atoms. The outgoing and scattered waves interfere in a manner that depends on the geometry of the absorber's environment and on the photoelectron wavelength which changes with photon energy. The constructive or destructive interference of the outgoing and scattered photoelectron waves increases or decreases the absorption probability, creating an energy-dependent fine structure of the absorption coefficient as can be seen in ***Fig.7.4***. Two regions are commonly distinguished, namely the X-ray absorption near edge structure (XANES) and the extended X-ray absorption fine structure (EXAFS) [7].

In our experiment, we used fluorescence mode confocal-XANES measurements to gather information on the Fe distribution and speciation within the insects that are trapped in amber. The region very close to the absorption edge is sensitive to the chemical bonding and thus characteristic for different oxidation states of the absorbing atom. The XANES features are also influenced by strong multiple scattering effects which depend on the three-dimensional geometry of the local structure around the central atom, and can distinguish between different coordination geometries. Theoretical

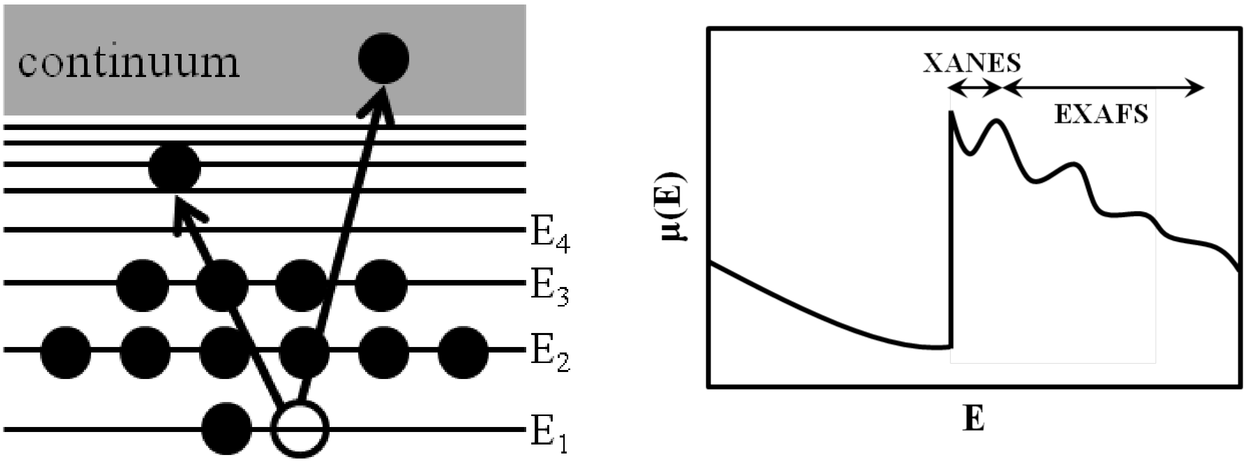

Figure 7.4: *Left: Schematic representation of the X-ray absorption process. Right: Absorption coefficient $\mu(E)$ versus photon energy E including the fine structure above the edge divided into the XANES and EXAFS regions [7].*

calculations of the fine structure in this region are complex and the accuracy of such simulations is still limited and therefore, analysis typically compares the measured spectra to those of known standards to know the oxidation state of the investigated elements [7].

7.3 Results

7.3.1 Preliminary studies using laboratory micro-XRF

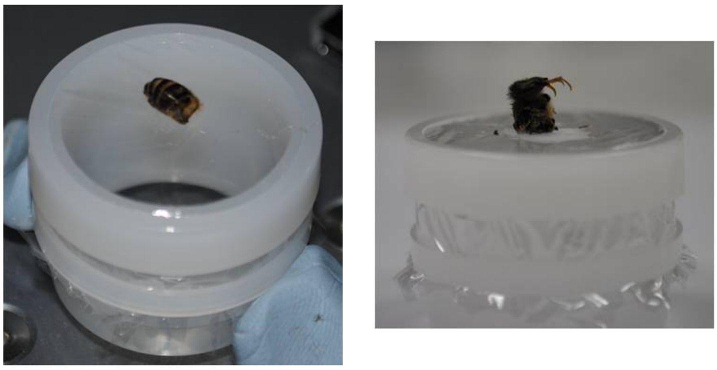

Figure 7.5: *Snapshot of part of freeze-dried bees, measured using the EDAX eagle III micro-XRF spectrometer.*

The preliminary studies using laboratory micro-XRF instrumentation were performed on sections of freeze-dried bees, provided by Prof. Dr. F. Jacobs (department of physiology, UGent), are attached on ultralene films which are stretched over a polymer cup as can be seen in ***Fig.7.5***. The insects are investigated using the EDAX Eagle III micro-XRF laboratory spectrometer both in point measurement mode and in scanning mode to map the abdomen and head of the samples respectively. The point measurements (1000 s LT, 25 μm beam size, 40 kV and 250 μA) on the abdomen of a bee revealed that the exoskeleton yields valuable elemental information compared to e.g. the hair present on the chitin of the shell resulting in no detectable elemental signal. These results are visualized ***Fig.7.6***

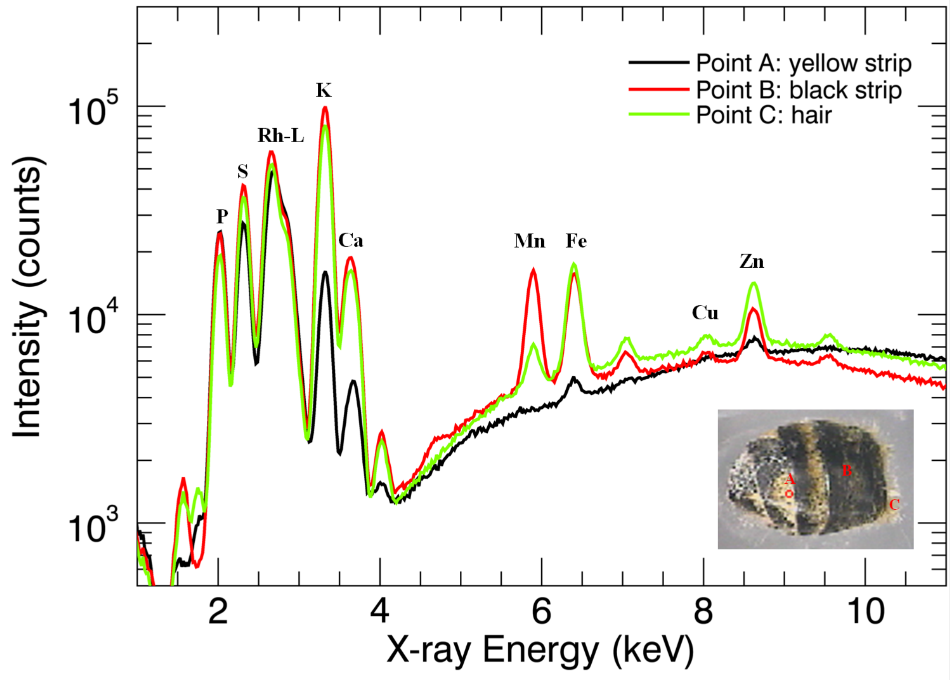

Figure 7.6: *XRF results of the point measurements on the torso of a bee, with indications of the measured points (A-C) on a picture of the abdomen at the bottom right (1000 s LT, 25 μm beam size, 40kv and 250 μA).*

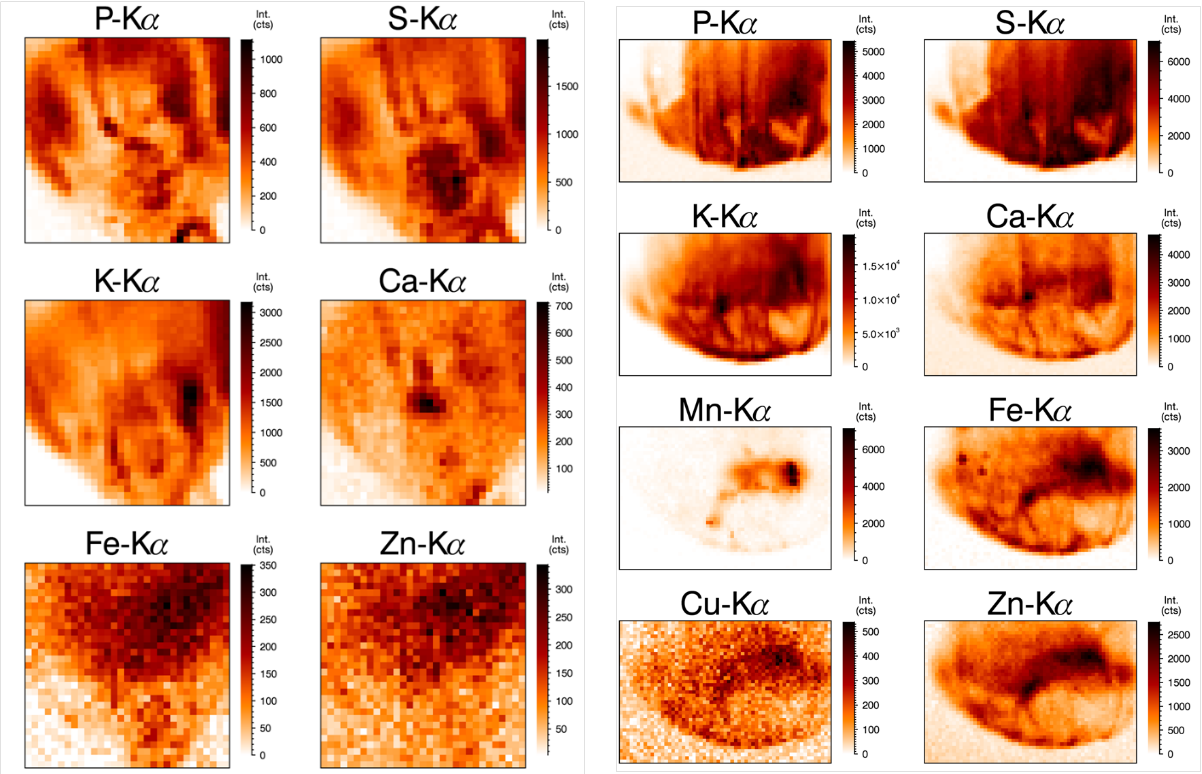

Figure 7.7: *XRF mapping results of the measurements on the abdomen (left) and head (right) of a bee: respectively dimensions of the maps: 61 x 41 (100 μm stepsize) and 31 x 31 (100 μm stepsize).*

Next to the point measurements, also mappings on the abdomen and the head of the bee were performed using the scanning mode of the instrument. Both mappings made use of a beam size of 100 μm and respectively a measuring time of 20 s or 5 s per point. The results of these mappings can be seen in ***Fig.7.7***. In spite of the short measuring time per point, the obtained elemental maps show sufficiently high intensities for all detectable characteristic chemical elements which is a promising observation regarding the possibility to perform confocal XRF/XANES imaging on insects trapped in amber. In the mapping of the chitin shell of the abdomen, it is even possible to discern the segmented structure in the elemental maps of P and S while the maps of K, Ca, Mn, Fe and Zn give apparent information about the inner structure of the bee.

7.3.2 Preliminary studies on insects trapped in amber

We had six samples of insects trapped in amber at our disposal and using the readily available laboratory micro-XRF EDAX Eagle spectrometer enabled us to select the most interesting samples. The limited measuring time available during the SR confocal micro-XRF investigations did not allow to measure all six samples. ***Fig.7.8*** shows an image of the amber sample as a whole and also an enlargement of the insects trapped in this amber using a microscope. First a fast mapping was performed using a measuring time of 0.5 s per pixel to get fast (in less than two hours) an idea about the possibility to detect the trapped insect underneath a certain layer of amber. ***Fig.7.9*** shows the results of this fast mapping and we can conclude that it is possible to image the trapped insect without removing it and thus the amber surrounding the insects does not result in significant absorption effects with respect to the detection of even low atomic number elements, such as Al, Si, P, etc. The image of the head of the trapped insects is quite faint because of the short measuring time per pixel, so to know more which characteristic elements are present, a long mapping was set up with measuring time per point of 10 s (total scanning time of ± 24h) and the results can be seen in ***Fig.7.9***. These results suggest that it is possible to perform the same measurements with confocal SR micro-XRF spectroscopy with guarantee to visualize the trapped insects.

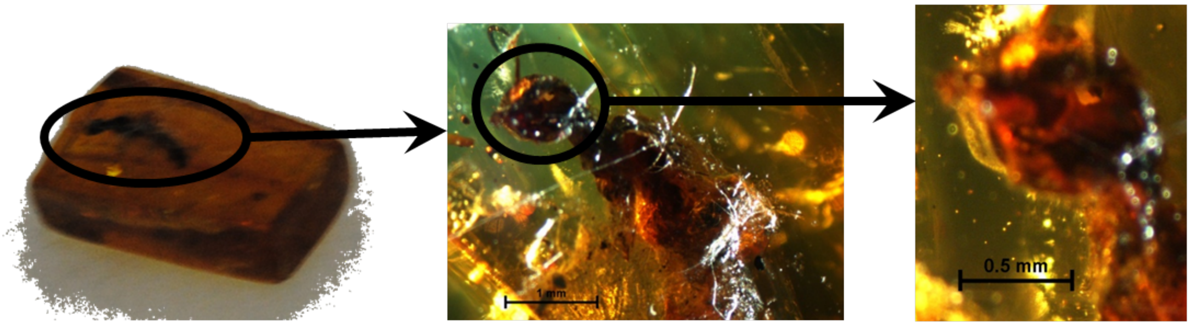

Figure 7.8: *Picture of the insect trapped in amber: mapping (dimension: 2.18 x 1.68 mm and 25 μm beam size and stepsize) was executed on the upper part on the insect using the EDAX Eagle.*

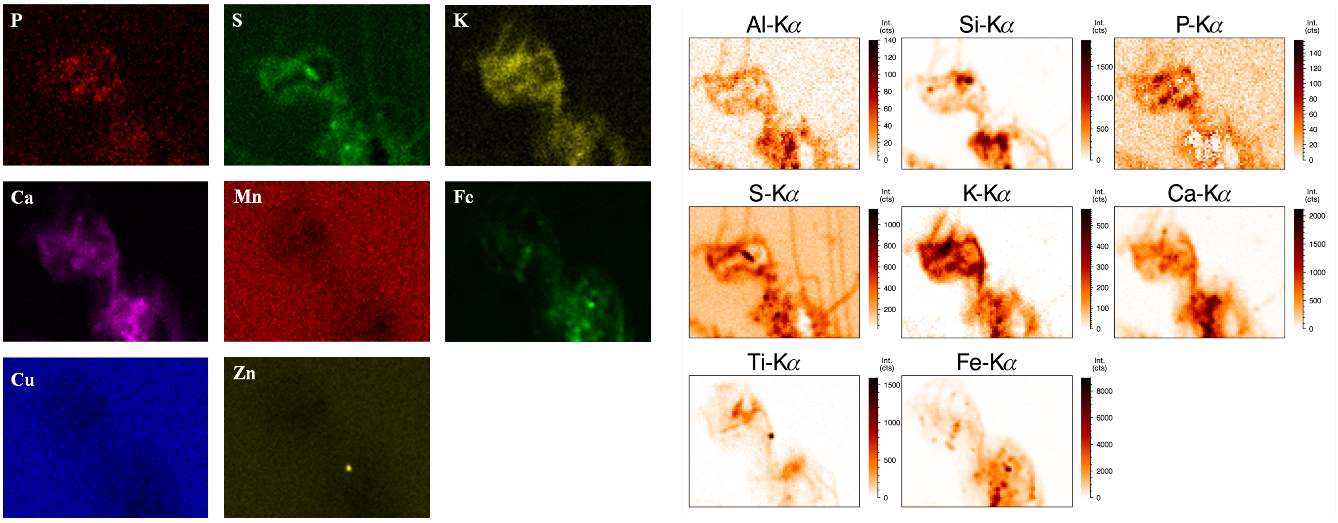

Figure 7.9: *XRF mapping results of insect trapped in amber with the EDAX Eagle. Left: fast mapping (LT = 0.5 s/pixel). Right: slow mapping (LT = 10 s/pixel).*

7.3.3 Confocal SR micro-XRF results

The advantages of performing the measurements using confocal SR micro-XRF, instead of being satisfied with the results of the EDAX Eagle measurements, include the possibility of three-dimensional analysis with lower background due to linear polarization, and due to the presence of confocal optics, tunable and higher (monochromatic) X-ray intensity, (sub)ppm detection limits and faster collection of results. A result of the *in situ* scanning measurement corresponding to a 22 μm thick slice across the head of the same (trapped) insect using confocal SR micro-XRF can be seen in ***Fig.7.10***. The mapping, with dimensions of 0.86 mm x 0.61 mm, was executed using an excitation energy of 7.2 keV, measuring-time of 5 sec/pixel with 10 μm stepsize and 22 μm beam size and also 22 μm polycapillary acceptance. Chlorine (Cl), vanadium (V), chromium (Cr) and manganese (Mn) are detectable with SR beside the elements already detected by the laboratory instrument.

As already discussed above, X-ray Absorption Near Edge Structure or XANES measures the absorption around the K or an L absorption edge of an element of interest which is Fe in the case of the insects trapped in amber. ***Fig.7.11* (left)** shows the obtained elemental map of Fe with the Fe-rich spots indicated by numbers from 1 to 5. The confocal XANES measurements were performed on these hotspots around the Fe-K edge (7112 eV) and the results can be seen in ***Fig.7.11* (right)** and ***Fig.7.12***. These XANES measurements are actually point measurements in a volume of 22x22x16 μm^3. The detected XANES spectra allowed us to obtain information on the Fe chemical-state within these specific sub-volumes of the trapped insect. In spot 2, 3 and 5 Fe is most likely present as Fe_2O_3, as demonstrated by the excellent overlap between the unknown spectra with that obtained from the Fe_2O_3 standard (red in ***Fig.7.11*, right**). Unfortunately, Spot 1 and 4 are still to be identified.

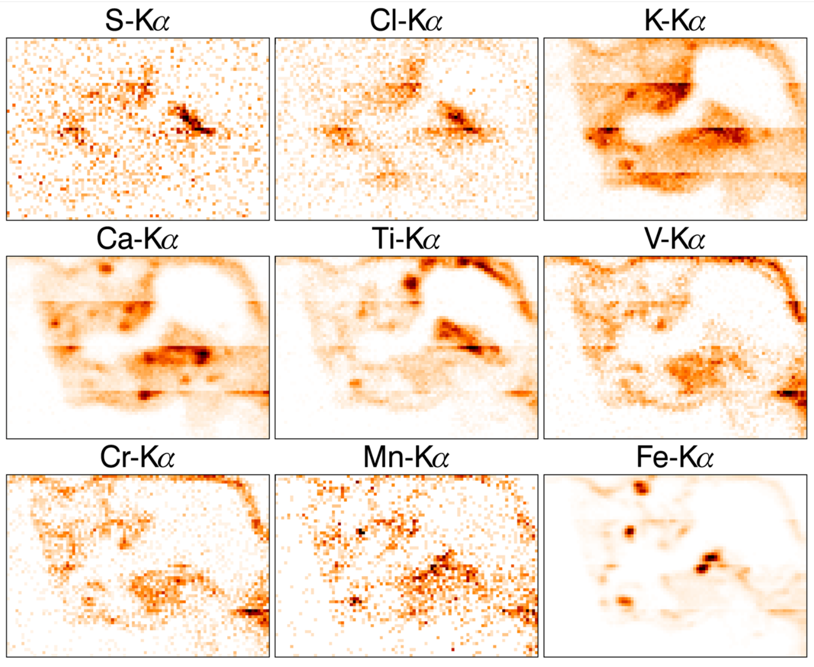

Figure 7.10: *Mapping results of the insect trapped in amber using SR.*

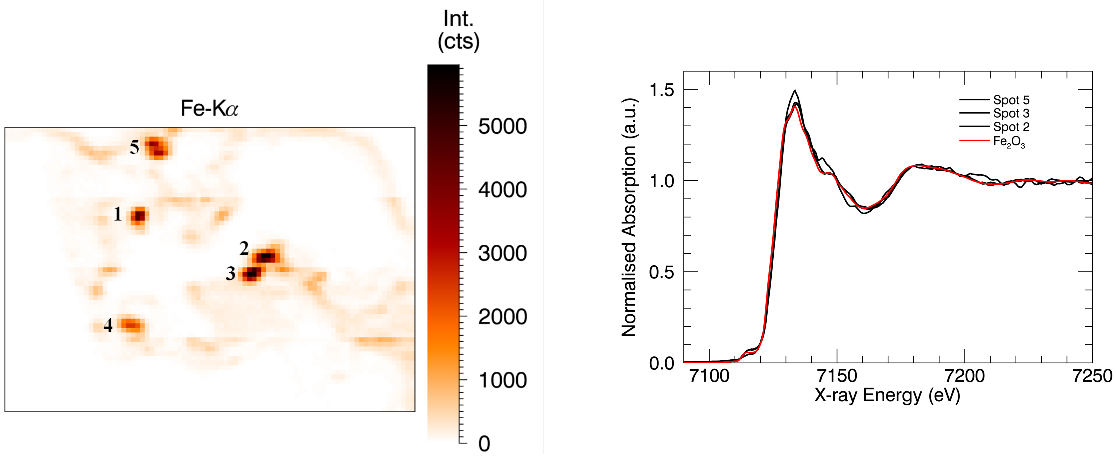

Figure 7.11: *XANES results. Left: Fe element map where the spots with high intensity are indicated and on these spots: XANES measurements were executed.*

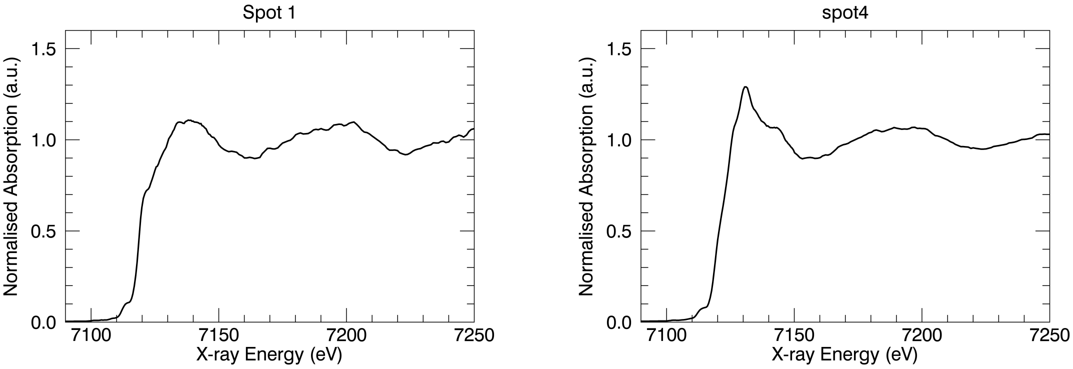

Figure 7.12: *XANES results of spot 1 (left) and 4 (right).*

7.4 Conclusion

This chapter gives an outlook towards more advanced non-destructive 3D micro-XRF/XAS experiments at SR-sources to be applied in the field of e.g. palaeontology. As a demonstration experiments, we demonstrated the possibility of confocal XRF and XANES on insects trapped in amber. By studying insects trapped in amber, it is possible to learn about ecology and environment that existed at the time the resin was exuded. In our research on insects trapped in amber (without extracting the insects), laboratory and confocal SR micro-XRF were used successfully to visualize the distribution of the chemical elements present. The use of confocal SR micro-XRF allows the exploration of trace-level distributions in 3D and unique confocal micro-XANES has been demonstrated to obtain information on the chemical-state of transition metals, such as Fe. In future work, further optimization of confocal micro-XRF/XANES for the 3D chemical analysis of different types of samples will take place.

Bibliography

[1] A. Ross, *Amber: the natural time capsule.* London: The natural history museum, 2010.

[2] I. B. Knor, E. N. Naumova, V. A. Trounova, I. P. Dolbnya, and K. V. Zolotarev, “Biological monitoring of meadow moths by SR-XRF technique,” *Nuclear Instruments and Methods in Physics Research Section A, Accelerators, Spectrometers, Detectors and Associated Equipment*, vol. 359, pp. 324–326, May 1995.

[3] H. G. M. Edwards, D. W. Farwell, and S. E. J. Villar, “Raman microspectroscopic studies of amber resins with insect inclusions,” *Spectrochimica Acta - Part A: Molecular and Biomolecular Spectroscopy*, vol. 68, pp. 1089–1095, Dec. 2007.

[4] D. Michez, A. Nel, J.-J. Menier, and P. Rasmont, “The oldest fossil of a melittid bee (Hymenoptera : Apiformes) from the early Eocene of Oise (France),” *zoological journal of the linnean society*, vol. 150, pp. 701–709, Aug. 2007.

[5] M. Lak, D. Neraudeau, A. Nel, P. Cloetens, V. Perrichot, and P. Tafforeau, “Phase contrast X-ray synchrotron imaging: Opening access to fossil inclusions in opaque amber,” *microscopy and microanalysis*, vol. 14, pp. 251–259, June 2008.

[6] M. Lak, G. Fleck, D. Azar, M. S. E. Fls, H. F. Kaddumi, D. Neraudeau, P. Tafforeau, and A. Nel, “Phase contrast X-ray synchrotron microtomography and the oldest damselflies in amber (Odonata: Zygoptera: Hemiphlebiidae),” *zoological journal of the linnean society*, vol. 156, pp. 913–923, Aug. 2009.

[7] C. S. Schnohr and M. C. Ridgway, “Introduction to X-Ray Absorption Spectroscopy,” in *X-Ray Absorption Spectroscopy of Semiconductors* (C. S. Schnohr and M. C. Ridgway, eds.), pp. 1–26, Springer, 2015.

Summary and conclusions

Conservation and restoration of art objects and cultural heritage materials are of a major concern worldwide. Advanced scientific methods and techniques may help in this respect to acquire a better understanding of the applied ancient production technology, and proved to be important in studies of authenticity or as diagnostic tools for preservation purposes. A main practical activity of this PhD work was to apply non-destructive/non-invasive analytical techniques on cultural heritage objects in order to reveal their elemental composition and its structure.

Acquiring full knowledge of the employed x-ray based scientific instrumentation was regarded as indispensable to effectively obtain and to interpret the resulting spectroscopic data. So, prior to investigating the cultural heritage objects, a real effort has been made to fully understand each of the applied methodology, so that they could be optimally employed taking into account possible constraints or limits that may apply. Before performing the actual scientific experiments, sampling and sample preparation are vital steps, very often imposed by the applied technique. E.g., the investigation of structures that are heterogeneous on the microscopic scale a dedicated sample preparation technique may be necessary to obtain reliable results from the selected objects. Methods that were used in this work are x-ray based techniques including XRF (x-ray fluorescence spectrometry) and micro-XRF (laboratory and synchrotron), SEM (scanning electron microscopy), and XRD (x-ray diffraction). Raman spectroscopy was added to this multi-methodological approach enhancing data interpretation. Experiments were preferably performed in the laboratories of the UGent-XMI group when possible, but in specific projects portable instrumentation was used to obtain results on site.

A major subject of this PhD work is the study of Antwerp Majolica. Majolica refers to earthenware covered with a layer of white opaque tin glaze, decorated with colored pigments. The microstructure and chemical composition of this type of glaze applied on an earthenware body are related to the materials used and the technological skills of the potters/manufactures in a specific historical period, and eventually information is obtained on the related (production) defects, that are the delicate zones in the object subjected to deterioration or alteration over time.

Within a project of Melissa Vandevijvere (Antwerp University, Department of Conservation/Restauration), a set of 30 majolica was selected from a vast amount of excavated artefacts found in Antwerp. Dating based on style of decoration and archaeological records indicates that these tiles cover a period of eight decades (1550-1630) of active majolica production centers in Antwerp. Because of the heterogeneous character of the material, the imaging capabilities SEM and micro-XRF were indispensable for the study of the multi-layered structure, identification of inclusions, retrieval of the matrix, minor and trace element composition of the glaze and the body, and identification of the coloring pigments. For each majolica sample, XRF measurements of several points-of-interest from micro-XRF line scans performed across the multi-layered structure were quantified. Based on the PCA representation of the derived quantified data set of the body, one does not observe significant differences amongst the 30 majolica samples (originating from different Antwerp majolica workshops). Comparison with majolica data from Italian, Portuguese and Spanish origin, it is observed that the white body part of Antwerp majolica contains significantly more CaO. This is indicating that Antwerp majolica workshops followed their own specific manufacturing process.

For the *in situ* study of the unique Antwerp majolica floor of Rameyenhof castle (Gestel, Belgium) experiments were performed on site by a multidisciplinary team using photography, optical microscopy, and portable complementary analytical instrumentation, including hXRF and MArtA. By this the major, minor and trace element signature of the tiles dated 16^{th} to 17^{th} century could be obtained, and used pigments could be identified. The additional study of a medallion, stored at the Rubens House Museum (Antwerp Belgium), confirmed that it was once replaced in the floor by another medallion.

This *in situ* multi-method and multidisciplinary approach performed in Rameyenhof was also applied for the study of a notorious oil-on-panel painting “Mad Meg” by the Flemish renaissance artist Pieter Bruegel the Elder, exhibited in museum Mayer van den Bergh (Antwerp, Belgium). Next to the *in situ* chemical characterization of this masterpiece employing hXRF and MArtA, also a mobile Surface Monitor XRF/XRD instrumentation was applied. The identification of the pigments is essential information for conservation and restoration purposes.

The application of the portable Surface Monitor XRF/XRD instrumentation requested a full characterization and practical knowledge how to efficiently use this combined XRF/XRD technique as time constraints are typically set when performing the actual experiments *in situ.* A case study on pigment identification with this instrument demonstrates its potential in studies of paintings. It can be concluded that this commercially available light-weight instrument is able to identify, in a non-destructive way, the main crystalline phases present in a variety of samples of different size with relative weak constrains regarding the sample size and position.

As a final application, to demonstrate the more advanced three-dimensional confocal micro-XRF/XAS methodology using synchrotron radiation, insects trapped in amber were investigated. The host material is a fossilized resin exuded from the bark of trees acting as a protective container for the insects and other organisms that have been trapped. The combined 3D micro-XRF/XAS results, performed at beamline L of HASYLAB (DESY, Hamburg, Germany), showed the 3D microscopic Fe distribution and speciation within the insects that were trapped in amber without actually the need for sample preparation.

The examples shown in this work demonstrate that XRF spectroscopy in a multi-method approach is a powerful tool for studying cultural heritage objects. The presented combined techniques are non-destructive methods providing complementary information. The availability for most of these techniques of mobile or portable instrumentation allows effective *in situ* analysis.

Samenvatting en conclusies

Wereldwijd is er een enorme bezorgheid over het bewaren en het behoud van het cultureel erfgoed. Vooruitstrevende wetenschappelijke methodes en technieken zijn een essentieel onderdeel voor de identificatie van materialen aanwezig in deze historische objecten en alle ontwikkelingen daaromtrent. Deze methodes kunnen ons ook helpen in het beter begrijpen hoe de oude meesterontwerpers van kunsthistorsiche objecten te werk gingen in hun tijd. Moderne analytische methodes zijn onontbeerlijk in het bestuderen van de echtheid van voorwerpen en kunnen ook toegepast worden als diagnostische technieken om de conservatie van objecten in de praktijk te kunnen omzetten. Het doel van dit doctoraatswerk was om het nut van voornamelijk X-stralen gebaseerde technieken gecombineerd met andere moderne (aanvullende) analytische technieken te bewijzen in de mogelijkheid om chemische/structurele informatie over objecten van cultureel erfgoed te achterhalen. Dit werk toont aan hoe (hoog-technologische) wetenschappers met hun expertise succesvol kunnen samenwerken met experten uit de kunstwereld (o.a. kunsthistorici, conservators en curators) die verantwoordelijk zijn voor het in stand houden en organiseren van collecties van kunstobjecten, net als het verspreiden van de nieuwste resultaten die behaald worden op het gebied van wetenschappelijk onderzoek op kunsthistorische voorwerpen. De niet-destructive en niet-invasieve analyse van deze voorwerpen kan nieuwe inzichten en noodzakelijke informatie verwerven over de structuur, samenstelling (op microscopische schaal), herkomst, geschiedenis en hoe deze geobserveerde objecten het best worden bewaard. Naast het bewijzen van de noodzaak om onderzoek op cultureel-historische kunstvoorwerpen uit te voeren zal ook de optimalisatie en karakterisatie van een X-stralen gebaseerd instrument voor de analyse van deze voorwerpen, onder de loep genomen worden.

Wanneer een waardevol kunstvoorwerp onderzocht wordt, is de belangrijkste bezorgheid dat het voorwerp in zijn geheel bewaard blijft zowel voor, tijdens als na de analyse. Archeologen en curators laten meestal niet toe dat er schade toegebracht wordt aan de objecten, zelfs geen microscopische, zo goed als onzichtbare schade. Deze voorwaarden sturen de eigenschappen van de te gebruiken analytische technieken: niet-destructief, snel, gevoelig, universeel en veelzijdig. Deze laatste twee eigenschappen slaan op het feit dat bij de analyse van het materiaal, dit met een minimum aan monstervoorbereiding moet uitgevoerd worden en toepasbaar moet zijn op alle mogelijke vormen qua objecten en met de mogelijkheid om naast de gemiddelde samenstelling ook zeer lokale informatie uit gebieden op het voorwerp met micrometer dimensies te bekomen. Omdat het niet altijd mogelijk is om werken te verplaatsen vanuit musea of andere tentoonstellingsruimtes naar het onderzoekslaboratorium is ook de beschikbaarheid van mobiele of draagbare (instrumenten waarmee met de hand kan gemeten worden) instrumentatie van essentieel belang in de exploratie van kunstvoorwerpen.

De focus van dit doctoraatswerk is het gebruik van een verscheidenheid aan instrumentatie, zowel laboratorium, als mobiele, waarvan de meerderheid gebaseerd zijn op X-stralen fluorescentie (XRF), om verschillende unieke werken te bestuderen. Daarom vat hoofdstuk 2 uit dit werk aan met de basisprincipes van dit type straling en worden de geheimen achter de interactie van deze X-stralen met materie onthult om op die manier kwalitatieve en kwantitatieve informatie te bekomen over de materialen gebruikt in de verschillende onderzochte kunsthistorische voorwerpen. Het onderzoek van deze voorwerpen werd uitgevoerd door gebruik te maken van verschillende soorten spectrometers waarvan de meeste beschikbaar zijn in het labo en/of mobiel, of zelfs door het gebruik van in een synchrotron opgewekte X-stralen (en dus verplaatsbare objecten). Het is van essentieel belang dat de verschillende onderdelen, waaruit deze verschillende instrumenten zijn opgebouwd, en waarmee X-stralen worden geproduceerd en gedetecteerd in detail worden uitgelicht om op deze manier de voor- en nadelen van elk instrument (gebruikt in dit werk) onder de knie te hebben. Bij voorkeur gebeurt een onderzoek op een kunstvoorwerp door gebruik te maken van verschillende soorten technieken (en dus niet enkel X-stralen gebaseerd) waardoor de individuele analytische resultaten kunnen bevestigd en/of aangevuld worden, wat de interpretatie van deze resultaten zal vergemakkelijken. Elk instrument verschilt in de manier waarop de metingen dienen uitgevoerd te worden en het mobiele equivalent zal altijd onder suboptimale condities werken in vergelijking met het laboratorium instrument waarmee in optimale omstandigheden kan gewerkt worden. Daarom werd in Hoofdstuk 2, naast de X-stralen gebaseerde technieken, ook de principes van twee andere gebruikte instrumenten behandeld, namelijk scanning elektronen microscopie (enkel beschikbaar als laboratorium instrument) en Raman spectroscopie (in dit werk enkel gebruik gemaakt van het mobiele instrument, namelijk de MArtA). Al deze technieken werden gebruikt in de succesvolle analyse van een brede waaier van kunsthistorische voorwerpen eveneens beschreven in dit hoofdstuk.

Een eerste belangrijk project beschreven in dit werk was de studie van majolica waarbij de structuur (op microscopische schaal) en chemische samenstelling van dit soort keramiek werd achterhaald. Majolica is opgebouwd uit gebrande klei, met daarop een bont gekleurde beschildering van glazuur waarbij beide lagen zeer waardevolle informatie bevatten over de gebruikte materialen en technieken van de pottenbakkers uit een specifieke periode. Deze informatie kan ook gerelateerd worden aan productiefouten uit die tijd, in de delicate zones van het te conserveren object. De onderzochte set bevat 30 verschillende majolica tegels afkomstig van vier verschillende productieplaatsen in het centrum van Antwerpen (België), gemaakt tussen de 16^{de} en 17^{de} eeuw. Het gebruik van micro X-stralen fluorescentie (zowel laboratorium als synchrotron) en scanning elektronen microscopie gecombineerd met een energie-dispersieve X-stralen spectrometer lieten toe om verschillende analytische resultaten op ingebedde fragmenten van deze tegels te bekomen. Conservators gaven ons de toestemming om van elke tegel een klein fragment te nemen en dit in te bedden. Tijdens dit onderzoek ging onze aandacht voornamelijk naar de structuur, op microscopische schaal, en samenstelling van de majolica glazuurlaag en aardewerk waarbij beiden zeer waardevolle informatie bevatten over de gebruikte materialen en technieken. Dit liet ons toe om de speciefieke major,minor en sporen-elementen van Antwerpse majolica uit de 16^{de} en 17^{de} eeuw te kennen en dus eigenlijk een soort vingerafdruk te bekomen van Antwerpse majolica en voor de verschillende kleuren gebruikt in de tekeningen aanwezig op de tegels. Naast het vastleggen van de samenstelling van Antwerpse majolica, werd ook de opbouw van de glazuurlaag onder de loep genomen, gebaseerd op XRF scans, zowel van volledige oppervlakken als lijnen doorheen de ingebedde fragmenten. Hierbij kon vastgesteld worden dat de glazuurlaag opgebouwd is uit twee lagen en deze bevindingen werden bevestigd aan de hand van fotos gemaakt met de scanning elektronen microscoop. Als laatste onderdeel van dit project rond Antwerpse majolica tegels werden alle bekomen XRF resultaten gekwantificeerd en deze cijfers lieten ons toe om een database aan te leggen waaruit opnieuw de element samenstelling (zowel van de major, minor als sporen elementen) kon worden afgeleid maar ook informatie over de equivalentie aanwezig in het productieproces van majolica van de vier verschillende productieplaatsen. Hierbij werd ook afgeleid dat de Antwerpse pottenbakkers het meest geïnspireerd werden door hun collega's uit Italië.

Naast het vastleggen van de typische samenstelling van Antwerpse majolica, aanwezig in de aardewerken basis en de kleurijke glazuur, werd ook een mogelijkse Antwerpse majolica vloer (ter plaatse) onderzocht geproduceerd door de pottenbakkers gehuisvest te Antwerpen tussen de 16de en de 17de eeuw. Deze unieke en waarschijnlijk enigste gekende 16de eeuwse Antwerpse majolica tegelvloer bevindt zich in een hoektoren van het Rameyenhof kasteel te Gestel (België). Dit uitzonderlijk kunstobject werd ter plaatste geanalyseerd door gebruik te maken van een bijzondere combinatie van non-destructieve en mobiele instrumententatie, waaronder een handheld XRF instrument om informatie qua chemische element samenstelling te bekomen en het mobiele Raman instrument (MArtA) die dan op zijn beurt gegevens verzamelt over de structurele en moleculaire samenstelling. Beide spectrometers werden gebruikt op de vloer aanwezig in het Rameyenhof kasteel alsook op een tweede, gelijkaardig medaillon (die ter bewaring ligt in het Rubenshuis museum te Antwerpen) maar dan uitsluitend met de handheld XRF. Deze instrumenten stelden ons in staat om de karakteristieke hoofd- en sporen-elementen van 16de - 17de eeuwse Antwerpse majolica terug te vinden op deze vloer en dus de bouw van deze vloer door Antwerpse pottenbakkers te bevestigen. Daarnaast werden andere kleuren teruggevonden op het kunstwerk gemaakt op de vloer dan het beperkt aantal kleuren op de losse tegel collectie en de pigmenten gebruikt in deze kleuren werden eveneens geïndentificeerd. Gebruik makende van de kennis rond de chemische element samenstelling van de witte glazuur, specifiek de aanwezigheid van zink, was het mogelijk om de oorsprong van de kasteelvloer en de twee centrale medaillons te achterhalen. Al de resultaten over Antwerpse majolica is terug te vinden in Hoofdstukken 3 en 4.

Een ander voorwerp van cultureel erfgoed dat geanalyseerd werd, als onderdeel van dit werk, opnieuw gebruik makende van een andere combinatie van verschillende beschikbare mobiele analytische instrumentatie, is een bekend olie-op-doek schilderij van de Vlaamse renaissance schilder Pieter Bruegel de Oude. Het desbetreffende schilderij is "Dulle Griet" genaamd, een figuur van de Vlaamse folklore, en tentoon gesteld in het Mayer van den Bergh musuem (te Antwerpen, België). De chemische karakterisatie van dit meesterwerk werd opnieuw te plaatste uitgevoerd gebruik makende van dezelfde mobiele toestellen als voorheen (handheld XRF en MArtA) gecombineerd met een mobiel instrument dat X-stralen fluorescentie combineerd met X-stralen diffractie. Hoofdstuk 5 bevat de materiele bepaling van de gebruikte pigmenten en verschillende onderlagen op het schilderij alsook het verifiëren van twee belangrijke historische hypothesen. Onder andere de economische manier van schilderen door Pieter Bruegel de Oude werd in vraag gesteld en deze werd beantwoord door de resultaten van de metingen op het pigment aanwezig in de geschilderde blauwe schuit (bovenaan het schilderij) te gebruiken. De geïdentificeerde pigmenten, gebruikt in het schilderij, waren smalt voor de blauwe kleur (aanwezig in alle blauw geschilderde oppervlakken van het meesterwerk), koper-resinaat (waarschijnlijk) voor de groene kleur, vermiljoen voor de rode kleur en het loodwitte pigment werd gebruikt in verschillende kleuren. Het vaststellen van de chemische samenstelling van de gebruikte pigmenten was zeer belangrijk in het onderzoek van dit meesterwerk, niet alleen door hun cultureel/historische relevantie en nodige kennis voor restoratie/conservatie maar mede ook omdat pigmenten de meest attractieve doelen zijn voor wetenschappelijke studies doordat hun kleur kan gezien worden als een schoonheidsideaal.

Tijdens het onderzoek van het Dulle Griet schilderij werd gebruik gemaakt van een multi-methode inclusief het mobiele instrument dat X-stralen fluorescentie en diffractie combineert. Dit commercieel beschikbare mobiele toestel werd in 2012 aangekocht door de vakgroep Analytisch Chemie van de Universiteit Gent en combineert dus X-stralen diffractie (XRD) met XRF om zowel chemische element- als kristalsamenstelling op een simultane manier te kunnen identificeren. De volledige karakterisatie en het uitgebreid testen van dit nieuwe toestel was een onderdeel van dit doctoraatswerk en de resultaten kunnen teruggevonden worden in Hoofdstuk 6. Het instrument, Surface Monitor genaamd, is aangekocht bij het bedrijf Assing S.p.A. uit Italië en is opgebouwd uit een koper of molybdeen gebaseerde X-stralen buis en een Silicon-Pin diode detector om de fotonen afkomstig van het bestraalde monster te kunnen opvangen. De X-stralen buis en detector zijn beide bevestigd op een XRD protractor zodat de Bragg-Brentano θ:θ methodologie kan toegepast worden. De Surface Monitor is één van de lichtste en meest compacte instrumenten van zijn soort (slechts 3,5 kg) en is dus zeer bruikbaar bij onderzoek dat ter plaatse moet uitgevoerd worden op voorwerpen van cultureel erfgoed. De gebruiksvriendelijke software laat toe om zowel het collecteren van data (en dus het uitvoeren van de metingen te sturen) als een volledige data analyse van de opgenomen spectra gebruikmakende van de ICDD (International Centre for Diffraction Data) databank uit te voeren. De karakterisatie van het instrument werd gecombineerd met een volledige case studie rond pigment identificatie om op die manier voeling te krijgen met de mogelijkheden van het toestel. Daarnaast kon dit toestel ook gebruikt worden op de analyse van lood gelegeerde letters, die gebruikt werden in de boekdrukkunst, dat dan model stond als "echt" kunsthistorisch voorwerp. De resultaten tonen aan dat dit lichtgewicht, commercieel beschikbare toestel in staat is om de kristallografische samenstelling van een waaier van monsters (van verschillende grote) te identificeren op een niet-destructieve manier met zeer geringe limieten qua monster grootte en positie.

In Hoofdstuk 7 werd de meer vooruitstrevende drie-dimensionale, confocale micro-XRF/XAS techniek (gebruik makende van synchrotron straling) belicht, ook een combinatie van niet-destructieve technieken, met toepassing in het onderzoek van de paleontologie. Synchrotron geïnduceerde X-stralen fluorescentie spectroscopie is een niet-destructieve methode voor kwalitatieve en kwantitatieve bepaling van chemische elementen met detectielimieten onder sub-ppm niveau. X-stralen absorptie spectroscopie (XAS) is een gelijkaardige X-stralen gebaseerde techniek dat het mogelijk maakt om informatie omtrent de lokale chemische, elektronische en structurele configuratie van een specifiek chemisch element in het monster te bekomen. Beide technieken werden toegepast in een confocale manier van meten om op die manier directe informatie te bekomen van een specifiek volume (microscopische dimensies) binnenin een monster. Beide technieken werden toegepast op insecten die gevangen zaten in amber om, zonder de insecten te verwijderen uit de amber, chemische informatie over deze insecten te bekomen. Amber, juister spreekt men van barnsteen, is een fossiele hars die afkomstig is van naaldbomen en deze hars is miljoenen jaren geleden uit de bomen gedropen en daarna versteend. Insecten blijven soms hangen aan dit plakkerig goedje en na miljoenen jaren vormt de versteende hars, inclusief het insect, eigenlijk een perfect reservoir voor deze organismen. Dit maakt dat de analyse van deze insecten, nog ingekapseld in de amber, een zeer interessant onderwerp vormen voor onderzoek. De resultaten van de gecombineerde micro-XRF/XAS metingen werden besproken, uitgevoerd aan beamline L van HASYLAB (DESY/Hamburg/Duitsland) welke waardevolle informatie geven omtrent de ijzer distributie en oxidatietoestand van de insecten omgeven door amber.

Tot slot, XRF spectroscopie gecombineerd met andere technieken is een zeer krachtig hulpmiddel in het onderzoek van kunsthistorische voorwerpen. Alle gebruikte technieken zijn niet-destructief en resulteren in een volledig kennis qua samenstelling van het voorwerp waarnaast voor de meeste technieken een mobiel toestel beschikbaar en dus geschikt voor onderzoekswerk ter plaatse. Dezez verschillende spectroscopische tehcnieken, gecombineerd met uitgebreide data verwerkingsprocessen geven aanleiding tot een meer accurate kennis over de chemische samenstelling van de materialen uit het verleden en de invloed ervan op de herkomst van deze voorwerpen. Toekomstig onderzoek kan onder andere bestaan uit het meer uitgebreid onderzoeken van de mogelijken van de software in het commercieel beschikbare XRF/XRD toestel wat hopelijk resulteert in kwalitatief betere evaluatie van XRD spectra alsook de identificatie van de aanwezige stoffen.

Appendix

Appendix A

XRD spectra of single pigments

During the characterization and testing the performance of the new mobile XRF/XRD Surface Monitor instrument, a number of test measurements were performed on a selection of 16 known pigments (single layer) mounted on tape to verify if it is possible with the Surface Monitor to obtain useful XRD spectra. If this is the case, we also test if it is possible to identify the spectra based on the available ICDD database. More information can be found in chapter 6. In this chapter, only the best results out of these 16 pigments are shown there, all the other spectra (whether or not with possible identification) are shown here.

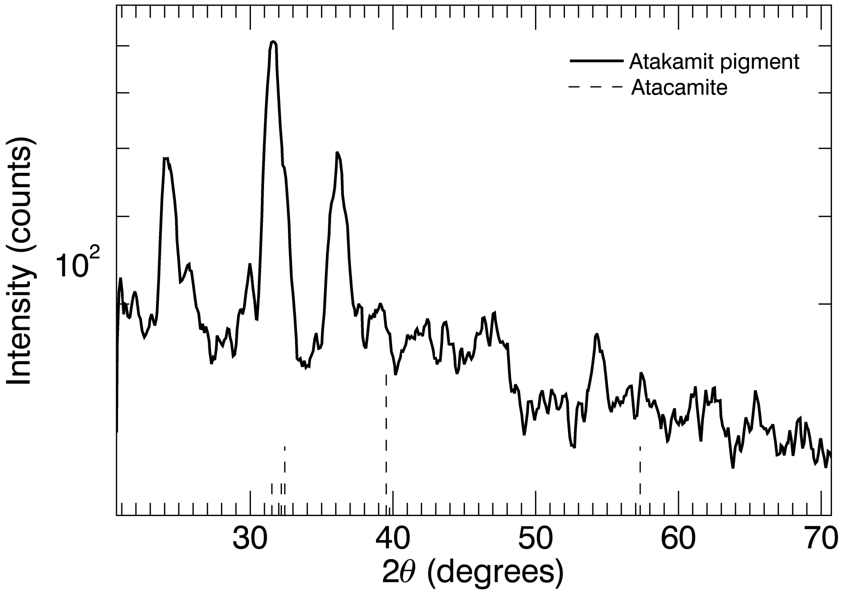

Figure A.1: *Atakamit pigment: No good match between spectrum of pigment and database.*

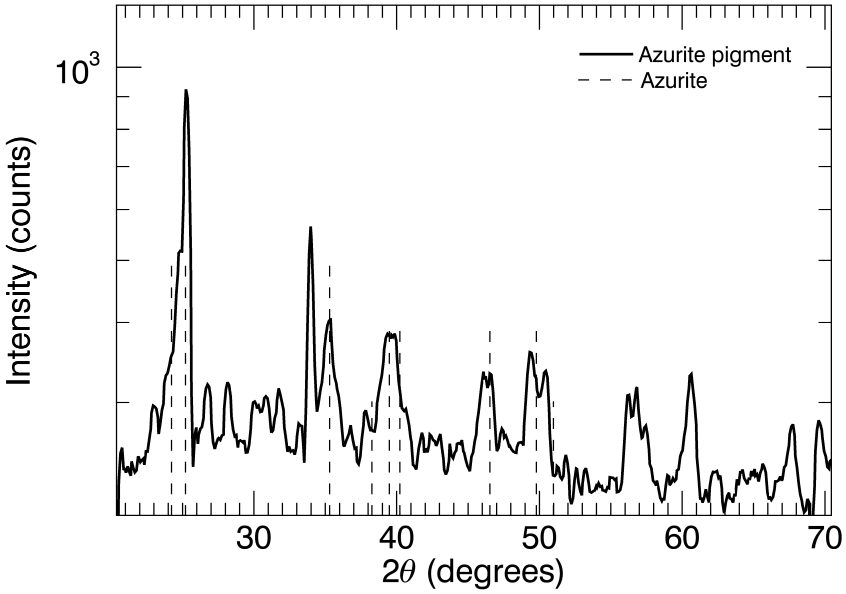

Figure A.2: *Azurite pigment: Match between spectrum of pigment and database but peaks available without knowledge of origin.*

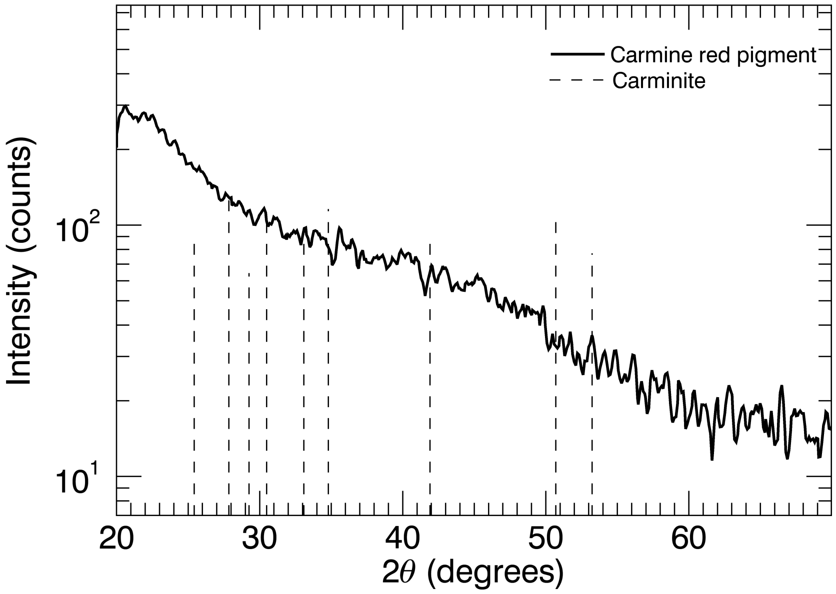

Figure A.3: *Carmin red pigment: No detectable diffraction peaks.*

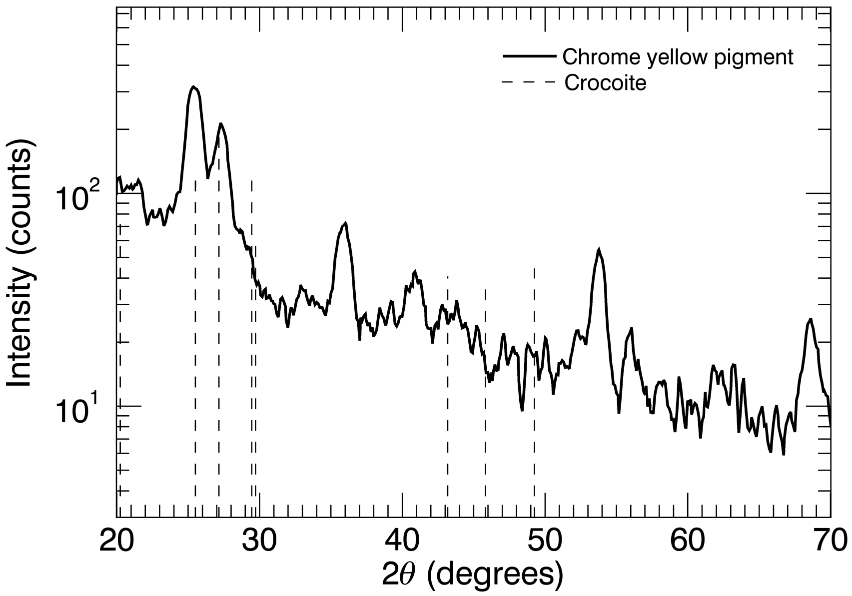

Figure A.4: *Chrome yellow pigment: Match between spectrum of pigment and database but peaks available without knowledge of origin.*

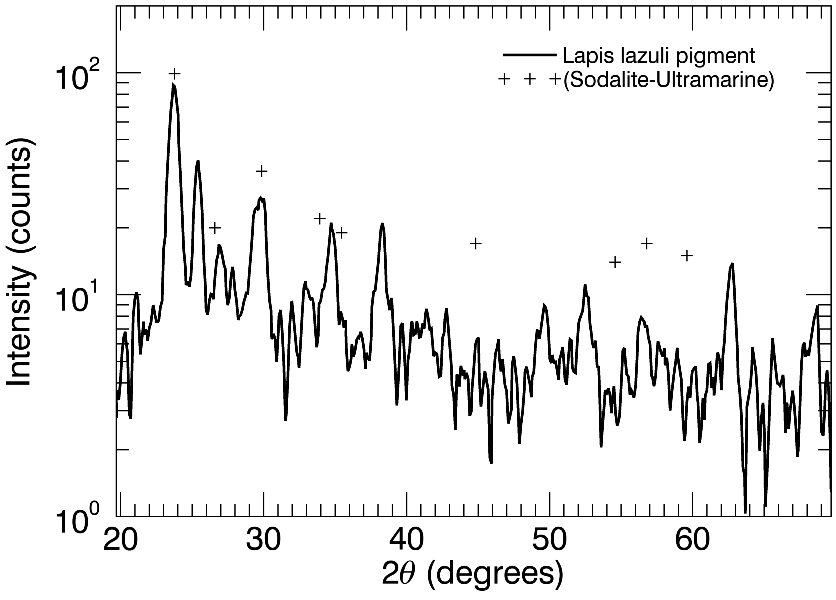

Figure A.5: *Lapis lazuli (or ultramarine) pigment: Very low intensities for the diffraction peaks which made a good match almost impossible.*

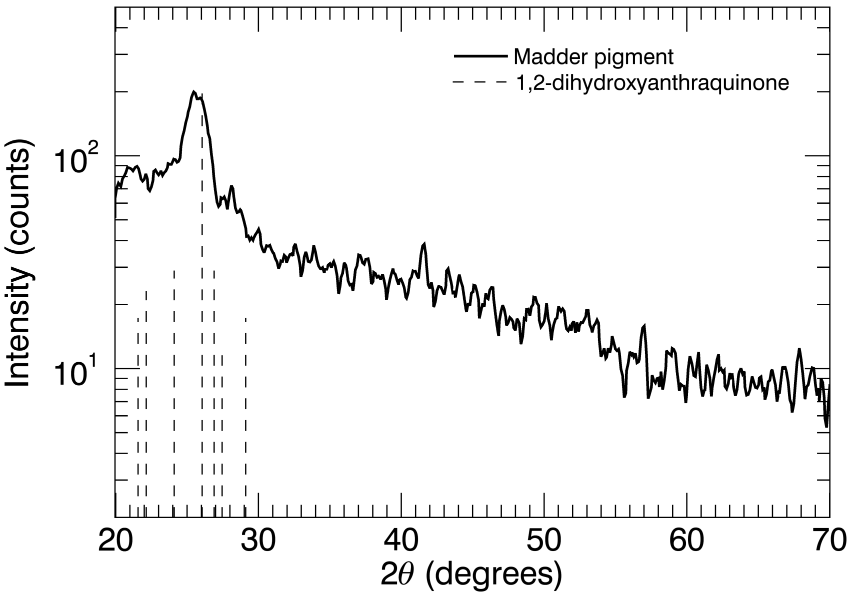

Figure A.6: *Madder pigment: Madder is an organic pigment which give rise to almost no intensity for the diffraction peaks and so no good match possible.*

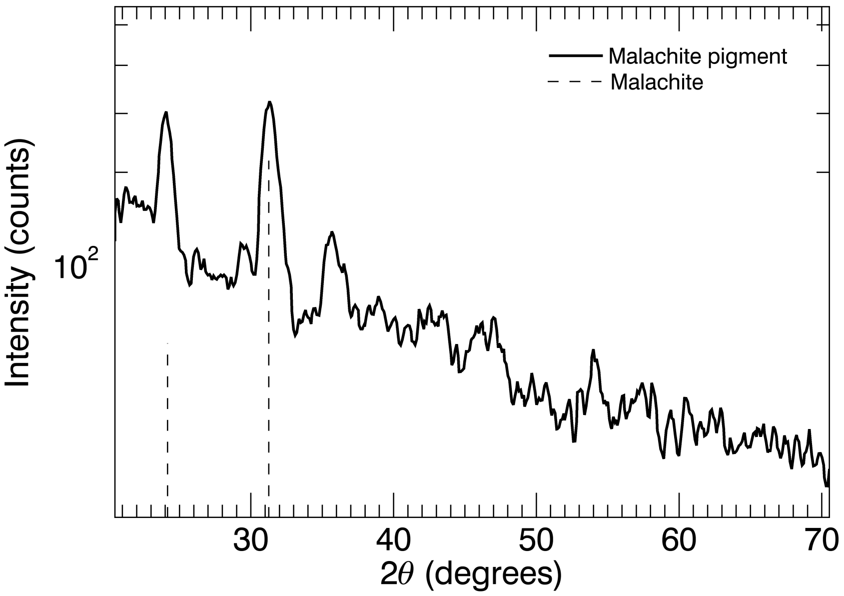

Figure A.7: *Malachite pigment: Match between spectrum of pigment and database but peaks available without knowledge of origin.*

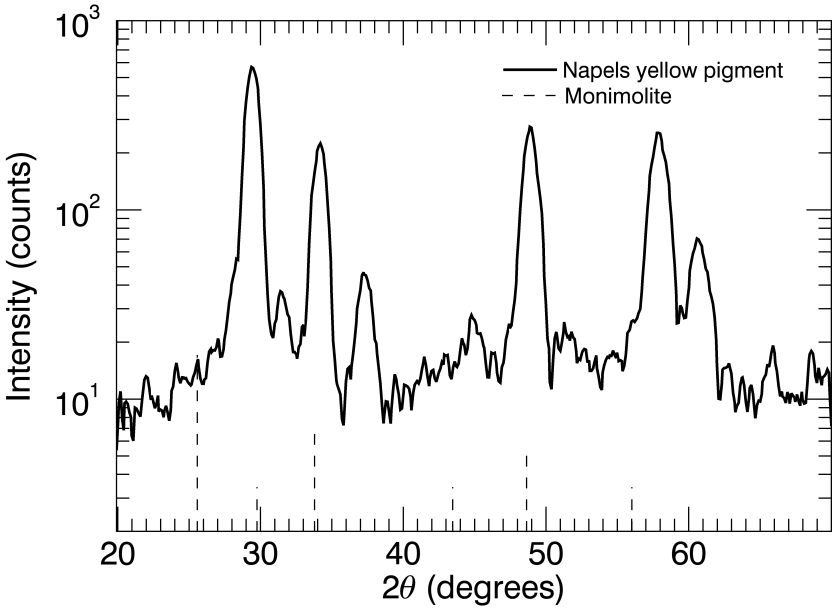

Figure A.8: *Napels yellow pigment: No good match between spectrum of pigment and database.*

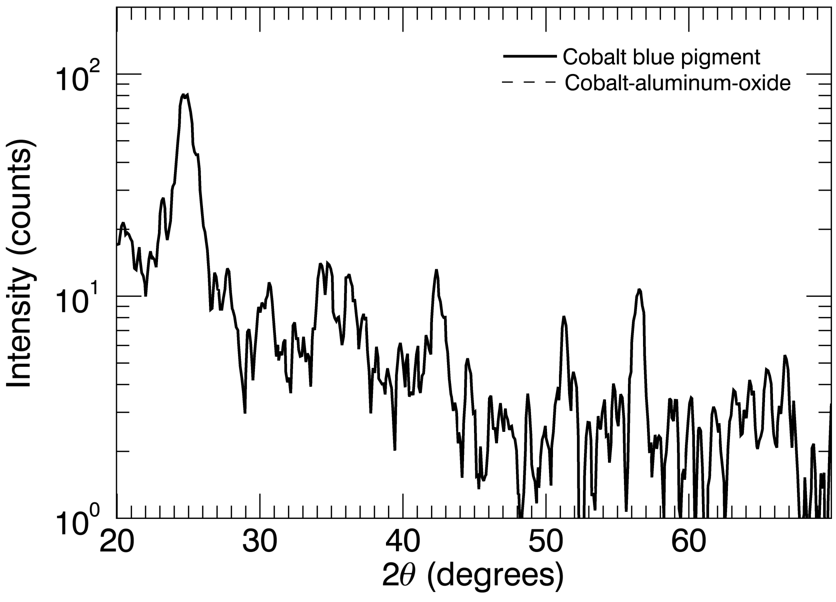

Figure A.9: *Cobalt blue pigment: Very low intensities for the diffraction peaks which made a good match almost impossible.*

Appendix B

Publications & activities

B.1 List of (contributions to) Publications

B.1.1 A1 (ISI Web of Science – Science Citation Index)

- L. Van de Voorde, B. Vekemans, E. Verhaeven, P. Tack, R. De Wolf, J. Garrevoet, P. Vandenabeele, L. Vincze, Analytical characterization of a new mobile X-ray fluorescence and X-ray diffraction instrument for non-destructive analysis, Spectrochimica acta part B 110 (2015).

- P. Storme, A. Selucka, K. Rapouch, M. Mazik, F. Vanmeert, K. Janssens, L. Van de Voorde, B. Vekemans, L. Vincze, J. Caen, K. De Wael, Composition and corrosion forms on archaeological and non-archaeological historic printing letters from the Moravian Museum, Memorial of Kralice Bible, the Czech Republic and the Museum Plantin-Moretus Antwerp, Belgium, Les Dossiers de l'IPW 15 (2015).

- L. Van De Voorde, M. Vandevijvere, B. Vekemans, J. Van Pevenage, J. Caen, P. Vandenabeele, P. Van Espen, L. Vincze, Study of a unique 16^{th} century Antwerp majolica floor in the Rameyenhof castle's chapel by means of X-ray fluorescence and portable Raman analytical instrumentation, Spectrochimica acta part B 102 (2014).

- L. Van De Voorde, J. Van Pevenage, K. De Langhe, R. De Wolg, B. Vekemans, L. Vincze, P. Vandenabeele, M.P.J. Martens, Non-destructive in situ study of "Mad Meg" by Pieter Bruegel the Elder using mobile X-ray fluorescence, X-ray diffraction and Raman spectrometers, Spectrochimica acta part B 97 (2014).

- A. Deneckere, B. Vekemans, L. Van de Voorde, P. De Paepe, L. Vincze, L. Moens, P. Vandenabeele, Feasibility study of the application of micro-Raman imaging as complement to micro-XRF imaging, Applied physics A 106 (2012)

- A. Deneckere, L. De Vries, B. Vekemans, L. Van de Voorde, F. Ariese, L. Vincze, L. Moens, P. Vandenabeele, Identification of Inorganic Pigments Used in Porcelain Cards Based on Fusing

Raman and X-ray Fluorescence (XRF) Data, Applied spectroscopy 65 (2011)

B.1.2 C3 (Conference - meeting abstracts)

- B. Vekemans, L. Van de Voorde, J. Van Pevenage, K. De Langhe, L. Vincze, P. Vandenabeele. Combining Non-destructive Scientific Methods as Tool to Investigate Cultural Heritage Objects. The great scientific exchange (SCIX), Reno, Nevada, USA, September 28 - October 3th 2014 (oral presentation)

- L. Van de Voorde, E. Verhaeven, B. Vekemans, R. De Wolf, P. Vandenabeel, L. Vincze. Use of a novel portable XRF/XRD instrument for studying pigments and model paintings. Synchrotron radiation and neutrons in art and archaeology (SR2A), Paris, France, September 9-12th 2014 (poster presentation)

- L. Van de Voorde, M. Vandevijvere, B. Vekemans, J. Garrevoet, P. Van Espen, J. Caen, L. Vincze. Use of synchrotron based, laboratory and portable micro-XRF techniques for the study of 16^{th}-17^{th} century majolica artifacts from Antwerp (Belgium). Synchrotron and neutron workshop (SYNEW), Antwerp, Belgium, November 28th 2013 (poster presentation)

- L. Moens, B. Vekemans, J. Garrevoet, L. Van de Voorde, M. Vandevijvere and L. Vincze. Non-destructive elemental imaging studies of 16^{th} - 17^{th} century majolica tiles from Antwerp (Belgium) using synchrotron and laboratory based micro-XRF techniques. Seventh International Workshop on Infrared Microscopy and Spectroscopy with Accelerator-Based Sources (WIRMS 2013), Melbourne, Australia, November 10-14th 2013 (poster presentation)

- L. Van de Voorde, M. Vandevijvere, B. Vekemans, J. Van Pevenage, P. Vandenabeele, P. Van Espen, J. Caen, L. Vincze. Use of portable XRF and Raman instrumentation for study of a unique 16^{th} century Antwerp majolica floor in the Rameyenhof castle's (Gestel, Belgium). International congress on X-ray optics and microanalysis (ICXOM 22), Hamburg, Germany, September 2-6th 2013 (poster presentation)

- L. Van de Voorde, J. Van Pevenage, B. Vekemans, K. De Langhe, R. De Wolf, L. Vincze, P. Vandenabeele, M.P.J. Martens. Non-destructive in-situ study of "Mad Meg" by Pieter Bruegel the Elder using mobile analytical instrumentation. Euroanalysis, Warsaw, Poland, August 25-29th 2013 (poster presentation)

- M. Vandevijvere, L. Van de Voorde, K. Witteveen, B. Vekemans, L. Vincze, P. Van Espen, J. Caen. Materiaalonderzoek van een Antwerpse huisnummerplaat in majolica uit de 16^{de} eeuw. Dag Van de Wetenschappen, Antwerp, Belgium, November 25th 2012 (oral and poster presentation)

- M. Vandevijvere, L. Van de Voorde, B. Vekemans, L. Vincze, P. Van Espen, J. Caen. Material Technical Characterisation of Majolica Tiles from Antwerp from the $16^{th}17^{th}$ Centuries by

SEM-EDX and micro-XRF as a Preliminary Study in Conservation and Restoration. Youth in Conservation of Cultural Heritage (Yococu), Antwerp, Belgium, June 18-20th 2012 (poster presentation)

- L. Van de Voorde, M. Vandevijvere, B. Vekemans, J. Van Pevenage, P. Vandenabeele, L. Vincze. Antwerp Majolica Tiles from the $16^{th}17^{th}$ Century: Study of Material Technical Aspects using X-ray Fluorescence Spectroscopy. Youth in Conservation of Cultural Heritage (Yococu), Antwerp, Belgium, June 18-20th 2012 (oral presentation)

- L. Van de Voorde, M. Vandevijvere, J. Van Pevenage, B. Vekemans, P. Vandenabeele, L. Vincze. X-ray Fluorescence Analysis of 16^{th} century Antwerp Majolica Tiles. Euroanalysis, Belgrade, Serbia, September 11-15th 2011 (oral presentation)

- J. Van Pevenage, M. Vandevijvere, L. Van de Voorde, B. Vekemans, L. Vincze, P. Vandenabeele , L. Moens. In situ Raman and XRF analysis of a 16^{th} century Majolica tile floor. 6^{th} International Congress on the Application of Raman Spectroscopy in Art and Archaeology, Parma, Italy, September 58th 2011 (oral presentation)

- A. Deneckere, B. Vekemans, L. De Vries, L. Van de Voorde, P. De Paepe, L. Vincze, L. Moens, P. Vandenabeele. Investigation of porcelain cards using combined spectroscopic techniques. 60^{th} annual Conference on Applications of X-ray Analysis, Colorado, USA), August 15th 2011 (oral presentation)

- L. Van de Voorde, B. Vekemans, G. Silversmit, T. Schoonjans, B. De Samber, L. Vincze. Confocal Micro-XRF/XANES Analysis on Insects Trapped in Amber. 3^{rd} International summerschool Hubert Curien, Molceular and Structural Archaeology, Non-invasive Analysis of Painting Materials, Erice, Sicily, Italy, June 14-21th 2010 (poster presentation)

B.1.3 other publications

- M. Vandevijvere, J. Caen, L. Van de Voorde, B. Vekemans, P. Van Espen, L. Vincze, O. Schalm, Manufacturing Techniques of 16^{th} - 17^{th} Century Majolica Tiles from Antwerp (Belgium): Production Defects and Consequences for Conservation Treatment, Conference Paper ICOM Amsterdam (2013)

- L. Van de Voorde, B. Vekemans, G. Silversmit, K. Appel, A. Deneckere, P. Vandenabeele, L. Moens, L. Vincze, Pigment analysis on porcelain cards using confocal μ-XANES, Report in Hasylab annual report book (2011)

- G. Silversmit, B. Vekemans, T.Schoonjans, L. Van De Voorde, S. Schmitz, K. Appel, F.E. Brenker, L. Vincze, Three-dimensional confocal -XANES on mineral inclusions in natural diamonds, Report in Hasylab annual report book (2009)

B.2 List of Attended Beamtimes: Hamburger Synchrotron Labor (HASYLAB), Hamburg, Germany

I-20130429 EC Full-field 3D XRF-imaging study of metal accumulation, distribution and effects in aquatic invertebrates exposed in complex environments. Project leader: Prof. Dr. Laszlo Vincze.

- October 1-7, 2013: P06

I-20100035 EC Development of new and improvement techniques for the immobilization of redox enzymes onto electrodes. Project leaders: Prof. Dr. Laszlo Vincze and Prof. Dr. Annemie Adriaens.

- Oktober 13-19, 2011: Beamline L
- June 10-14, 2011: Beamline L
- November 12-16, 2010: Beamline L

I-20090058 EC Development of new and improvement techniques for the immobilization of redox enzymes onto electrodes. Project leaders: Prof. Dr. Laszlo Vincze and Prof. Dr. Annemie Adriaens.

- June 2-8, 2010: Beamline L
- November 27-December 1, 2009: Beamline L

II-20070159 EC Development of three-dimensional XRF/XANES microanalysis using confocal detection mode for the non-destructive characterisation of inclusions in diamond. Project leader: Dr. Geert Silversmit.

- March 27-31, 2011: Beamline L
- March 07-15, 2010: Beamline L
- October 16-22, 2009: Beamline L

B.3 Followed courses

Single occurrence course

- 2014: Curios uitgebreide mogelijkheden
- 2014: Training smartboard
- 2012: Photoshop
- 2011: Archeometrie, Prof. A. Adriaens - 15/20

- 2011: Multivariate Resolution, R. Tauler
- 2011: Introduction to PCA and PLS, R. Bro
- 2011: Advanced Academic English: Presentation skills in English - 13/20, English Proficiency for presentations 14/20, Academic Poster 15/20
- 2010: Matlab Recipes for Earth Sciences, Trauth Martin and Finke Peter
- 2010: Non-invasive Analysis of Painting Materials, D. Strivay and P. Walter
- 2010: Workshop Basisassistententraining

Nijverheidshelper

- 2015: Herhalingscursus module 4
- 2014: Herhalingscursus module 3
- 2013: Herhalingscursus module 2
- 2012: Herhalingscursus module 1
- 2011: Basisopleiding

Brandweeropleiding

- 2012: Herhalingscursus
- 2010: Basisopleiding

B.4 Overview of practica and exercises related activities

Bachelor projects

- 2014: Can X-ray spectroscopy help us to become a 'Robert Langdon' to discover hidden secrets of cultural heritage?
- 2013: Invitations for parties around 1846: are they real or are we uninvited?
- 2012: Cultural heritage objects and analytical chemistry: a good marriage?
- 2011: Invitations for parties around 1846: are they real or are we uninvited?
- 2010: Invitations for parties around 1846: are they real or are we uninvited?

Exercises analytische chemie Prof. Dr. A. Adriaens 2^{de} Bachelor Biochemie en Biotechnologie

- 2013
- 2012
- 2011

Practica analytische chemie: beginselen Prof. Dr. K. Strijckmans 2^{de} Bachelor Chemie

- 2013
- 2012
- 2011
- 2010
- 2009

Practica analytische chemie: beginselen Prof. Dr. K. Strijckmans 2^{de} Bachelor Biochemie en Biotechnologie

- 2014
- 2013

Pratica analytische chemie Prof. Dr. K. Strijckmans 2^{de} Bachelor Geologie

- 2014

Pratica analysis and abatement of Water, Partim: Chemistry Prof. Dr. Karel Strijckmans, Prof. Dr. Arne Verliefde and Dr. Karen Van Hoecke Master of Science in Environmental Sanitation

- 2013
- 2012
- 2011
- 2010

Practica advanced spectroscopic methods of analysis (XRF) Prof. Dr. L. Vincze 1^{ste} Master Chemie

- 2012
- 2011
- 2010

Practica spectroscopische analysemethoden Prof. Dr. F. Vanhaecke and Prof. Dr. K. Strijckmans 2^{de} Bachelor Chemie

- 2014
- 2013
- 2012
- 2011
- 2010